SYNTHESIS OF PHOTOCLEAVABLE SUPRAMOLECULAR ROTAXANES TOWARDS THE CONTROLLED BINDING OF NUCLEIC ACID THREE-WAY JUNCTIONS

by

CATHERINE AMELIA JOSEPHINE HOOPER

A thesis submitted to the University of Birmingham for the degree of

DOCTOR OF PHILOSOPHY

Department of Chemistry

College of Engineering and Physical Sciences

University of Birmingham

January 2024

Abstract

This work aimed to develop a supramolecular system which is responsive to an external trigger for the controlled formation of nucleic acid three-way junctions. Metallo-helicates capable of junction formation were modified with photocleavable capping groups and encapsulated in cucurbit[10]uril rings to form supramolecular rotaxanes. Removal of the capping groups by irradiation for the release of the metallo-helicate to trigger junction formation was investigated.

In Chapter 2, the structure of an imidazole-based nickel helicate is modified to include a photocleavable protecting group. Synthesis of a supramolecular rotaxane is then attempted via two different pathways. The photocleavage and junction binding of the nickel complexes are investigated by UV-visible spectroscopy, mass spectrometry, and polyacrylamide gel electrophoresis in Chapter 3.

Alternative designs for supramolecular rotaxanes are detailed in Chapters 4 and 5 where the terminal imidazole rings of the helicates investigated in Chapters 2 and 3 are exchanged for 4- and 5-hydroxypyridines. The formation of supramolecular rotaxanes from the 4- and 5-hydroxypyridine based helicates with photocleavable capping groups is then investigated. Chapter 5 also includes the synthesis of a 3-hydroxypyridine based metal helicate designed to permit the control of junction binding activity without encapsulation in the cucurbit[10]uril macrocycle.

The removal of the capping groups from the hydroxypyiridne-based complexes in response to irradiation is then explored by UV-visible spectroscopy and mass spectrometry in Chapter 6. The formation of nucleic acid three-way junctions by the 5-hydroxypyridine based complexes is then investigated by polyacrylamide gel electrophoresis.

Acknowledgements

This research was completed as part of the Midlands Integrative Biosciences Training Partnership (MIBTP) doctoral training programme funded by the Biotechnology and Biological Sciences Research Council (BBSRC) of UK Research and Innovation (UKRI) and the University of Birmingham.

This work would not have been possible without the guidance and support of Professor Michael Hannon. I would also like thank Professor Zoe Pikramenou for her suggestions and advice during my research project. A special thank you must also go to the Hannon and Pikramenou research group members, both past and present, who have provided advice, suggestions, answers, and given endless support during my time at the University of Birmingham.

I would also like to thank all the staff in the Department of Chemistry at the University of Birmingham and particularly the analytical team who have always been willing to offer their assistance and advice. Thank you to the Liu research group at the Wuhan University of Science and Technology who provided the cucurbit[10]uril used throughout this thesis, and the Pike research group at the University of Birmingham, who allowed me to use their irradiation set up.

Finally, I would like to family and friends for their unwavering support throughout this degree. I cannot express how grateful I am to you all.

List of Abbreviations

3D	Three-Dimensional
3WJ	Three-Way Junction (of a nucleic acid)
4WJ	Four-Way Junction (of a nucleic acid)
AFM	Atomic Force Microscopy
ASAP	Atmospheric Solids Analysis Probe
ATMND	2-amino-5,6,7-trimethyl-1,8-naphthyridine
B18C6	Benzo-18-crown-6
CB10	Curcurbit[10]uril
CBn	Curcurbit[n]uril
CBPQT	Cyclobis(paraquat-p-phenylene)
CD	Cyclodextrin
CI	Chemical Ionisation
COSY	Homonuclear Correlation Spectroscopy
DCC	1,3-dicyclohexylcarboiimide
DCM	Dichloromethane
DMF	Dimethylformamide
DMNB	4,5-(dimethoxy)-2-nitrobenzyl
DMNB-Br	4,5-(dimethoxy)-2-nitrobenzyl bromide
DMSO	Dimethylsulphoxide
DNA	Deoxyribonucleic acid
dsDNA	Double stranded DNA
EI	Electron Ionisation

ES	Electrospray
ES MS	Electrospray Mass Spectrometry
EtOH	Ethanol
FRET	Fluorescence Resonance Energy Transfer
FTMS	Fourier Transform Mass Spectrometry
HMBC	Heteronuclear Multiple Bond Correlation
HSQC	Heteronuclear Single Quantum Correlation
ITMS	Ion Trap Mobility Spectrometry
IUPAC	International Union of Pure and Applied Chemistry
LD	Linear Dichroism
MDA	4,4'-methylenedianiline
MeCN	Acetonitrile
MeOH	Methanol
MIMs	Mechanically Interlocked Molecules
NMR	Nuclear Magnetic Resonance
***o*NB**	*ortho*-Nitrobenzyl
PAGE	Polyacrylamide Gel Electrophoresis
RNA	Ribonucleic acid
ssDNA	Single Stranded DNA
TAR	Transactivation Response
TEMED	Tetramethylethylenediamine
TLC	Thin Layer Chromatography
TOF	Time of Flight
VdW	Van der Waals

Table of Contents

1. INTRODUCTION

1.1. Mechanically Interlocked Molecules

Rotaxanes are a class of a wider group of supramolecular architectures called mechanically interlocked molecules (often abbreviated to MIMs)[1]. These architectures are characterised by the inclusion of a bond which is mechanical in nature so that the structure cannot be rearranged without breaking a covalent bond. Alternative structures in this category include molecular knots, in which one molecule is tangled within itself[2], and catenanes, 2 or more interlocked rings.

The synthesis of catenanes and rotaxanes are similar, with one often inspiring the other due to the macrocyclic component in both. The name catenane is derived from the latin “catena” and was suggested by Wasserman in 1960 in a report giving the first experimental evidence of catenane formation[3]. This catenane was formed by the intramolecular cyclisation of a chain in the presence of the previously cyclised and reduced macrocyclic product and gave less than a 1% yield.

While the first representations[4] or discussions[5] of rotaxanes came in the years before, the first examples of rotaxane structures were published in 1967 by Harrison and Harrison[6] and the name “rotaxane”, derived from the latin for wheel (rota) and axle or axis (axem/axis), was suggested by Schill and Zollenkopf[7].

1.2. Nomenclature

A working group representing IUPAC define a rotaxane as[8]:

> *"Molecular arrangement comprising at least one molecule with a linear section threaded through at least one macrocyclic part of another or the same molecule and having end-groups large enough to prevent dethreading."*

Rotaxanes are made from two key components, rings and axles, which can be separate molecules, or motifs within the same molecule. The axle must pass through the ring cavity, and each end of the axle must have a blocking moiety which prevents the ring from dethreading, often referred to as a dumbbell for its characteristic shape. For a classical rotaxane (Figure 1C), sterically bulky capping groups at the termini of the axle mechanically lock the threaded ring(s) in place. Other structures of importance are the ***pseudo*rotaxane** (Figure 1A) and **semi-rotaxane** (Figure 1B), in which the axle is thread through the macrocycle but not capped at either or one end, respectively, so there is no physical barrier to prevent dethreading of the macrocycle. Threading multiple macrocyclic rings on to a polymeric chain forms an uncapped **poly*pseudo*rotaxane** or a capped **polyrotaxane** (Figure 1D). A number in brackets before, or within, any of these terms indicates the number of individual molecules involved in the structure (e.g. Figure 1B shows a [2]rotaxane).

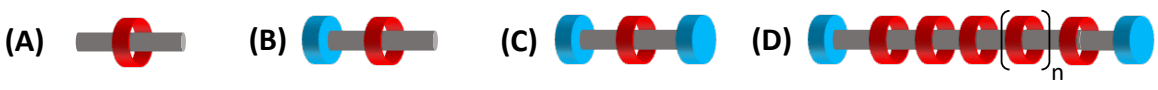

Figure 1: Key structures of rotaxanes; (A) Pseudorotaxane, (B) Semi-Rotaxane, (C) Rotaxane, and (D) Polyrotaxane.

1.3. Synthesis of Rotaxanes

The different methods of rotaxane synthesis have been categorised in a review by Xue *et al.*[9]. **Snapping** (Figure 2D) and **capping** (Figure 2C) both involve the attachment of one or two bulky groups to the ends of a semi- or *pseudo*-rotaxane, respectively. Alternatively, **clipping** (Figure 2A) and **slipping** (Figure 2B) both start with the capped dumbbell-shaped axle and the macrocycle is either formed around the axle or "slipped" over the capping groups. For the slippage mechanism, a driving force (such as heat) forces the macrocycle over the bulky capping group meaning these structures are not truly mechanically interlocked. Mechanisms are also highlighted such as metal-templating and the shrinking of a macrocycle or expansion of capping groups after threading (not shown)[9].

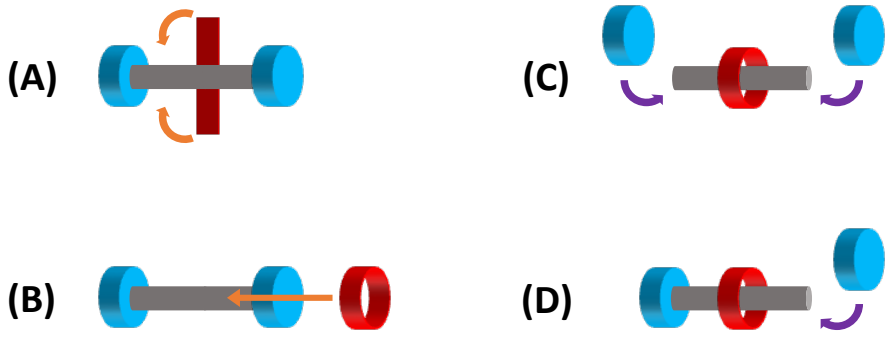

Figure 2: Common synthetic pathways towards rotaxane synthesis as shown in reference [9]; (A) Clipping, (B) Slipping, (C) Capping, and (D) Snapping.

Non-covalent interactions between the ring and axle to promote threading is a key factor in the synthesis of rotaxanes. While the first examples of rotaxane synthesis relied on statistical threading[6], more recent examples have utilised metal complexing, hydrogen bonding, π-stacking, electrostatic, and hydrophobic interactions to increase the synthetic yield of rotaxanes.

1.4. Templating Interaction

A range of different macrocycles have been utilised for rotaxane synthesis since the simple 30-membered alkyl chain used by Harrison and Harrison[6]. To promote threading or templated synthesis, the macrocycle must first have a wide enough cavity for the axle, as well as a non-covalent binding motif complimentary to the axle.

Crown ethers (Figure 3i) are cyclic chains of ethylene-bridged oxygen atoms (the ether functional group)[10]. The lone pair electrons of the oxygen atoms are able to coordinate to cationic charges in axle molecules, such as ammonium cations[11].

Macrocycles containing at least one aromatic group within the ring can be broadly classed as **cyclophanes**. The aromatic surface provides the opportunity for π-stacking interactions with guest molecules. A key group of cyclophanes are **calixarenes** (Figure 3ii), formed from phenol monomers bridged by methylene units in the ortho-position, which have both aromatic surfaces for π-stacking interactions and alcohol groups for hydrogen bonding[12,13]. **Pillarenes** (or pillararenes, Figure 3iii) are very similar to calixarenes differing only in the symmetry of their hydroquinone monomers and 2,5-linkages which forms an open pillar-like structure more suited to guest threading than the basket of calixarenes[14]. Due to higher synthetic yields the pentamer and hexamer pillarenes are commonly used and have demonstrated differing affinities for electron deficient guests due to their different cavity sizes[15,16].

Cyclodextrins (Figure 3vi) are naturally produced macrocycles of α-(1,4)-linked glucose monomers commonly between 6 and 8 units (named α-, β-, and γ-cyclodextrins with increasing ring size) although larger ring sizes have been reported[17,18]. Cyclodextrins have a hydrophobic cavity of high electron density due the oxygen of the ring of each monomer. The primary alcohols and secondary alcohols of

the glucose units are directed towards different faces, causing a smaller effective opening to the cavity on the primary alcohol side, and making cyclodextrins easy to modify for different purposes[17,18]. Early examples of cyclodextrin-based rotaxane synthesis showed that the overall yield of the rotaxane could be improved by appropriate choice of cyclodextrin size and axle guest[19].

Cucurbiturils (Figure 3v) were first isolated by Freeman, Mock, and Shih and named after their squashed, spherical shape which is similar to a pumpkin[20]. Using alkylammonium derivatives as model guests, dipole-ion electrostatic interactions (and not hydrogen bonding) between the electron dense carbonyl oxygen portal and positively charged ammonium, and hydrophobic interactions between the alkyl chain and cucurbituril cavity were found to be key interactions driving threading[21]. The contribution of the hydrophobic interaction is due to displacement of water molecules from the unfavourable environment inside the cavity [22]. Cucurbit[6]uril was the first isolated and studied, however the reaction between glycoluril and formaldehyde forms an array of differently sized macrocycles (abbreviated to CBn, where n is the number of monomers), and those between 5 to 8 glycoluril units have since been isolated in good yield[23]. Cucurbit[10]uril (CB10) was first isolated as a complex with CB5 encapsulated in the cavity, forming a “molecular gyroscane”[24], and was purified by replacement of the CB5 with an alternative small organic guest which could then be removed by heating in acetic anhydride and washing with various organic solvents[25]. 1,12-diaminododecane (protonated under acidic conditions) was identified as a suitable alternative organic guest which is commercially available and can be easily removed by deprotonation under basic conditions[26]. A figure of 8 structure is adopted by larger, “twisted”, cucurbiturils (tCB13-15) in crystal structures, reducing the effective

cavity size compared to the open structure making CB10 the largest cucurbituril to be isolated which maintains an open cavity[27,28].

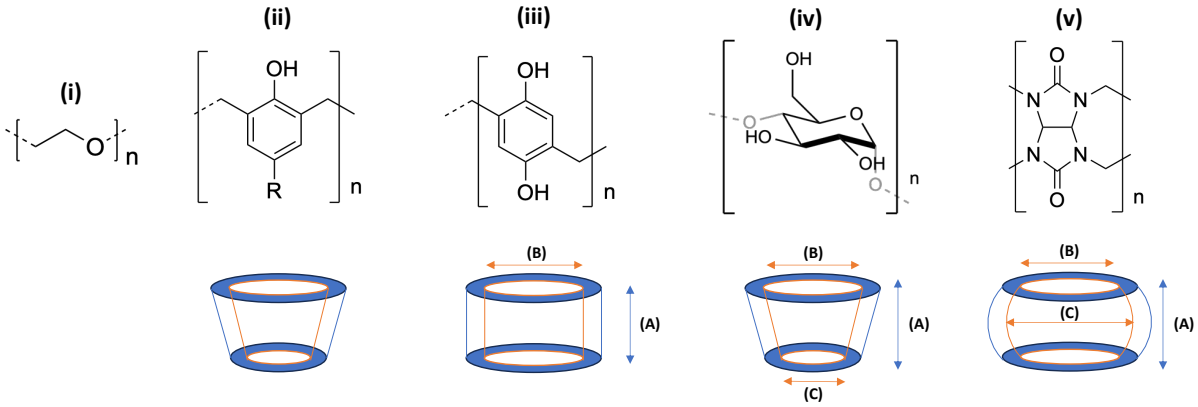

		Pillar[5]arene	Pillar[6]arene	α-CD	β-CD	γ-CD	CB5	CB6	CB7	CB8	CB10
Units	n	5	6	6	7	8	5	6	7	8	10
Height (Å)	A	-	-	7.9	7.9	7.9	9.1	9.1	9.1	9.1	9.1
Cavity diameter (Å)	B	5.5	7.5	4.7	6.0	7.5	2.4	3.9	5.4	6.9	13.1
Cavity diameter (Å)	C	-	-	5.3	6.5	8.3	4.4	5.8	7.3	8.8	10.6

Figure 3: The monomer structures of (i) crown ethers[10], (ii) calixarenes[13], (iii) pillarenes (dimensions from reference[16]), (iv) cyclodextrins (dimensions from refereces[17,18]), and (v) cucurbiturils (dimensions from references[23,24]).

In some cases, macrocycles have been designed to take advantage of a particular non-covalent interaction between two motifs or to host a specific guest of interest. **Cyclobis(paraquat-p-phenylene)** ($CBPQT^{4+}$, Figure 4), known as the "blue box", is a tetracationic macrocycle consisting of two methylviologen (paraquat, N,N'-dimethyl-4,4'-bipyridinium) units linked by two phenylene moieties[29]. This design was developed after studies of bisphenylene substituted crown ethers which were shown to be good receptor molecules for diquat and paraquat dications due to π-stacking interactions between the electron rich hydroquinol and electron poor guest[30–33]. Reversing this interaction, the $CBPQT^{4+}$ π-electron poor macrocycle was synthesised as a receptor for π-electron rich guest molecules, including methoxybenzene moieties[29]. Following the synthesis of a $CBPQT^{4+}$ catenane, formed by clipping the

macrocycle around a crown ether (bisparaphenylene-34-crown-10 ether)[34], the first example of a $CBPQT^{4+}$ rotaxane was synthesised[35]. The macrocycle was clipped around a dumbbell-shaped guest similar to the crown ether with two methoxybenzene units featured along an ether chain and capped by bulky triisopropylsilyl groups[35].

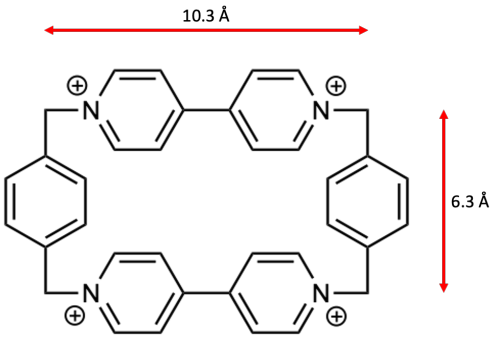

Figure 4: The structure of the $CBPQT^{4+}$ "blue box" macrocycle[29].

An isophthaloyl and xylylene based **amide-containing** macrocycle (Figure 5) was originally designed to sequester carbon dioxide gas, however the reaction between the isophthaloyl dichloride and para-xylylenediamine caused exclusive formation of the interlocked [2]catenane due to intermolecular hydrogen bonding between the amide hydrogens and the carbonyl oxygens[36]. A rotaxane was formed by the clipping method as an intermediate product to isolate the macrocycle by providing a template for the ring formation[37]. The dumbbell template centred an isophthaloyl diamide, for hydrogen bonding to the ring constituents during synthesis, between two benzyl rings with diphenyl methylene stoppers, to prevent the macrocycle templating the formation of another interlocked macrocycle[37]. The formation of the macrocyclic ring around an appropriate hydrogen bonding template (the clipping method) such as two amide bonds was used to form rotaxanes from peptide sequences which improved the apolar-solubility and stability of the peptides[38].

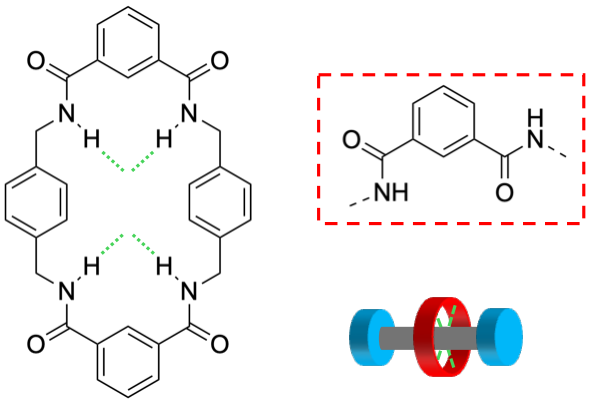

Figure 5: Amide-based macrocycle highlighting potential hydrogen bonding sites. An alternative arrangement of the amide bond is also shown for hydrogen bonding via the carbonyl oxygen.

Sauvage and co-workers developed a system in which threading could be driven by the **metal ion coordinating** units (phenanothroline) in both the macrocycle and axle (Figure 6)[39]. The macrocycle was thread onto a phenanthroline containing axle with one porphyrin stopper in the presence of copper(I) before completing the dumbbell with a second porphyrin cap (snapping). The copper ion could later be removed, leaving the mechanically interlocked porphyrin capped axle and phenanthroline containing ligand, and replaced with alternative metals such as zinc(II)[40,41]. Terpyridine was included as an alternative copper binding site which was controlled by oxidation state as the oxidised copper(II) shows a preference for the five-coordinate site formed by terpyridine and phenanthroline[42–44].

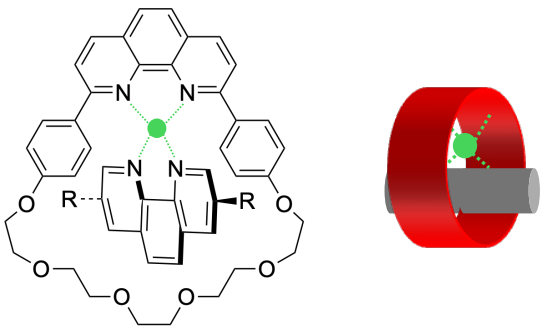

Figure 6: Macrocycle and axle containing a phenanthroline motif for metal-templating. A metal ion is shown in green.

This section highlighted the various non-covalent interactions which have been used to encourage pre-association between ring and axle (templating) so that they could be mechanically interlocked. These interactions are often designed using a pair of interacting motifs which can be incorporated into the macrocycle and axle.

1.5. Applications of rotaxanes

The multicomponent nature of rotaxanes and other mechanically interlocked molecules is of interest for molecular machines. By including more than one binding site, or "station", in an axle, the macrocycle can switch between the two points forming a **molecular shuttle**[35,45,46]. Shuttling of the macrocycle between inequivalent binding sites is determined by different binding affinities which can be designed to be controlled by external triggers, forming a **molecular switch**[47–49]. Increasingly complex systems are being developed for various applications[50].

This work focuses on the use of rotaxanes for the delivery of biologically active compounds. Properties of molecules, such as size, solubility, and stability, can be changed by interlocking with another molecule, and functionalities, such as fluorescence, can be added without covalent modification. These alterations can be applied to overcome the limitations of some biologically active molecules.

1.5.1. Delivery to Biological Targets

The encapsulation of an active compound inside a macrocycle can increase the stability of the compound during delivery to a target site and can increase cellular uptake. For example, A RAPTA-C inspired rotaxane (Figure 7) was synthesised by

threading a diaminobutyl chain through a CB6 or 7 ring before capping with the ruthenium piano-stool complexes characteristic of the antimetastatic drug[51]. The encapsulated compound was shown to have increased cellular uptake in MCF7 cells and to reduce cellular migration at lower doses than RAPTA-C. Encapsulation also aided the synthesis of the dumbbell molecule which was prevented in the absence of the CB ring due to the formation of oligomeric side products[51].

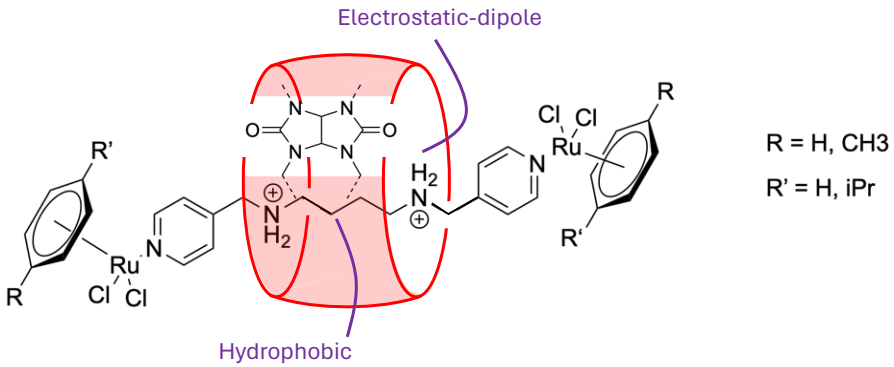

Figure 7: A RAPTA-C style anti-metastatic rotaxane[51].

Amide-based macrocycles were clipped around squaraine dyes, templated by hydrogen bonding of the macrocycle amine to the squaraine oxygen, to increase the chemical stability and decrease broadening of the absorption band by aggregation of the dye (Figure 8)[52]. By changing the stopper groups, these dyes could then be fine-tuned to target specific cellular environments and structures such as the mitochondria, lysosomes and bacterial membranes[53–55]. Adjustment of the macrocycle to include a larger aromatic anthrylene instead of a xylylene bridge allowed the squaraine axle to thread under biological conditions and could be capped in high yield by both copper-catalysed and copper free click reactions[56,57]. The macrocycle could also be modified with peptide sequences which are recognised by cell surface receptors overexpressed

in tumour cells to increase the tumour cell selectivity of these rotaxanes[55]. Unlike squaraines, thiosquaraines produce radical oxygen species upon irradiation and this is enhanced by rotaxanation to be comparable to methylene blue, a photosensitizer[58]. Exchanging the squaraine oxygens for larger sulphur atoms pushes the macrocycle off-centre, decreasing the stability of the complex. This could be a benefit for a photodynamic therapy agent as degradation after use is desirable but also highlights the importance of the steric protection provided by the macrocycle[58].

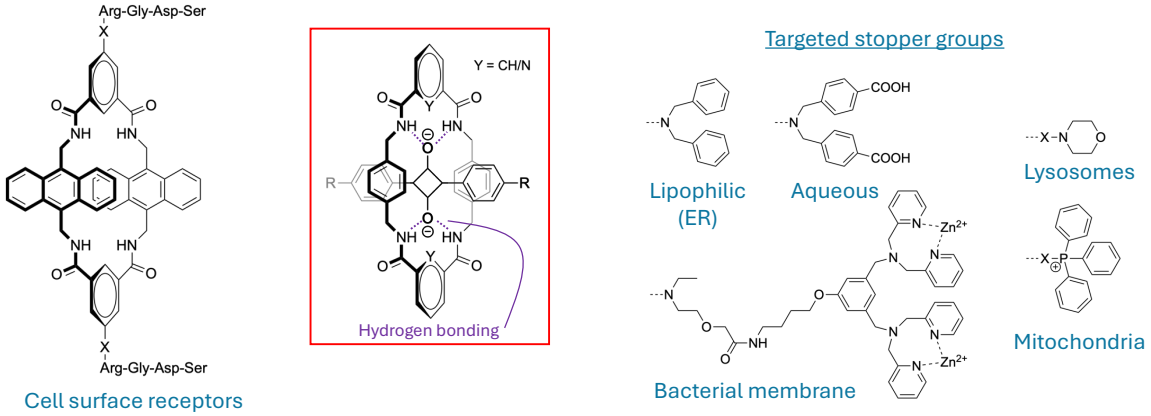

Figure 8: Highlighting the hydrogen bonding interaction between the macrocycle and squaraine dye and stopper groups (R) for different cellular targets[52–55]. X represents triazole-based linkers not involved in targeting.

Alternatively, d'Orchymont and Holland used the modular nature of a rotaxane to attach various functional groups to different components which could then be used for the capping synthesis of rotaxanes via CB6 catalysed click reactions[59]. Both the capping groups and a β-CD could be modified or exchanged for metal-binding motifs, fluorescent groups, or moieties to promote host-guest binding, as well as tumour targeting peptide sequences, small molecules, and antibodies (trastuzumab). Coordination of radioactive metal isotopes (^{68}Ga and ^{89}Zr) produced rotaxanes for radioactive labelling, which were shown to accumulate in targeted tumour cells[59].

Some rotaxane structures aim to increase cellular uptake of an active compound by providing a shield for passive diffusion through the lipid bilayer. For example, Smithrud and co-workers have developed host-rotaxane structures for the binding of substrates inspired by proteins[60–68]. Host-rotaxanes are utilised for the conformational flexibility provided by the macrocycle ring, which is free to move along the axle component finding the best conformation for binding substrates[60]. These rotaxanes are synthesised from a 1,3-dicyclohexylcarboiimide (DCC) capped rotaxane via the snapping method, using the affinity of crown ethers for ammonium ions to drive the initial formation of a semi-rotaxane via threading[61]. DCC is a reagent used for the formation of peptide bonds[69] and can be therefore replaced by alternative amide-containing capping groups, including attachment of peptide chains and hydrophobic cavities (Figure 9A).

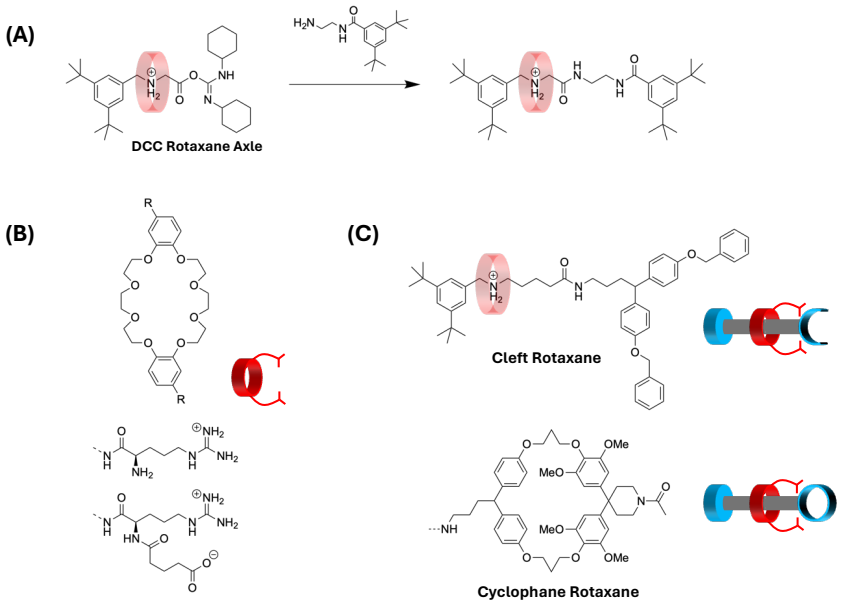

Figure 9: (A) Replacing the DCC-cap[61], (B) the modified macrocycle[64], and (C) highlighting capping groups for the cleft and cyclophane rotaxanes[64].

A flexible guest binding area was formed with a calixarene, cyclophane or open cyclophane-based motif (“cleft”) as one stopper, to promote hydrophobic binding (Figure 9C), and the dibenzyl crown either was modified with arginine or carboxylic acid residues to promote electrostatic interactions to model the salt-bridges in proteins (Figure 9B)[62–64]. The rotaxanes were found to change conformation to maximise different non-covalent interactions in different environments (aqueous or organic) to increase the binding to a variety of guest molecules[62,64]. Host-rotaxanes were found to transport substrates, such as fluorescently tagged peptides, via passive diffusion through the cell membrane and efficiency varied with factors such as aqueous solubility and binding affinity to the guest (Figure 10)[62,65,66]. Incorporation of an ethylene glycol chain in the axle for increased aqueous solubility and potential attachment to nanoparticles also showed an increase in peptide delivery compared to an alkyl chain of similar length[67]. Incorportation of pyrene and rhodamine B fluorophore caps allowed cellular uptake of the rotaxane to be tracked alongside the uptake of fluorescein and doxorubicin, the latter of which was shown to reduce cell viability even in drug-resistant MCF-7/ADR cells in the presence of the rotaxane[70].

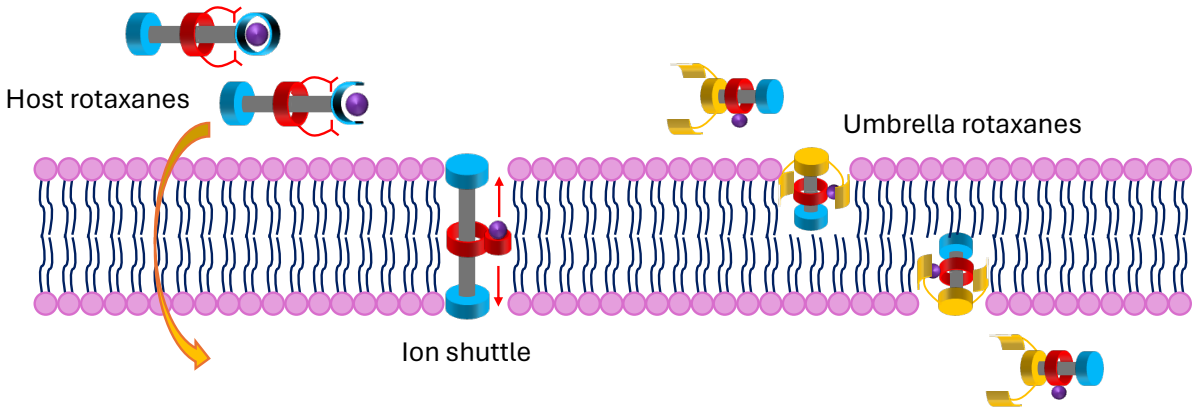

Figure 10: Methods of crossing the cell membrane by rotaxanes.

A similar technique is used by umbrella rotaxanes (Figure 10), which have been shown to release a fluorescently modified macrocycle into liposomes after transport through the lipid bilayer[71,72]. Chloride ions were transported across a lipid bilayer by electrostatic binding to a dibenzylammonium that was then protected by the two large cholic acid groups attached at one end[71]. A pyridine containing crown ether could complex the ammonium via electrostatic dipole interactions to form a semi-rotaxane, preventing the binding of chloride ions to the axle and instead binding chlorides to the pyridine of the macrocycle[71]. A similar rotaxane was formed by adding a di-tert-butylbenzene to the end of the axle and clipping the macrocycle which was modified with a fluorescent dansyl group[72]. The fluorescence of the dansyl group was used to report the polarity of the environment experienced by the macrocycle, which was altered by the protective cholic acid groups, and enzymatic hydrolysis of the cholic acid groups was shown to release the macrocycle inside liposomes[72].

Unlike the previous two examples, where shielding groups are used to protect the cargo across the lipid bilayer, the shuttling action of a macrocycle along an axle can also be utilised for transport across a cell membrane (Figure 10)[73,74]. An amphiphilic axle was designed to be long enough to extend across a lipid bilayer and contain two terminal ammonium and one central triazolium cationic binding site for a crown ether ring[73]. A smaller crown ether known for selective binding of potassium ions (B18C6) was covalently attached to the macrocycle so that the ions could be transported across the bilayer by the shuttling along the rotaxane axle. Removal of the central triazolium cation, and deprotonation of the ammonium moieties were both shown to increase the energy barrier and slow down or stop ion shuttling, respectively[73]. Incorporating a *trans* azobenzene into the centre of the axle allowed

control of the shuttling by photoisomerization as the *cis* azobenzene showed a reduced shuttling[74]. The uptake of potassium ions has been shown to be controlled by both environmental (pH[73]) and external (light[74]) triggers.

1.5.2. Triggered Release

Encapsulation in a macrocycle or rotaxane has been shown to be an effective method for increasing the stability and cellular uptake of active agents. Control of uptake by enzyme triggered hydrolysis, irradiation and pH has also been demonstrated by umbrella rotaxane and molecular cable cars[72–74]. In the following cases, release of the compounds of interest is controlled by an external trigger. Triggered release is an effective method for reducing the systemic toxicity of drugs, and the delivery of biologically unstable compounds to sites of interest.

The increased concentration of β-galactosidase in tumour cells has been used as a mechanism for selective delivery of both pro-peptides and pro-drugs by Papot and collegues[75–77]. The original design aimed to protect a pentapeptide (Met-Enkephalin) against proteases during delivery to cellular targets by threading through a macrocycle, which could then be removed when the target was reached[75]. A peptide chain with sterically bulky residues at the C-terminus thread an amide-based macrocycle driven by hydrogen bonding to the amide bonds around central glycine monomers. The rotaxane was then synthesised by attachment of a capping group to the semi-rotaxane (snapping) which would degrade upon removal of a galactose moiety by β-galactosidase[75]. After the initial success, in which 90% of the peptide was preserved during incubation in plasma for 5 days, the macrocycle was modified with an azide group to provide an additional point for functionalisation[76]. Attachment of hydrophilic

glucose residues via ethylene glycol chains was shown to increase the aqueous solubility of the rotaxane. Switching to a clipping mechanism for the attachment of the macrocyclic ring and addition of a diphenyl capping group made the design suitable for delivery of a range of peptides (Figure 11A)[76].

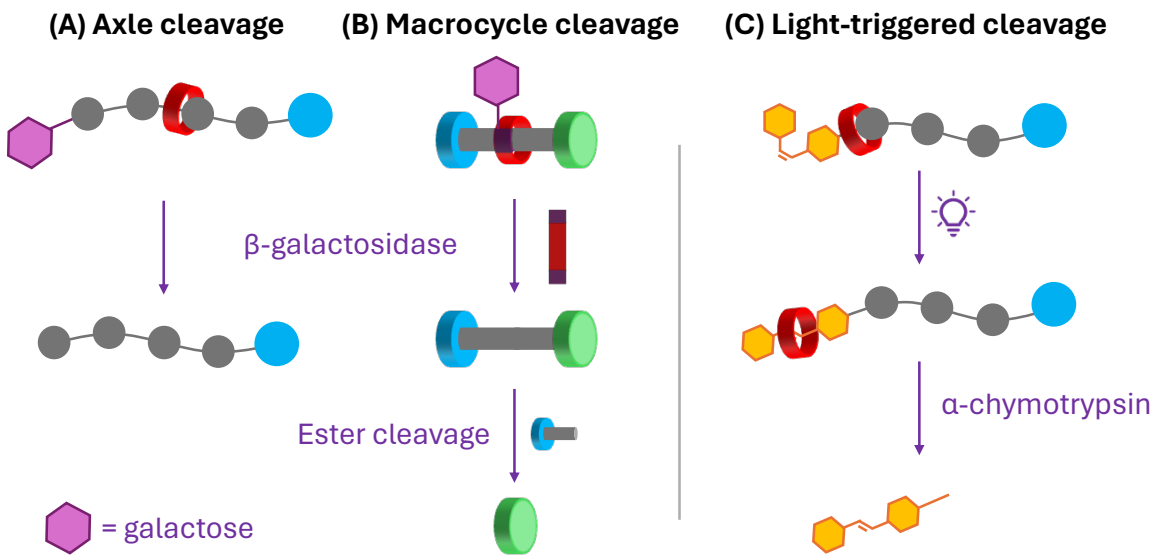

Figure 11: Release of rotaxanes via enzyme cleavage mechanisms.

Moving the galactosidase sensitive trigger to an alternatively modified macrocycle containing carbamate bonds demonstrated that release of the axle could be achieved by degradation of the ring (Figure 11B)[77]. Threading of the pre-formed macrocycle was driven by the copper(I) catalyst for the click reaction (snapping method) which forms the esterase sensitive axle. The axle is terminated in a hydrophilic, glucose-decorated cap at one end and paclitaxel, an anticancer drug, at the other end. The macrocycle was shown to protect the ester bond to paclitaxel until the removal of galactose by β-galactosidase which triggered degradation of the ring, after which cleavage of the ester bond released the paclitaxel[77].

The first rotaxane synthesised by an enzyme-catalysed reaction was published by Cheetham *et al.* and was designed for enzyme cleavage by the same enzyme (α-chymotrypsin) following irradiation (Figure 11C)[78]. Arginine modified with an azobenzene stopper was thread through an α-cyclodextrin, driven by hydrophobic interactions, before the addition of a phenylaniline unit by α-chymotrypsin which selectively formed rotaxanes in which the narrow, secondary alcohol side of the macrocycle was directed towards the peptide chain. In the *cis* conformation, the α-cyclodextrin was forced to lie over and protect the enzyme sensitive amide bond between the arginine and phenylaniline units, however upon isomerisation to the *trans* isomer the α-cyclodextrin moved to the azo-benzene unit, allowing cleavage of the bond[78].

Release of active small molecules in acidic environments is also a viable targeting strategy as the extracellular environment surrounding tumour cells is often a lower pH[79], and the internalisation of materials by cells into endosomes and lysosomes also exposes the material to an acidic environment (pH 4.5-6.0)[80]. A dual targeted rotaxane, containing both a mitochondrial targeted triphenylphosphonium stopper and a pH dependent doxorubicin modified pillar[5]arene macrocycle, was investigated for aggregation induced fluorescence of a tetraphenylene capping group[81]. The rotaxane, formed by a snapping method after non-covalent binding of the electron dense pillarene cavity to the pyridinium of the tetraphenylethene, showed aggregation in aqueous solvents due to hydrophobic hexane chain modifications on the macrocycle which caused the fluorescence of the tetraphenylethene. The emission wavelengths coincide with the absorbance of doxorubicin allowing fluorescence resonance energy transfer (FRET) to the doxorubicin, the fluorescence of which is conversely quenched

by aggregation. Upon pH dependent degradation of an imine bond in endosomes, doxorubicin was released, and fluorescence observed in the nucleus of both HeLa and HEK293 while the tetraphenylethene fluorescence of the rotaxane aggregates was found in the mitochondria[81].

The pH dependent aggregation of rotaxanes has been used to form vesicle-like structures which could be used to release active compounds upon changes in environment[82]. A doxorubicin loaded vesicle was designed by Cui *et al.* by the aggregation of pillarene-based [1]rotaxanes, in which a poly-ethylene glycol molecule thread through the macrocycle cavity and attached to the pillarene via a disulphide bond[83]. Amide bonds either side of the disulphide bond hydrogen bond to the oxygen lined portals of the pillarene, holding the disulphide bond in the macrocyclic cavity where it is protected. Glutathione was shown to reduce the disulphide bond, and can therefore release doxorubicin into the cytoplasm of cells[83].

1.5.3. Rotaxanes for nucleic acid binding

Delivery of deoxyribonucleic acid (DNA) binding agents and controlling DNA structure are other potential applications of rotaxanes which have not been widely investigated, although examples of inclusion complexes and *pseudo*rotaxanes have been identified for similar purposes.

A host rotaxane (see section 1.5.1) was used as a scaffold for the delivery of cisplatin into cells and showed an increase in toxicity relative to the unmodified drug[68]. Unlike other examples using host rotaxanes a platinum binding benzenediamide moiety was covalently attached to the axle, replacing one of the capping groups, and

positively charged arginine groups of the modified macrocycle were used to promote DNA backbone binding by electrostatic attraction.

Encapsulation of a spermine and acridine containing axle in a CB6 macrocycle provided proof of concept for the delivery of non-targeted molecules (CB6) to DNA via non-covalent binding to targeted moieties, however this study also showed that encapsulation reduced the binding efficiency of the axle to the DNA[84].

An encapsulation approach was also adopted to disrupt the DNA binding, and therefore fluorescent response, of a bis-styryl dye which aggregates in the minor-groove causing fluorescence quenching[85]. Addition of CB7 disrupted the stacking between dye molecules in the minor groove increasing the fluorescence response but could not completely remove the dye from the minor groove as only one end of the dye was encapsulated[85]. Similarly, a macrocyclic host for spermine was synthesised using a dynamic library of aromatic constituents containing carboxylic acids to promote threading via electrostatic attraction to the polyamine axle[86]. Circular dichroism (CD) was used to monitor the change in DNA conformation caused by complex formation on addition of the macrocycle from spermine-bound Z-DNA to free B-DNA (Figure 12A)[86].

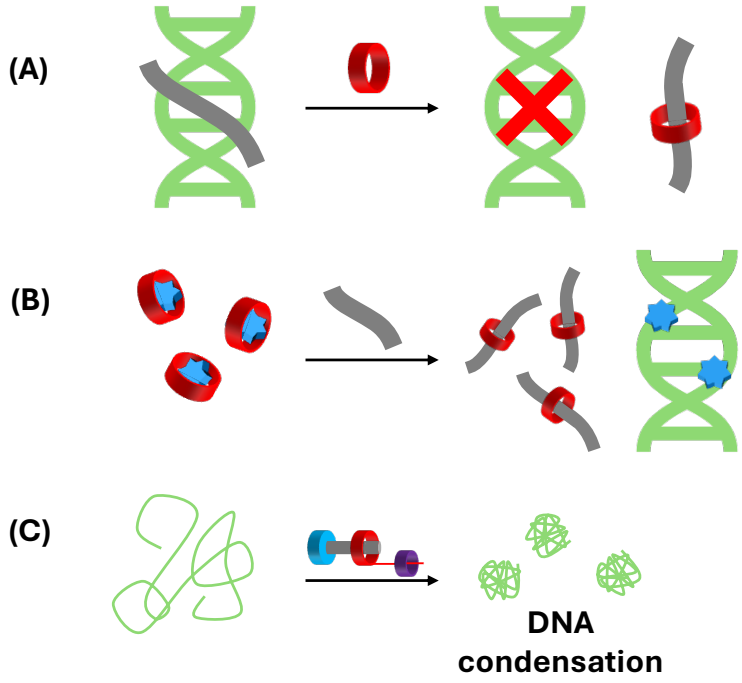

Figure 12: Strategies for the control of DNA binding and structure including (A) encapsulation to prevent DNA binding, (B) competitive replacement to activate DNA binding, and (C) rotaxanes for DNA condensation.

Overexpression of spermine in some tumour cells has been suggested as a target for the selective release of active agents from cucurbituril-based *pseudo*rotaxanes (supramolecular chemotherapy, Figure 12B)[87,88]. The cytotoxicity of methylviologen and oxaliplatin, a cisplatin analogue, was reduced by CB7 encapsulation in healthy lung and colorectal cells, respectively, but displayed increased activity in cancerous cells overexpressing spermine, due to competitive binding of spermine to CB7 causing the release of the DNA binding agent[87,88]. Cucurbituril macrocycles have also been reported to impact the activity of DNA regulating enzymes such as topoisomerases and endonucleases, possibly by encapsulation of available amino acids or peptides[89,90].

In an alternative study, CB6 was added to an alkylammonium-modified β-CD and anthracene-adamantane complex to improve DNA condensation by increasing the

rigidity and stabilising the positive charge of the ammonium upon encapsulation (Figure 12C)[91]. This facilitated the groove binding of DNA by electrostatic attraction to the backbone, π-conjugation by anthracene, and hydrogen bonding by the CD macrocycle[91]. Poly(*pseudo*)rotaxanes of cationic polymers have also been shown to condense nucleic acid[92], however the method in which this is achieved, often through aggregation or hydrogel formation[93], differs from that of the smaller rotaxanes investigated here, and is therefore beyond the scope of this work.

The formation of mechanically interlocked rotaxanes by the addition of capping groups that are removed or neutralised in response to an external signal or a chosen environment may improve both the stability and selectivity of these inclusion complexes or *pseudo*rotaxanes as another layer of control is implemented. Examples use light as an external trigger for the release of an active moiety or compound.

A CB8 ring encapsulating both a methylviologen and trans-azobenzene linked by an alkyl or alkylimdazole chain was shown to condense DNA into 10 nm particles by electrostatic attraction and hydrophobic interactions between the ring and DNA bases (Figure 13)[94]. Irradiation caused the conformational change to the cis-azobenzene isomer triggering the removal of either the methylviologen or both encapsulated moieties from CB8 cavity, depending on the connecting chain. When irradiated in the presence of DNA, release of the methylviogen caused DNA damage by oxygen radical production and no DNA condensation was observed[94].

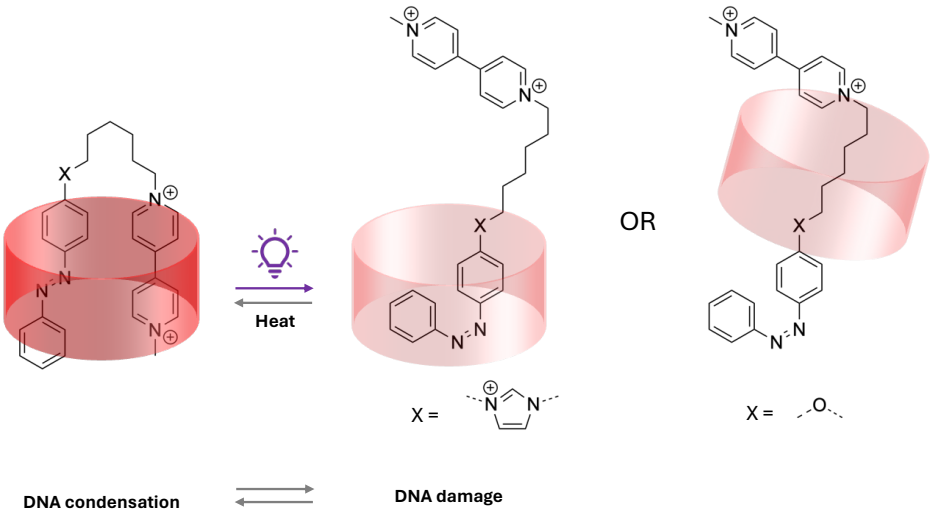

Figure 13: Control of DNA condensation by photo-isomerism of an azobenzene[94]. X indicates two possible linkers in the axle.

Platinum salphen, a fluorescent G-quadruplex (GQ) binder, was used to cap an amide containing axle which thread a bipyridine ring by hydrogen bonding (Figure 14)[95]. The semi-rotaxane was capped via a click reaction (snapping method) to a benzoate based capping group with either two enzyme-cleavable pivalic groups or two photocleavable 4,5-dimethoxy-2-nitrobezyl groups. GQ binding was inhibited by the steric bulk of the rotaxane architecture in both cases. The GQ binding affinity was recovered upon exposure to the selected trigger, as removal of the sensitive capping groups released the macrocycle, exposing the benzoate ester group for hydrolysis. The photocleavable rotaxane was not cytotoxic unless irradiated, and the enzyme cleavable rotaxane showed an increasing cytotoxicity with increasing concentration, suggesting that cytotoxic activity is only observed when the active salphen agent is released[95].

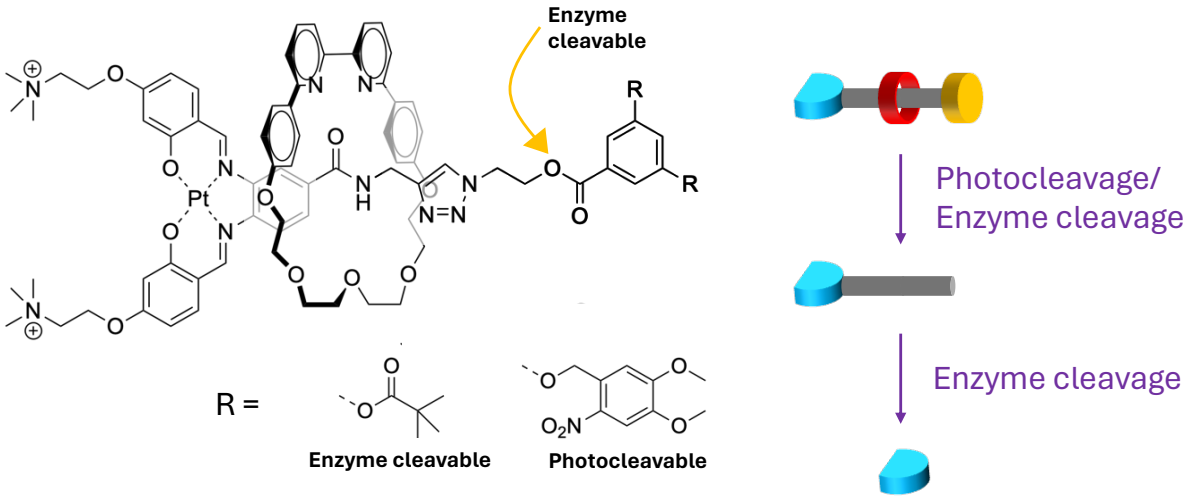

Figure 14: Triggered released of a GQ binder[95].

1.6. Targeting Junctions

1.6.1. Nucleic Acid Junctions

The double helix is the most well-known tertiary structure of DNA[96,97], however nucleic acids (including ribonucleic acid, RNA) can arrange into many different forms supported by both Watson-Crick and alternative base pairings. There is growing evidence that these non-canonical structures, such as G-quadruplexes[98] and i-motifs[99], have regulatory roles in the folding and processing of nucleic acids in cells. Both three-way junctions (3WJ) and four-way junctions (4WJ) in nucleic acids are required for the formation of alternative nucleic acid structures. Junctions arise during the cellular processing of DNA and RNA, as 4WJs are vital for nucleic acid repair[100], and 3WJs are found at the DNA replication fork.

The importance of junctions in cells for regular function makes them interesting cellular targets. Junctions can form from a range of primary base sequences so targeting of specific bases for global junction binding would be ineffective. The

targeting of junctions, and particularly 3WJs, by non-covalent interactions specific to the three-dimensional (3D) structure has been investigated and this section aims to highlight the key motifs supporting junction binding (Figure 15).

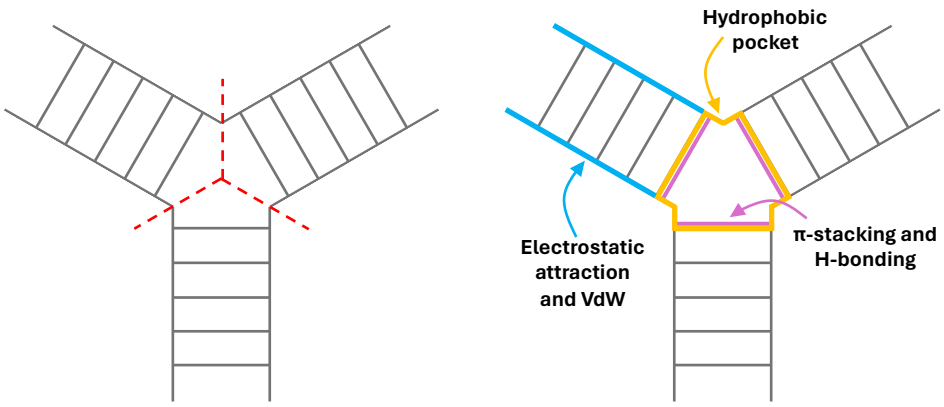

Figure 15: Showing the three-way symmetry at nucleic acid junctions.

1.6.2. Binding Three-Way Junctions

Three-way junctions were identified as a binding site for cholic acid when aptamers, nucleic acid structures with high affinity for a specific target, developed for cholic acid binding showed only similarities in tertiary structure and not the base sequences[101]. Chemical modifications and sequence mutations were used to determine that the fully Watson-Crick base paired junction was required for binding, and competition studies with similarly structured steroids suggested that the affinity of the aptamer for the targets was due to hydrophobic interactions[102]. A similar hydrophobic interaction was suggested for the binding of cocaine to a 2-base bulged site near a 3WJ in aptamers developed for fluorescent detection[103–105]. Possible hydrogen bonding to base pairs at the junction was also implicated for the binding of

ATMND (2-amino-5,6,7-trimethyl-1,8-naphthyridine), a fluorescent dye[106], however further structural features required for, or for the improvement of, junction binding were not investigated.

The DNA binding of pyridylimine-based helical metal complexes, termed “cylinders” due to their shape, was investigated as their dimensions (1 nm by 2 nm) was noted to be similar to those found in the zinc finger of DNA binding proteins[107–109]. Condensation of double stranded DNA (dsDNA) was observed by both linear dichroism (LD) and atomic force microscopy (AFM) studies for the iron and ruthenium parent cylinder ($[M_2L_3]^{4+}$, Figure 16)[107,109,110]. The M (Λ, or left-handed) helical enantiomer was found to cause greater coiling and displacement of ethidium bromide from dsDNA, and a greater thermal stability of the M enantiomer when bound to the DNA lead to the conclusion that the M enantiomer may bind in the major groove, where it has greater protection, while the P enantiomer may bind the minor groove[111].

A crystal structure of the cylinder with a palindromic dsDNA sequence instead indicated the formation of a three-way junction (3WJ) through multiple non-covalent interactions[112]. The aromatic helicate surface sits in the hydrophobic pocket at the centre of the junction positioning the imine hydrogen for hydrogen bonding to nitrogen atoms in the bases. The terminal pyridine rings on the minor groove side of the junction can bind to the backbones by Van der Waals (VdW) interactions while electrostatic attraction between the tetracationic charge and the phosphate backbone strengthen the binding. A key feature of the cylinder is the C_3 symmetry which aligns the central phenyl rings to the aromatic bases exposed at the junction for π-stacking interactions (Figure 16). This binding was confirmed in solution by ^{1}H NMR studies with the junction DNA[113]. A similar interaction is observed for RNA 3WJs, where the more open cavity

reduces VdW interactions with the minor groove but allows the cylinder to fit further into the cavity for improved π-stacking interactions with the bases[114].

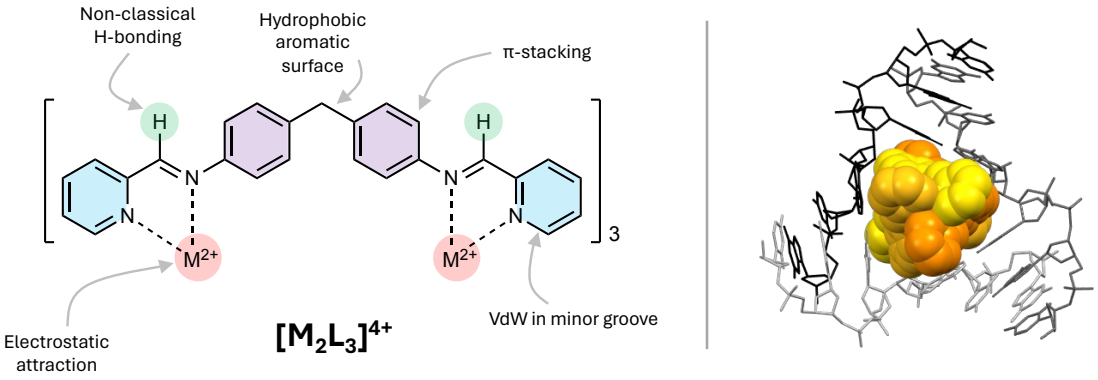

Figure 16: Highlighting the features of the parent cylinder which contribute to the non-covalent binding of nucleic acid three-way junctions and binding to the 3WJ (2ET0)[112].

Low concentrations (< 10 μM) of the parent cylinder caused cell cycle arrest in the G_0/G_1 phase, inhibiting cell growth, while higher concentrations (25 μM) caused an increase in apoptotic cells without damage to cellular DNA[115]. The thermally stable ruthenium parent cylinder was also used to show inhibition of DNA replication by polymerase chain reaction due to competition with Taq polymerase for DNA binding[116].

The iron parent cylinder can also stabilise DNA bulges with between two and five unpaired bases but has shown the greatest stabilisation for bulges with two or three unpaired bases which form cavities lined by six or seven bases, similar to the 3WJ[117]. Binding of the cylinder to a three-base bulge in the transactivation response (TAR) RNA of HIV-1, which is a key protein binding site for replication, was shown to reduce recognition of the sequence by the protein ADP-1[118]. The effect of the iron, ruthenium, and nickel parent cylinders against HIV-1 replication was also investigated, showing a decrease in replication for the nickel and ruthenium, but increase for the iron

parent[119]. The cylinders have also been suggested to stabilise G-quadruplex structures with enantiomeric selectivity[120].

The importance of the three-dimensional helicate structure for junction binding is highlighted by alterations to the parent cylinder design (Figure 17A). Addition of steric bulk to the central methylene of the spacer (CF_3, Figure 17B) was shown to prevent both DNA and RNA junction binding[114,121], while substitution of the CH_2 group for sulphur atom (S, Figure 17B), which did not affect the overall shape, had no effect on the ability of the cylinder to form junctions[122]. Addition of a phenyl group (Figure 17C) at the imine bond also disrupted junction binding[121], but attachment of large L- and D-arginine residues to the 5-position of the terminal pyridine ring (CF_3, Figure 17D) enhanced junction formation[123]. The data suggests that additional bulk around the central surface of the cylinder prevents junction binding, likely due to steric hinderance preventing the cylinder sitting in the 3WJ cavity. Alternatively, additions to the end of the cylinder structure do not prevent junction binding, and may increase the binding affinity through additional non-covalent interactions to other structural features at the junction, such as the backbone.

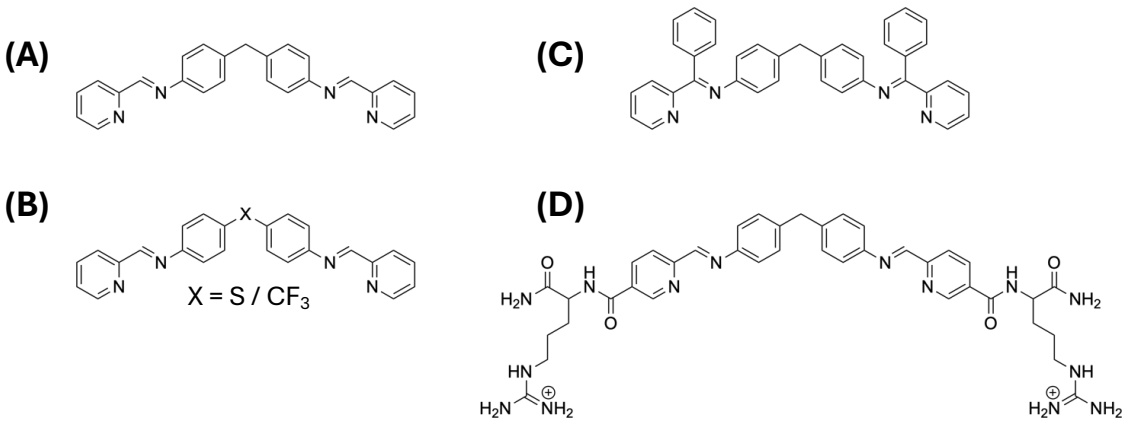

Figure 17: Alternative ligands for the parent cylinder for which the 3WJ binding has been reported (A[108], B[121,122], C[121], D[123]).

The non-covalent interactions highlighted by the junction binding of the cylinder can be recognised in other junction-targeted agents. A series of **triazacyclononane**-based compounds (Figure 18) with quinoline (TACN-Q), naphthalene (TACN-N), or acridine (TACN-A) aromatic groups attached form structures that are similar to the central diphenylmethylene motif of the parent cylinder[124]. TACN-N showed poor junction binding while TACN-A gave improved junction binding due to the extended π-surface for stacking interactions. Quinoline (in TACN-Q) differs from naphthanlene (TACN-N) by a single nitrogen atom that can impose a helical arrangement by metal binding (Li^+, Zn^{2+}, Cu^{2+}, and Fe^{2+}). This increased both 3WJ binding and selectivity particularly for the lithium bound complex as the tighter binding to the dications decreased the size of the complex[124].

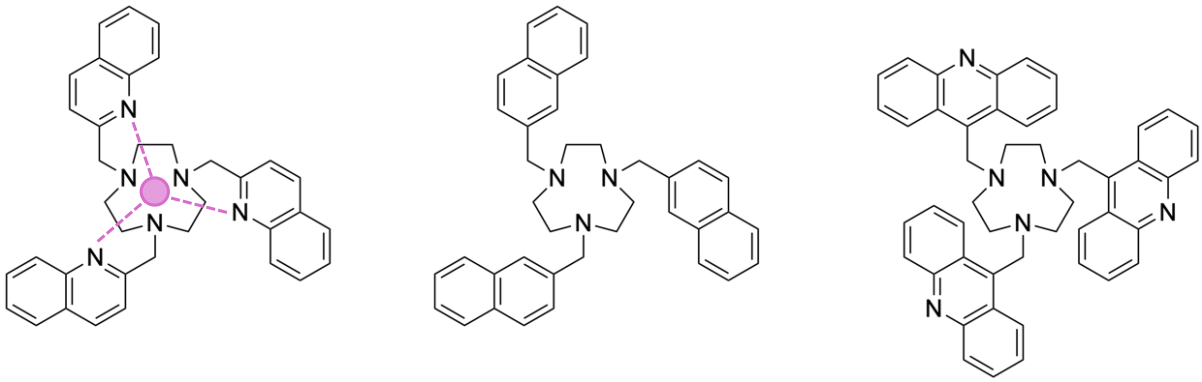

Figure 18: TACN-Q, TACN-N, and TACN-A[124].

In comparison to cylinders, **azacryptands** (Figure 19) have similar, three-way symmetric aromatic groups and are tri- or tetra-cationic (at physiological pH) but are non-helical and are a less rigid structure, giving the molecule the flexibility to arrange into the conformation that maximises the non-covalent binding interactions[125,126]. Azacryptands show a binding affinity for G-quadruplexes but have preference for 3WJs, which has been demonstrated both *in vitro* and *in vivo*, and generally show

greater stabilisation of the junction than TACN-Q[125–127]. Different aromatic groups have been incorporated into the azacryptand structure, all containing two aromatic rings except for the phenazine based cryptand, which only showed non-specific binding to DNA[125]. Investigating the 3WJ binding modes of a naphthalene and oxybiphenyl based azacryptand suggest that both bind in the junction cavity and cause one of the adjacent base pairs to break, which is followed by the transient formation of an inclusion complex of one of the unpaired bases with the naphthalene based azacryptand[127]. Functionalisation of one of the amine groups with an alkene appeared to lower the affinity of the naphthalene azacryptand for junctions but allows the attachment of fluorophores which revealed the localisation of azacryptands in the nuclei of cells[127]. DNA damage by double strand breaks has been implicated as the cause of the cytotoxic activity of these compounds, and a synergistic response has been revealed with DNA damage repair inhibitors[126,127].

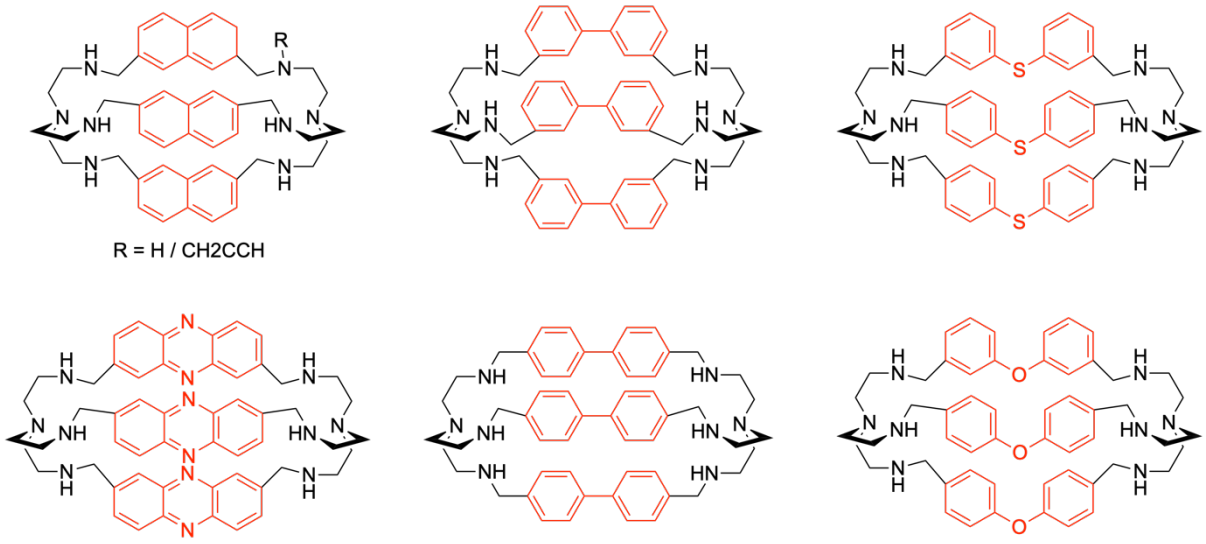

Figure 19: Azacryptand-based structures for junction binding[125–127].

Attaching metal binding bipyridine to a trimeric peptide gave pre-organised ligands for the enantiospecific synthesis of iron helicates[128]. In the absence of metal ions, the bipyridine ligands stack with each other and show no junction binding, however addition of the metal ion enforces the helicate structure and shows junction binding.

Similar properties are observed by **metallopeptides**, in which bipyridine metal binding units are incorporated into a peptide sequence between residues (proline and arginine) specifically selected to mimic the β-fold in proteins and control the helicity of the final complex depending on the enantiomers used[129–131]. Both iron(II) and colbalt(III), oxidised from cobalt(II) for increased stability, helicates were synthesised and shown to form a 3WJ band by gel electrophoresis, although the cobalt complex showed a reduced selectivity[130]. The same peptide formed a copper(II) complex of opposite helicity with improved junction binding of the P over the M enantiomer, and was able to induce selective DNA cleavage at the junction[129]. Rhodamine labelling of the iron and copper metallopeptides highlights their colocalization with proliferating nuclear antigen suggesting effective junction targeting, however cellular uptake of arginine containing peptides is only achieved in the presence of digitonin[129,130].

Amino acids and peptides were also used to functionalise **triptycene** (Figure 20), an aromatic 3WJ binder[132–135]. To maintain the three-way symmetry, each benzene ring must be functionalised in the same position, or the structure must be functionalised at the bridgehead if only one attachment point is required, such as for solid phase peptide synthesis, which was used for the attachment short peptide sequences[133,134]. This structure has been shown to bind both DNA, RNA and “slipped out” junctions which occur at triplet repeat sequences[132,135,136]. The nature of the interaction between

the triptycene and nucleic acid junctions has not been established, however stabilisation of an RNA 3WJ in rpoH gene of *E. coli* by the lysine and arginine modified triptycenes has been demonstrated to prevent the translation of a heat shock response protein (σ^{32})[136].

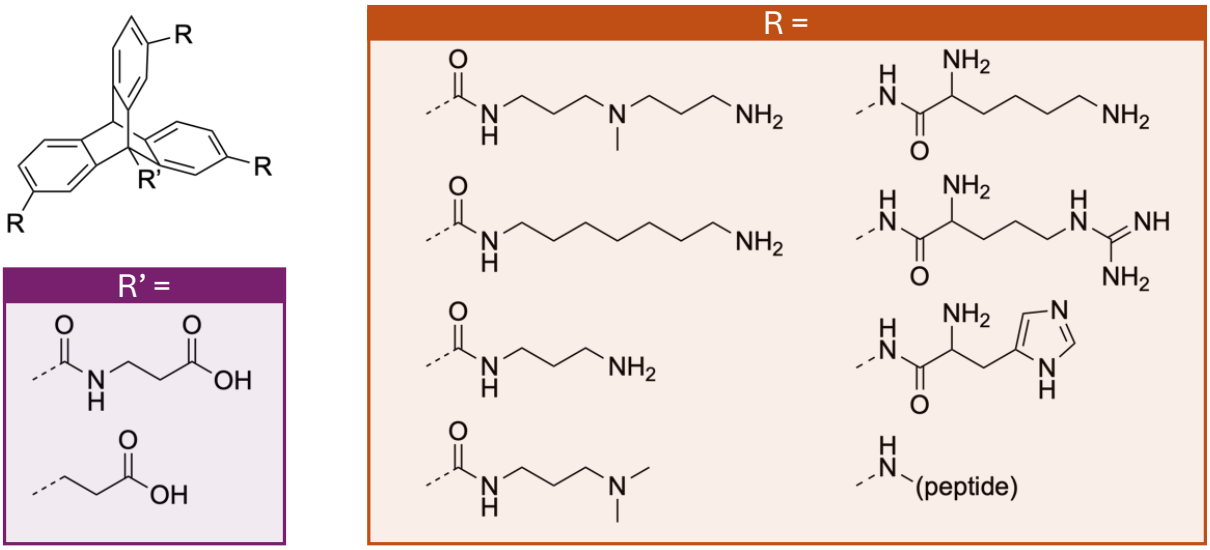

Figure 20: Triptycene-based structures for junction binding[132–136].

Calix[3]carbazole (Figure 21) is a carbazole based macrocycle which is too large for intercalation or effective groove binding, but has a large hydrophobic, aromatic surface for binding a 3WJ cavity[137]. Restricted movement of the cabazole units in the presence of junction DNA increases the fluorescence of the calix[3]carbazole, forming a fluorescent indicator of junction binding. Despite the three-way symmetry of the structure, NMR experiments indicate that the carbazole takes a chair-like structure when bound to the junction DNA, in which the cationic arm of one carbazole is turned below the macrocyclic plane, reducing the symmetry of the macrocycle[137].

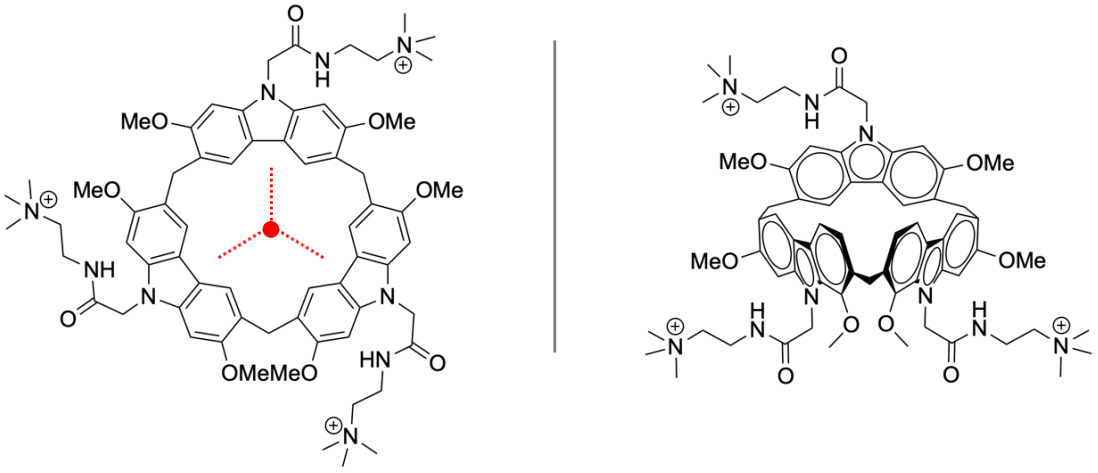

Figure 21:Structure of the calix[3]carbazole, highlighting the three-way symmetry, and the chair structure adopted[137].

The three-way junction binding affinity of an iron-based **supramolecular tetrahedron** (Figure 22) has also been investigated[138]. Pyridylimine ligands, with a similar structure to the ligands of the parent cylinder, form the aromatic faces of the three-way symmetric, cationic tetrahedron which is thought to bind in the cavity of a 3WJ. The fluorescence of fluorophores linked to the 5' end of DNA strands involved in various structures (ssDNA, dsDNA, 3WJ and 4WJ) was quenched by the metallocage upon binding, with a greater quenching observed when the distance between the tetrahedron binding site and fluorophore was decreased. The tetrahedron is not selective for 3WJs, showing binding to ssDNA and to a lesser extent dsDNA and 4WJs, and it is thought that this binding is driven by the presence of unpaired bases which can then form a cavity for binding[138].

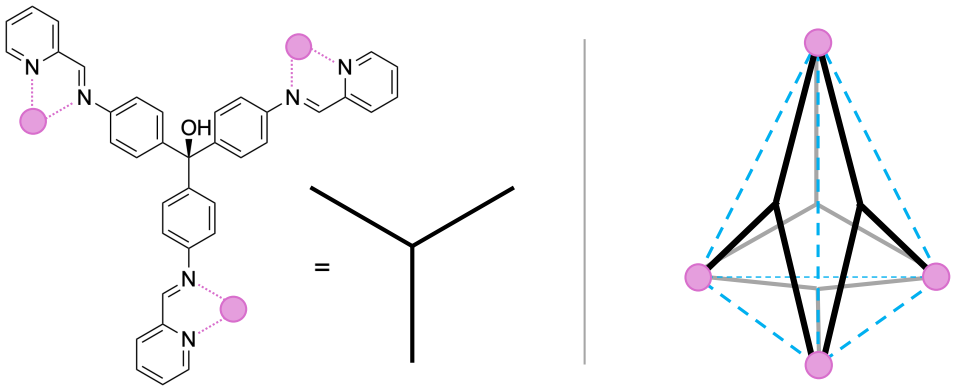

Figure 22: Ligand and 3D structure of the supramolecular tetrahedron[138]. Pink circles indicate metal ions.

1.6.3. Controlling Junction Binding

The 3WJ targeted molecules discussed in the previous section bind via the junction cavity, which requires a specific size and shape. Exchanging the aromatic moieties of azacryptand and triazacyclononane molecules demonstrated that junction binding can be improved or disrupted by alterations to the hydrophobic and π-stacking interactions. The addition of steric bulk along the surface of cylinders perpendicular to the metal-metal axis (effectively making the cylinder wider) was also shown to prevent junction binding, either due to the cylinder being too large to thread through the cavity or because the aromatic surface was sterically prohibited from interacting with the junction. Encapsulation of the central binding motif of cylinders would therefore be expected to "turn off" junction binding. This thesis aims to build on published work in this area[139].

A *pseudo*rotaxane was synthesised by threading the parent cylinder through CB10 driven by hydrophobic interactions between the aromatic core and CB10 cavity, and electrostatic-dipole interactions between the carbonyl oxygen-lined CB10 portals and the cationic metal centres of the helicate[139]. Junction binding was not prohibited

for the *pseudo*rotaxane as the cylinder could dethread from the macrocycle. Competition between the macrocycle and the junction for cylinder binding therefore reduced the junction formation of the *pseudo*rotaxane compared to the parent cylinder. To prevent junction binding completely the macrocyclic ring was mechanically locked in place by the addition of capping groups to the *pseudo*rotaxane, forming a rotaxane[139,140]. Unlike the parent cylinder, a previously investigated imidazole-based cylinder[141,142] (Figure 23) has a nucleophilic nitrogen available for alkylation, providing a route to a "capped" cylinder axle[143]. After threading the imidazole cylinder, six methylpyridine capping groups could be attached to lock the macrocycle in place[139,140].

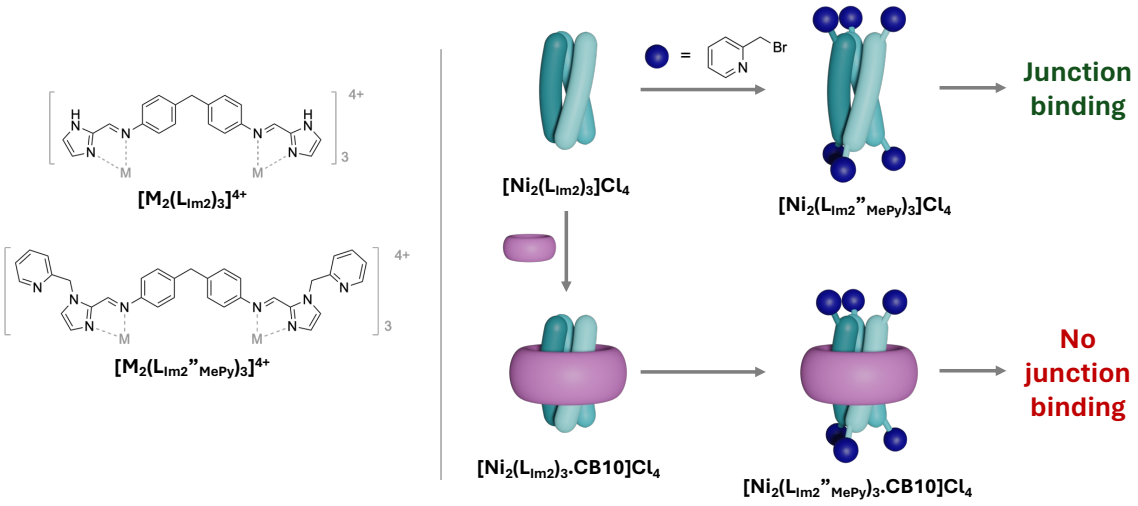

Figure 23: Showing (left) the structure of the 2-imidazole cylinder ($[M_2(L_{Im2})_3]^{4+}$) and the capped cylinder ($[M_2(L_{Im2"MePy})_3]^{4+}$), and (right) the synthesis of the capped cylinder and rotaxane[139,140].

In agreement with previous alterations to the termini of the cylinder[123] (extending the cylinder length), the formation of 3WJs was not inhibited by the methylpyridine caps[139]. The presence of the CB10 ring in the rotaxane inhibited junction formation as the macrocyclic ring sterically prevented interaction between the junction binding core of the cylinder and the DNA. Rotaxanation was therefore used as a method to prevent

junction binding[139]. As with the examples in section 1.5.2, release of the cylinder from the macrocyclic ring in response to an external stimulus should allow junction formation, providing a strategy for the control of junction binding.

1.7. List of References

1 J. F. Stoddart, *Angew. Chem. Int. Ed.*, 2017, **56**, 11094–11125.
2 Z. Ashbridge, S. D. P. Fielden, D. A. Leigh, L. Pirvu, F. Schaufelberger and L. Zhang, *Chem. Soc. Rev.*, 2022, **51**, 7779–7809.
3 E. Wasserman, *J. Am. Chem. Soc.*, 1960, **82**, 4433–4434.
4 A. Lüttringhaus, F. Cramer, H. Prinzbach and F. M. Henglein, *Justus Liebigs Ann. Chem.*, 1958, **613**, 185–198.
5 H. L. Frisch and E. Wasserman, *J. Am. Chem. Soc.*, 1961, **83**, 3789–3795.
6 I. T. Harrison and Shuyen. Harrison, *J. Am. Chem. Soc.*, 1967, **89**, 5723–5724.
7 G. Schill and H. Zollenkopf, *Justus Liebigs Ann. Chem.*, 1969, **721**, 53–74.
8 A. Yerin, E. S. Wilks, G. P. Moss and A. Harada, *Pure Appl. Chem.*, 2008, **80**, 2041–2068.
9 M. Xue, Y. Yang, X. Chi, X. Yan and F. Huang, *Chem. Rev.*, 2015, **115**, 7398–7501.
10 G. W. Gokel, W. M. Leevy and M. E. Weber, *Chem. Rev.*, 2004, **104**, 2723–2750.
11 D. Thibeault and J.-F. Morin, *Molecules*, 2010, **15**, 3709–3730.
12 C. D. Gutsche, *Calixarenes: An Introduction*, Royal Society of Chemistry, Cambridge, 2nd edn., 2008.
13 V. Böhmer, *Angew. Chem. Int. Ed. Engl.*, 1995, **34**, 713–745.
14 T. Ogoshi, S. Kanai, S. Fujinami, T. Yamagishi and Y. Nakamoto, *J. Am. Chem. Soc.*, 2008, **130**, 5022–5023.
15 H. Tao, D. Cao, L. Liu, Y. Kou, L. Wang and H. Meier, *Sci. China Chem.*, 2012, **55**, 223–228.
16 T. Ogoshi and T. Yamagishi, *Eur. J. Org. Chem.*, 2013, **2013**, 2961–2975.
17 E. M. M. Del Valle, *Process Biochem.*, 2004, **39**, 1033–1046.
18 J. Szejtli, *Chem. Rev.*, 1998, **98**, 1743–1754.
19 H. Ogino, *J. Am. Chem. Soc.*, 1981, **103**, 1303–1304.
20 W. A. Freeman, W. L. Mock and N. Y. Shih, *J. Am. Chem. Soc.*, 1981, **103**, 7367–7368.
21 W. L. Mock and N. Y. Shih, *J. Org. Chem.*, 1986, **51**, 4440–4446.
22 W. L. Mock and N. Y. Shih, *J. Am. Chem. Soc.*, 1988, **110**, 4706–4710.
23 J. Kim, I.-S. Jung, S.-Y. Kim, E. Lee, J.-K. Kang, S. Sakamoto, K. Yamaguchi and K. Kim, *J. Am. Chem. Soc.*, 2000, **122**, 540–541.
24 A. I. Day, R. J. Blanch, A. P. Arnold, S. Lorenzo, G. R. Lewis and I. Dance, *Angew. Chem. Int. Ed.*, 2002, **41**, 275–277.
25 S. Liu, P. Y. Zavalij and L. Isaacs, *J. Am. Chem. Soc.*, 2005, **127**, 16798–16799.
26 M. J. Pisani, Y. Zhao, L. Wallace, C. E. Woodward, F. R. Keene, A. I. Day and J. G. Collins, *Dalton Trans.*, 2010, **39**, 2078–2086.
27 X.-J. Cheng, L.-L. Liang, K. Chen, N.-N. Ji, X. Xiao, J.-X. Zhang, Y.-Q. Zhang, S.-F. Xue, Q.-J. Zhu, X.-L. Ni and Z. Tao, *Angew. Chem. Int. Ed.*, 2013, **52**, 7252–7255.

28 Q. Li, S.-C. Qiu, J. Zhang, K. Chen, Y. Huang, X. Xiao, Y. Zhang, F. Li, Y.-Q. Zhang, S.-F. Xue, Q.-J. Zhu, Z. Tao, L. F. Lindoy and G. Wei, *Org. Lett.*, 2016, **18**, 4020–4023.
29 B. Odell, M. V. Reddington, A. M. Z. Slawin, N. Spencer, J. F. Stoddart and D. J. Williams, *Angew. Chem. Int. Ed. Engl.*, 1988, **27**, 1547–1550.
30 B. L. Allwood, H. Shahriari-Zavareh, J. F. Stoddart and D. J. Williams, *J. Chem. Soc., Chem. Commun.*, 1987, 1058–1061.
31 B. L. Allwood, N. Spencer, H. Shahriari-Zavareh, J. F. Stoddart and D. J. Williams, *J. Chem. Soc., Chem. Commun.*, 1987, 1061–1064.
32 B. L. Allwood, N. Spencer, H. Shahriari-Zavareh, J. F. Stoddart and D. J. Williams, *J. Chem. Soc., Chem. Commun.*, 1987, 1064–1066.
33 P. R. Ashton, A. M. Z. Slawin, N. Spencer, J. F. Stoddart and D. J. Williams, *J. Chem. Soc., Chem. Commun.*, 1987, 1066–1069.
34 P. R. Ashton, T. T. Goodnow, A. E. Kaifer, M. V. Reddington, A. M. Z. Slawin, N. Spencer, J. F. Stoddart, C. Vicent and D. J. Williams, *Angew. Chem. Int. Ed. Engl.*, 1989, **28**, 1396–1399.
35 P. L. Anelli, N. Spencer and J. F. Stoddart, *J. Am. Chem. Soc.*, 1991, **113**, 5131–5133.
36 A. G. Johnston, D. A. Leigh, R. J. Pritchard and M. D. Deegan, *Angew. Chem. Int. Ed. Engl.*, 1995, **34**, 1209–1212.
37 A. G. Johnston, D. A. Leigh, A. Murphy, J. P. Smart and M. D. Deegan, *J. Am. Chem. Soc.*, 1996, **118**, 10662–10663.
38 D. A. Leigh, A. Murphy, J. P. Smart and A. M. Z. Slawin, *Angew. Chem. Int. Ed. Engl.*, 1997, **36**, 728–732.
39 J.-C. Chambron, V. Heitz and J.-P. Sauvage, *J. Chem. Soc., Chem. Commun.*, 1992, 1131–1133.
40 J.-C. Chambron, V. Heitz and J.-P. Sauvage, *J. Am. Chem. Soc.*, 1993, **115**, 12378–12384.
41 J.-C. Chambron, A. Harriman, V. Heitz and J.-P. Sauvage, *J. Am. Chem. Soc.*, 1993, **115**, 7419–7425.
42 J.-P. Collin, P. Gavinã and J.-P. Sauvage, *Chem. Commun.*, 1996, **8**, 2005–2006.
43 P. Gaviña and J.-P. Sauvage, *Tetrahedron Lett.*, 1997, **38**, 3521–3524.
44 L. Raehm, J. M. Kern and J.-P. Sauvage, *Chem. Eur. J.*, 1999, **5**, 3310–3317.
45 P. R. Ashton, D. Philp, N. Spencer and J. F. Stoddart, *J. Chem. Soc., Chem. Commun.*, 1992, 1124–1128.
46 P. R. Ashton, C. L. Brown, E. J. T. Chrystal, K. P. Parry, M. Pietraszkiewicz, N. Spencer and J. F. Stoddart, *Angew. Chem. Int. Ed. Engl.*, 1991, **30**, 1042–1045.
47 R. A. Bissell, E. Córdova, A. E. Kaifer and J. F. Stoddart, *Nature*, 1994, **369**, 133–137.
48 M. Gómez-López, J. A. Preece and J. F. Stoddart, *Nanotechnology*, 1996, **7**, 183–192.
49 H. Murakami, A. Kawabuchi, K. Kotoo, M. Kunitake and N. Nakashima, *J. Am. Chem. Soc.*, 1997, **119**, 7605–7606.
50 D. Qu, Q. Wang and H. Tian, *Angew. Chem. Int. Ed.*, 2005, **44**, 5296–5299.
51 M. Sojka, M. Fojtu, J. Fialova, M. Masarik, M. Necas and R. Marek, *Inorg. Chem.*, 2019, **58**, 10861–10870.

52 E. Arunkumar, C. C. Forbes, B. C. Noll and B. D. Smith, *J. Am. Chem. Soc.*, 2005, **127**, 3288–3289.
53 J. R. Johnson, N. Fu, E. Arunkumar, W. M. Leevy, S. T. Gammon, D. Piwnica-Worms and B. D. Smith, *Angew. Chem.*, 2007, **119**, 5624–5627.
54 R. S. Das, P. C. Saha, N. Sepay, A. Mukherjee, S. Chatterjee and S. Guha, *Org. Lett.*, 2020, **22**, 5839–5843.
55 R. S. Das, A. Mukherjee, S. Kar, T. Bera, S. Das, A. Sengupta and S. Guha, *Org. Lett.*, 2022, **24**, 5907–5912.
56 J. J. Gassensmith, L. Barr, J. M. Baumes, A. Paek, A. Nguyen and B. D. Smith, *Org. Lett.*, 2008, **10**, 3343–3346.
57 J. J. Gassensmith, E. Arunkumar, L. Barr, J. M. Baumes, K. M. DiVittorio, J. R. Johnson, B. C. Noll and B. D. Smith, *J. Am. Chem. Soc.*, 2007, **129**, 15054–15059.
58 E. M. Peck, C. G. Collins and B. D. Smith, *Org. Lett.*, 2013, **15**, 2762–2765.
59 F. d'Orchymont and J. P. Holland, *Angew. Chem. Int. Ed.*, 2022, **61**, e202204072.
60 I. Smukste and D. B. Smithrud, *J. Org. Chem.*, 2003, **68**, 2547–2558.
61 D. W. Zehnder and D. B. Smithrud, *Org. Lett.*, 2001, **3**, 2485–2487.
62 X. Bao, I. Isaacsohn, A. F. Drew and D. B. Smithrud, *J. Am. Chem. Soc.*, 2006, **128**, 12229–12238.
63 I. Smukste, B. E. House and D. B. Smithrud, *J. Org. Chem.*, 2003, **68**, 2559–2571.
64 V. Dvornikovs, B. E. House, M. Kaetzel, J. R. Dedman and D. B. Smithrud, *J. Am. Chem. Soc.*, 2003, **125**, 8290–8301.
65 J. Zhu, B. E. House, E. Fleck, I. Isaacsohn, A. F. Drew and D. B. Smithrud, *Bioorg. Med. Chem. Lett.*, 2007, **17**, 5058–5062.
66 X. Wang, X. Bao, M. McFarland-Mancini, I. Isaacsohn, A. F. Drew and D. B. Smithrud, *J. Am. Chem. Soc.*, 2007, **129**, 7284–7293.
67 J. Zhu, M. McFarland-Mancini, A. F. Drew and D. B. Smithrud, *Bioorg. Med. Chem. Lett.*, 2009, **19**, 520–523.
68 X. Wang and D. B. Smithrud, *Bioorg. Med. Chem. Lett.*, 2011, **21**, 6880–6883.
69 J. C. Sheehan and G. P. Hess, *J. Am. Chem. Soc.*, 1955, **77**, 1067–1068.
70 J. Shi, Y. Xu, X. Wang, L. Zhang, J. Zhu, T. Pang and X. Bao, *Org. Biomol. Chem.*, 2015, **13**, 7517–7529.
71 C. Chhun and A. R. Schmitzer, *MedChemComm*, 2011, **2**, 987–990.
72 C. Chhun, J. Richard-Daniel, J. Kempf and A. R. Schmitzer, *Org. Biomol. Chem.*, 2013, **11**, 6023–6028.
73 S. Chen, Y. Wang, T. Nie, C. Bao, C. Wang, T. Xu, Q. Lin, D.-H. Qu, X. Gong, Y. Yang, L. Zhu and H. Tian, *J. Am. Chem. Soc.*, 2018, **140**, 17992–17998.
74 C. Wang, S. Wang, H. Yang, Y. Xiang, X. Wang, C. Bao, L. Zhu, H. Tian and D. Qu, *Angew. Chem. Int. Ed.*, 2021, **60**, 14836–14840.
75 A. Fernandes, A. Viterisi, F. Coutrot, S. Potok, D. A. Leigh, V. Aucagne and S. Papot, *Angew. Chem. Int. Ed.*, 2009, **48**, 6443–6447.
76 A. Fernandes, A. Viterisi, V. Aucagne, D. A. Leigh and S. Papot, *Chem. Commun.*, 2012, **48**, 2083–2085.
77 R. Barat, T. Legigan, I. Tranoy-Opalinski, B. Renoux, E. Péraudeau, J. Clarhaut, P. Poinot, A. E. Fernandes, V. Aucagne, D. A. Leigh and S. Papot, *Chem. Sci.*, 2015, **6**, 2608–2613.

78 A. G. Cheetham, M. G. Hutchings, T. D. W. Claridge and H. L. Anderson, *Angew. Chem. Int. Ed.*, 2006, **45**, 1596–1599.
79 A. Bogdanov, A. Bogdanov, V. Chubenko, N. Volkov, F. Moiseenko and V. Moiseyenko, *Front. Oncol.*, 2022, **12**, 979154.
80 Y.-B. Hu, E. B. Dammer, R.-J. Ren and G. Wang, *Transl. Neurodegener.*, 2015, **4**, 18.
81 G. Yu, D. Wu, Y. Li, Z. Zhang, L. Shao, J. Zhou, Q. Hu, G. Tang and F. Huang, *Chem. Sci.*, 2016, **7**, 3017–3024.
82 J. Ye, R. Zhang, W. Yang, Y. Han, H. Guo, J. Xie, C. Yan and Y. Yao, *Chin. Chem. Lett.*, 2020, **31**, 1550–1553.
83 Y.-H. Cui, R. Deng, Z. Li, X.-S. Du, Q. Jia, X.-H. Wang, C.-Y. Wang, K. Meguellati and Y.-W. Yang, *Mater. Chem. Front.*, 2019, **3**, 1427–1432.
84 H. Isobe, N. Tomita, J. W. Lee, H.-J. Kim, K. Kim and E. Nakamura, *Angew. Chem. Int. Ed.*, 2000, **39**, 4257–4260.
85 E. Y. Chernikova, A. Y. Ruleva, V. B. Tsvetkov, Y. V. Fedorov, V. V. Novikov, T. M. Aliyeu, A. A. Pavlov, N. E. Shepel and O. A. Fedorova, *Org. Biomol. Chem.*, 2020, **18**, 755–766.
86 L. Vial, R. F. Ludlow, J. Leclaire, R. Pérez-Fernández and S. Otto, *J. Am. Chem. Soc.*, 2006, **128**, 10253–10257.
87 Y. Chen, Z. Huang, J.-F. Xu, Z. Sun and X. Zhang, *ACS Appl. Mater. Interfaces*, 2016, **8**, 22780–22784.
88 Y. Chen, Z. Huang, H. Zhao, J.-F. Xu, Z. Sun and X. Zhang, *ACS Appl. Mater. Interfaces*, 2017, **9**, 8602–8608.
89 C. P. Carvalho, A. Norouzy, V. Ribeiro, W. M. Nau and U. Pischel, *Org. Biomol. Chem.*, 2015, **13**, 2866–2869.
90 H. Isobe, S. Sato, J. W. Lee, H.-J. Kim, K. Kim and E. Nakamura, *Chem. Commun.*, 2005, 1549–1551.
91 X.-J. Zhang, Y.-M. Zhang, Z. Wang, Y. Chen and Y. Liu, *ChemistrySelect*, 2016, **1**, 685–690.
92 J. Li and X. J. Loh, *Adv. Drug. Deliv. Rev.*, 2008, **60**, 1000–1017.
93 T. R. Hoare and D. S. Kohane, *Polymer*, 2008, **49**, 1993–2007.
94 H.-B. Cheng, Y.-M. Zhang, C. Xu and Y. Liu, *Sci. Rep.*, 2014, **4**, 4210.
95 T. Kench, P. A. Summers, M. K. Kuimova, J. E. M. Lewis and R. Vilar, *Angew. Chem. Int. Ed.*, 2021, **60**, 10928–10934.
96 J. D. Watson and F. H. C. Crick, *Nature*, 1953, **171**, 737–738.
97 R. E. Franklin and R. G. Gosling, *Nature*, 1953, **172**, 156–157.
98 J. Spiegel, S. Adhikari and S. Balasubramanian, *Trends Chem.*, 2020, **2**, 123–136.
99 S. S. Masoud and K. Nagasawa, *Chem. Pharm. Bull.*, 2018, **66**, 1091–1103.
100 Y. Liu and S. C. West, *Nat. Rev. Mol. Cell Biol.*, 2004, **5**, 937–944.
101 T. Kato, T. Takemura, K. Yano, K. Ikebukuro and I. Karube, *Biochim. Biophys. Acta, Gene Struct. Expr.*, 2000, **1493**, 12–18.
102 T. Kato, K. Yano, K. Ikebukuro and I. Karube, *Nucleic Acids Res.*, 2000, **28**, 1963–1968.
103 M. N. Stojanovic and D. W. Landry, *J. Am. Chem. Soc.*, 2002, **124**, 9678–9679.
104 M. N. Stojanovic, P. de Prada and D. W. Landry, *J. Am. Chem. Soc.*, 2000, **122**, 11547–11548.

105 M. A. D. Neves, O. Reinstein and P. E. Johnson, *Biochemistry*, 2010, **49**, 8478–8487.
106 D. Roncancio, H. Yu, X. Xu, S. Wu, R. Liu, J. Debord, X. Lou and Y. Xiao, *Anal. Chem.*, 2014, **86**, 11100–11106.
107 A. Rodger, K. J. Sanders, M. J. Hannon, I. Meistermann, A. Parkinson, D. S. Vidler and I. S. Haworth, *Chirality*, 2000, **12**, 221–236.
108 M. J. Hannon, C. L. Painting, A. Jackson, J. Hamblin and W. Errington, *Chem. Commun.*, 1997, 1807–1808.
109 M. J. Hannon, V. Moreno, M. J. Prieto, E. Moldrheim, E. Sletten, I. Meistermann, C. J. Isaac, K. J. Sanders and A. Rodger, *Angew. Chem. Int. Ed.*, 2001, **40**, 879–884.
110 G. I. Pascu, A. C. G. Hotze, C. Sanchez-Cano, B. M. Kariuki and M. J. Hannon, *Angew. Chem. Int. Ed.*, 2007, **46**, 4374–4378.
111 I. Meistermann, V. Moreno, M. J. Prieto, E. Moldrheim, E. Sletten, S. Khalid, P. M. Rodger, J. C. Peberdy, C. J. Isaac, A. Rodger and M. J. Hannon, *Proc. Natl. Acad. Sci. U. S. A.*, 2002, **99**, 5069–5074.
112 A. Oleksy, A. G. Blanco, R. Boer, I. Usón, J. Aymamí, A. Rodger, M. J. Hannon and M. Coll, *Angew. Chem. Int. Ed.*, 2006, **45**, 1227–1231.
113 L. Cerasino, M. J. Hannon and E. Sletten, *Inorg. Chem.*, 2007, **46**, 6245–6251.
114 S. Phongtongpasuk, S. Paulus, J. Schnabl, R. K. O. Sigel, B. Spingler, M. J. Hannon and E. Freisinger, *Angew. Chem. Int. Ed.*, 2013, **52**, 11513–11516.
115 A. C. G. Hotze, N. J. Hodges, R. E. Hayden, C. Sanchez-Cano, C. Paines, N. Male, M.-K. Tse, C. M. Bunce, J. K. Chipman and M. J. Hannon, *Chem. Biol.*, 2008, **15**, 1258–1267.
116 C. Ducani, A. Leczkowska, N. J. Hodges and M. J. Hannon, *Angew. Chem. Int. Ed.*, 2010, **49**, 8942–8945.
117 J. Malina, M. J. Hannon and V. Brabec, *FEBS J.*, 2014, **281**, 987–997.
118 J. Malina, M. J. Hannon and V. Brabec, *Sci. Rep.*, 2016, **6**, 29674.
119 L. Cardo, I. Nawroth, P. J. Cail, J. A. McKeating and M. J. Hannon, *Sci. Rep.*, 2018, **8**, 13342.
120 C. Zhao, H. Song, P. Scott, A. Zhao, H. Tateishi-Karimata, N. Sugimoto, J. Ren and X. Qu, *Angew. Chem. Int. Ed.*, 2018, **57**, 15723–15727.
121 J. Malina, M. J. Hannon and V. Brabec, *Chem. Eur. J.*, 2007, **13**, 3871–3877.
122 D. R. Boer, J. M. C. A. Kerckhoffs, Y. Parajo, M. Pascu, I. Usón, P. Lincoln, M. J. Hannon and M. Coll, *Angew. Chem. Int. Ed.*, 2010, **49**, 2336–2339.
123 L. Cardo, V. Sadovnikova, S. Phongtongpasuk, N. J. Hodges and M. J. Hannon, *Chem. Commun.*, 2011, **47**, 6575–6577.
124 S. Vuong, L. Stefan, P. Lejault, Y. Rousselin, F. Denat and D. Monchaud, *Biochimie*, 2012, **94**, 442–450.
125 J. Novotna, A. Laguerre, A. Granzhan, M. Pirrotta, M.-P. Teulade-Fichou and D. Monchaud, *Org. Biomol. Chem.*, 2015, **13**, 215–222.
126 K. Duskova, P. Lejault, É. Benchimol, R. Guillot, S. Britton, A. Granzhan and D. Monchaud, *J. Am. Chem. Soc.*, 2020, **142**, 424–435.
127 J. Zell, K. Duskova, L. Chouh, M. Bossaert, N. Chéron, A. Granzhan, S. Britton and D. Monchaud, *Nucleic Acids Res.*, 2021, **49**, 10275–10288.
128 J. Gómez-González, D. G. Peña, G. Barka, G. Sciortino, J.-D. Maréchal, M. Vázquez López and M. Eugenio Vázquez, *Front. Chem.*, 2018, **6**, 520.

129 A. Alcalde-Ordóñez, N. Barreiro-Piñeiro, B. McGorman, J. Gómez-González, D. Bouzada, F. Rivadulla, M. Eugenio Vázquez, A. Kellett, J. Martínez-Costas and M. Vázquez López, *Chem. Sci.*, 2023, **14**, 14082–14091.
130 J. Gómez-González, Y. Pérez, G. Sciortino, L. Roldan-Martín, J. Martínez-Costas, J. Maréchal, I. Alfonso, M. Vázquez López and M. Eugenio Vázquez, *Angew. Chem. Int. Ed.*, 2021, **60**, 8859–8866.
131 I. Gamba, G. Rama, E. Ortega-Carrasco, J.-D. Maréchal, J. Martínez-Costas, M. Eugenio Vázquez and M. Vázquez López, *Chem. Commun.*, 2014, **50**, 11097–11100.
132 S. A. Barros and D. M. Chenoweth, *Angew. Chem. Int. Ed.*, 2014, **53**, 13746–13750.
133 I. Yoon, S. E. Suh, S. A. Barros and D. M. Chenoweth, *Org. Lett.*, 2016, **18**, 1096–1099.
134 S. A. Barros, I. Yoon, S. E. Suh and D. M. Chenoweth, *Org. Lett.*, 2016, **18**, 2423–2426.
135 S. A. Barros and D. M. Chenoweth, *Chem. Sci.*, 2015, **6**, 4752–4755.
136 S. A. Barros, I. Yoon and D. M. Chenoweth, *Angew. Chem.*, 2016, **128**, 8398–8401.
137 Z. Yang, Y. Chen, G. Li, Z. Tian, L. Zhao, X. Wu, Q. Ma, M. Liu and P. Yang, *Chem. Eur. J.*, 2018, **24**, 6087–6093.
138 J. Zhu, C. J. E. Haynes, M. Kieffer, J. L. Greenfield, R. D. Greenhalgh, J. R. Nitschke and U. F. Keyser, *J. Am. Chem. Soc.*, 2019, **141**, 11358–11362.
139 C. A. J. Hooper, L. Cardo, J. S. Craig, L. Melidis, A. Garai, R. T. Egan, V. Sadovnikova, F. Burkert, L. Male, N. J. Hodges, D. F. Browning, R. Rosas, F. Liu, F. V. Rocha, M. A. Lima, S. Liu, D. Bardelang and M. J. Hannon, *J. Am. Chem. Soc.*, 2020, **142**, 20651–20660.
140 C. A. J. Hooper, MRes Thesis, University of Birmingham, 2020.
141 F. Tuna, M. R. Lees, G. J. Clarkson and M. J. Hannon, *Chem. Eur. J.*, 2004, **10**, 5737–5750.
142 M. Pascu, PhD Thesis, University of Birmingham, 2007.
143 V. Sadovnikova, PhD Thesis, University of Birmingham, 2011.

2. SYNTHESIS OF AN IMIDAZOLE-BASED SUPRAMOLECULAR ROTAXANE

2.1. Previous Work

As discussed at the end of Chapter 1, locking the DNA binding motif of a cylinder, formed from the central phenyl rings, inside a macrocycle (CB10) can prevent 3WJ formation[1]. The supramolecular rotaxane differs from a traditional rotaxane as a 3D helicate replaces the linear thread axle, and instead of one large capping group at each end, the combined steric bulk of three capping groups is used to form the mechanical bond (Figure 24).

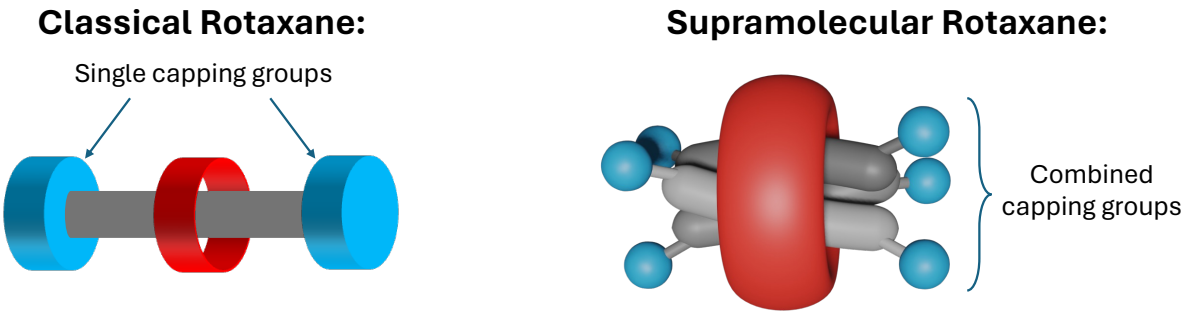

Figure 24: Showing the difference in capping groups between a classical rotaxane and the supramolecular rotaxane.

Formation of the supramolecular rotaxane requires a site on the cylinder which can be modified (a post-assembly modification). Imidazole-based cylinders ($[M_2(L_{Im4})_3]^{4+}$ and $[M_2(L_{Im2})_3]^{4+}$, Figure 25A) had been investigated by previous Hannon group members, F. Tuna *et al.*[2] and M. Pascu[3], for spin-crossover behaviour, however they also contain a free nitrogen which is available to act as a nucleophile. The methylpyridine capped cylinder ($[M_2(L_{Im2}{}^{"}{}_{MePy})_3]^{4+}$) had also already been synthesised

by V. Sadovnikova[4] via the alkylation of 2-imidazolecarboxaldehyde with methylpyridine prior to cylinder synthesis. Modifying the reaction conditions allowed alkylation of the pre-formed nickel imidazole cylinder[1] (Figure 25B) and provided a strategy for the synthesis of a supramolecular rotaxane via capping.

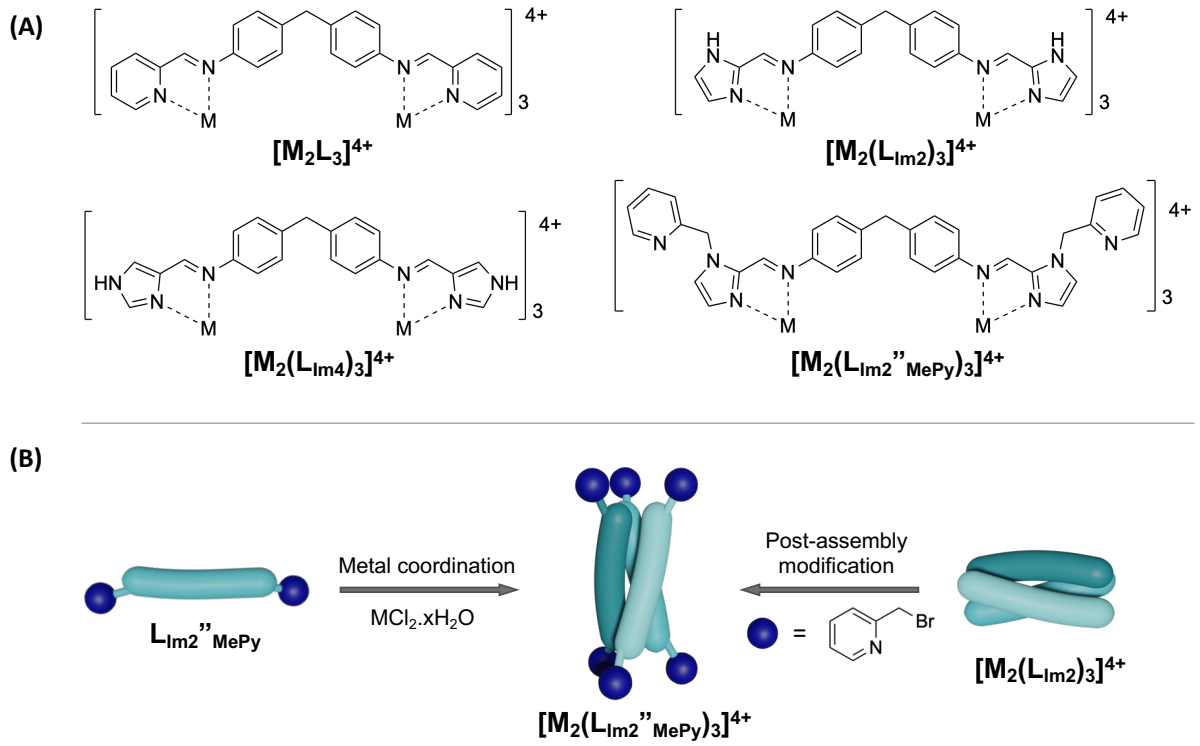

Figure 25: (A) Structure of the parent cylinder ($[M_2L_3]^{4+}$), the 4-imidazole cylinder ($[M_2(L_{Im4})_3]^{4+}$)[2], the 2-imidazole cylinder ($[M_2(L_{Im2})_3]^{4+}$)[3], and the methylpyridine capped cylinder ($[M_2(L_{Im2}"_{MePy})_3]^{4+}$)[1]. (B) Synthesis of the methylpyridine capped cylinder via metal coordination from a pre-formed ligand[4] and via post-assembly modification[1].

The nickel 2-imidazole based cylinder was thread through a CB10 macrocycle under aqueous conditions ($[Ni_2(L_{Im2})_3.CB10]^{4+}$) and capped with three methylpyridine groups at each end to form the supramolecular rotaxane ($[Ni_2(L_{Im2}"_{MePy})_3.CB10]^{4+}$, Figure 26)[1]. Gel electrophoresis was then used to demonstrate that the 3WJ formation of the cylinder axle was "turned off" without disruption or chemical modification of the central 3WJ recognition motif.

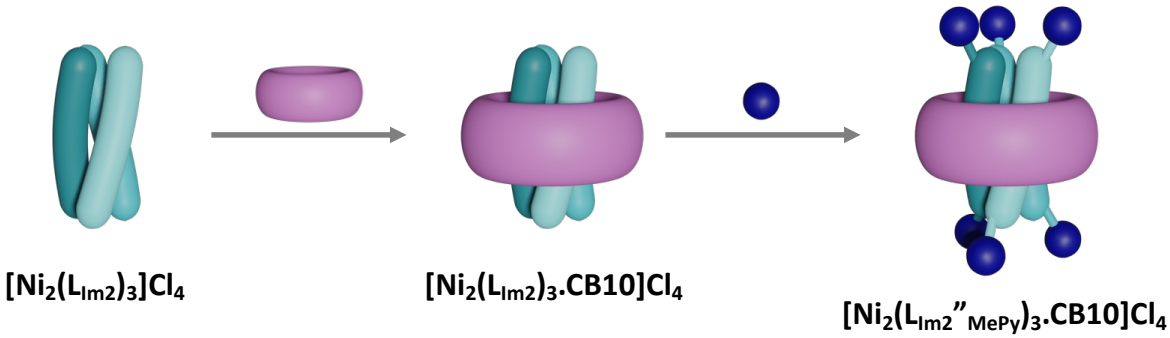

Figure 26: Synthetic route to the supramolecular rotaxane[1].

2.2. Research Aims

The aim of this project was to design a cylinder-based system able to control 3WJ formation with an external stimulus (Figure 27). This can be achieved by breaking the mechanical bond of a supramolecular rotaxane to release the cylinder and "turn on" junction binding. Liberation of the cylinder axle from the rotaxane requires either degradation of the macrocycle or removal of the capping groups. CB10 was used for the synthesis of the supramolecular rotaxane as it is the correct size to bind the cylinder, and threading, which is essential for rotaxane synthesis, is promoted under aqueous conditions due to hydrophobic and electrostatic-dipole interactions. Investigating removable capping groups prevents disruption to the interaction between the macrocyclic host and cylinder guest which was shown to be successful in previous studies[1].

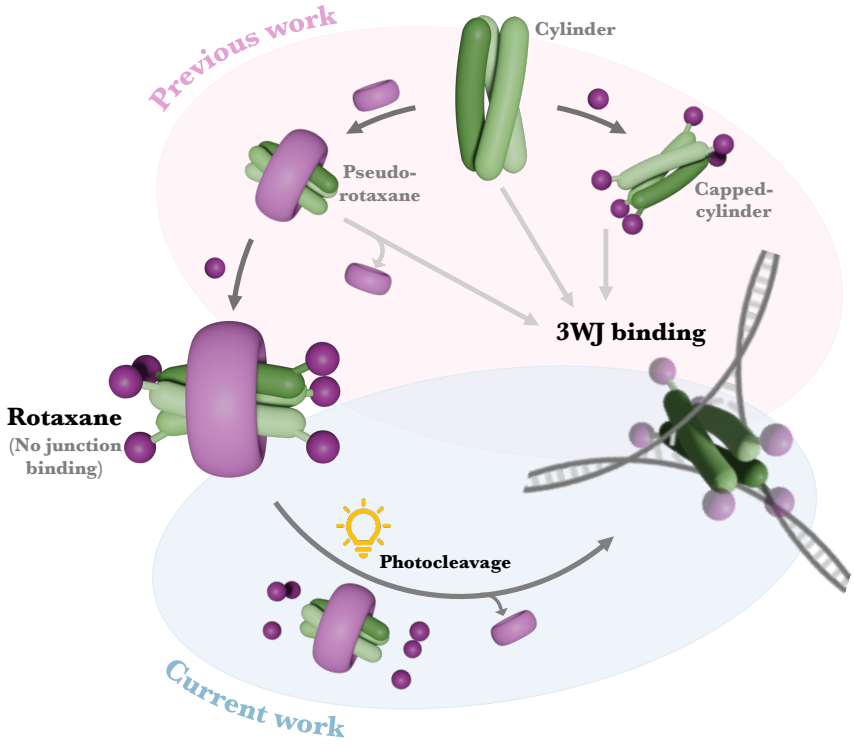

Figure 27: Graphical summary of previous work and the research aims.

To form a stimuli responsive supramolecular rotaxane, the capping groups must be attached in high yield under cylinder-compatible conditions, and be sterically bulky enough to prevent dethreading of the macrocycle. The cylinder should also be stable under the conditions required for the removal of the capping groups, and the removal should be triggered by an external stimulus.

Light is an attractive external stimulus to control junction binding as the duration, location, and intensity of application can be modified for different purposes. The metallohelicate should be unaffected by irradiation whereas other stimuli, such as changes to pH or enzymatic hydrolysis, may cause degradation of the complex. A range of photocleavable protecting groups and their different properties have already been documented[5].

4,5-Dimethoxy-2-nitrobenzyl bromide (DMNB-Br) is a commercially available photo-protecting group with a similar structure to the original 2-(bromomethyl)pyridine alkylating agent. 4,5-Dimethoxy-2-nitrobenzyl (DMNB) should therefore cap the 2-imidazole cylinder under similar conditions and should provide enough steric bulk to prevent dethreading of the CB10 ring (Figure 28).

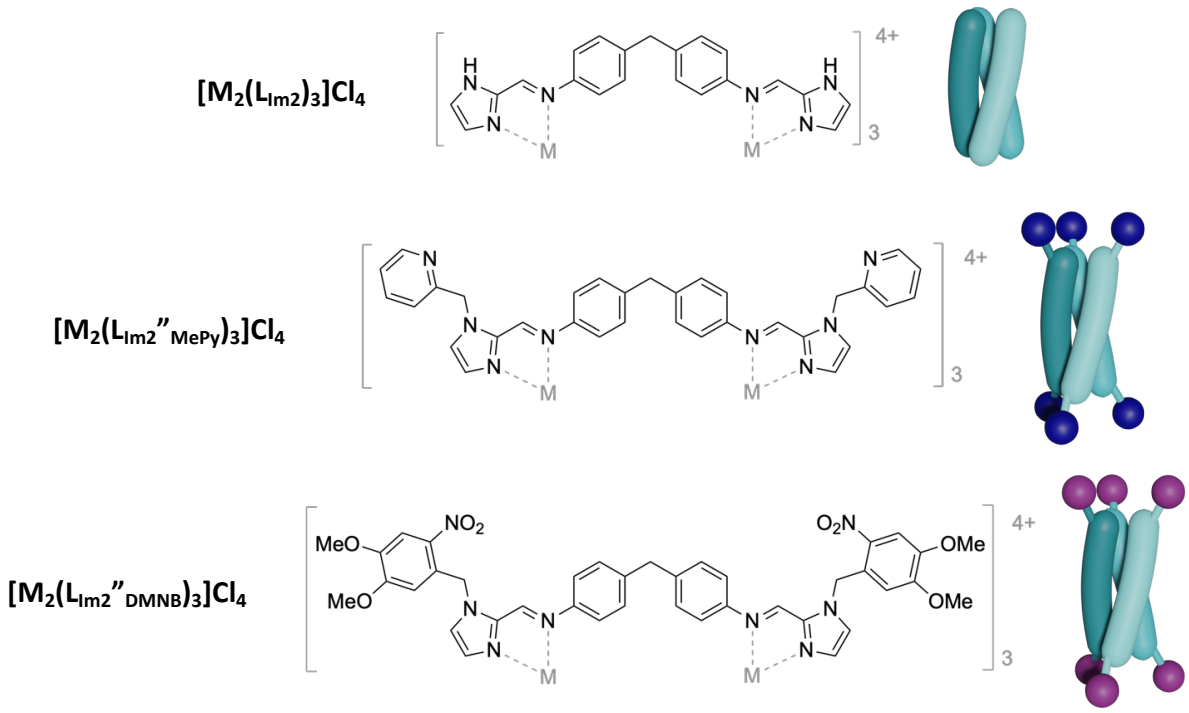

Figure 28: Structures of the uncapped 2-imidazole ($[M_2(L_{Im2})_3]^{4+}$), methylpyridine-capped ($[M_2(L_{Im2}"_{MePy})_3]^{4+}$), and the new DMNB-capped ($([M_2(L_{Im2}"_{DMNB})_3]^{4+}$) cylinders.

2.3. Nomenclature

A naming system is used throughout this thesis to describe different helicate structures and their ligands (Figure 29). Ligands (L) are differentiated by the terminal aromatic groups, and the number of caps per ligand is equal to the number of succeeding dashes or "X" if the number is not specified. Following the dashes, a

subscript identifier has been used to indicate the capping group (e.g. MePy), however DMNB will be the assumed capping group from this point. Half ligands (hL) have been hydrolysed at one imine bond so only have one terminal aromatic group available for alkylation.

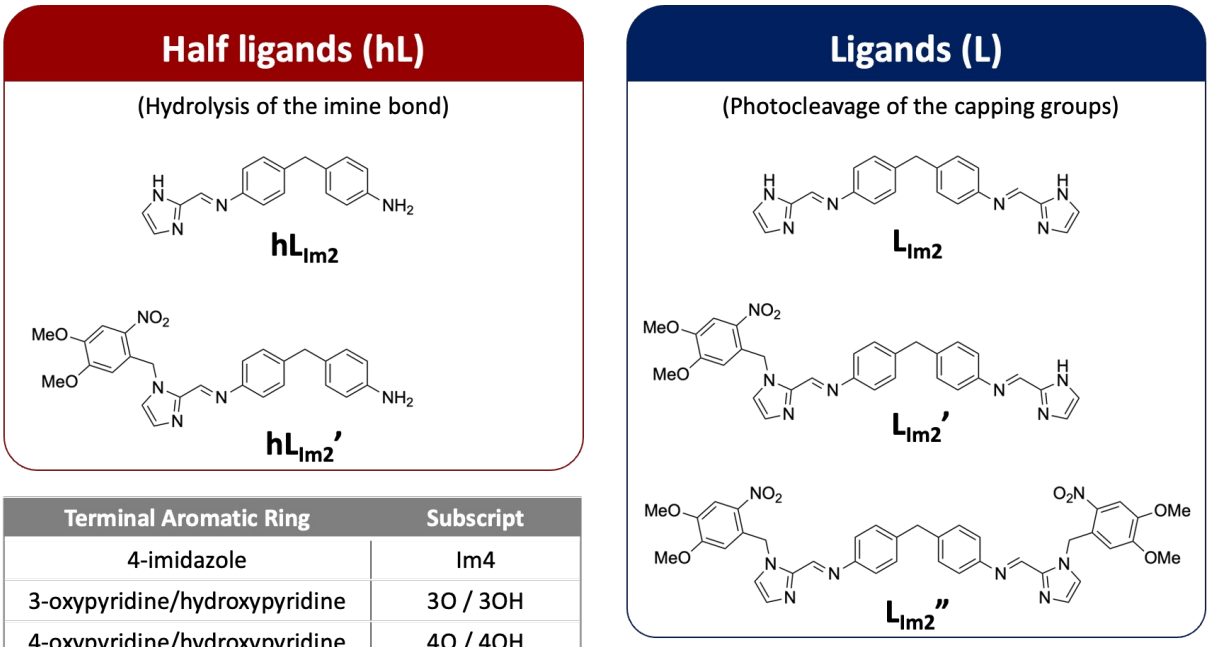

Terminal Aromatic Ring	Subscript
4-imidazole	Im4
3-oxypyridine/hydroxypyridine	3O / 3OH
4-oxypyridine/hydroxypyridine	4O / 4OH
5-oxypyridine/hydroxypyridine	5O / 5OH
Pyridine (Parent Cylinder)	(None)

Figure 29: Variations of the 2-imidazole ligands and a table showing the subscript for each ligand discussed in this thesis.

"Partially capped" cylinders with between one and five capping groups are shown by a mixture of ligand structures so that the total number of caps is correct. This does not indicate the exact arrangement of the capping groups between the three ligands as this cannot be deduced from the data collected.

2.4. Cylinder Synthesis

The synthesis of both the 2-imidazole[1,4] and 4-imidazole cylinders[2] have been previously reported. 2- or 4-imidazolecarboxaldehyde and 4,4'-methylenedianiline (MDA) are stirred under reflux in methanol with acetic acid to catalyse the condensation reaction. The solid white ligand product (L_{Im2} or L_{Im4}, respectively) precipitates and is collected by filtration in high yield and purity. The ligands were characterised by ^1H NMR (nuclear magnetic resonance, Figure 30) and mass spectrometry (*m/z* = 355, L_{Im2} or L_{Im4}, and *m/z* = 277, hL_{Im2} or hL_{Im4}).

The ligand is designed to promote the self-assembly of helicates upon metal-coordination. Condensation between a dianiline and an aromatic aldehyde forms an imine bond which is stabilised by the adjacent aromatic group[6] and provides a bidentate metal binding site[7]. The rigid diphenylmethylene spacer prevents the two metal binding sites coordinating the same ion but allows the twisting required to form the helicate. Six-coordinate octahedral metal ions, such as iron(II) and nickel(II), can coordinate three of the bidentate ligand each to form the triple helical structure with either a left-handed (M, Λ) or right-handed (P, Δ) twist[8].

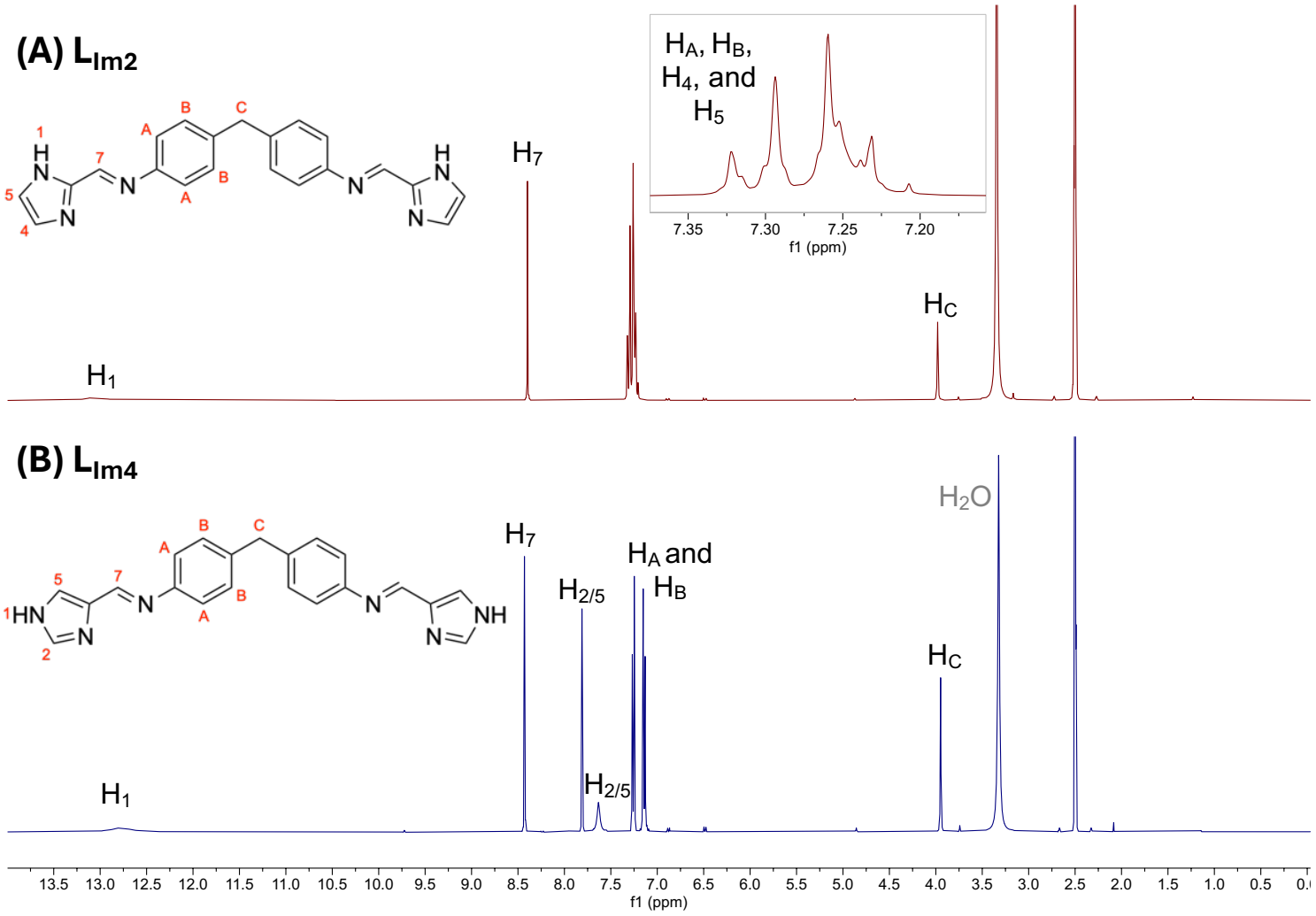

Figure 30: ^{1}H NMR (DMSO-d$_6$) of the 2-imidazole ligand (A, 300 MHz), and 4-imidazole ligand (B, 400 MHz).

The imidazole-based cylinders can therefore be formed by addition of the methanolic metal salts, iron(II) or nickel(II), to a suspension of the ligand (L_{Im2} or L_{Im4}) in methanol. A colour change from a cloudy white solution to a clear coloured solution is observed, indicating the formation of the metal complex, and uncomplexed ligand is removed from the solution by filtration. The cylinder is purified by anion exchange in which ammonium hexafluorophosphate is added to the methanolic filtrate and the hexafluorophosphate salt of the cylinder is collected as a precipitate. Conversion back to the chloride salt is achieved by suspending the hexafluorophosphate salt in methanol with an excess of chloride-form Dowex ion exchange resin. When the complex is fully dissolved, the resin can be removed by filtration and the solvent removed from the filtrate to yield the cylinder. In cases where anion exchange is not possible, the reaction filtrate is concentrated, and the cylinder is precipitated in diethyl ether to be collected by filtration.

Nickel(II) is a d^8 metal ion, and iron(II) is a d^6 metal ion which can exist as a high spin complex in the imidazole helicate[2], making both imidazole-based cylinders paramagnetic. The unpaired electrons distort the magnetic field experienced by adjacent protons during ^{1}H NMR, increasing the range of chemical shifts (<0 ppm and >200 ppm) and broadening the peaks which can prevent accurate measurement of the integration values. Using a lower strength magnetic field (300 MHz) reduced broadening, and assignments were made considering the relative chemical shifts, distance to the paramagnetic centre, and by comparison to previously reported spectra[1,2].

The iron (Figure 31A and C) imidazole cylinders give sharper peaks in the ^{1}H NMR compared to the nickel (Figure 31B and D) complexes, in which some peaks are

lost in the baseline due to broadening. The phenyl ($H_{A/B}$, integration = 2) and methylene (H_C, integration = 1) protons are furthest from the paramagnetic ions, so show smaller shifts from the diamagnetic region (-10 to 30 ppm), whereas the imine (H_7) and imidazole ($H_{4/5}$ or $H_{2/5}$) protons show large shifts.

NMR is key for the characterisation of organic molecules but is difficult to interpret for the paramagnetic cylinders. Both nickel and iron have distinctive isotope patterns so mass spectrometry is used as a primary source of structural information. The mass spectra (Figure 32) of the 2-imidazole cylinders shows peaks for the mono- to tri-cationic cylinder species formed by deprotonation at the imidazole ring. Free ligands (L_{Im2} and hL_{Im2}) and the two-metal, two-ligand species ($[M_2(L_{Im2})_2]^{2+}$), from which these ligands may have been lost are also observed, however it is unclear if these species exist in solution.

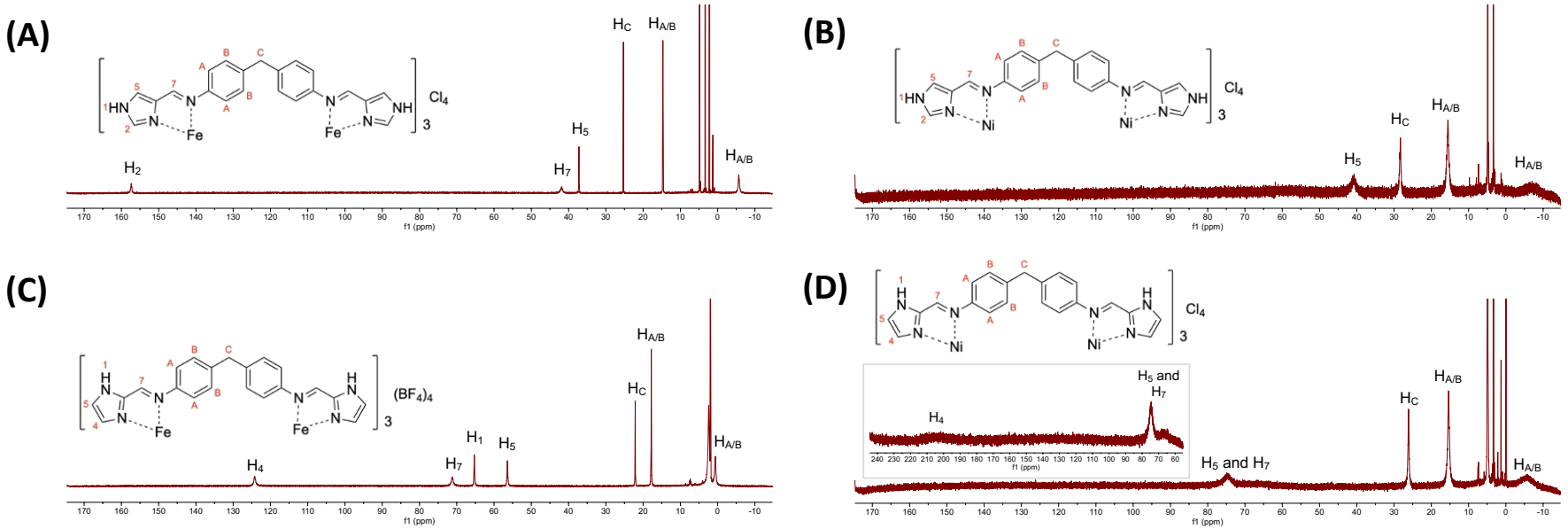

Figure 31: ^{1}H NMR spectra with suggested assignments of the imidazole-based iron and nickel cylinders: (A, B, and, D, 300 MHz, Methanol-d4) $[Fe(L_{Im4})_3]Cl_4$, $[Ni_2(L_{Im4})_3]Cl_4$, and $[Ni_2(L_{Im2})_3]Cl_4$, and (C, 300 MHz, Acetonitrile-d3) $[Fe_2(L_{Im2})_3](BF_4)$.

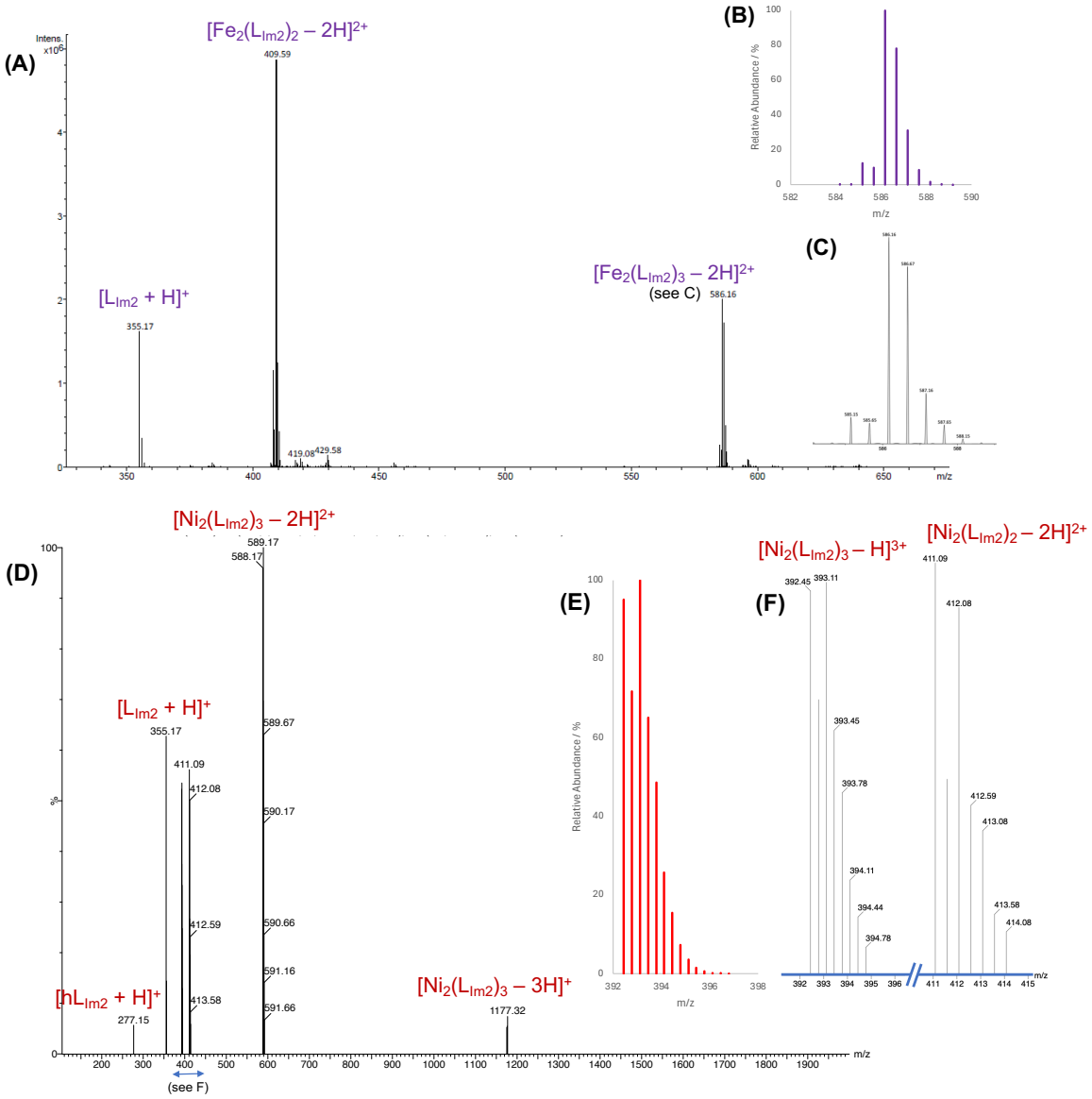

Figure 32: Mass spectra (TOF ES+) of (A and C, MeCN, microTOF) $[Fe_2(L_{Im2})_3](BF_4)_4$, and (D and F, MeOH, Waters Xevo G2-XS) of $[Ni_2(L_{Im2})_3]Cl_4$. (B) and (E) show models of peaks 586 m/z (from spectrum A) and 392 m/z (from spectrum D), respectively, as calculated using Envipat[9].

2.5. Supramolecular Rotaxane Synthesis

Both the "capping" (Figure 33i-iv) and "slipping" (Figure 33I-IV) methods for rotaxane synthesis (Chapter 1, Section 1.3) have been attempted for the formation of the supramolecular rotaxane.

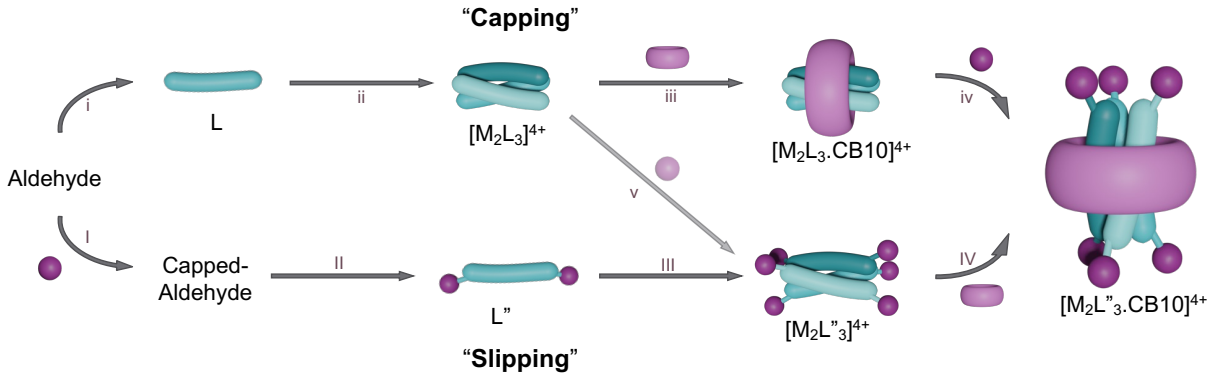

Figure 33: Routes towards the supramolecular rotaxane.

The capping method gives access to a wide range of rotaxanes with different capping groups from the same *pseudo*rotaxane, however the addition of six capping groups is required to form the rotaxane. The structural similarity of partially capped side products would make purification of the fully capped rotaxane difficult. Slipping avoids the formation of partially capped products as the capped aldehyde (Ald_{Im2}') can be purified before carrying forward (Figure 33I), however the choice of capping groups is limited they must be small enough to thread through the macrocycle upon heating.

2.5.1. Cylinder Capping Reaction

The capping reaction was first attempted without the macrocycle (Figure 33v, Figure 34A) as CB10 is isolated with a low yield[10,11], unlike the uncapped cylinder which is synthesised in high yield from commercially available reagents. Following similar methods of post-assembly modification[1,12], the nickel 2-imidazole cylinder ($[Ni_2(L_{Im2})_3]Cl_4$) was heated to reflux with nine equivalents of DMNB-Br (50% stoichiometric excess) and three equivalents of the base (stoichiometric amount). The reaction was completed in water to mimic the conditions required for rotaxane synthesis (Figure 34B).

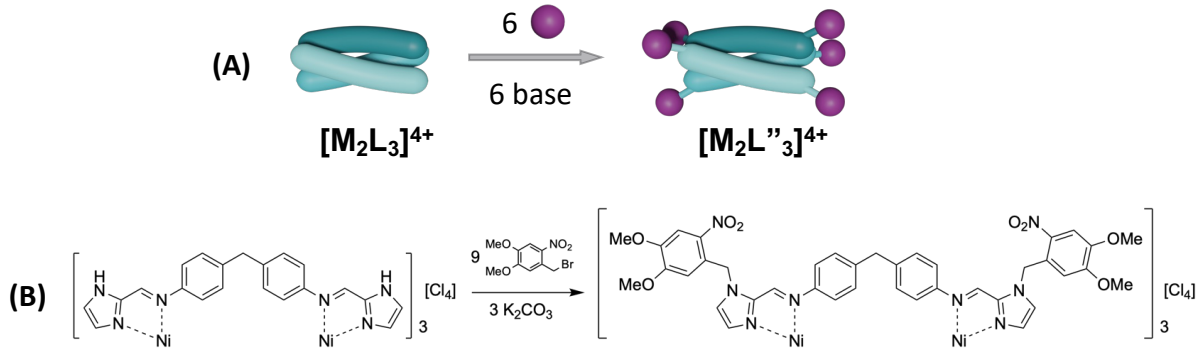

Figure 34: (A) General reaction scheme for the capping reaction, and (B) capping of $[Ni_2(L_{Im2})_3]Cl_4$ with DMNB-Br in water.

The reaction mixture was investigated by low resolution mass spectrometry after an overnight reflux and showed different fully and partially capped cylinder species were present with a high level of capping overall (Figure 35). The resolution was too low to identify the charge of each peak, so the exact species could not be assigned where the expected mass to charge ratio (m/z) between two different species differed by less than 1 m/z (Table 1). Assignments were made by considering whether peaks with similar charges or number of caps are also observed. The free imidazole rings of partially capped cylinders can be deprotonated to form lower charged species, however this is not possible for the fully capped cylinder. Bromide ions from the DMNB-Br starting material can act as a counter ion for the cylinder species causing a lower overall charge.

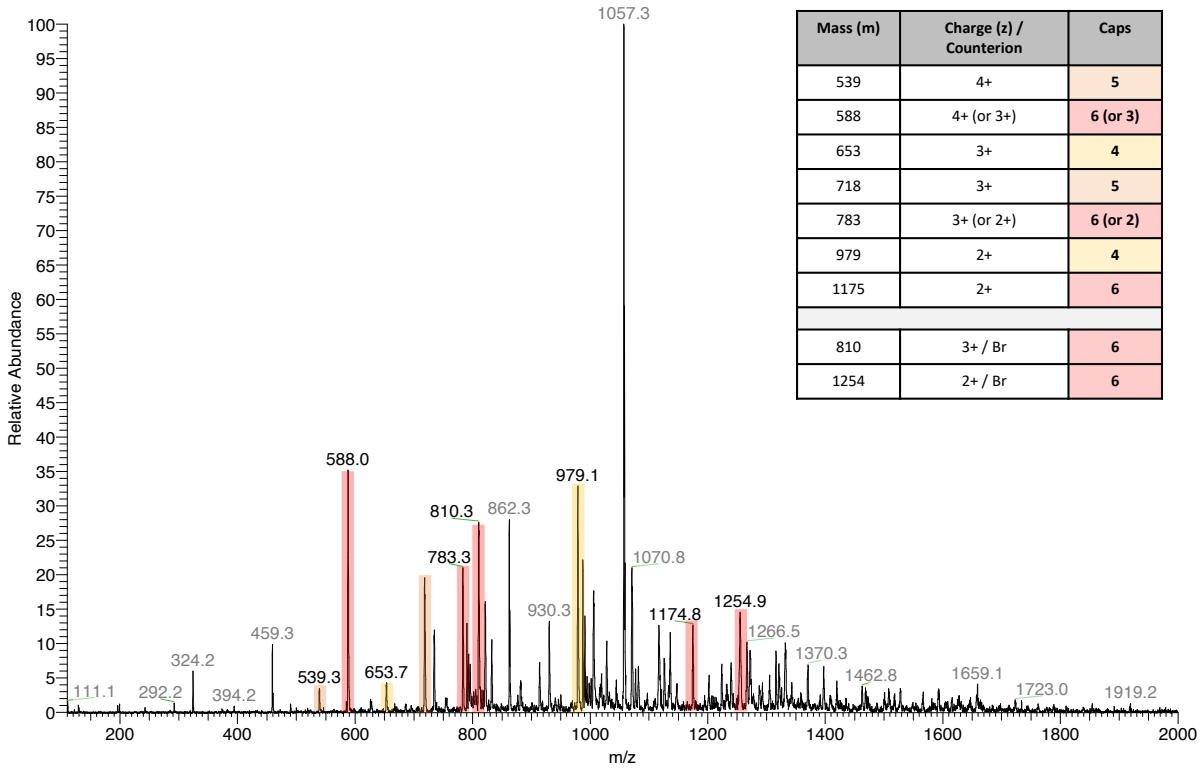

Mass (m)	Charge (z) / Counterion	Caps
539	4+	5
588	4+ (or 3+)	6 (or 3)
653	3+	4
718	3+	5
783	3+ (or 2+)	6 (or 2)
979	2+	4
1175	2+	6
810	3+ / Br	6
1254	2+ / Br	6

Figure 35: Low resolution mass spectrum (ITMS ES+, MeOH) of the capping reaction mixture after overnight reflux in water.

	Charge / ions gained or lost								
Number of caps	4+	3+ / - H	3+ / + Cl	3+ / + Br	3+ / + PF_6	2+ / - 2H	2+ / + 2Cl	2+ / + 2Br	2+ / + 2PF_6
0	294.79	392.71	404.86	419.68	441.37	588.56	625.02	669.47	734.53
1	343.48	457.64	469.79	484.61	506.30	685.96	722.42	766.87	831.93
2	392.18	522.57	534.72	549.54	571.23	783.35	819.81	864.26	929.32
3	440.88	587.50	599.65	614.47	636.16	880.75	917.21	961.66	1026.72
4	489.96	652.94	665.10	679.91	701.60	978.91	1015.37	1059.82	1124.88
5	538.66	717.87	730.03	744.84	766.53	1076.31	1112.77	1157.22	1222.28
6	587.55	783.06	795.21	810.03	831.72	1174.09	1210.55	1255.00	1320.06

Table 1: Calculated m/z values for the differently capped and charged nickel cylinder species. Values differing by <1 m/z have been outlined.

The reaction was dried and the residue resuspended in methanol for anion exchange to the hexafluorophosphate salt. A light brown precipitate was collected from an orange solution, however mass spectrum of the filtrate showed peaks for the fully capped cylinder (588 and 783 m/z, 4+ and 3+ charged, respectively) as well as some partially capped species, suggesting some loss of the product at this stage. The mass

spectrum of the final product was taken in both low and high resolution for comparison (Figure 36A and B, respectively). At high resolution the charge of each species can be deduced allowing exact assignment of the species present and showed only the 5- and 6-capped species had been isolated. The peaks at 1028 and 1093 m/z are suspected to be a 3+ charged nickel species due to their isotope pattern, however the exact assignment could not be deduced.

Attempts to optimise the reaction while monitoring with low resolution mass spectrometry were unsuccessful. The reaction was repeated with the nickel 4-imidazole cylinder ($[Ni_2(L_{Im4})_3]Cl_4$), however, the reaction solution showed a lower degree of capping overall (Figure 37). The nucleophilic nitrogen atoms of the imidazole ring are held in close proximity in the 4-imidazole cylinder which could cause steric crowding with an increasing number of capping groups. The partially capped two-metal, two-ligand species is also observed which is not present for the 2-imidazole cylinder.

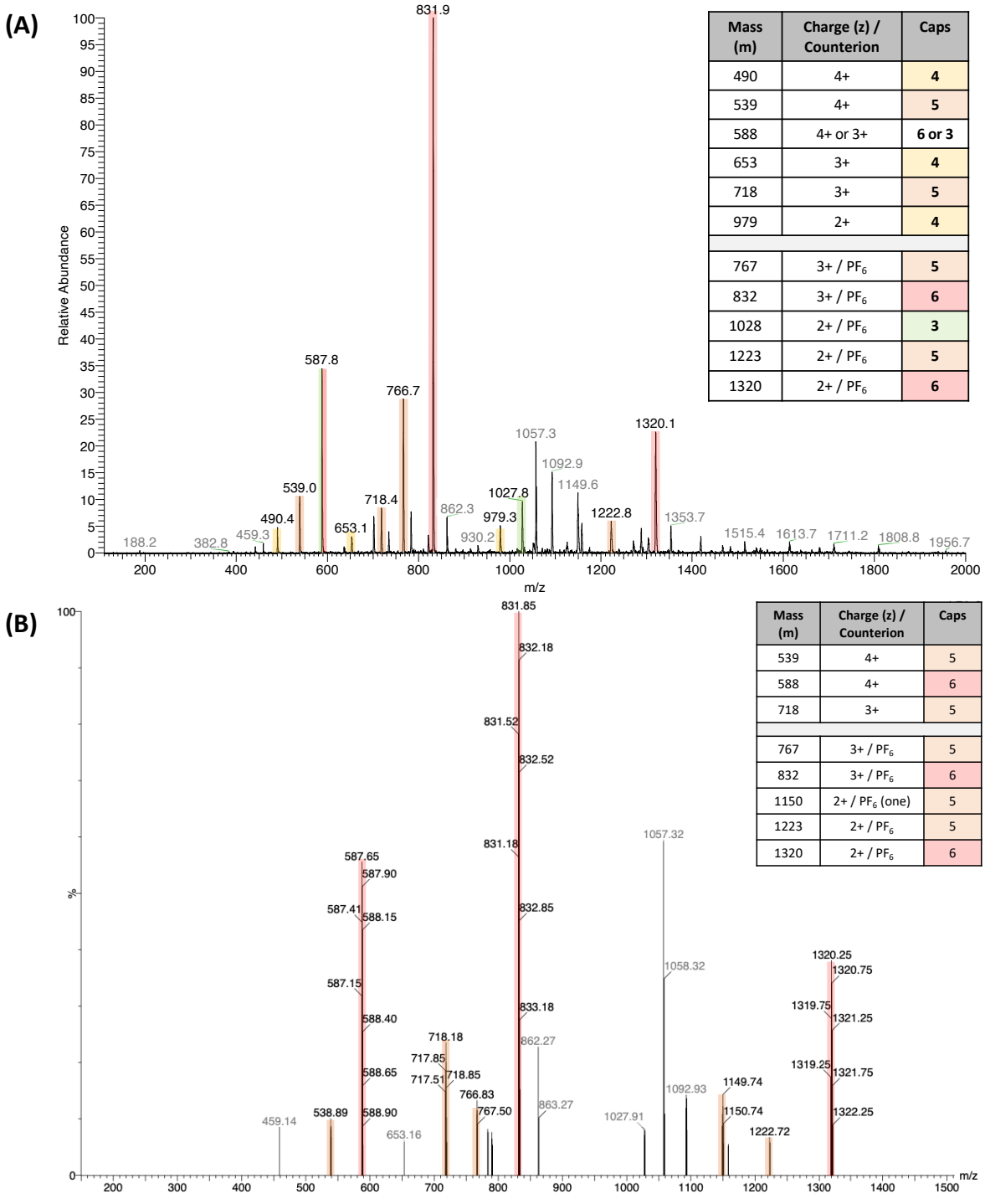

Figure 36: Mass spectra of the capping reaction product at low (A, ITMS, ES+, MeCN) and high (B, TOF ES+, MeCN) resolution.

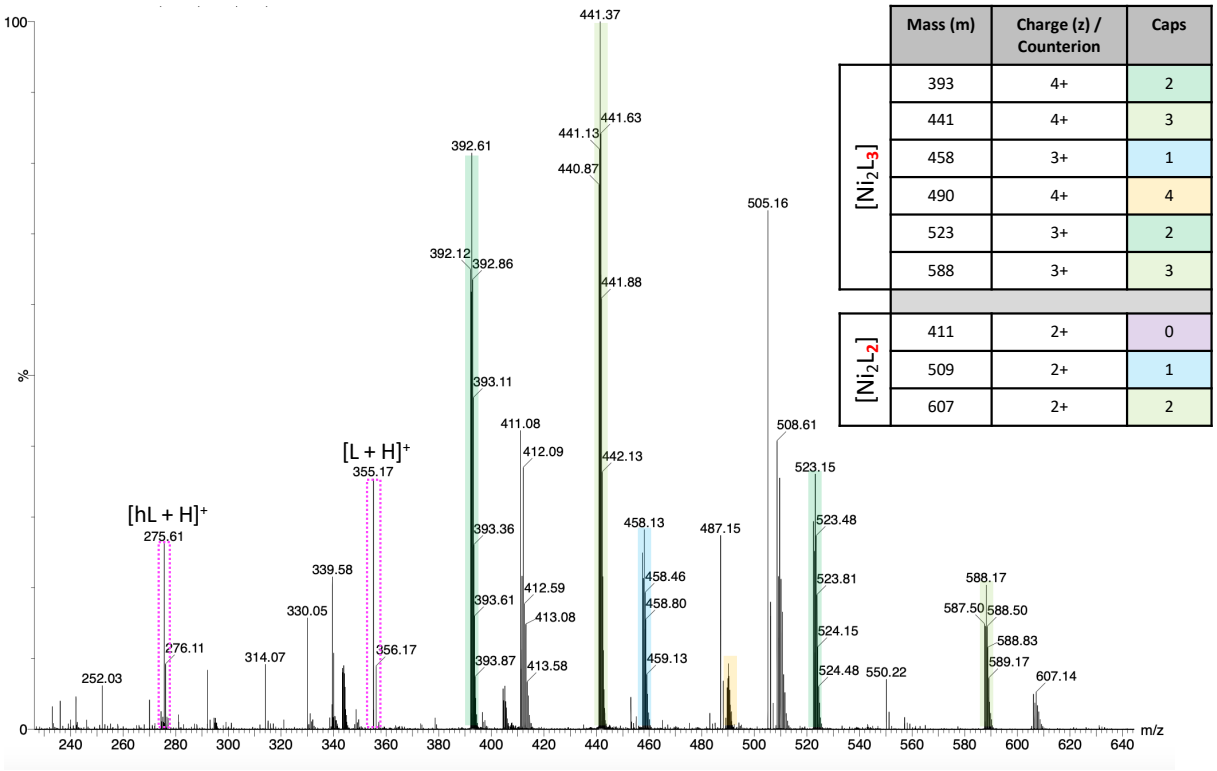

	Mass (m)	Charge (z) / Counterion	Caps
$[Ni_2L_3]$	393	4+	2
	441	4+	3
	458	3+	1
	490	4+	4
	523	3+	2
	588	3+	3
$[Ni_2L_2]$	411	2+	0
	509	2+	1
	607	2+	2

Figure 37: Mass spectrum (TOF ES+, H_2O) of the reaction solution from capping $[Ni_2(L_{Im4})_3]Cl_4$.

2.5.2. Rotaxane synthesis by capping

As the cylinder capping reaction was completed in water, the only change required for synthesis of the rotaxane was the addition of the macrocycle. Insoluble CB10 was dissolved in an aqueous solution of the nickel 2-imidazole cylinder, indicating the formation of the *pseudo*rotaxane ($[Ni_2(L_{Im2})_3$.CB10$]Cl_4$). DMNB-Br and potassium carbonate were added and the mixture heated to reflux overnight. The rotaxane was precipitated from the aqueous solution by anion exchange before converting back to the chloride salt for analysis (as described in section 2.4). Addition of CB10 to the complex changed the mass of the possible partially capped species so they no longer overlapped and could be assigned by low resolution mass spectrometry (Figure 38). Rotaxanated species with between 0-5 caps are observed with the 3-

capped species having the highest relative abundance. The appearance of the 5-capped species confirms that the rotaxane can accommodate 3 caps at each end of the cylinder.

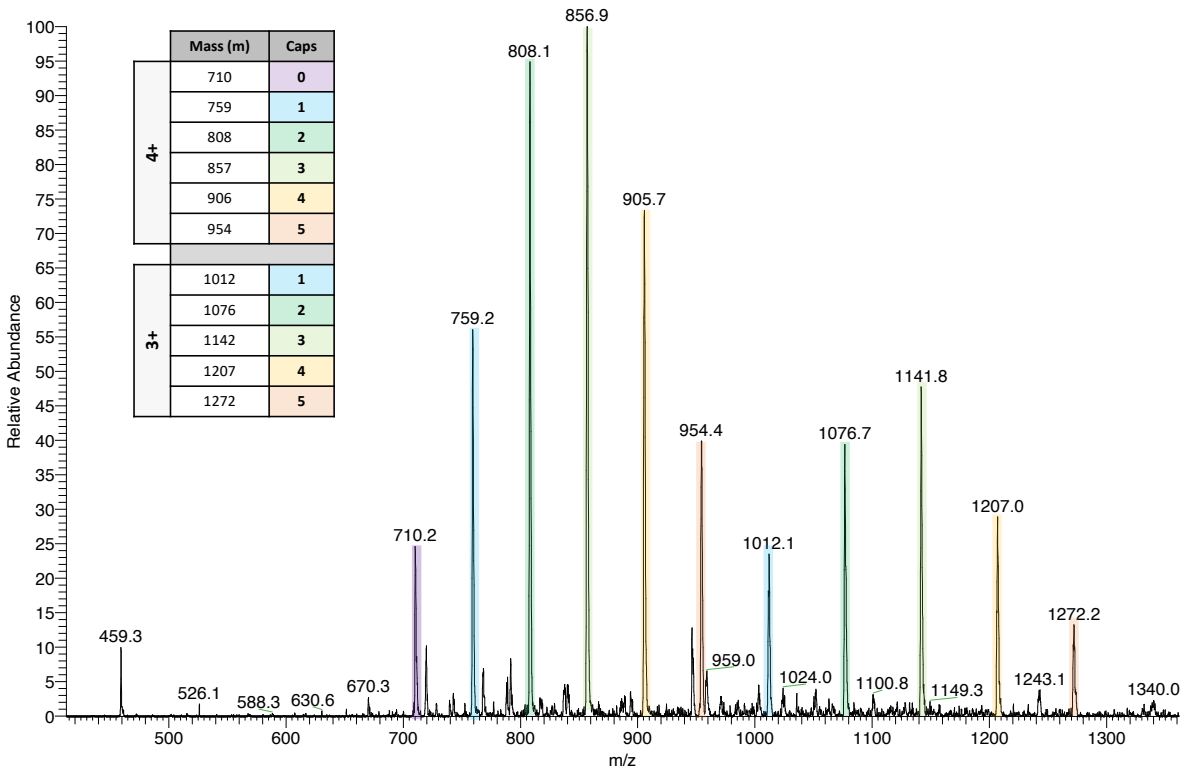

Figure 38: Mass spectrum (ITMS, ES+, H_2O) of the pseudorotaxane capping reaction after overnight reflux.

The partially reacted product was redissolved in water with 8 further equivalents of DMNB-Br and 4 equivalents of the base before heating to reflux overnight. The solution was filtered, and the mass spectrum of the filtrate was recorded (Figure 39) showing that a higher degree of capping (between 3-6 caps) had been achieved. An organic peak was also observed at 459 m/z, however this peak could not be assigned.

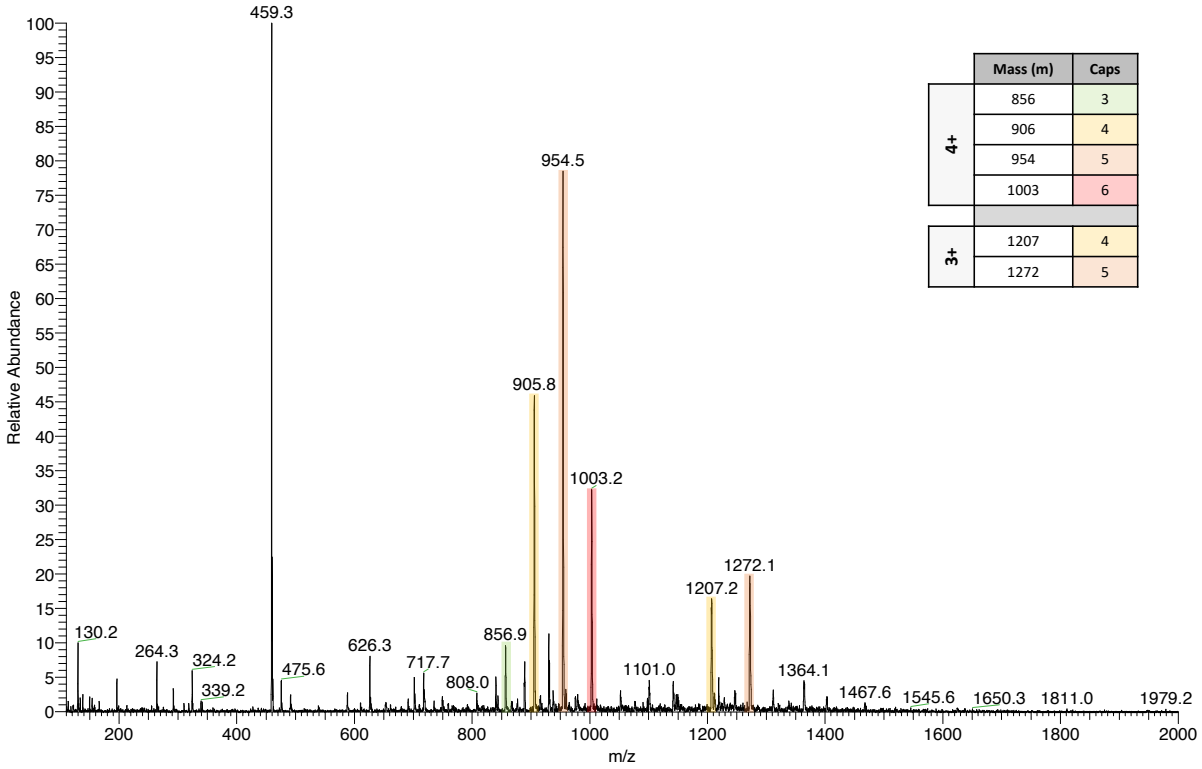

Figure 39: Mass spectrum (ITMS, ES+, MeOH) of the pseudorotaxane capping reaction after a second overnight reflux.

The capping reaction was repeated with a greater amount of DMNB-Br (12 equivalents) and potassium carbonate (6 equivalents) to see if the fully capped rotaxane could be isolated in one step. After refluxing for 24 hours the product was precipitated by anion exchange and the mass spectrum recorded (Figure 40). A range of differently capped species were observed but the uncapped species was the most abundant, suggesting that the alkylation was less successful.

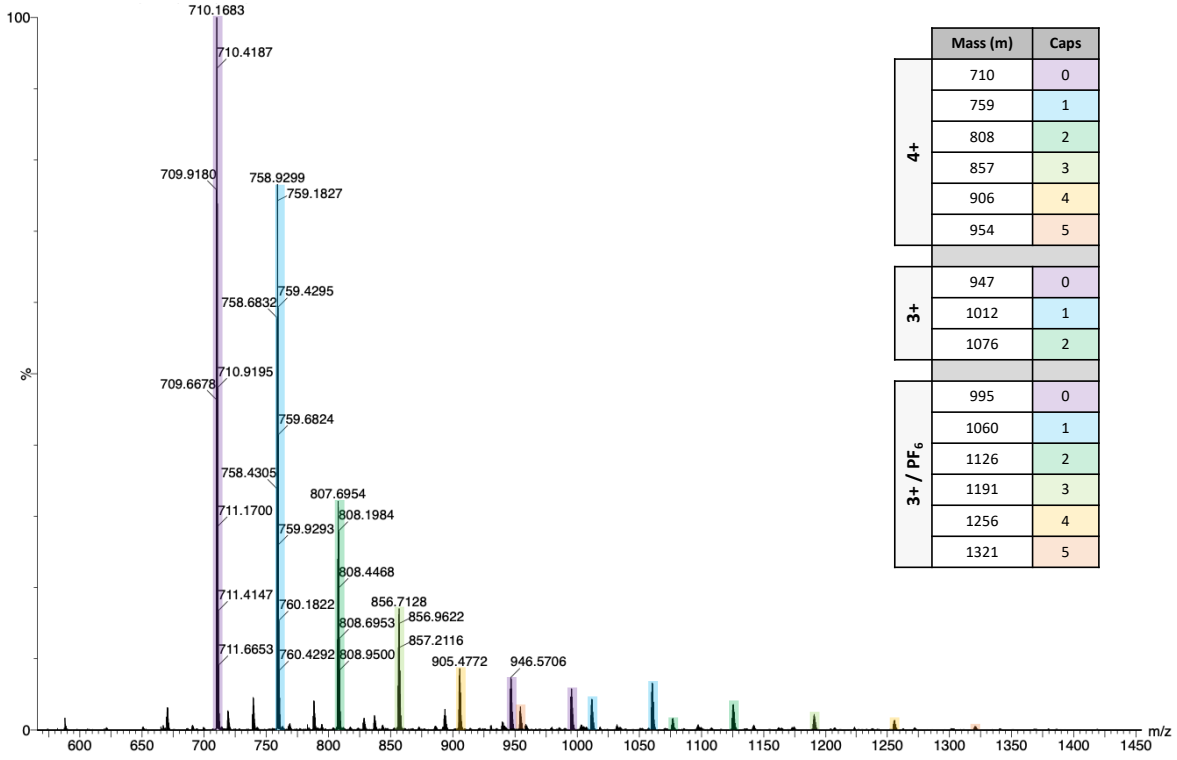

Figure 40: Mass spectrum (TOF ES+, MeCN) of the hexafluorophophate product from the capping reaction.

While the alkylation reaction is successful, isolation of the fully capped rotaxane has not been achieved. Optimisation of the reaction would be possible, however mass spectrometry does not indicate the relative amounts of each species in solution and multiple repeats of the reaction would use limited starting materials.

2.6. Rotaxane synthesis by slipping

Slipping is an alternative route to the supramolecular rotaxane which avoids the production of partially capped side-products as the 2-imidazolecarboxaldehyde is capped prior to synthesis of the ligand and metal complex (Figure 41).

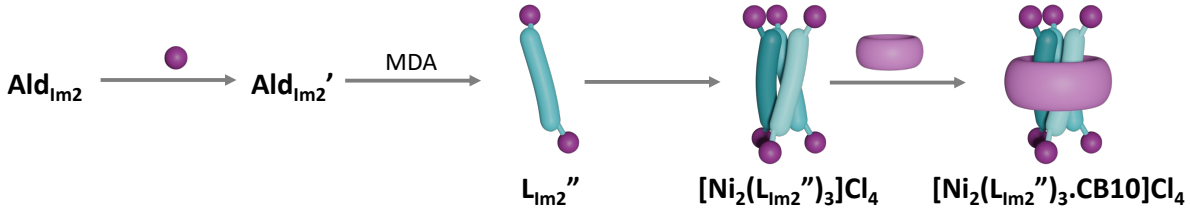

Figure 41: Synthesis of a supramolecular rotaxane by slipping.

This method has been used by J. Craig to demonstrate that the methylpyridine capped cylinder ([$Ni_2(L_{Im2}"_{MePy})_3$]Cl_4) could be thread through a CB10 ring by refluxing in aqueous methanol overnight[13]. Alternatively, R. Egan found that the 2,4-dinitrobenzene capped rotaxane ([$Ni_2(L_{Im2}"_{DNB})_3$]Cl_4) could not be formed by slipping[12]. This could be due to the lack of bridging methyl group between the cylinder and aromatic cap, which reduces the conformational flexibility of the capping group and prevents threading even under reflux. The suitability of the slipping method for synthesis of a rotaxane is therefore dependent on the capping group used.

2.6.1. Synthesis of the capped cylinder

Alkylation of the aldehyde was first completed in aqueous acetonitrile with an inorganic base (potassium carbonate). The product was extracted into DCM and purified by column chromatography

The alkylation was scaled up and the product investigated by ^{1}H NMR (Figure 42). The imidazole peaks (H_4 and H_5) show coupling to each other with a smaller coupling constant than expected (J = 1 Hz) and one of these protons also shows coupling to the carboxaldehyde proton (H_7) with the same coupling constant (J = 1 Hz). The remaining singlets could be identified by their integration values.

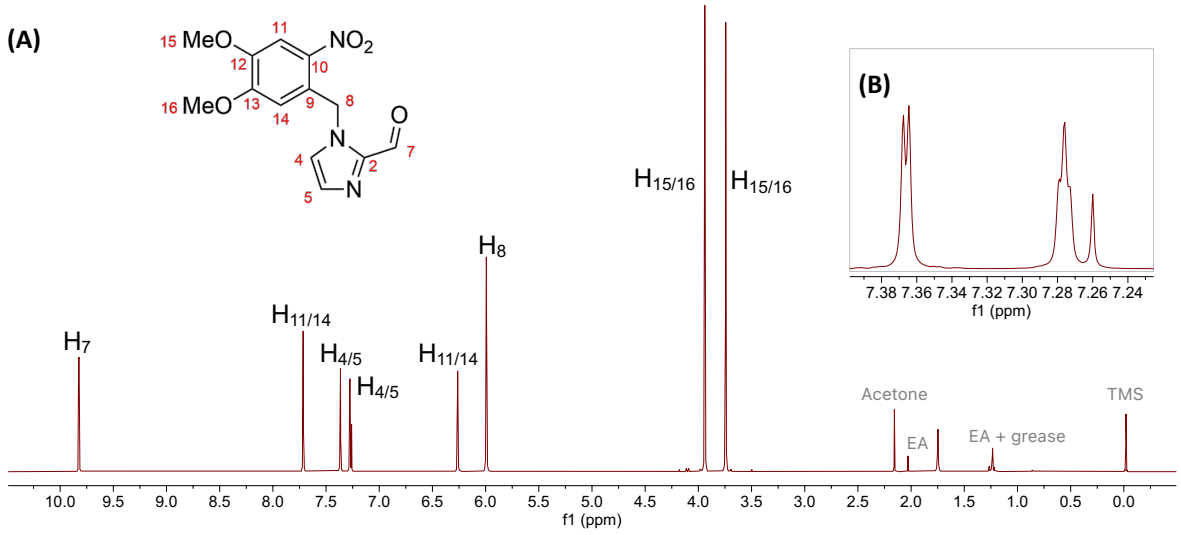

Figure 42: ^{1}H NMR (300 MHz, Chloroform-d) of (A) Ald$_{Im2}$', and (B, inset) the H_4 and H_5 proton peaks.

Following the synthesis of the methylpyridine capped ligand (L_{Im2}"$_{MePy}$)^4, the spacer (MDA) was dissolved in ethanol and added to an ethanolic solution of the capped aldehyde (Ald$_{Im2}$') to produce the DMNB-capped ligand (L_{Im2}"). After stirring at room temperature overnight the ^{1}H NMR spectrum of the reaction precipitate indicated that only the aldehyde was present. The precipitate and filtrate were recombined and heated to reflux for 2 hours with catalytic acetic acid similar to the synthesis of the 2-imidazole ligand (see section 2.4). The ^{1}H NMR of the reaction precipitate was retaken and showed that the capped ligand (L_{Im2}") had been successfully synthesised. A small proportion of the capped aldehyde (integration = 0.05) was observed in the spectrum along with additional peaks which were assigned to the half ligand (hL_{Im2}') suggesting that the ligand was hydrolysed in the deuterated chloroform. To ensure the reaction had gone to completion, following reactions were heated to reflux overnight with acetic acid under an inert atmosphere. The reaction precipitate was collected by filtration and the ^{1}H NMR spectrum recorded in less acidic deuterated dichloromethane (Figure 43).

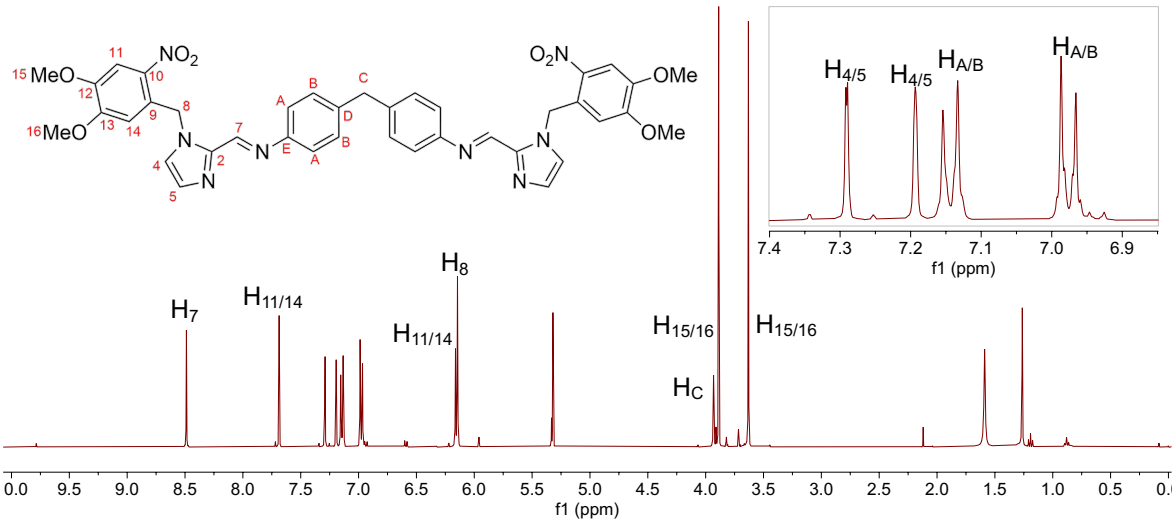

Figure 43: ^{1}H NMR (400 MHz, Methylene Chloride-d2) of L_{Im2}".

The capped ligand (L_{Im2}") was suspended in methanol and a methanolic solution of nickel chloride hexahydrate was added to form the capped cylinder ($[Ni_2(L_{Im2}")_3]Cl_4$). An excess (3-10%) of the ligand was used to account for any impurities (hL_{Im2}' or Ald_{Im2}') so the reaction solution was filtered before the cylinder was isolated by anion exchange. The mass spectrum (Figure 44) confirms the synthesis of the capped cylinder as the 4+ species and peaks for the 3+ species with various anions are observed, and no species containing the half ligand are recorded. The 5-capped cylinder species (718 m/z) is also observed which is unexpected as the capped aldehyde was purified after alkylation, however this could have formed under the ionisation conditions for mass spectrometry, or due to photocleavage when exposed to ambient light.

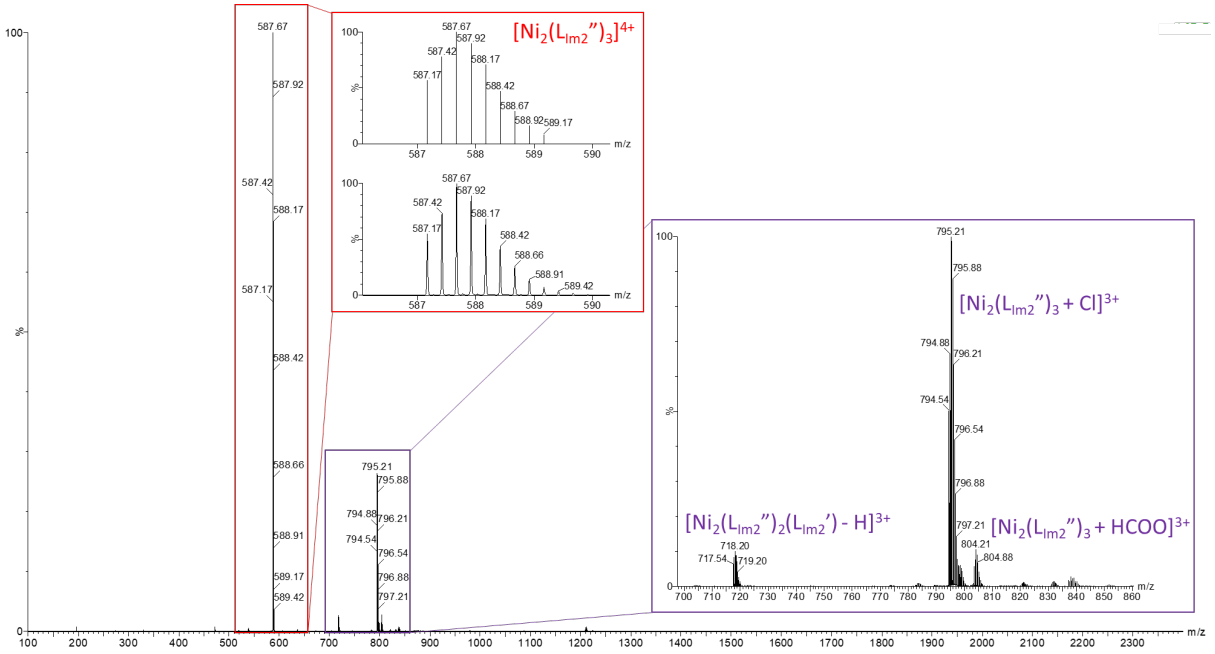

Figure 44: Mass spectrum (Waters Synapt, TOF ES+, MeOH) of $[Ni_2(L_{Im2}")_3]Cl_4$ with assignments.

The ^{1}H NMR spectrum of both the hexafluorophosphate (Figure 45) and chloride salts (Figure 46) of the capped cylinder were recorded and initial assignments have been made by comparison to the NMR of the respective uncapped cylinder. The capping group protons are far from the paramagnetic metal ions so remain in the diamagnetic region of the spectrum (0 – 10 ppm). A peak around 4 ppm is assigned to the methyl protons (H_{15} and H_{16}) due to the large integration value (12 protons). Two peaks between 6 and 8 ppm have a relative integration of 1 compared to the H_C peak (representing 6 protons each) so these peaks are assigned to the phenyl protons (H_{11} and H_{14}) of the capping groups. The peak of these two protons with lower chemical shift is broader in both spectra which could imply that it is closer to the paramagnetic centre. The bridging methyl protons (H_8) are assigned to a broad peak around 0 ppm in acetonitrile (hexafluorophosphate salt), however this appears to split into two broad peaks in methanol (chloride salt) suggesting the two protons are held in different

environments. These peaks are too broad for an accurate integration value to be calculated.

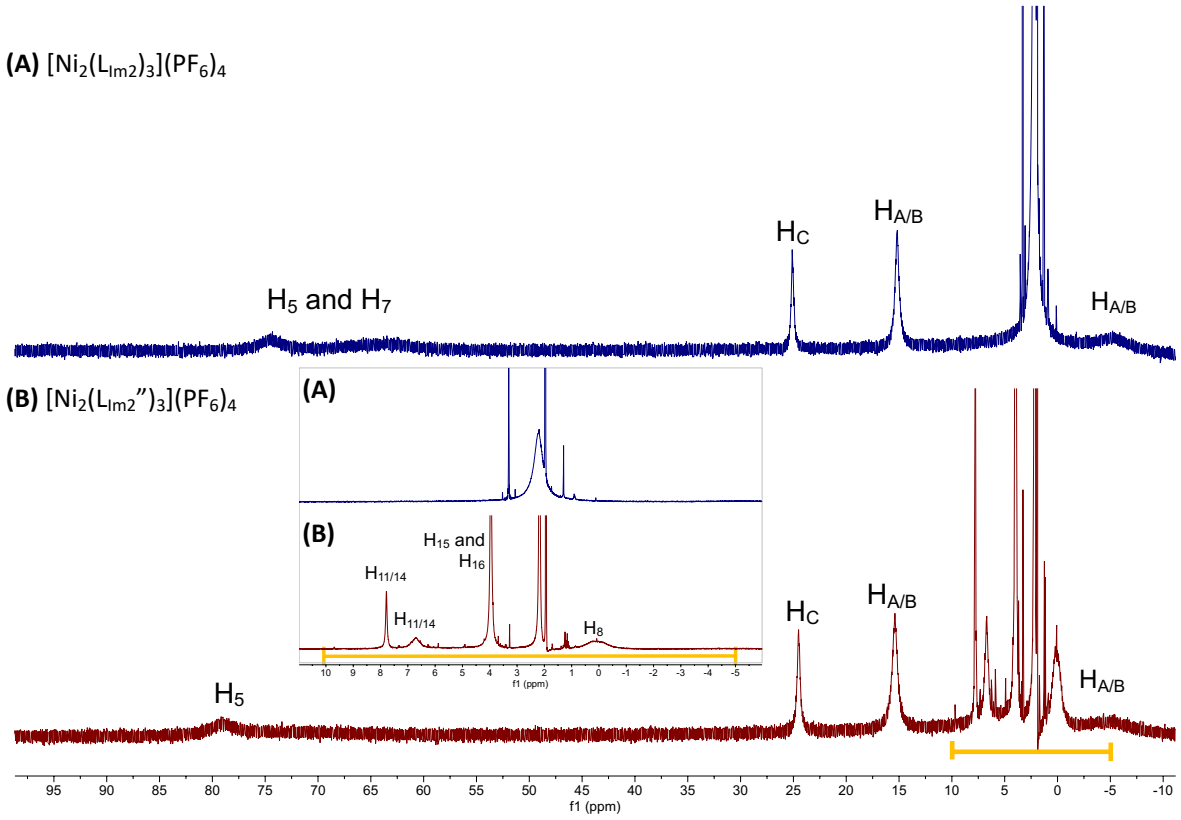

Figure 45: ^{1}H NMR (300 MHz, Acetonitrile-d3) of (A) $[Ni_2(L_{Im2})_3](PF_6)_4$, and (B) $[Ni_2(L_{Im2}")_3](PF_6)_4$.

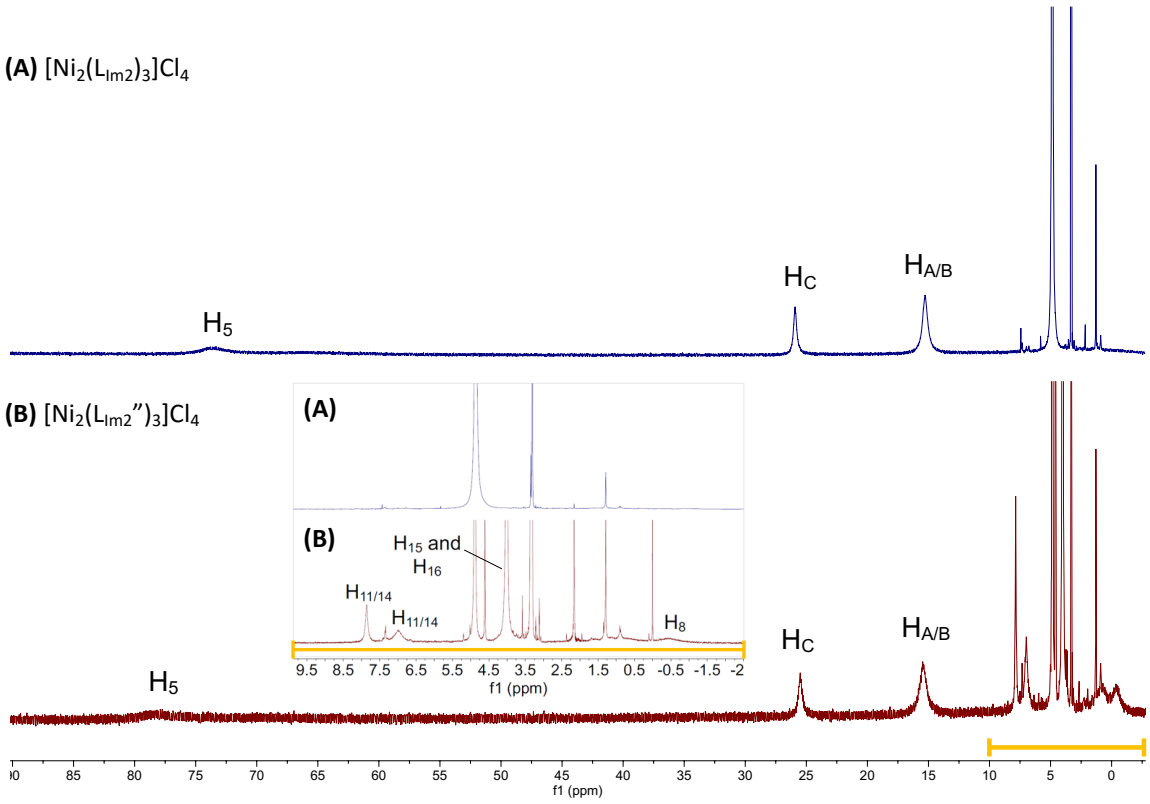

Figure 46: ^{1}H NMR (300 MHz, Methanol-d$_4$)of (A) the uncapped nickel imidazole cylinder ([Ni$_2$(L$_{Im2}$)$_3$](Cl)$_4$), and (B) the capped nickel imidazole cylinder ([Ni$_2$(L$_{Im2}$")$_3$](Cl)$_4$).

The NMR of the iron uncapped cylinders showed a reduced broadening effect compared to the nickel cylinders (Figure 31) so synthesis of the iron capped cylinder ([Fe$_2$(L$_{Im2}$")$_3$]Cl$_4$) was attempted but was unsuccessful. Previous attempts to cap the iron 2-imidazole cylinder ([Fe$_2$(L$_{Im2}$)$_3$]Cl$_4$) with methylpyridine had also been unsuccessful due to the instability of the cylinder under the basic conditions required for alkylation, so the iron capped cylinder was not isolated.

2.6.2. Rotaxane formation by slipping

Following previous attempts[13], the capped nickel imidazole cylinder ([Ni$_2$(L$_{Im2}$")$_3$]Cl$_4$) and CB10 were suspended in aqueous methanol (10%) and heated to 60^{o}C to form the thermal rotaxane ([Ni$_2$(L$_{Im2}$")$_3$.CB10]Cl$_4$). The product could not be

dissolved in high enough concentration for NMR analysis so mass spectrometry was used to show that the fully capped rotaxane had been synthesised (Figure 47). The two-metal, two-ligand species ($[Ni_2(L_{Im2}")_2.CB10]^{4+}$), the 5-capped rotaxane formed by hydrolysis ($[Ni_2(L_{Im2}")_2(hL_{Im2}').CB10]^{4+}$), and the capped cylinder (very small peak, $[Ni_2(L_{Im2}")_3]^{4+}$) were observed. This suggests that the cylinder or rotaxane may be prone to hydrolysis under the aqueous reaction conditions, but the photocleavable caps are stable.

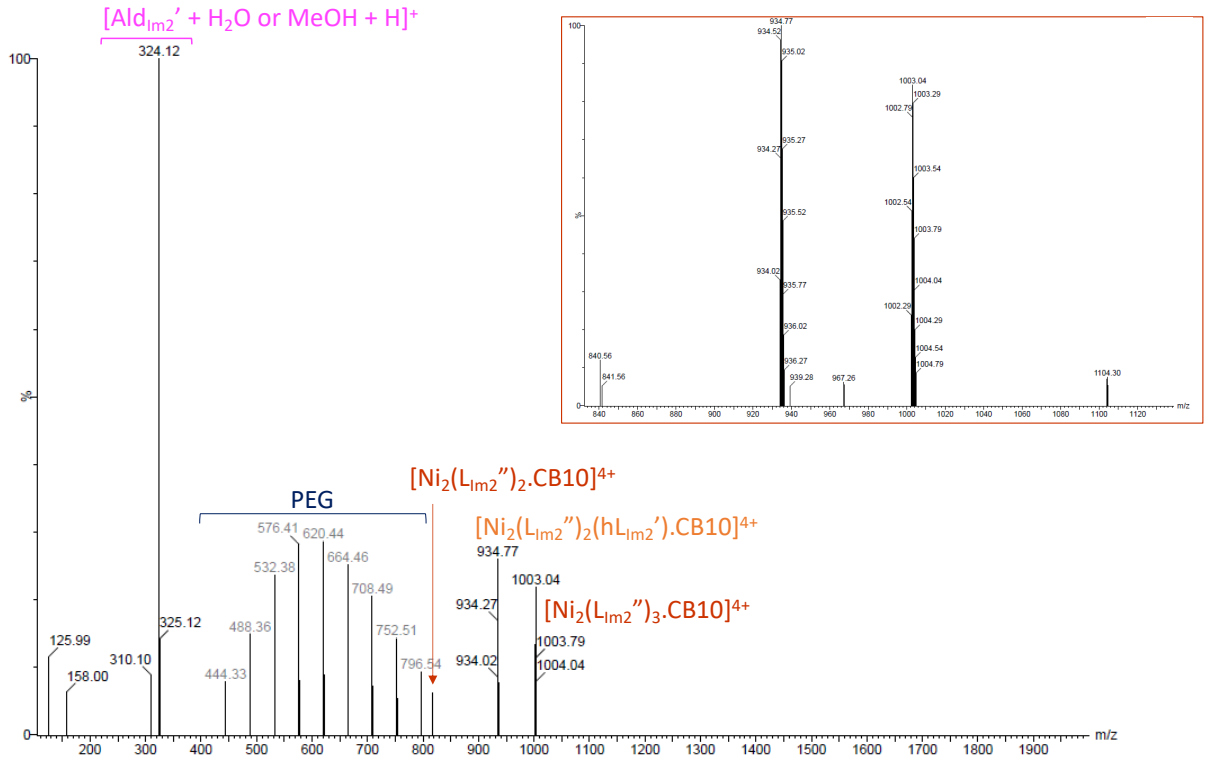

Figure 47: Mass spectrum (Waters Xevo G2-XS, TOF MS ES+, H2O) of the rotaxane after heating overnight at 60°C.

The experiment was repeated at 50°C and monitored by mass spectrometry to see if the hydrolysis of the cylinder before encapsulation could be prevented, however the hydrolysed species was observed after just 40 minutes. The slipping reaction was completed after three hours at 40°C after which the aqueous methanolic solvent was

removed. The product resuspended in water to remove the free cylinder as a precipitate and the filtrate was freeze dried to give a 65% yield of the rotaxane. The mass spectrum (Figure 48) shows the same rotaxane species are present as well as a two-metal, two-ligand species containing a half ligand ($[Ni_2(L_{Im2}")(hL_{Im2}').CB10]^{4+}$).

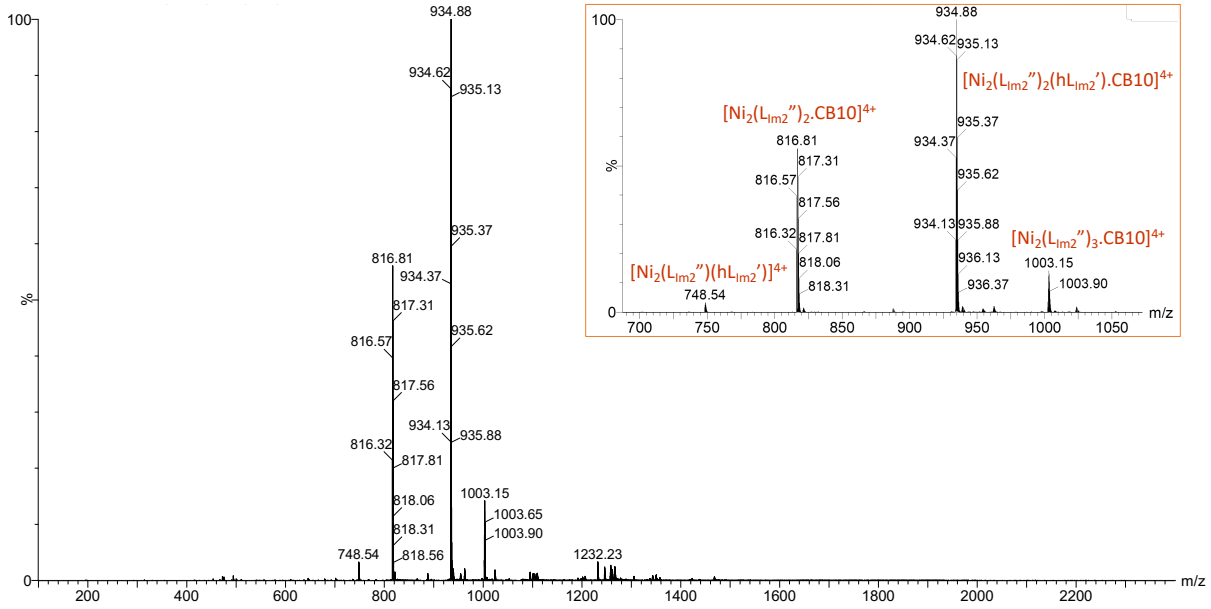

Figure 48: Mass spectrum (TOF MS ES+, H_2O) of the rotaxane product after 3 hours at 40°C.

2.7. Conclusions

Post-assembly modification of the 2-imidazole based nickel cylinder was achieved using the photocleavable alkylating group (DMNB-Br) however the capping method was found to be less efficient for the formation of the rotaxane, preventing the isolation of the fully capped species. For this reason, synthesis of the rotaxane was attempted via a slippage mechanism to give only fully capped species. Similar results were obtained for the rotaxane species and the slippage mechanism was concluded as the better synthetic route towards this new rotaxane.

2.8. List of References

1 C. A. J. Hooper, L. Cardo, J. S. Craig, L. Melidis, A. Garai, R. T. Egan, V. Sadovnikova, F. Burkert, L. Male, N. J. Hodges, D. F. Browning, R. Rosas, F. Liu, F. V. Rocha, M. A. Lima, S. Liu, D. Bardelang and M. J. Hannon, *J. Am. Chem. Soc.*, 2020, **142**, 20651–20660.

2 F. Tuna, M. R. Lees, G. J. Clarkson and M. J. Hannon, *Chem. Eur. J.*, 2004, **10**, 5737–5750.

3 M. Pascu, PhD Thesis, University of Birmingham, 2007.

4 V. Sadovnikova, PhD Thesis, University of Birmingham, 2011.

5 P. Klán, T. Šolomek, C. G. Bochet, A. Blanc, R. Givens, M. Rubina, V. Popik, A. Kostikov and J. Wirz, *Chem. Rev.*, 2013, **113**, 119–191.

6 J. Clayden, N. Greeves and S. G. Warren, in *Organic Chemistry*, Oxford University Press, Oxford, 2nd edn., 2012, ch. 11, pp. 222–239.

7 M. J. Hannon, C. L. Painting, A. Jackson, J. Hamblin and W. Errington, *Chem. Commun.*, 1997, 1807–1808.

8 M. J. Hannon, I. Meistermann, C. J. Isaac, C. Blomme, J. R. Aldrich-Wright and A. Rodger, *Chem. Commun.*, 2001, 1078–1079.

9 M. Loos, C. Gerber, F. Corona, J. Hollender and H. Singer, *Anal. Chem.*, 2015, **87**, 5738–5744.

10 A. Day, A. P. Arnold, R. J. Blanch and B. Snushall, *J. Org. Chem.*, 2001, **66**, 8094–8100.

11 S. Liu, P. Y. Zavalij and L. Isaacs, *J. Am. Chem. Soc.*, 2005, **127**, 16798–16799.

12 R. T. Egan, PhD Thesis, University of Birmingham, 2023.

13 J. S. Craig, PhD Thesis, University of Birmingham, 2023.

3. PHOTOCLEAVAGE OF THE IMIDAZOLE-BASED CYLINDERS

3.1. Light-Triggered Activity

Pro-drugs sensitive to external stimuli, such as temperature, ultra-sound sonication, and light, have been used to control the delivery of active compounds[1–3]. The area and time over which light is administered is easily altered, and multiple different photo-protecting groups have been identified with ortho-nitrobenzyl (*o*-nitrobenzyl, or *o*NB) being one of the most common[4–6]. *o*NB groups can be excited (n – π*) by light of the appropriate wavelength to form a 1,4-diradical[7]. Following a Norrish type II reaction pathway, a γ-hydrogen can be abstracted by the nitro group, to form the Z-nitronic acid[8,9]. The Z-nitronic acid isomerises via an aci-nitro anion to for the E-nitronic acid, and decay of the aci-nitro structure, the rate limiting step, can then continue by ring closure (Figure 49)[9].

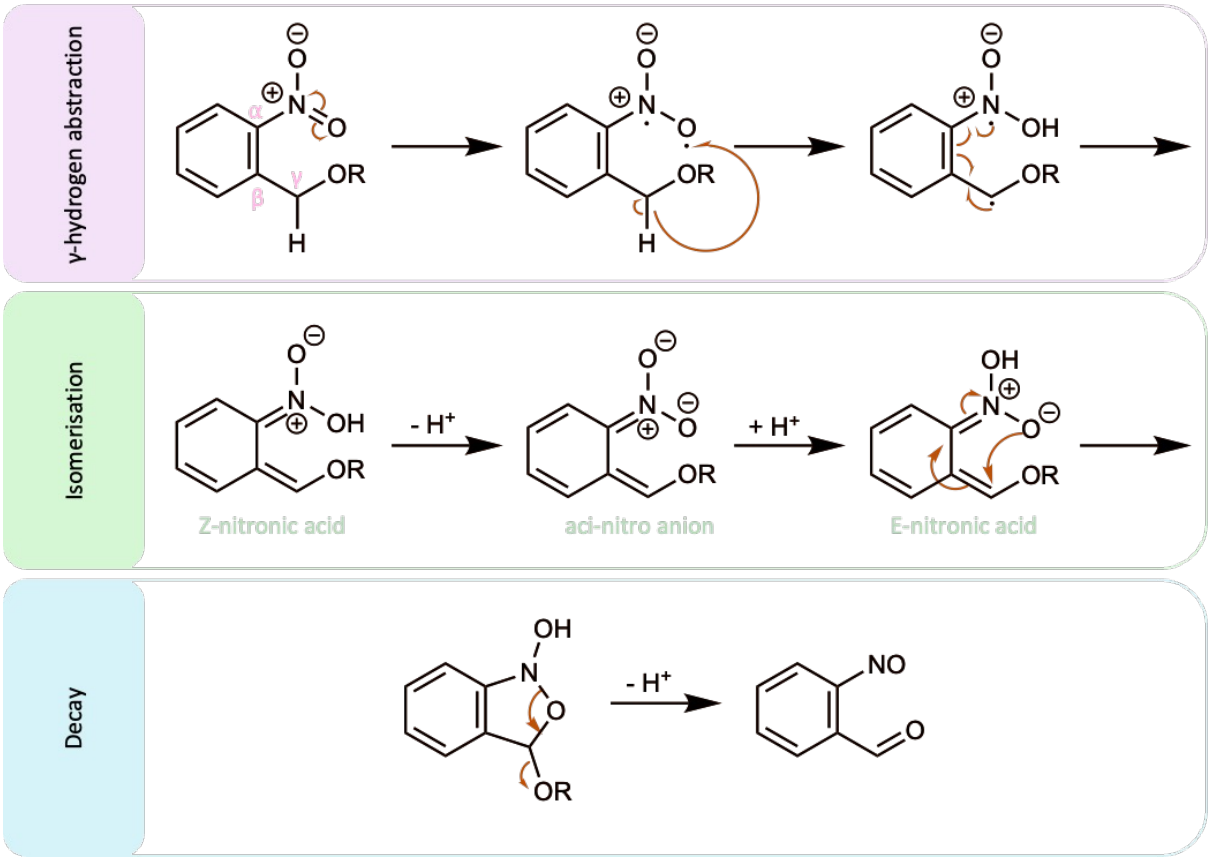

Figure 49: Reaction mechanism for photocleavage of o-nitrobenzyl derivatives.

Substitutions to the α-carbon of *o*-NB groups increase the leaving group efficiency whereas substitutions to the aromatic ring may change the photocleavage properties, such as the irradiation wavelength[4]. DMNB falls into the latter category, with two methoxy groups opposite the nitro and methylene substituents on the benzene ring which increases the absorption and photocleavage efficiency at longer wavelengths (420 nm)[4,10]. The efficiency of photocleavage at shorter wavelengths (254 nm) is reduced compared to the unsubstituted *o*-NB group which may be due to the formation of a triplet state[11].

3.2. Photocleavage Studies

To control 3WJ binding, a supramolecular rotaxane was designed in which the macrocycle (CB10) would sterically block the central 3WJ recognition motif of a cylinder (as demonstrated previously[12]) until the capping groups locking the macrocycle in place are removed in response to irradiation. Following the successful synthesis of the 2-imidazole based rotaxane ($[Ni_2(L_{Im2}")_3.CB10]Cl_4$), removal of the photocleavable DMNB caps was investigated.

Up to six photocleavage reactions can occur per rotaxane to form the uncapped *pseudo*rotaxane so aside from the expected photocleavage product, 4,5-dimethoxy-2-nitrobenzaldehyde, the reaction will also produce partially capped intermediates (Figure 50). Removal of all six capping groups is not necessary for the release of the cylinder as the combined steric bulk of the three capping groups at each end is reduced with each cap that is removed. The minimum number of capping groups required to mechanically lock the macrocycle in place is unknown, so removal of one or two capping groups from one end of the rotaxane may allow release of the cylinder from the rotaxane.

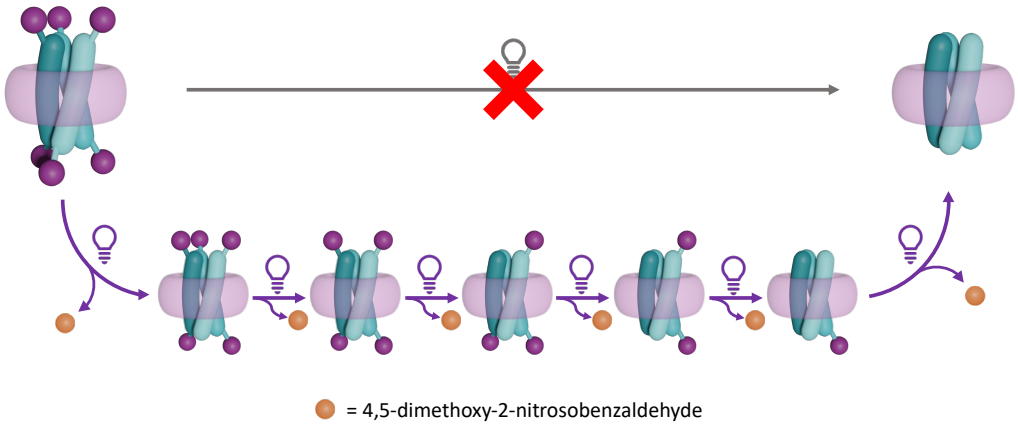

Figure 50: Photocleavage of the capped cylinder or rotaxane via the partially capped species.

3.2.1. UV-visible Absorbance

DMNB-Br was used as a positive control to assess the suitability of the light source for photocleavage as it is a readily available reagent and the photocleavage followed by UV-visible spectroscopy had already been reported in both methanol and acetonitrile[13,14]. As methanol is also compatible with the supramolecular helicates, DMNB-Br was dissolved in methanol (10 μM) and irradiated in a quartz cuvette to ensure that no light was absorbed by the vessel. A UV lamp (4W, 4.5 x 3.5 cm, 365 nm) was used to irradiate for 1-minute intervals up to 5 minutes. Photocleavage was monitored by UV-visible absorption spectroscopy and gave a very similar spectrum to the previously reported results with the characteristic DMNB-Br peaks decreasing in intensity while the absorbance of the photocleavage product increases (Figure 51).

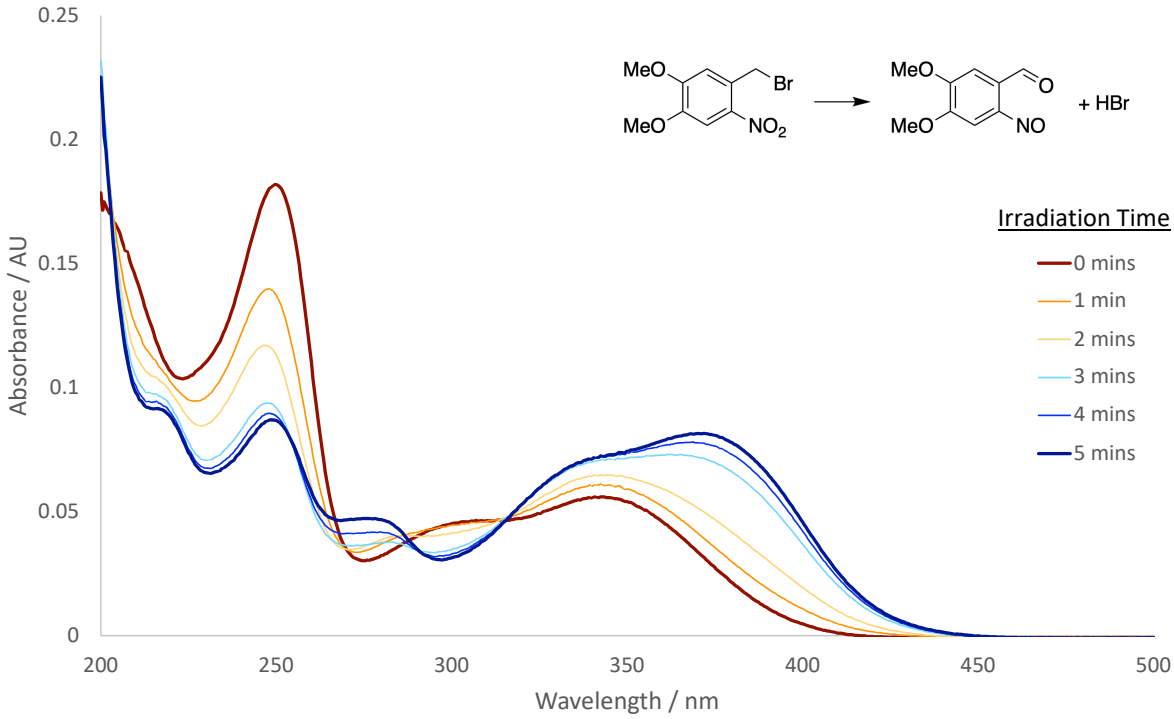

Figure 51: UV-visible absorbance of DMNB-Br (10 μM, methanol) with increasing irradiation time.

Photocleavage experiments must be carefully designed to minimise the impact of external factors and be reproduceable. The area subjected to irradiation and pathlength of the sample, as well as the distance of the sample from the light source are factors which should be controlled. The wavelength and intensity of the irradiating light as well as environmental factors such as ambient light and heat, a by-product of light for most sources, can also influence the results of the irradiation experiment.

An alternative irradiation set up was used (Figure 52) in which a quartz cuvette was placed approximately 0.5 cm away from LED strip lights (4.8 Wm^{-1}, 365-370 nm) fixed to the interior of a glass dish. The samples were irradiated in a quartz cuvette of set path length (1 cm) and area (3 cm^3 for 3 mL) and cooled by a fan. The entire set up was covered to prevent the effects of ambient light.

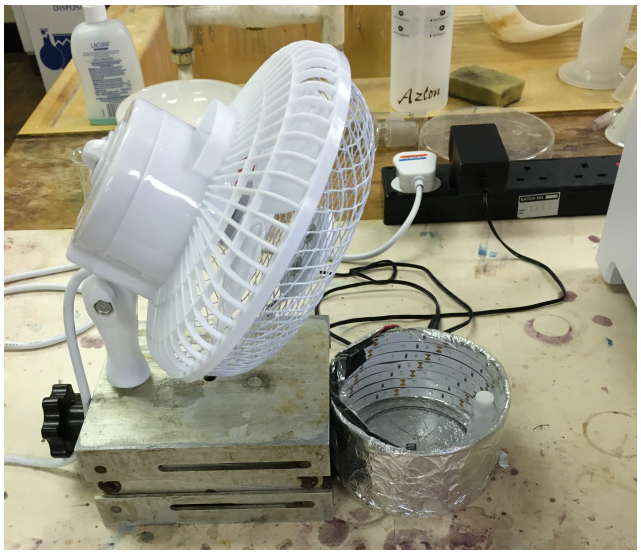

Figure 52: Alternative irradiation set up.

The DMNB-Br photocleavage experiment was repeated with the new irradiation set up and shows a faster change in absorbance compared to the previous light source, with no further increase to the product peaks after 3 minutes (Figure 53). This could

indicate that the power of the irradiation source in the new set up is greater than the previous source, increasing the effective irradiation felt by the sample. The estimated total power of the LED lights is 11 W.

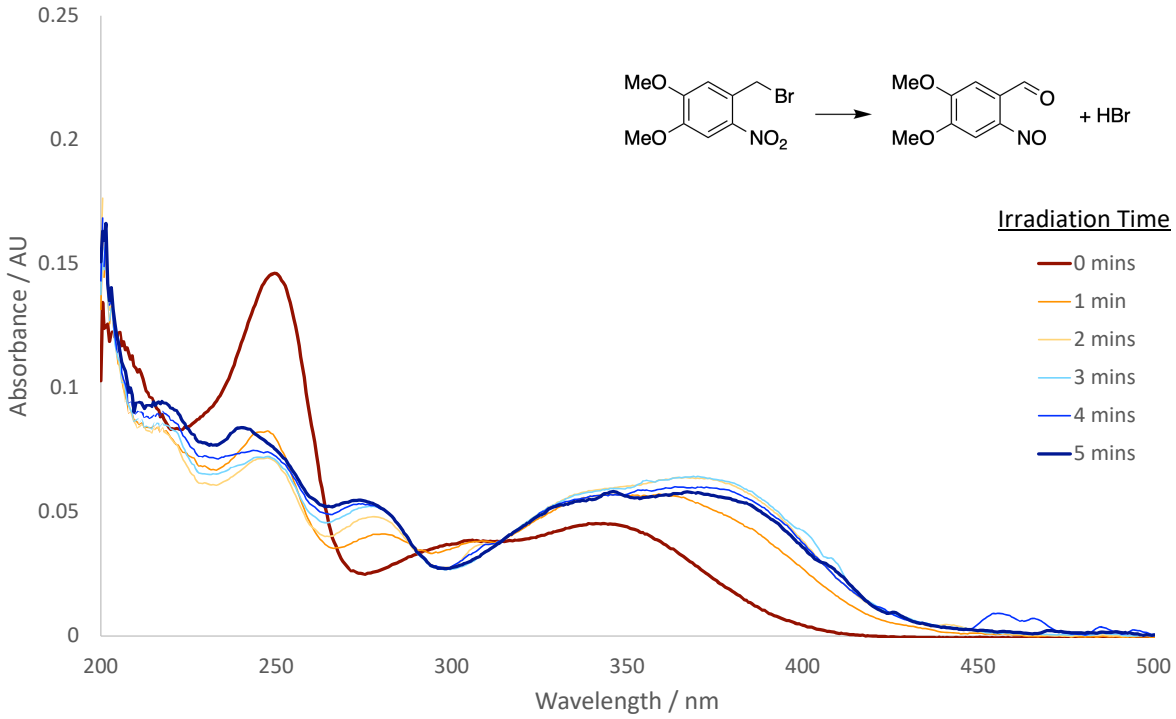

Figure 53: UV-visible absorbance of DMNB-Br (10 μM, methanol) with increasing irradiation time using the new irradiation set up.

The nickel imidazole-based complexes were irradiated for up to 60 minutes and the photocleavage monitored by UV-visible spectroscopy at different time points. The uncapped cylinder ($[Ni_2(L_{Im2})_3]Cl_4$,Figure 54A) shows a 9% decrease in absorbance at 325.5 nm over 60 minutes. The decrease in absorbance between each time point is smaller between the increasing time suggesting an initial change in solution which finishes within 30 minutes of irradiating.

The absorbance of the capped cylinder ($[Ni_2(L_{Im2}")_3]Cl_4$, Figure 54B) decreases by 11% at both absorption maxima (244 and 324 nm). The decrease is more regular

with irradiation time, which could suggest a different process is occurring compared to the uncapped cylinder.

Rotaxane formation is driven by the hydrophobic bonding between the cylinder and macrocycle, and this can be disrupted in the presence of organic solvents such as methanol. The rotaxane ($[Ni_2(L_{Im2})_3.CB10]Cl_4$, Figure 54C) was therefore irradiated in water to minimise any dethreading, and shows larger changes in the absorbance intensity compared to the cylinders. The absorbance intensity at 328.5 nm reduced by 39% whereas the intensity at 242 nm is only reduced by 6%. There is an additional peak adjacent to the peak at 328 nm which does not decrease in intensity as quickly. This peak emerges as a new absorbance maximum at 299.5 nm after 20 minutes of irradiation and the maximum absorbance shifts to 291.5 nm after 60 minutes of irradiation.

There is a larger change in the absorbance of the capped cylinder and rotaxane than for the uncapped cylinder, as would be expected from a successful photocleavage reaction.

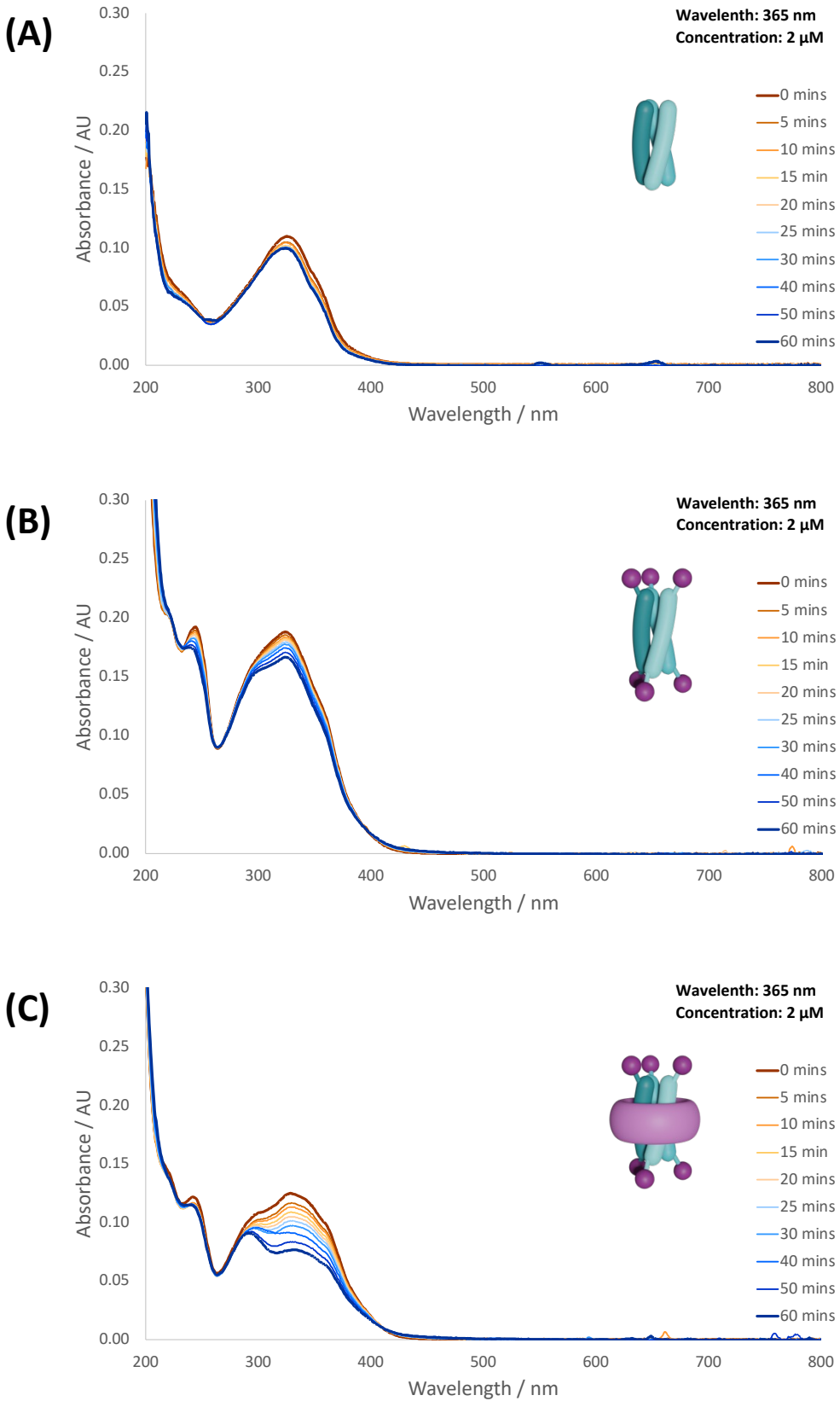

Figure 54: UV-visible absorbance of (A) $[Ni_2(L_{Im2})_3]Cl_4$ in methanol, (B) $[Ni_2(L_{Im2}")_3]Cl_4$ in methanol, and (C) $[Ni_2(L_{Im2}").CB10_3]Cl_4$ in water, over 60 minutes of irradiation (365 nm).

3.2.2. Mass Spectrometry

UV-visible absorbance is a quantitative method measuring the overall change in solution but does not indicate which species are involved in this change. Two key methods which provide structural data are mass spectrometry and NMR. NMR is a powerful quantitative method however it may not be possible to deconvolute the spectrum of a sample containing multiple supramolecular complexes with differing numbers and arrangements of capping groups. This, combined with the paramagnetism of the nickel cylinders, makes NMR an unsuitable method to monitor photocleavage of the supramolecular system.

High resolution mass spectrometry has already been used in this work to unambiguously assign the differently capped supramolecular species in solution. For this technique to be useful, the conditions used to introduce the sample to the mass analyser must avoid fragmentation of the complex. Electrospray ionisation mass spectrometry (ES MS) was originally developed for the investigation of large biological molecules which were too unstable to be ionised by prior methodologies[15]. ES MS is a “soft” ionisation technique as it avoids the use of harsh conditions, such as high temperature or electron bombardment, allowing the measurement of the charged ions present in solution[16].

Electrospray is the mechanism used to disperse the sample solution into fine droplets which are around 200 nm in size for a nanoelectrospray source such as the one used in this work[17]. Singular ions are then thought to be isolated from these droplets by different methods depending on their size[18,19]. Smaller ions (<1000 amu) are ejected from droplets as the droplet radius is decreased by evaporation and the surface charge density cannot be maintained (ion evaporation). For larger ions (>1000

amu) there is only one charged particle per droplet from which the solvent evaporated (charge residue model)[18,19]. Volatile solvents are used to aid evaporation in both cases.

To understand the changes in the absorbance spectra, a small sample of the irradiated solution was taken at each time point for mass spectrometry. Unlike other techniques, the “intensity” of the peak in the mass spectrum corresponds to the number of ions recorded by the mass analyser (relative abundance), which is not an accurate indicator of the concentration of each species in solution. The supramolecular species investigated here can also exist as different charged ions which may be favoured differently when recording the mass spectrum. Changes in the species which appear in the mass spectrum over time are therefore of interest, rather than changes in the peak intensity of each specific species.

The mass spectra of the uncapped imidazole cylinder ($[Ni_2(L_{Im2})_3]^{4+}$, Figure 55) show no significant change over 60 minutes of irradiation and most peaks are due to singly charged organic species. The low concentration of the cylinder (2 μM) required to monitor the absorbance may have caused the low abundance of the cylinder species in the mass spectrum. The three-ligand complex was no longer visible after 5 minutes of irradiation and was followed by the disappearance of the two-ligand complex after 15 minutes.

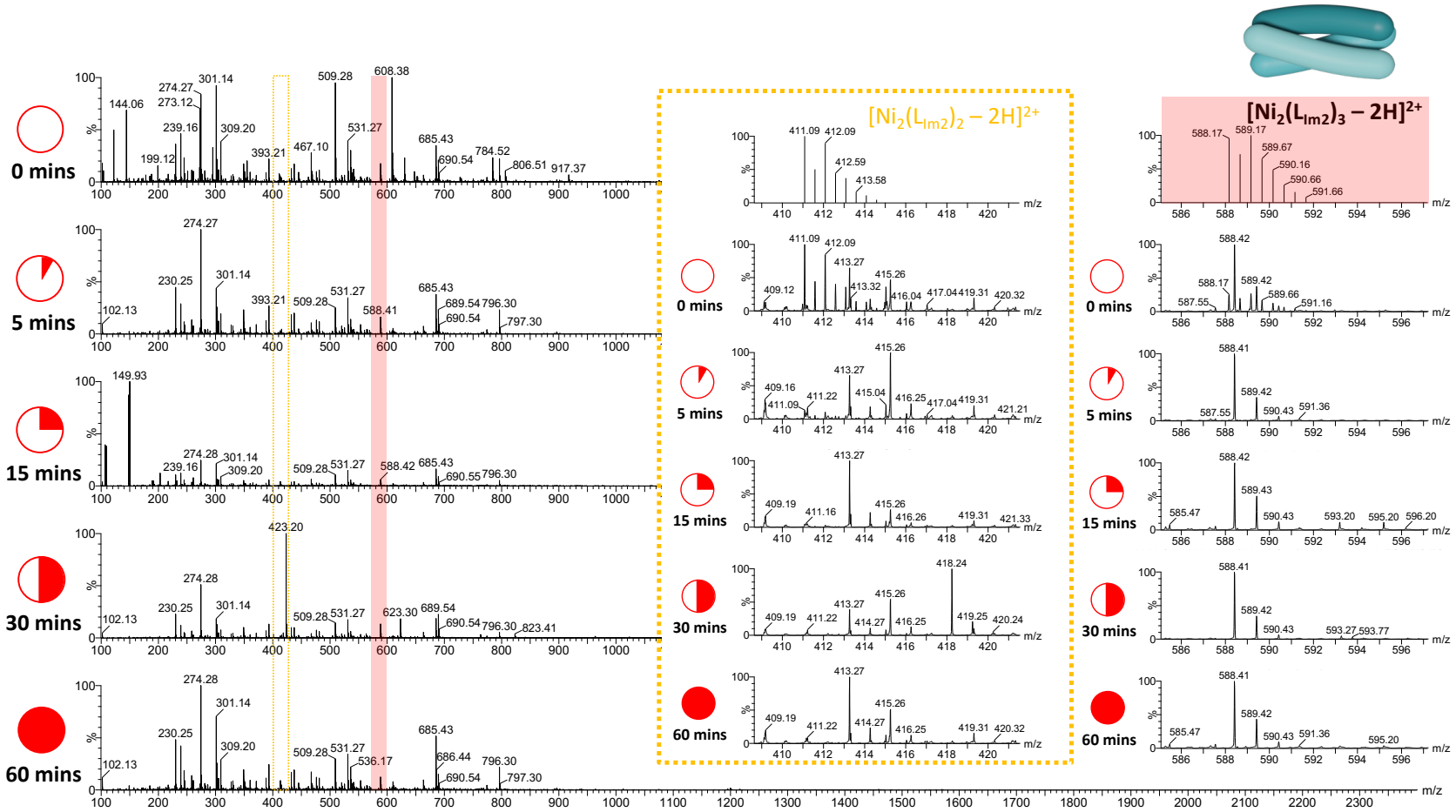

Figure 55: Mass spectrum (TOF ES+, MeOH) following $[Ni_2(L_{Im2})_3]Cl_4$ over 60 minutes of irradiation. Inset spectra: progression of the 411 (yellow dotted outline on large spectra) and 588 (shaded pink on large spectra) m/z peaks over 60 minutes of irradiation with the isotope pattern for the assigned species (top).

The mass spectra of the capped cylinder ($[Ni_2(L_{Im2}")_3]Cl_4$, Figure 56) show the appearance of the 5- and 4-capped cylinder over 60 minutes of irradiation. Both the 5- and 6-capped species is observed in the spectrum before irradiation, the latter of which is predominant across the spectra (588 m/z). The abundance of 4- and 5-capped species (653 and 539 m/z, respectively) appear to increase with increasing irradiation time (Figure 57).The 4-capped species is not present before irradiating which suggests it is formed during the irradiation process as expected from the successful photocleavage reaction.

The mass spectra of the rotaxane ($[Ni_2(L_{Im2}")_3$.CB10$]Cl_4$, Figure 58 and Figure 59) indicates that all nickel containing species, including the 5- and 6-capped rotaxanes and the two-metal, two-ligand encapsulated species, decrease in abundance with increasing irradiation time. A decrease in these species is expected for the photocleavage reaction, however peaks corresponding to the lesser capped photocleavage products are not observed.

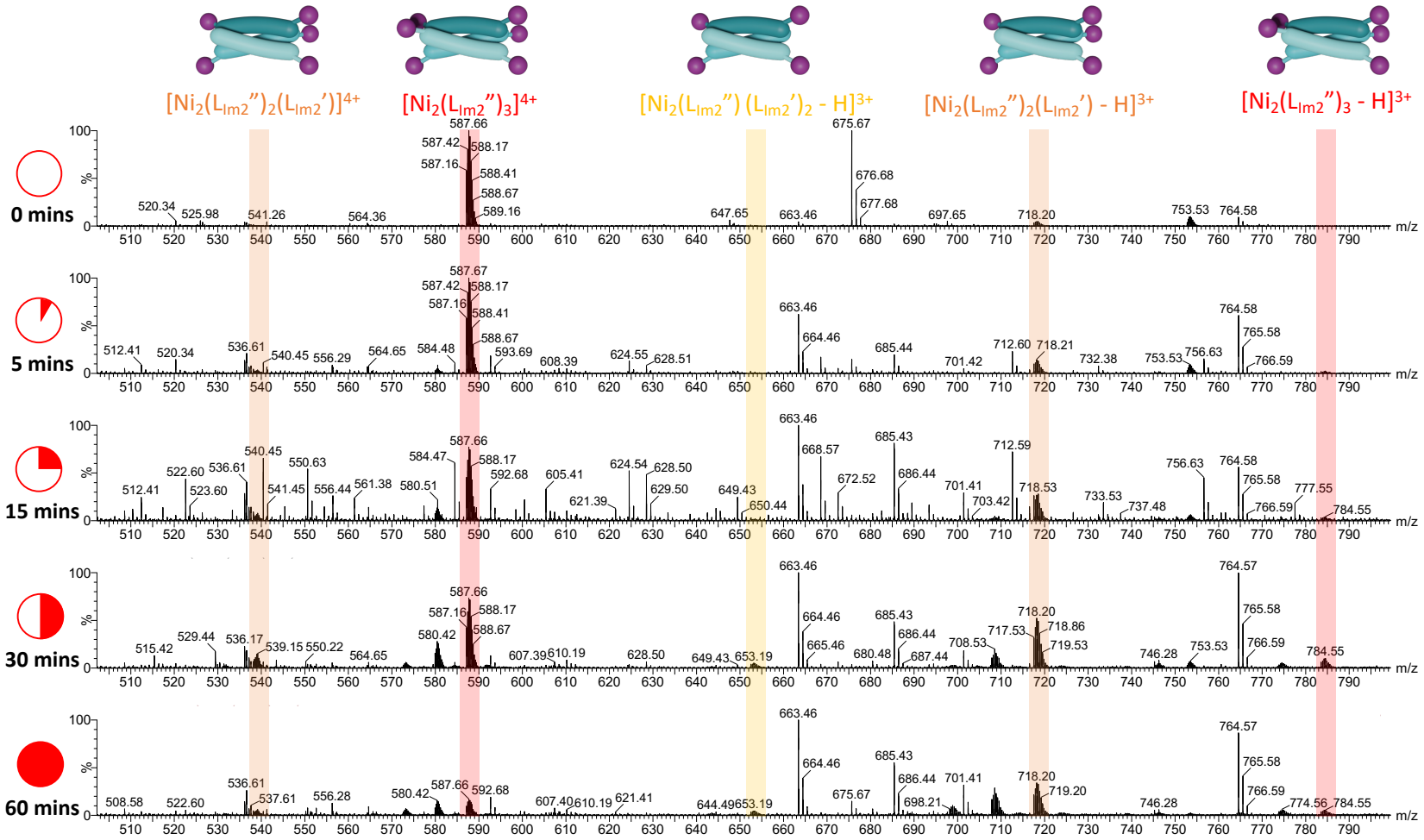

Figure 56: Mass spectra (TOF ES+, MeOH) following $[Ni_2(L_{Im2}")_3]Cl_4$ over 60 minutes of irradiation.

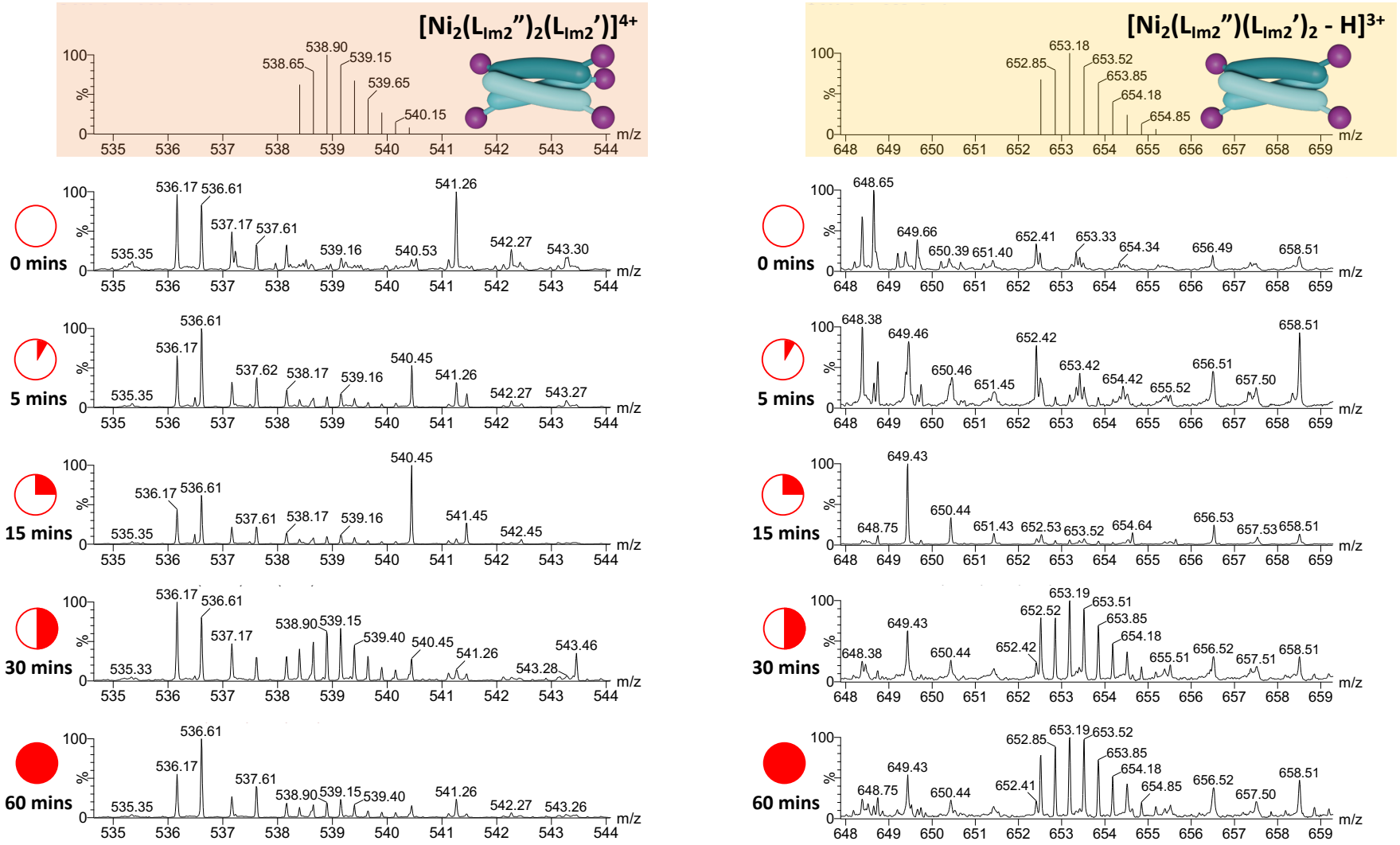

Figure 57: Following the progression of the 539 m/z (left) and 653 m/z (right) peaks in the mass spectra (TOF ES+, MeOH) of $[Ni_2(L_{Im2}")_3]Cl_4$ (shown in Figure 56) over 60 minutes of irradiation with the isotope pattern for the assigned species (top).

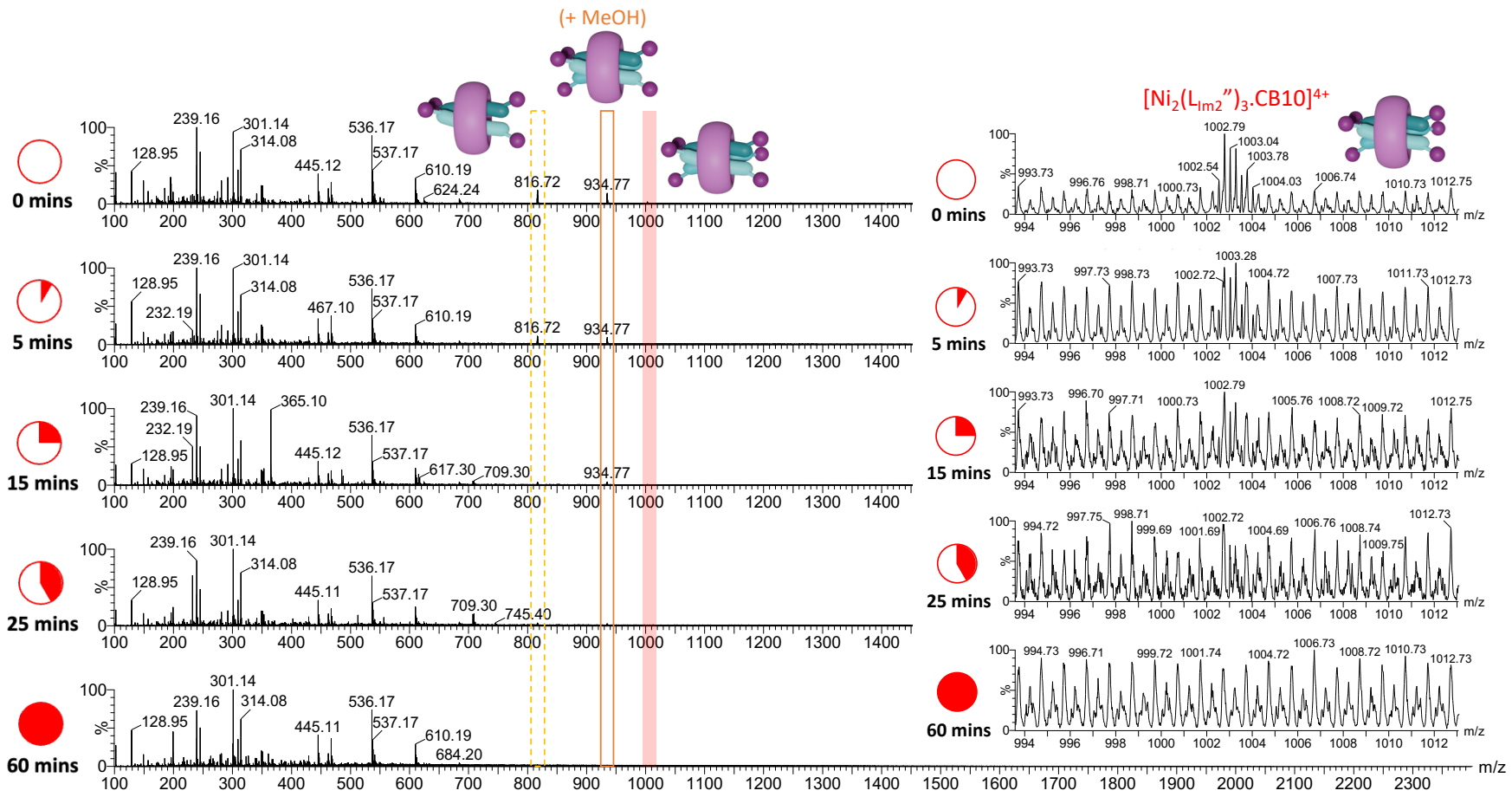

Figure 58: Mass spectra (TOF ES+, H_2O) following $[Ni_2(L_{lm2}")_3.CB10]Cl_4$ over 60 minutes of irradiation. Inset spectra: the progression of the 1003 m/z peak (highlighted in pink in the large spectrum) over 60 minutes of irradiation.

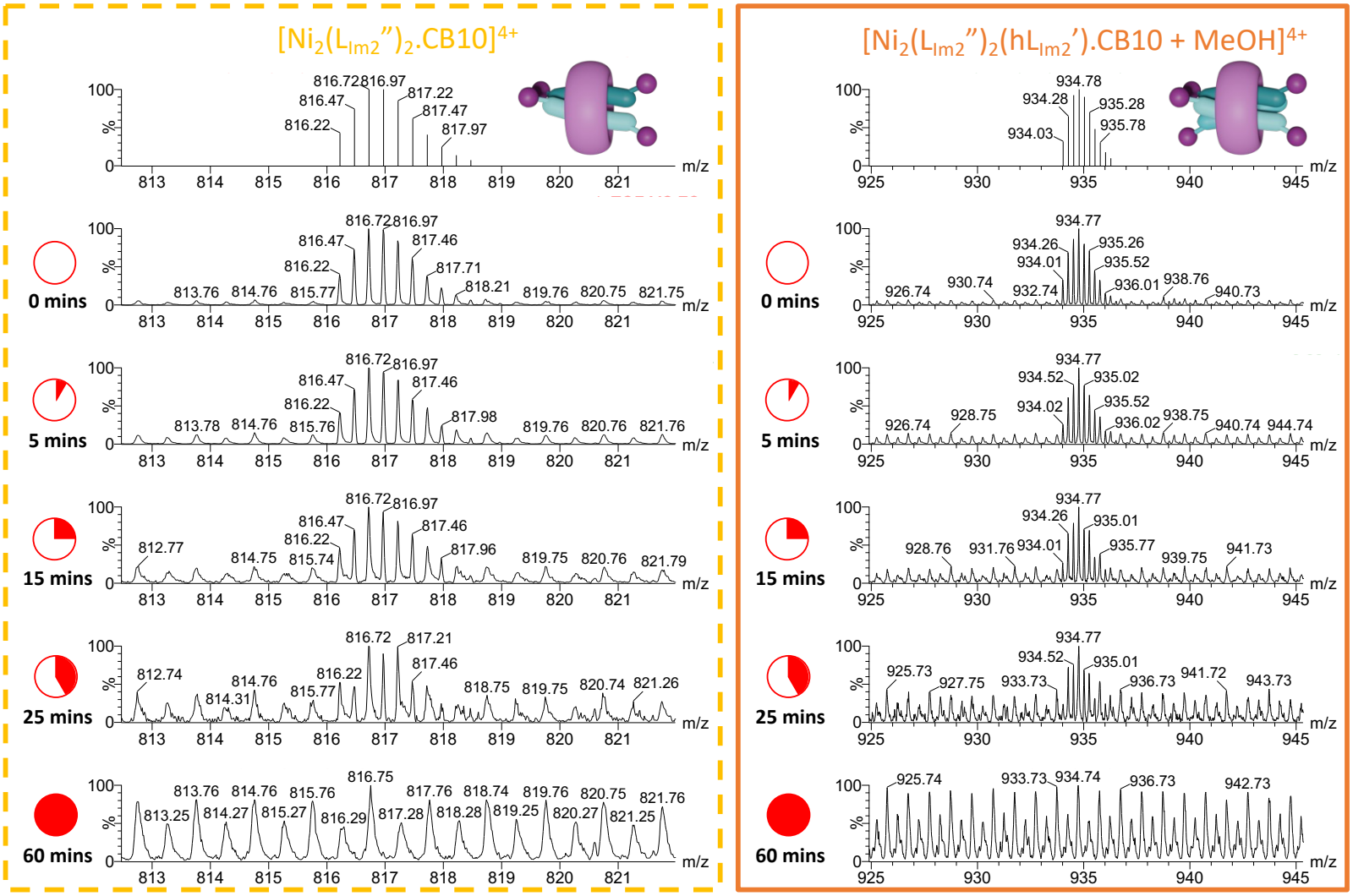

Figure 59: Following the progression of the 935 m/z (left) and 817 m/z (right) peaks in the mass spectra (TOF ES+, MeOH) of $[Ni_2(L_{Im2}")_3.CB10]Cl_4$ (as seen in Figure 59) over 60 minutes of irradiation with the isotope pattern for the assigned species (top).

Mass spectrometry was used to elucidate the structures present in solution before irradiation however the spectra after 60 minutes of irradiation contained mostly mono-cationic organic species. The decreasing presence of the capped metal complexes matches the results of the absorbance spectra but do not prove the successful photocleavage of the supramolecular species as photocleavage product peaks are not observed. The low initial sample concentration used may have prevented the lesser capped species from being observed as photocleavage would divide the metal complexes into seven differently capped species (0-6 caps) so the concentration of each individual species may be too low to be recorded. A peak for the photocleavage side product (4,5-dimethoxy-2-nitrosobenzaldehyde, $C_9H_9NO_4$, M_r = 195.17) is also not observed which would be expected from the successful photocleavage reaction.

3.3. Junction Binding

Gel electrophoresis is used for the separation of nucleic acid and peptide sequences based on their size and charge. Samples are loaded into wells and an electric field is applied to move the samples through the porous gel (Figure 60). The phosphate backbone of nucleic acids imparts an overall negative charge, so the nucleic acids move towards a positively charged electrode. The speed of migration is dependent on a characteristic property termed electrophoretic mobility[20], and molecules with a lower charge or larger hydrodynamic radius, due to increased mass or overall shape, move slower through the pores of the gel. This separates samples into bands which can be visualised by various staining techniques.

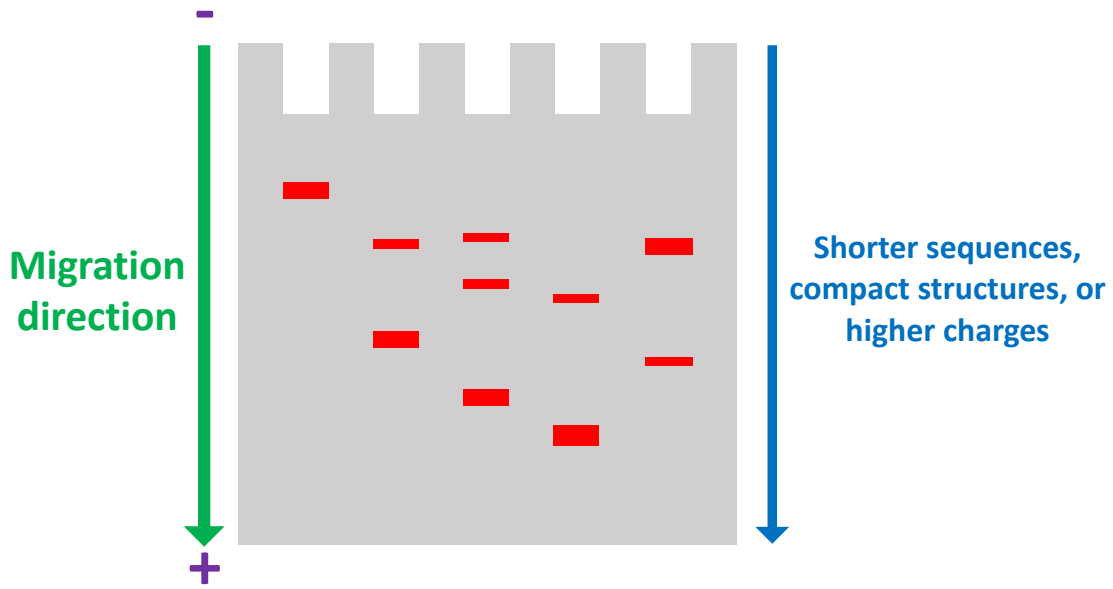

Figure 60: Direction of migration of nucleic acids across a gel (grey) to form bands (red) of different sequence lengths, shapes, or charges.

Polyacrylamide and agarose are the two most common polymers used for gel electrophoresis. Polyacrylamide forms a gel with smaller pores than agarose so provides better resolution for the separation of shorter nucleic acid sequences (5-3,000 bases) than agarose, which is used for longer sequences (50-50,000 bases)[21]. A polyacrylamide gel is formed by the polymerisation of acrylamide monomers using tetramethylethylenediamine (TEMED) and ammonium persulphate to initiate a radical reaction[22,23]. The acrylamide strands are crosslinked by bisacrylamide additives, forming the porous gel. Pore sizes are optimised to give the best separation between species by adjusting the amount of acrylamide used per volume (%T, see reference for recommended amounts[23])[24].

An electric field is applied across the gel to move the charged particles and is conducted by ions in the buffer solution[20,25]. The ion concentration must be high enough to allow migration without causing a high current and excess heating. The pH

of the buffer must also be appropriate for the experiment as some nucleic acid structures are dependent on pH, such as the i-motif[26]. Urea is added to denaturing buffers to prevent the formation of secondary structures when separation by size alone is required, such as when sequencing[23].

External factors such as voltage and temperature also alter the speed of migration through a gel. While voltage is evenly applied, dissipation of heat occurs fastest at the edges of the gel, causing a higher temperature in the middle where samples can migrate faster ("smiling effect")[20]. External cooling may be applied to avoid this however this must also be applied evenly as a "venetian blind" effect is observed when one surface of a gel is cooler than the other[20].

Polyacrylamide gel electrophoresis (PAGE) has been used as the primary method to investigate the recognition of 3WJs by supramolecular cylinders. This was initially achieved using three complimentary 14-mer DNA sequences (Figure 61) which can form 3WJs at low temperatures (5^{o}C) but is unstable at room temperature[27,28]. A band for the 3WJ is still observed at room temperature in the presence of the cylinder, indicating that the junction is formed and stabilised by the helicate[28].

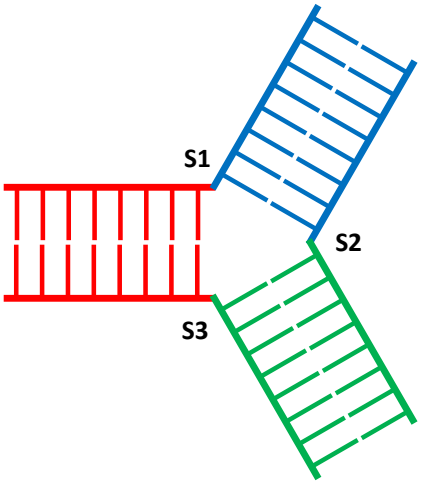

	5’												3’
S1:	C	G	G	A	A	C	G	G	C	A	C	T	C	G
S2:	C	G	A	G	T	G	C	A	G	C	G	T	G	G
S3:	C	C	A	C	G	C	T	C	G	T	T	C	C	G

Figure 61: 14-mer sequences used for recognition of 3WJs[28].

PAGE was used to investigate the formation of 3WJs by the imidazole-based cylinders ($[Ni_2(L_{Im2})_3]Cl_4$ and $[Ni_2(L_{Im2}")_3]Cl_4$) and rotaxane ($[Ni_2(L_{Im2}")_3.CB10]Cl_4$) by increasing the equivalents of cylinder per junction from 0.5 to 4 at constant DNA concentration (1 μM). A DNA stock solution containing the three strands (S1, S2, and S3, Figure 62, wells 2 and 3) shows no formation of the slower migrating 3WJ band while the nickel parent cylinder ($[Ni_2L_3]Cl_4$, Figure 62, wells 4-7) shows increasing fluorescence intensity for the 3WJ band with increasing concentration. A faint band is observed across multiple samples which was later found to be an impurity in the DNA stock solution.

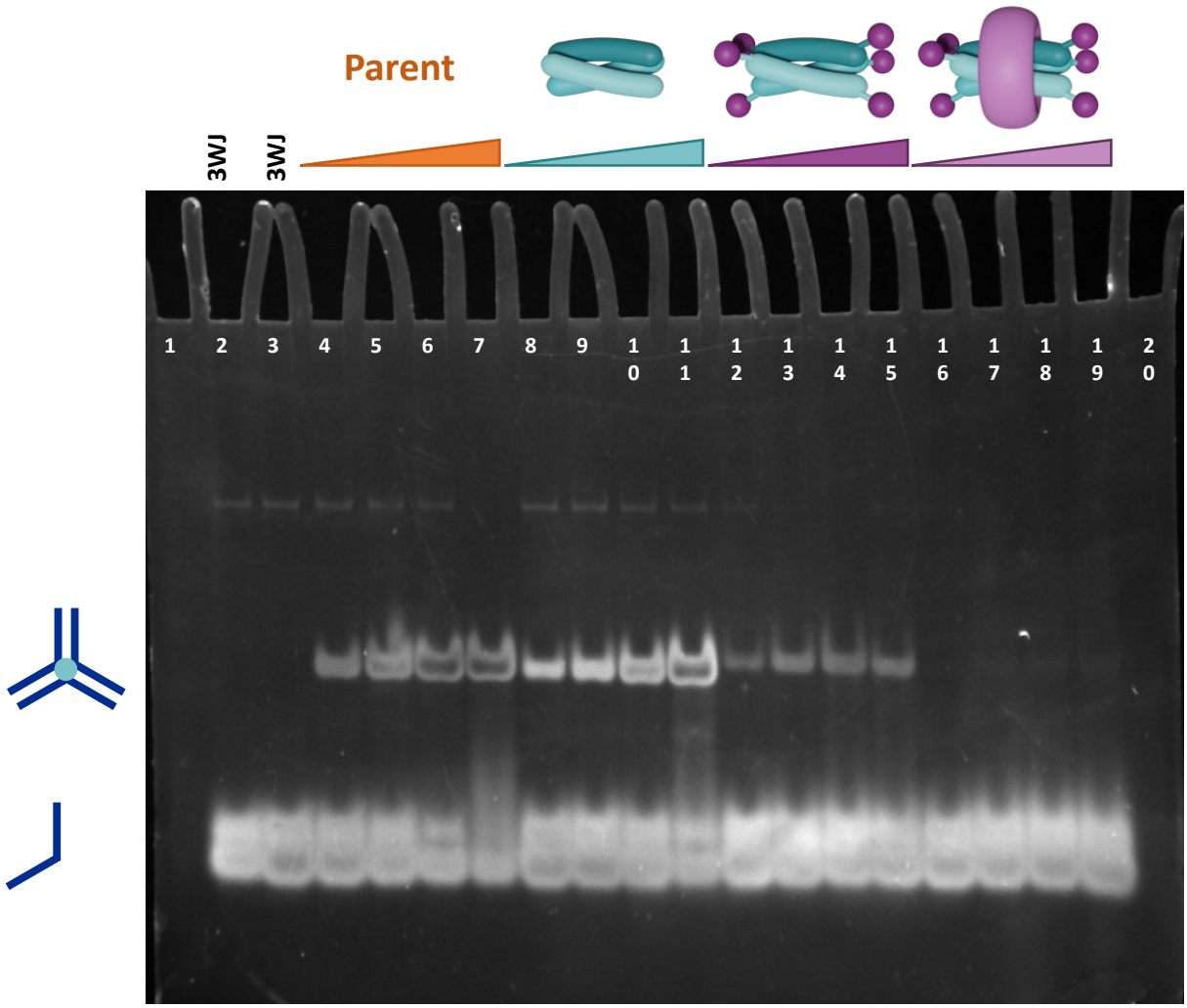

Figure 62: PAGE of 3WJ formation in the presence of increasing concentration of complexes (0.5, 1, 2, and 4 μM). Wells: (1,20) running dye; (2,3) 3WJ stock solution; (4-7) $[Ni_2L_3]Cl_4$; (8-11) $[Ni_2(L_{Im2})_3]Cl_4$; (12-15) $[Ni_2(L_{Im2}")_3]Cl_4$; (16-19) $[Ni_2(L_{Im2}")_3.CB10]Cl_4$.

The uncapped ($[Ni_2(L_{Im2})_3]Cl_4$, *Figure 62*, wells 8-11) and capped ($[Ni_2(L_{Im2}")_3]Cl_4$, Figure 62, wells 12-15) imidazole cylinders also show an increase in fluorescence intensity of the 3WJ band with increasing concentration. The uncapped cylinder shows a greater fluorescence than the parent cylinder, which is unexpected as when investigated by radiolabelled PAGE the iron parent cylinder showed greater junction stabilisation[12]. This could be due to the different visualisation methods used, as each cylinder species may interfere with the observed fluorescence intensity. The methylpyridine-capped cylinder ($[Ni_2(L_{Im2}"_{MePy})_3]Cl_4$) investigated previously also

showed increased junction formation compared to the parent and uncapped cylinder[12] whereas the capped cylinder in this study shows the weakest fluorescence for the 3WJ band as the larger cap which may sterically hinder junction binding.

The rotaxane ($[Ni_2(L_{Im2}")_3.CB10]Cl_4$, Figure 62, wells 16-19) gives a very faint 3WJ band which suggests that some junction formation is taking place. This could be due to partially capped impurities which would be released more easily from the CB10 ring, allowing junction formation.

Photocleavage of the supramolecular species was also investigated by gel electrophoresis as release of the cylinder from the macrocycle or removal of the sterically bulky caps should increase the intensity of the 3WJ band. Solutions of each complex were irradiated up to 60 minutes with samples taken at each time point to incubate with the junction DNA. One equivalent of the cylinder was used per 3WJ as this is the expected binding ratio for cylinders and this ratio gave observable bands in the previous gel without saturation of the fluorescence signal.

The uncapped cylinder (Figure 63, wells 4-7) shows no change in the fluorescence with increasing irradiation time, suggesting that the cylinder was not degraded under the irradiation conditions. Similar results were observed for the capped cylinder (Figure 63, wells 8-11) suggesting that the photocleavage experiment was unsuccessful.

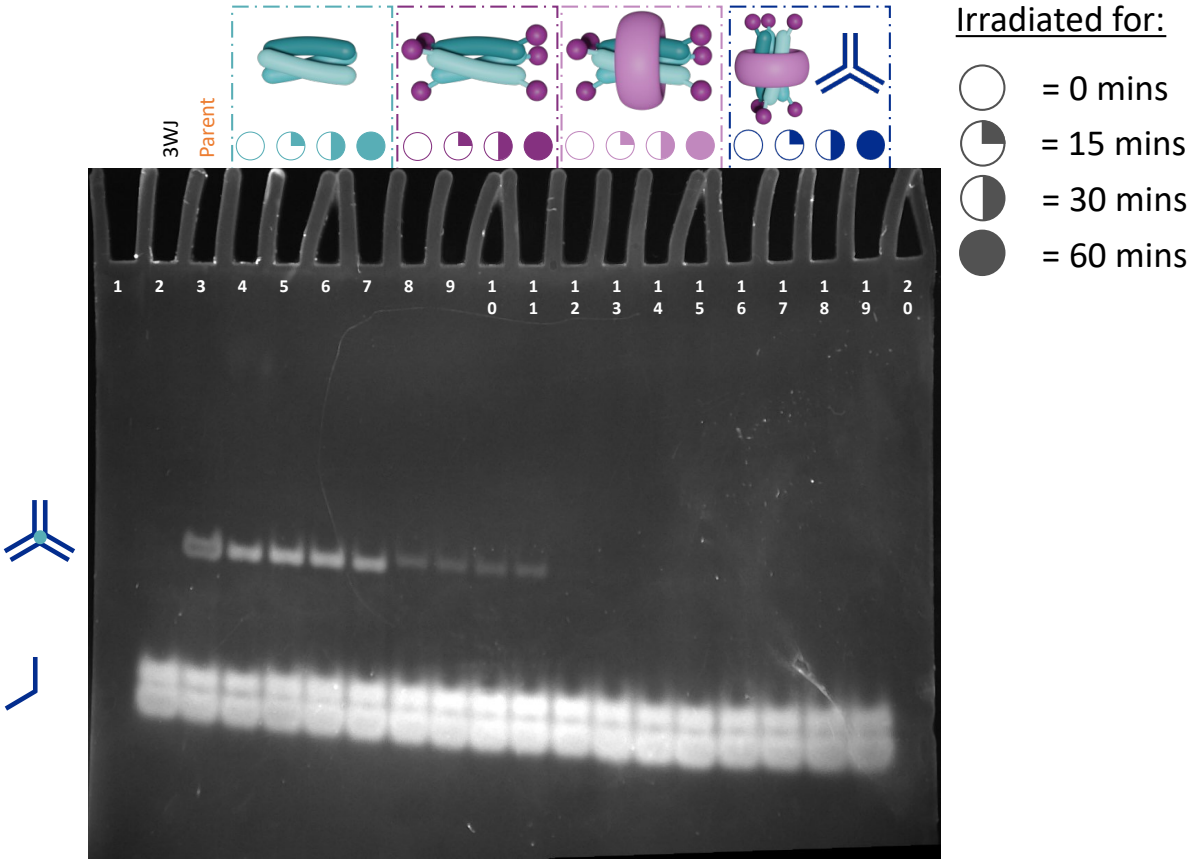

Figure 63: PAGE of 3WJ formation by supramolecular complexes (1 μM) after increasing irradiation times (0, 15, 30 and 60 minutes). Wells: (1,20) running dye; (2) 3WJ stock solution; (3) $[Ni_2L_3]Cl_4$; (4-7) $[Ni_2(L_{lm2})_3]Cl_4$; (8-11) $[Ni_2(L_{lm2}")_3]Cl_4$; (12-15) $[Ni_2(L_{lm2}")_3.CB10]Cl_4$; (16-19) $[Ni_2(L_{lm2}")_3.CB10]Cl_4$ irradiated with 3WJ.

The rotaxane also displayed no increase in the fluorescence of the 3WJ band when irradiated on its own (Figure 63, wells 12-15), or in the presence of the junction DNA (wells 16-19). Photocleavage of the rotaxane is expected to yield the *pseudo*rotaxane. A competitive binding effect has been observed between CB10 and the 3WJ previously, however the presence of CB10 is not expected to prevent junction binding[12]. It is possible that the rotaxane was only partially decapped under the irradiation conditions and not enough of the caps are removed to release the cylinder from the macrocycle.

3.4. Conclusions

The aim of this work was to assess the photocleavage of the new imidazole based supramolecular rotaxane. An appropriate irradiation source was first identified by using DMNB-Br, the alkylating agent, as a model compound for photocleavage.

Irradiation of the supramolecular complexes was monitored by UV-visible absorbance and mass spectrometry. Larger changes in absorbance were observed for the rotaxane than the capped and uncapped cylinders with increasing irradiation, however formation of a reaction product was not observed. Mass spectrometry of the capped cylinder identified the appearance of the 5- and 4-capped cylinders with increasing irradiation time, however further removal of capping groups was not observed. Photocleavage of the rotaxane was not supported by mass spectrometry as only species which were fully alkylated were observed in the spectra.

PAGE was used to confirm that the imidazole cylinders were able to form 3WJs, with the uncapped cylinder giving the highest intensity 3WJ band. By comparison, the capped cylinder gave a reduced intensity band, implying that the caps impede the junction formation. The rotaxane showed a very faint band for junction formation, which could be due to the release of partially capped cylinders from the CB10 ring. Upon incubation of irradiated samples of the complexes with junction DNA, the intensity of the 3WJ band remained unchanged for all species, confirming that the photocleavage of the capped cylinder and rotaxane were unsuccessful.

3.5. List of References

1 D. Liu, F. Yang, F. Xiong and N. Gu, *Theranostics*, 2016, **6**, 1306–1323.
2 A. Raza, T. Rasheed, F. Nabeel, U. Hayat, M. Bilal and H. Iqbal, *Molecules*, 2019, **24**, 1117.
3 G. C. R. Ellis-Davies, *Acc. Chem. Res.*, 2020, **53**, 1593–1604.
4 P. Wang, *Asian J. Org. Chem.*, 2013, **2**, 452–464.
5 P. Klán, T. Šolomek, C. G. Bochet, A. Blanc, R. Givens, M. Rubina, V. Popik, A. Kostikov and J. Wirz, *Chem. Rev.*, 2013, **113**, 119–191.
6 J. M. Silva, E. Silva and R. L. Reis, *J. Control. Release*, 2019, **298**, 154–176.
7 S. Majhi, *Photochem. Photobiol. Sci.*, 2021, **20**, 1357–1378.
8 C. G. Bochet, *J. Chem. Soc. Perkin Trans. 1*, 2002, **2**, 125–142.
9 J. E. T. Corrie, T. Furuta, R. Givens, A. L. Yousef and M. Goeldner, in *Dynamic Studies in Biology*, M. Goeldner, R. S. Givens, Wiley-VCH Verlag GmbH & Co. KGaA, Weinheim, 1st edn., 2005, ch. 1, pp. 1–94.
10 C. G. Bochet, *Tetrahedron Lett.*, 2000, **41**, 6341–6346.
11 H. Görner, *Photochem. Photobiol. Sci.*, 2005, **4**, 822–828.
12 C. A. J. Hooper, L. Cardo, J. S. Craig, L. Melidis, A. Garai, R. T. Egan, V. Sadovnikova, F. Burkert, L. Male, N. J. Hodges, D. F. Browning, R. Rosas, F. Liu, F. V. Rocha, M. A. Lima, S. Liu, D. Bardelang and M. J. Hannon, *J. Am. Chem. Soc.*, 2020, **142**, 20651–20660.
13 S. Shaban Ragab, S. Swaminathan, E. Deniz, B. Captain and F. M. Raymo, *Org. Lett.*, 2013, **15**, 3154–3157.
14 S. Swaminathan, M. Petriella, E. Deniz, J. Cusido, J. D. Baker, M. L. Bossi and F. M. Raymo, *J. Phys. Chem. A*, 2012, **116**, 9928–9933.
15 J. Griffiths, *Anal. Chem.*, 2008, **80**, 5678–5683.
16 S. Banerjee and S. Mazumdar, *Int. J. Anal. Chem.*, 2012, **2012**, 282574.
17 M. Wilm and M. Mann, *Anal. Chem.*, 1996, **68**, 1–8.
18 M. Wilm, *Mol. Cell. Proteom.*, 2011, **10**, M111.009407.
19 C. S. Ho, C. W. K. Lam, M. H. M. Chan, R. C. K. Cheung, L. K. Law, L. C. W. Lit, K. F. Ng, M. W. M. Suen and H. L. Tai, *Clin. Biochem. Rev.*, 2003, **24**, 3–12.
20 R. Westermeier, *Electrophoresis in Practice: A Guide to Methods and Applications of DNA and Protein Separations*, Wiley-VCH Verlag GmbH & Co. KGaA, Weinheim, 5th edn., 2016.
21 Thermo Fisher Scientific: Steps in Nucleic Acid Gel Electrophoresis, https://www.thermofisher.com/uk/en/home/life-science/cloning/cloning-learning-center/invitrogen-school-of-molecular-biology/na-electrophoresis-education/na-electrophoresis-workflow.html, (accessed January 2024).
22 Acrylamide Polymerisation – A Practical Approach, https://www.bio-rad.com/webroot/web/pdf/lsr/literature/Bulletin_1156.pdf, (accessed January 2024).
23 P. Barril and Silvia Nates, in *Gel Electrophoresis - Principles and Basics*, ed. S. Magdeldine, InTech, Rijeka, 2012, ch. 1, pp. 1-14.

24 N. C. Stellwagen, *Electrophoresis*, 2009, **30**, S188-S195.
25 M. Querci, D. Kagkli, F. Gatto, N. Foti, M. Maretti, and M. Mazzara, *The Analysis of Food Samples for the Presence of Genetically Modified Organisms – User Manual*, EUR 30145 EN, Publications Office of the European Union, Luxembourg, 2020.
26 H. A. Day, P. Pavlou and Z. A. E. Waller, *Bioorg. Med. Chem.*, 2014, **22**, 4407–4418.
27 J. L. Kadrmas, A. J. Ravin and N. B. Leontis, *Nucleic Acids Res*., 1995, **23**, 2212–2222.
28 J. Malina, M. J. Hannon and V. Brabec, *Chem. Eur. J.*, 2007, **13**, 3871–3877.

4. 5-OXYPYRIDINE BASED SUPRAMOLECULAR COMPLEXES

4.1. Redesigning the photocleavable system

In the previous chapter photocleavage of the imidazole-based supramolecular complexes was found to be unsuccessful. Successful photocleavage of the capping group alone (DMNB-Br) was confirmed by comparison to literature results[1,2] so redesign focused on the helicate structure.

The *pseudo*rotaxane formation and junction binding of pyridine-based parent cylinder ($[M_2L_3]Cl_4$) has already been demonstrated[3–6], however the pyridine ring does not contain a site available for alkylation. The attachment of alcohol substituents has been investigated by previous Hannon group members[7–11]. Following this work, two picolinaldehydes have been investigated, both with an alcohol group in the 5-position of the pyridine ring (Figure 64).

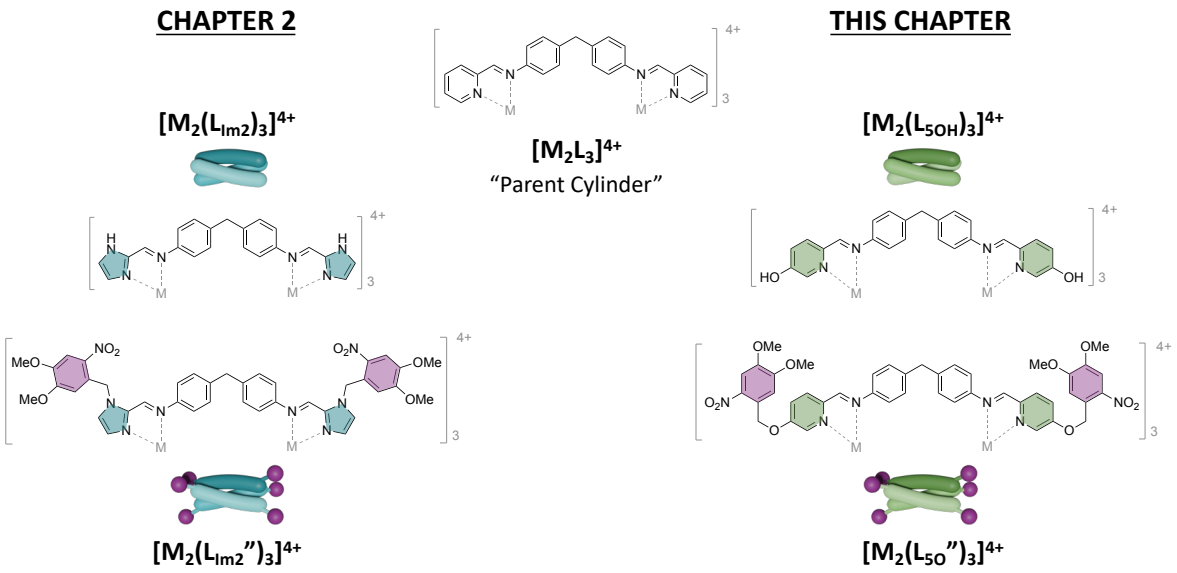

Figure 64: Showing the redesign of the cylinder structure discussed in this chapter compared to the structure of the cylinder in Chapter 2.

4.2. Aldehyde synthesis

4.2.1. 5-(Hydroxymethyl)picolinaldehyde (Ald_{5MeO})

5-(Hydroxymethyl)picolinaldehyde (Ald_{5MeO}) has been synthesised previously by Hannon group members[9–11] to functionalise the parent cylinder with moieties such as a methylalcohol, or azide group. Of the two synthetic pathways considered (Scheme 1), the method used by G. Pascu has fewer steps, avoids the use of harsh reagents, and uses a cheaper starting material[12,13].

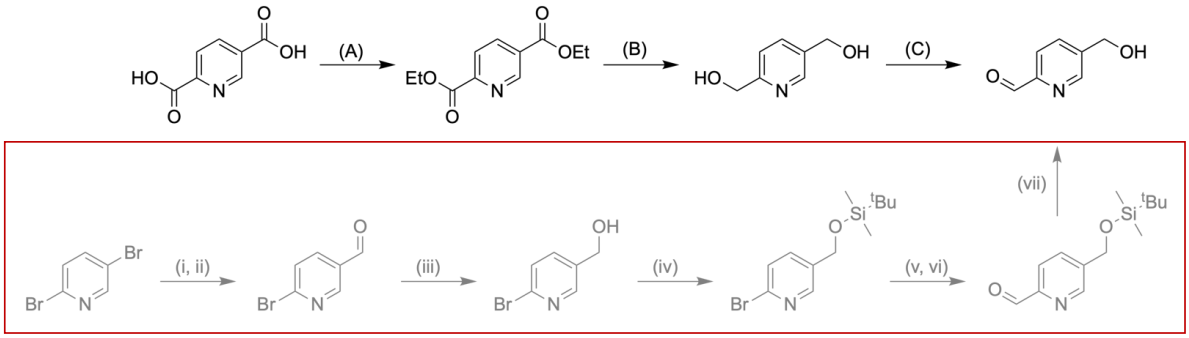

Scheme 1: Approaches used by G. Pascu[9] (above) and C. Campbell[10] (below, highlighted in red), to synthesise the 2,5-hydroxymethylpyridine.

Following the route used by G. Pascu, 2,5-pyridinedicarboxylic acid was reacted with ethanol in an acid catalysed esterification to produce the diester, diethylpyridine-2,5-carboxylate (Scheme 1A)[9]. Water is removed from the reaction by formation of an azeotrope with ethanol and cyclohexane which pushes the reaction to completion. The diester was isolated as a white solid by silica column chromatography and characterised by mass spectrometry (224 m/z, $[M + H]^+$) and ^1H NMR (Figure 65) which shows chemical shifts within 0.1 ppm of those reported by G. Pascu[9].

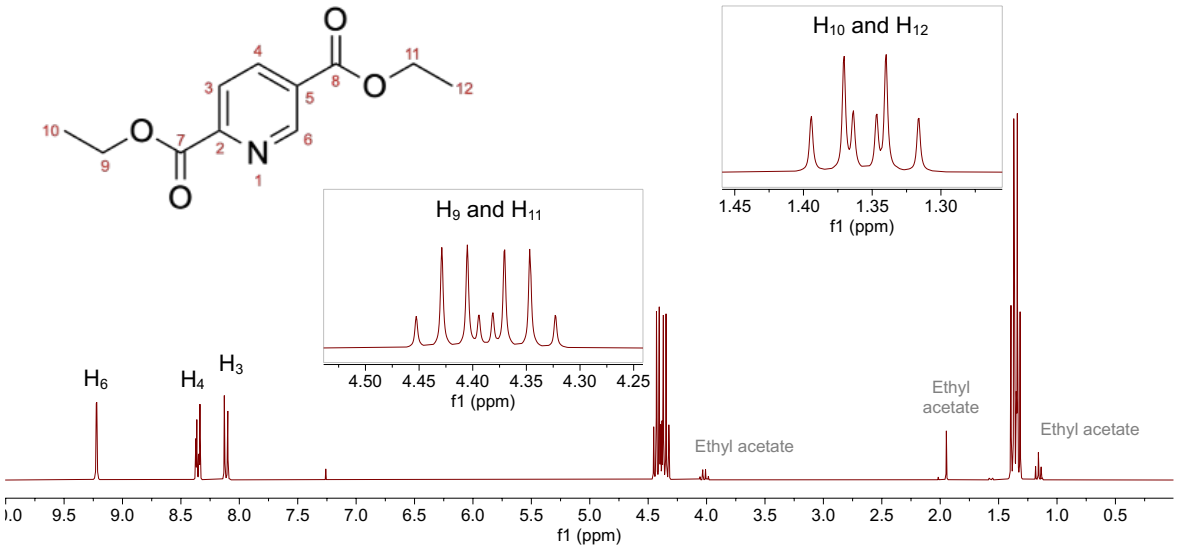

*Figure 65: ^{1}H NMR (300 MHz, Chloroform-*d*) of diethylpyridine-2,5-carboxylate.*

An alternative method was attempted following the reported esterification of terephthalic acid[14] which used a reduced amount of the sulphuric acid catalyst and did not require a reflux with cyclohexane, however this decreased the yield from 42% to 17-21%. Returning to the original synthesis and doubling the reaction scale, a maximum of yield of 54% was achieved.

Diethylpyridine-2,5-carboxylate was then reduced by sodium borohydride to 2,5-pyridinedimethanol. The method used by G. Pascu reports a 51% yield but used only two equivalents of sodium borohydride, which is half the amount suggested by the reaction mechanism (Scheme 2), so an alternative synthesis was used[15].

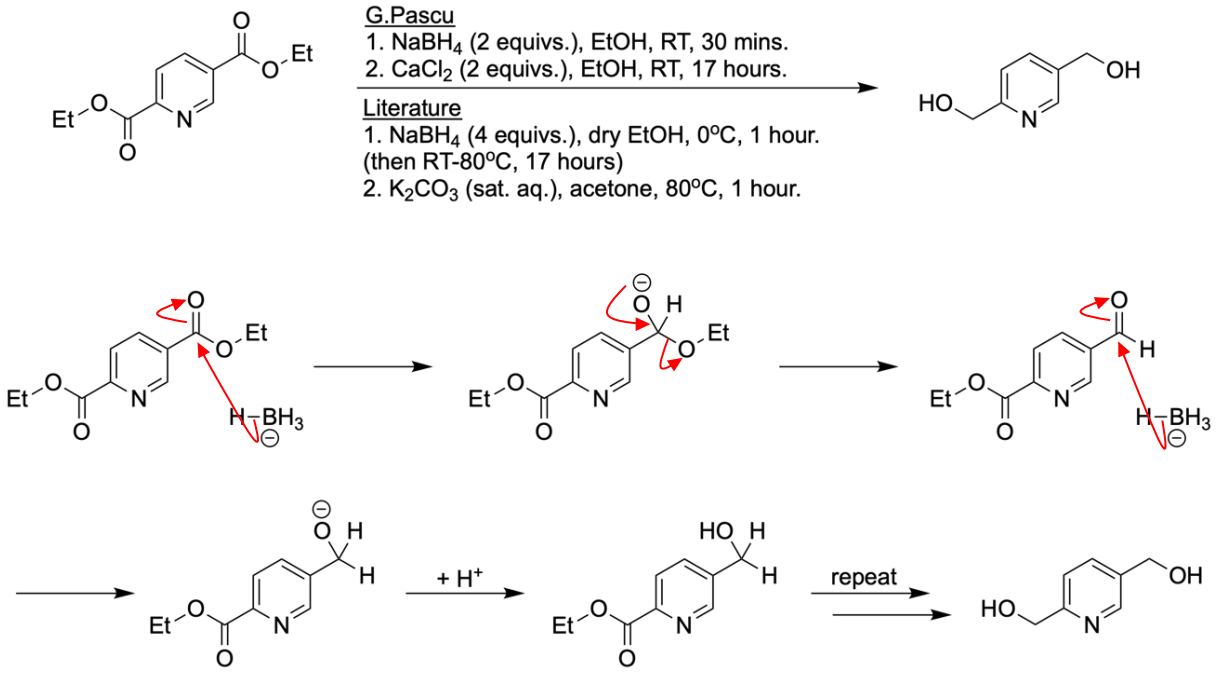

Scheme 2: Reaction scheme and mechanism for the reduction of diethylpyridine-2,5-dicarboxylate by sodium borohydride[9,15].

An initial 40% yield after column chromatography was improved to a 93% yield upon repeating the reaction. The ^{1}H NMR (Figure 66) was assigned by comparison to the spectrum reported by G. Pascu[9], and by considering the characteristic J-values for coupling between pyridine protons. Assignments of the aliphatic peaks are suggested by considering the electron withdrawal of the pyridine nitrogen which should be stronger in the ortho-position (H_7 and H_9) than the meta-position (H_8 and H_{10}).

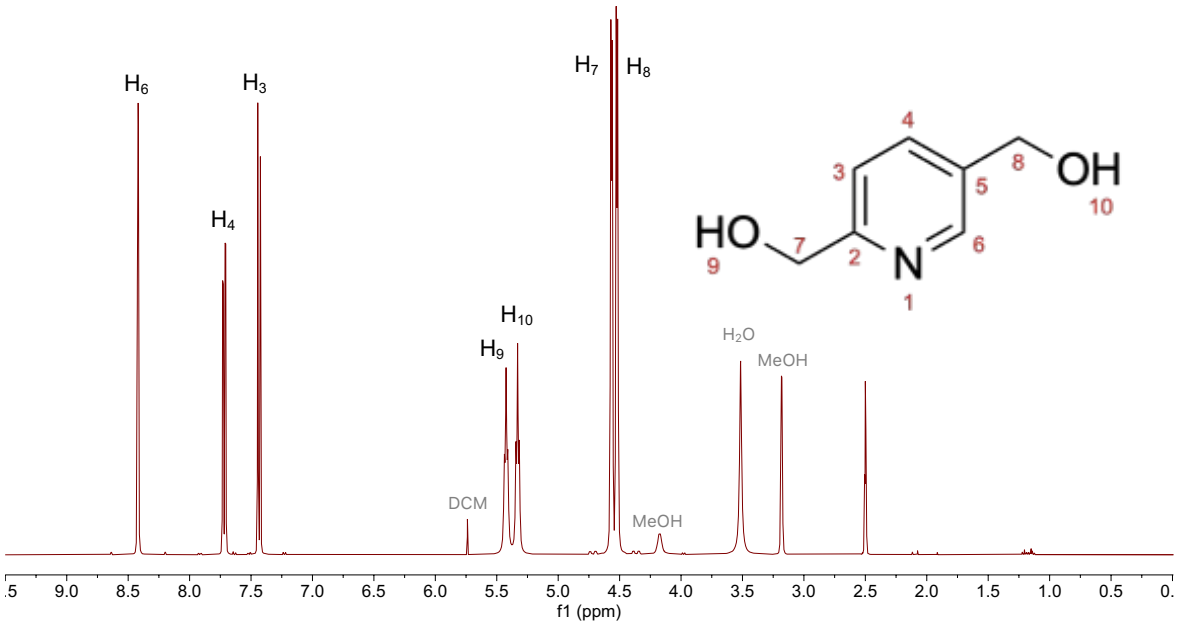

Figure 66: ^{1}H NMR (400 MHz, DMSO-d$_6$) of 2,5-pyridinedimethanol.

Selective oxidation of 2,5-pyridinedimethanol by selenium dioxide gave 5-(methylhydroxy)picolinaldehyde as reported by G. Pascu[9]. A 58% yield after column chromatography, similar to the reported 50%, was achieved using degassed solvents and exchanging Celite for a nylon membrane to filter. The structure was confirmed by ^{1}H NMR (Figure 67) and mass spectrometry (138.06 m/z, $[M + H]^{+}$).

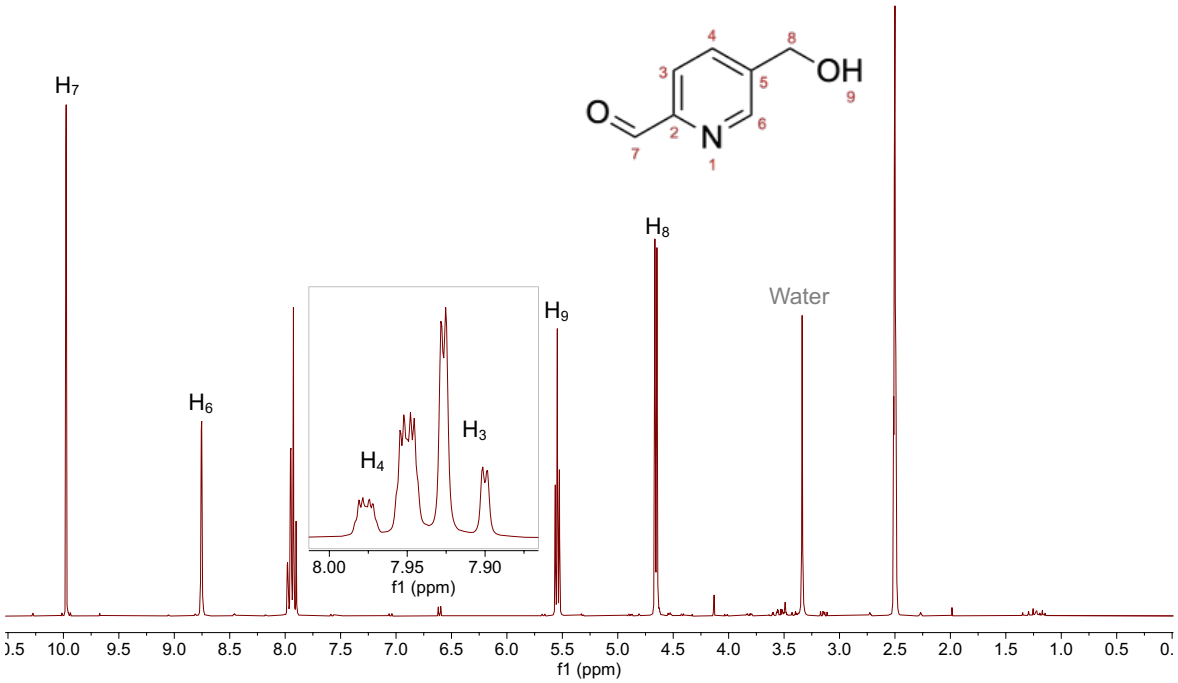

Figure 67: ^{1}H NMR (300 MHz, DMSO-d_6) of 5-(hydroxymethyl)picolinaldehyde.

4.2.2. Alkylation of 5-(hydroxymethyl)picolinaldehyde (Ald_{5MeO}')

To alkylate the primary alcohol, 5-(hydroxymethyl)picolinaldehyde and DMNB-Br were stirred in aqueous methanol with potassium carbonate. No change in the reaction mixture was observed by TLC over the first five hours, so the reflux was continued overnight. A pale-yellow precipitate was isolated by filtration, however, the mass spectrum suggested only the starting aldehyde and the photocleaved 4,5-dimethoxy-2-nitrosobenzaldehyde were present (Figure 68).

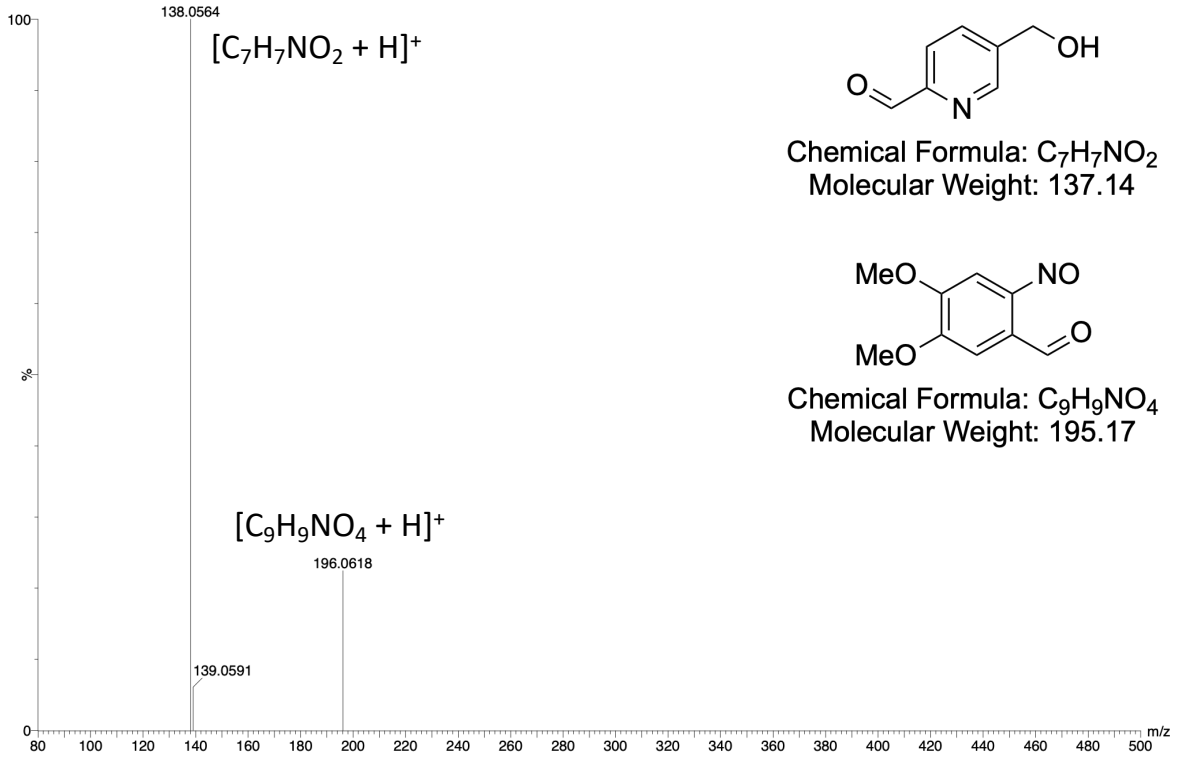

Figure 68: Mass spectrum (TOF ASAP+) of the 5-(hydroxymethyl)picolinaldehyde alkylation reaction precipitate.

4.2.3. 5-hydroxypicolinadelhyde (Ald_{5OH})

5-hydroxypicolinaldehyde has been used by members of the Hannon group as a precursor for the attachment of additional functional groups[8,10], however the alcohol functionalised cylinder has not been reported. The route to 5-hydroxypicolinaldehyde used by C. Campbell has been followed (Scheme 3)[10].

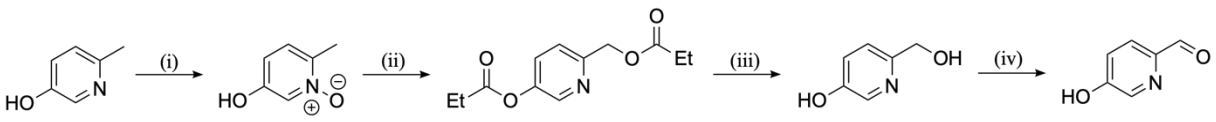

Scheme 3: Synthesis of the 5-hydroxypicolinaldehyde (as reported by C. Campbell[10]): (i) H_2O_2 (aq.), acetic acid, 120°C, 3.5 hours, then RT for 17 hours; (ii) acetic anhydride, 130°C, 2 hours; (iii) conc. HCl, 110°C, 1 hour; (iv) activated MnO_2, iPrOH, Ar, 100°C, 2.5 hours.

5-hydroxy-2-methylpyridine was oxidised to the N-oxime using peracetic acid formed from hydrogen peroxide and acetic acid. The product was collected by filtration after precipitated in acetone and was characterised by mass spectrometry (126.06 m/z, $[M + H]^+$) and ^1H NMR (Figure 69) which was assigned by comparison to the reported chemical shifts.

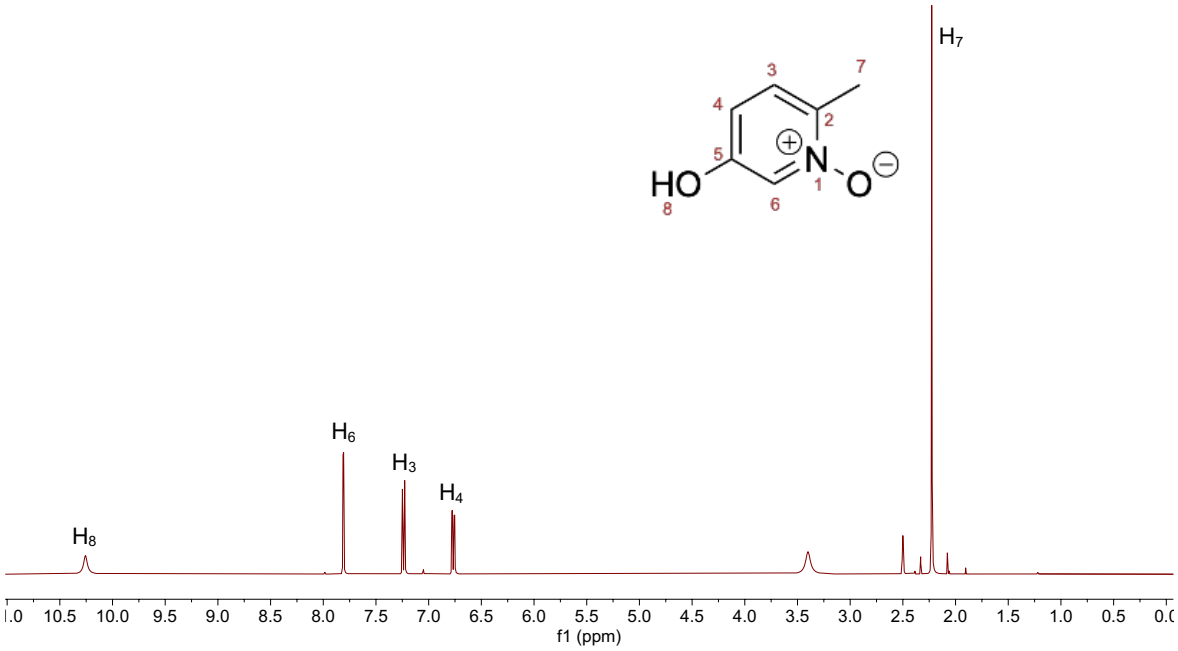

Figure 69: ^1H NMR (400 MHz, DMSO-d_6) of 5-hydroxy-2-methylpyridine N-oxime.

The N-oxime was then converted to 2-(acetoxymethyl)pyridine-5-yl by reflux in ethyl acetate and precipitated from cold acetone. The product was characterised by mass spectrometry (210 m/z, $[M + H]^+$) and ^1H NMR (Figure 70) which matches the shifts and coupling constants reported by C. Campbell[10].

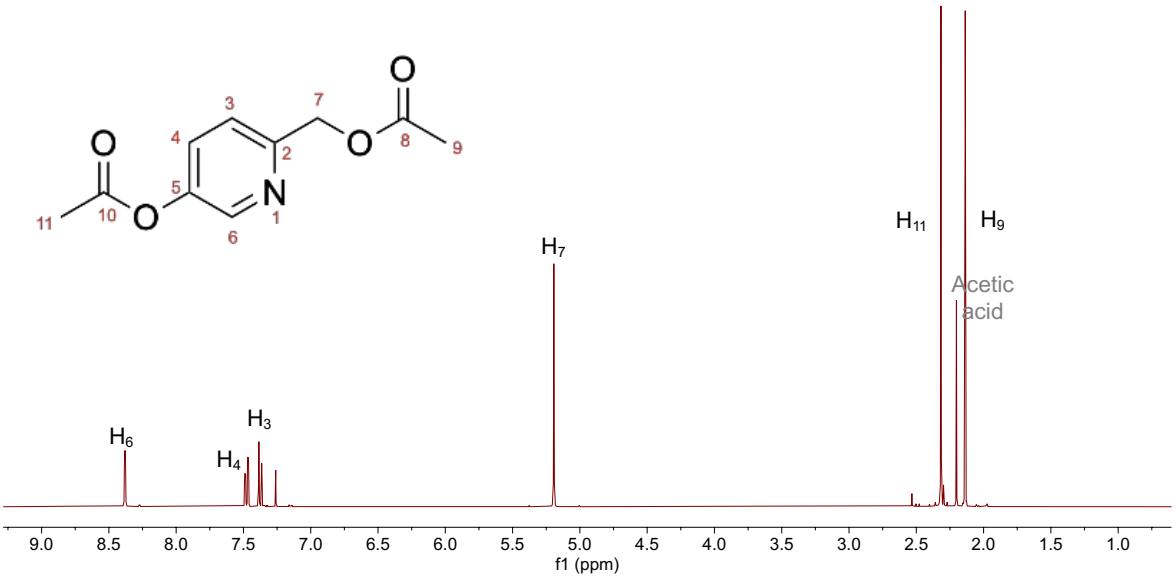

*Figure 70: ^{1}H NMR (400 MHz, Chloroform-*d*) of 2-(acetoxymethyl)pyridine-5-yl.*

The diester was reduced by reflux in concentrated hydrochloric acid which was then neutralised and a crude product isolated by separation. Only a small proportion of the product could be collected by trituration with acetonitrile, so isopropyl alcohol was used as an alternative solvent. A silica plug was used to purify the crude product when the scale of the reaction was increased and the product was then washed with chloroform until the filtrate ran clear. Although multiple spots were observed by TLC the ^{1}H NMR spectrum (Figure 71) indicated that the 5-(hydroxymethyl)pyridine-2-ol was the major product.

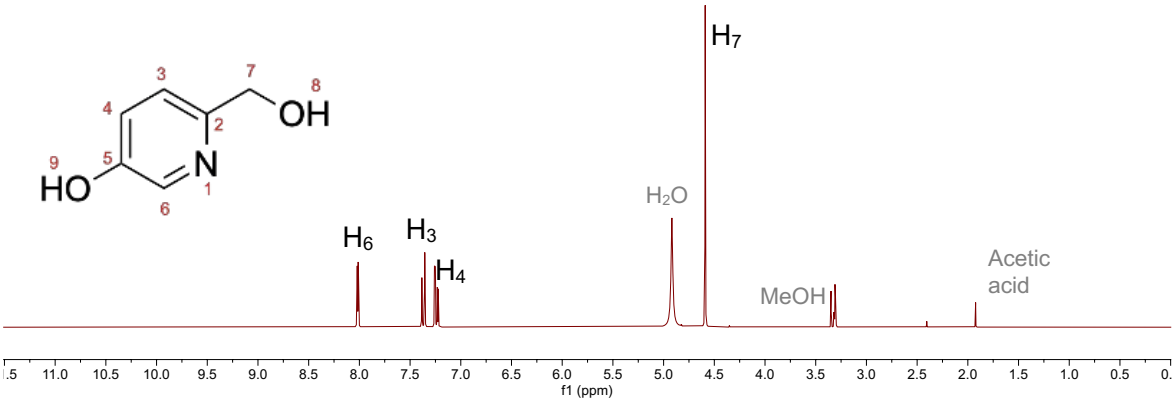

Figure 71: ^{1}H NMR (300 MHz, Methanol-d$_4$) of 5-(hydroxymethyl)pyridine-2-ol.

Selective oxidation of the primary alcohol was achieved using manganese dioxide following the method detailed by C. Campbell[10] and the product peak observed by mass spectrometry (122 m/z, $[M - H]^-$). The ^{1}H NMR (Figure 72) spectrum of the product was assigned in agreement with the previously reported spectrum, including a broad alcohol peak at high chemical shift (11.1 ppm)[10]. HSQC (heteronuclear single quantum correlation) and HMBC (heteronuclear multiple bond correlation) spectra suggest alternative assignments for the carbon peaks than reported[10]. C_3, C_4 and C_6 are assigned following the coupling observed in the HSQC spectrum between the carbon and proton peaks while the remaining protons (C_2, C_5 and C_7) can be assigned from the HMBC spectrum. C_5 shows a strong signal to all the pyridine protons, whereas C_2 shows a signal to the aldehyde H_7 proton as well as the pyridine protons. There is also a strong signal for coupling between H_3 and C_7, and a weaker coupling to H_4, but no coupling to H_6 or H_7 as would be expected for a HMBC, as this only coupling through multiple bonds should be observed.

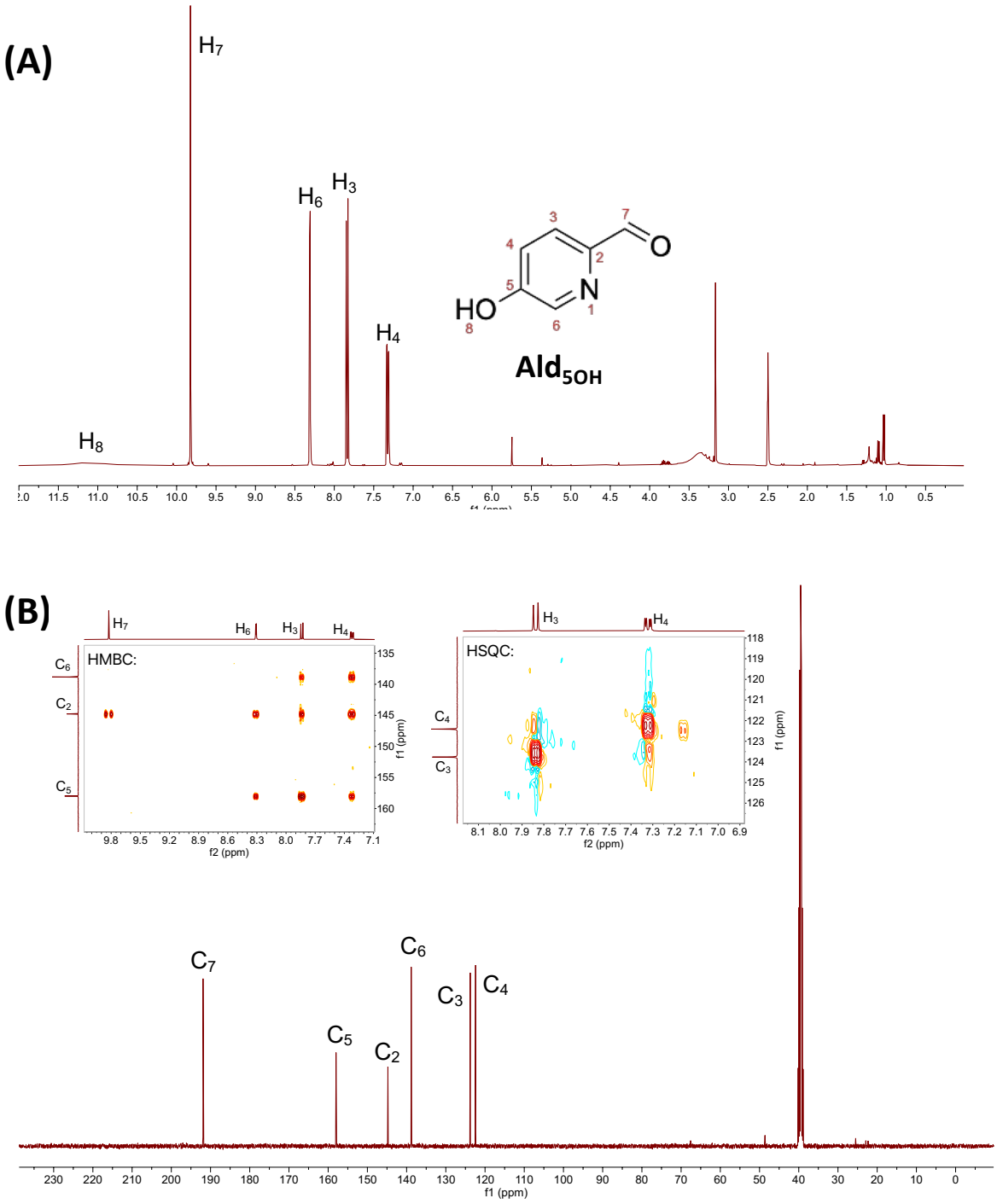

Figure 72: (A) ^{1}H NMR (400 MHz, DMSO-d$_6$), and (B) ^{13}C NMR (101 MHz, DMSO) of Ald$_{5OH}$, with HMBC and HSQC inset.

4.3. 5-hydroxypicolinaldehyde based cylinders ($[M_2(L_{5OH})_3]Cl_4$)

The 5-hydroxypyridine ligand (L_{5OH}) are based on the same pyridyl-imine system as the parent ligand[16], so a similar synthesis was attempted (Scheme 4).

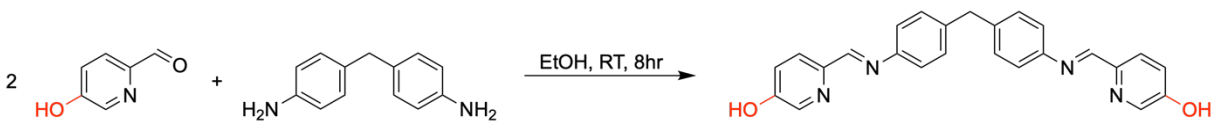

Scheme 4: Synthesis of the parent (black) and 5-hydroxypyridine (black and red) ligands[16].

A precipitate was observed after stirring for 5 minutes at room temperature and 5-hydroxypicolinaldehyde was no longer observed by TLC after 5 hours, although MDA was still present. The precipitate was collected by filtration and characterised by mass spectrometry (407 m/z, $[L_{5OH} - H]^-$) and ^1H NMR (Figure 73A) with comparison to the 5-hydroxypicolinaldehyde spectrum (Figure 72A). The appearance of some smaller peaks (3.8, 6.5, and 6.9 ppm) in the spectrum indicated a small amount of the half ligand (hL_{5OH}) was present in the product so the precipitate was recombined with the filtrate and the reaction continued overnight. The integration remained unchanged between the two spectra, suggesting the reaction would go no further under these conditions.

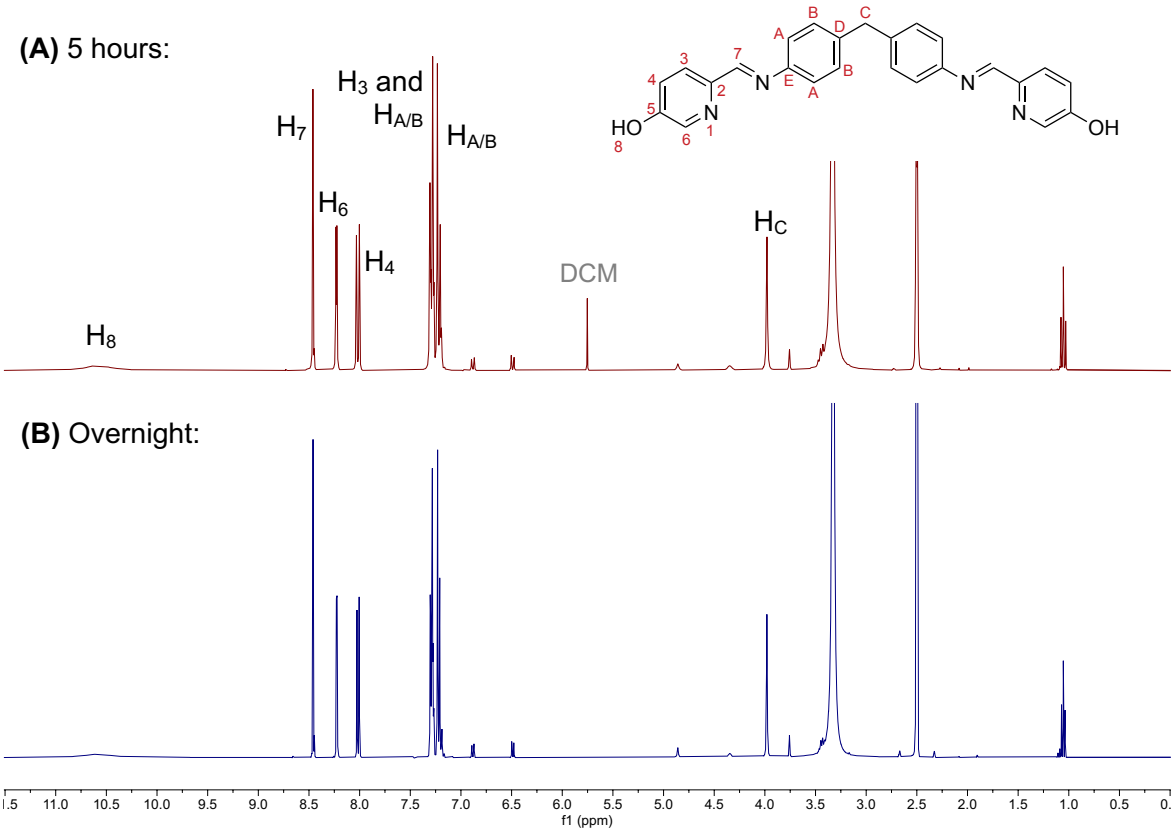

Figure 73: ^{1}H NMR (300 MHz, DMSO-d$_6$) of L_{5OH} after stirring at RT in EtOH for 5 hours (top, maroon) and overnight (bottom, navy).

A repeat of the reaction was monitored by TLC overnight. The 5-hydroxypicolinaldehyde spot was lost within 10 minutes although the MDA spot was still observed, and no further change was observed over 19 hours. The ^{1}H NMR suggested a small decrease in the integration of the additional peaks (see Figure 74A).

Synthesis of the uncapped iron cylinder ($[Fe_2(L_{5OH})_3]Cl_4$) was achieved by dissolving both the ligand and iron chloride tetrahydrate in methanol which quickly gave a dark purple solution. The reaction solution was filtered after 2 hours to remove any solid impurities and the filtrate concentrated before precipitating in diethyl ether. The purple product was characterised by ^{1}H NMR (Figure 74B) and compared to the ligand spectrum. The pyridine and imine peaks (H_3, H_4, and H_7) show a characteristic upward shift compared to the free ligand due to electron withdrawal caused by metal cation

coordination. Alternatively, the proton in the 6-position (H_6) is directed to the metal centre where it is shielded by the metal electrons. The phenyl protons (H_A and H_B) show the shielding, due to face-edge π-stacking with each other, and broadening, caused by different environments in fast exchange, characteristic of metal complex formation.

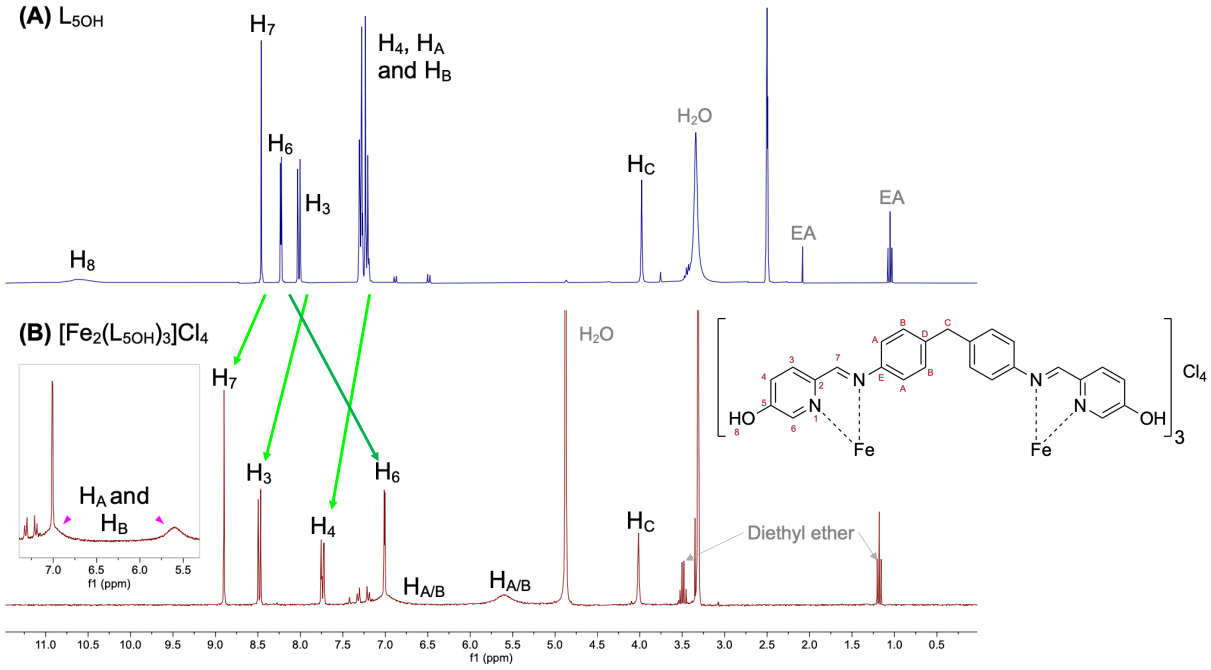

Figure 74: ^{1}H NMR (300 MHz) of (A) L_{5OH} in DMSO-d_6, and (B) $[Fe_2(L_{5OH})_3]Cl_4$ in methanol-d_4. Inset: Highlighting the phenyl peaks (pink arrows).

The mass spectrum of the iron cylinder ($[Fe_2(L_{5OH})_3]Cl_4$, Figure 75) shows the 3+ and 2+ charged cylinder species as well as the two metal, two ligand species which could be formed during the ionisation process. Clusters or peaks caused by multiple cylinders grouping together can be observed in concentrated samples which could be caused by hydrogen bonding between the terminal hydroxyl groups.

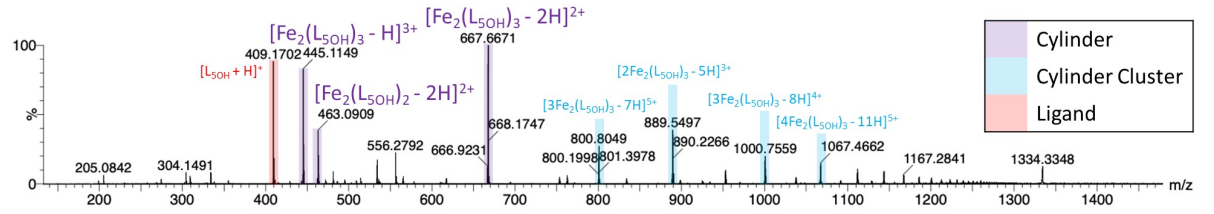

Figure 75: Mass spectrum (TOF ES+, MeOH) of $[Fe_2(L_{5OH})_3]Cl_4$.

Purification by anion exchange using ammonium hexafluorophosphate was also attempted, however incomplete precipitation of the cylinder was indicated by a coloured filtrate which could indicate the increased solubility of the cylinder in polar solvents due to the terminal alcohol groups. The collected precipitate was insoluble in most solvents, but formed a coloured solution in DMSO, which is unexpected as DMSO can coordinate the metal ions to form a colourless solution. ^{1}H NMR of the solution gave a very broad spectrum and appeared to contain some free ligand.

The formation of the nickel cylinder was also achieved using the diethyl ether precipitation work up. The cylinder could not be dissolved at high enough concentration to record the ^{1}H NMR spectrum so the product was characterised by mass spectrometry (Figure 76). The two-metal, two-ligand, two-half ligand species ($[Ni_2(L_{5OH})_2(hL_{5OH})_2]Cl_4$) appears both as both 2+ and 3+ ions as well as a three-metal, four-ligand species ($[Ni_3(L_{5OH})_4]Cl_4$) which cannot be formed by a combination of cylinder units. It is unclear whether this is a product of the ionisation process or whether these species exist in solution.

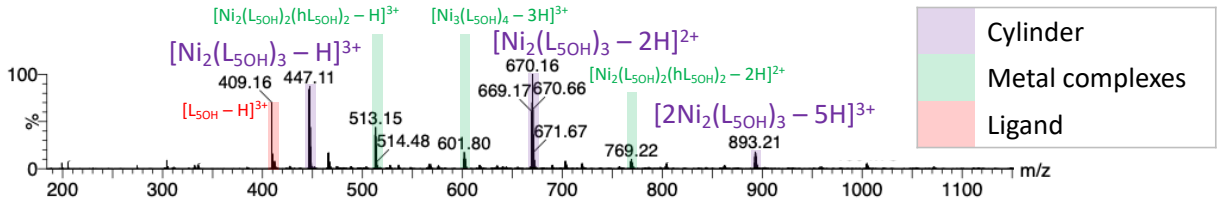

Figure 76: Mass spectrum (TOF ES+, MeOH) of $[Ni_2(L_{5OH})_3]Cl_4$.

4.4. Capped 5-oxypyridine based cylinders ($[M_2(L_{5O}")_3]Cl_4$)

As with the imidazole-based cylinder system, the capped 5-oxypyridine based cylinders can be synthesised from the ligand or by post-assembly modification of the uncapped cylinder. The former route was preferred by the imidazole system, so was attempted first.

Alkylation of 5-hydroxypicolinaldehyde with DMNB-Br was attempted by a previously reported method (Scheme 5)[17]. The reaction was completed under dark and inert conditions and a bright orange crude product was extracted from the reaction mixture by separation. The product was purified by silica gel column chromatography to give the final product in high yield (70-95%).

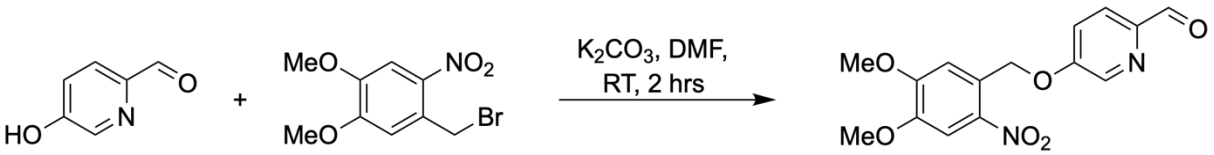

Scheme 5: Synthesis of Ald_{5O}'.

Assignment of the ^1H NMR spectrum was completed as far as possible using the expected integration and coupling constants, and the benzyl protons (H_{11} and H_{14}) were distinguished by the coupling between H_8 and H_{14} in the COSY (homonuclear correlation spectroscopy) NMR spectrum (Figure 77). The chemical shifts of both the

^{1}H and ^{13}C NMR also match the reported values, except for a 4 ppm shift of one peak in the ^{13}C spectrum.

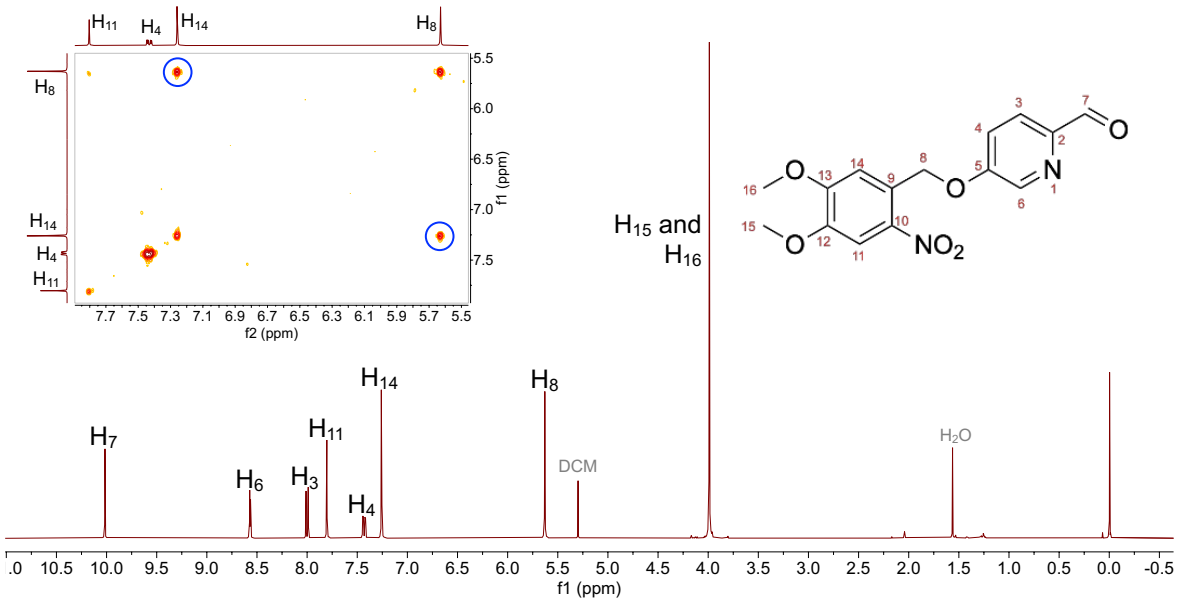

Figure 77: 1H NMR (400 MHz, Chloroform-d) of Ald5O'. Inset: COSY NMR highlighting the coupling between H8 and H14 (blue circle).

The capped ligand (L_{5O}") was synthesised from the capped aldehyde (Ald_{5O}') via the imine formation reaction used for the uncapped ligand (L_{5OH}). The aldehyde was stirred with MDA in ethanol for 2 hours before a pale orange precipitate was collected by filtration and characterised. The mass spectrum gave a peak for the ligand (799 m/z, $[L_{5O}" + H]^+$) but the ^{1}H NMR gave the same spectrum as the aldehyde alone, indicating that the reaction had not taken place.

The reaction was repeated and a second set of peaks became visible in the ^{1}H NMR of the precipitate after 3 hours of stirring, indicating that the ligand had begun to form. The precipitate was recombined with the filtrate and the reaction mixture heated to reflux for 90 minutes. The ligand peaks in the ^{1}H NMR of the precipitate had

increased in intensity so the reflux was continued for a further 3.5 hours, however only a small change in the NMR was observed (Figure 78).

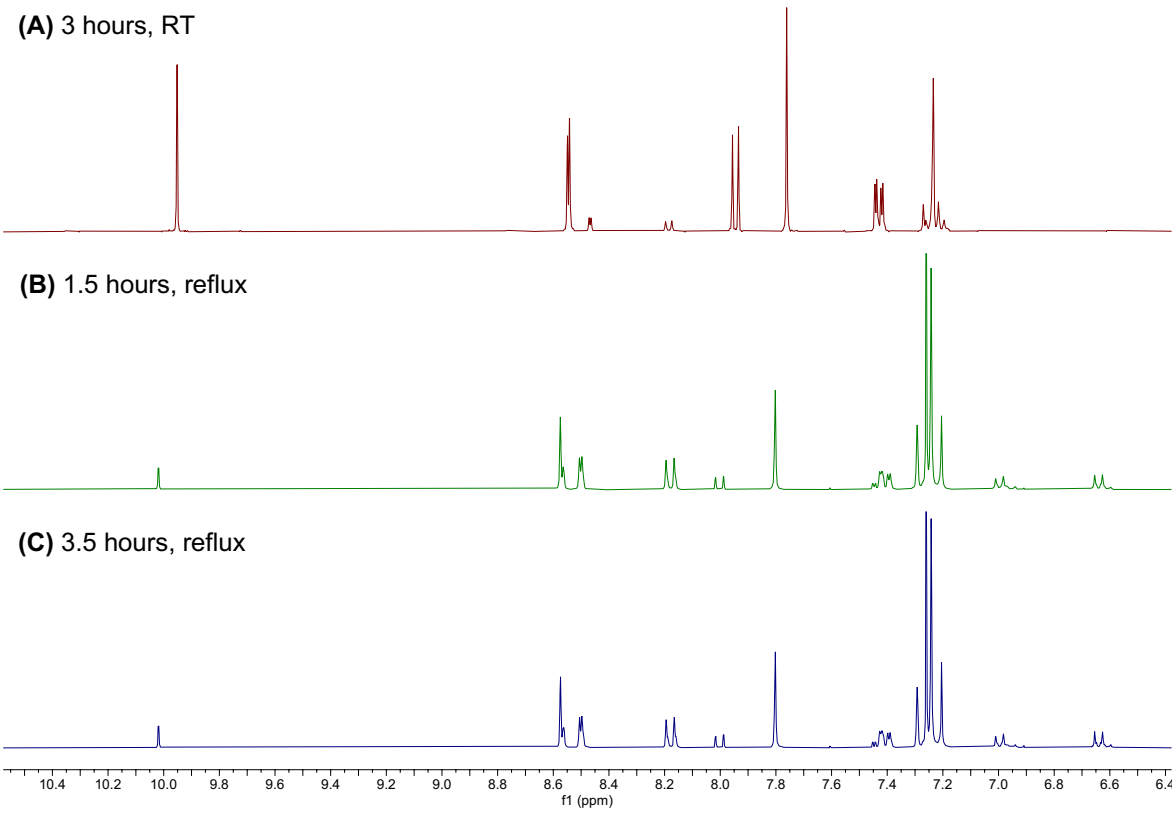

Figure 78: ^{1}H NMR (6.5-10.5 ppm) of the reaction precipitate after (A) (400 MHz, Methylene Chloride-d2) 3 hours at room temperature, (B) (300 MHz, Chloroform-d) 1.5 hours at reflux, and (C) (300 MHz, Chloroform-d) 3.5 hours at reflux.

The reaction was repeated and a sample of the precipitate taken after 24 hours at reflux for ^{1}H NMR (Figure 79A). The spectrum indicated that the ligand had been synthesised, so the precipitate was collected from the reaction mixture. The off-white precipitate turned a pale pink during the work up and a few small peaks were visible in the isolated product which suggested the presence of an aldehyde and some half ligand (Figure 79B). The precipitate was washed with ethanol and the NMR repeated which showed an increase in the intensity of the aldehyde peaks (Figure 79C). The

product was dried under *vacuo* overnight before the NMR spectrum was retaken in dichloromethane (Figure 79D). Appearance of the same peaks confirms that the aldehyde is not formed due to hydrolysis of the ligand in chloroform.

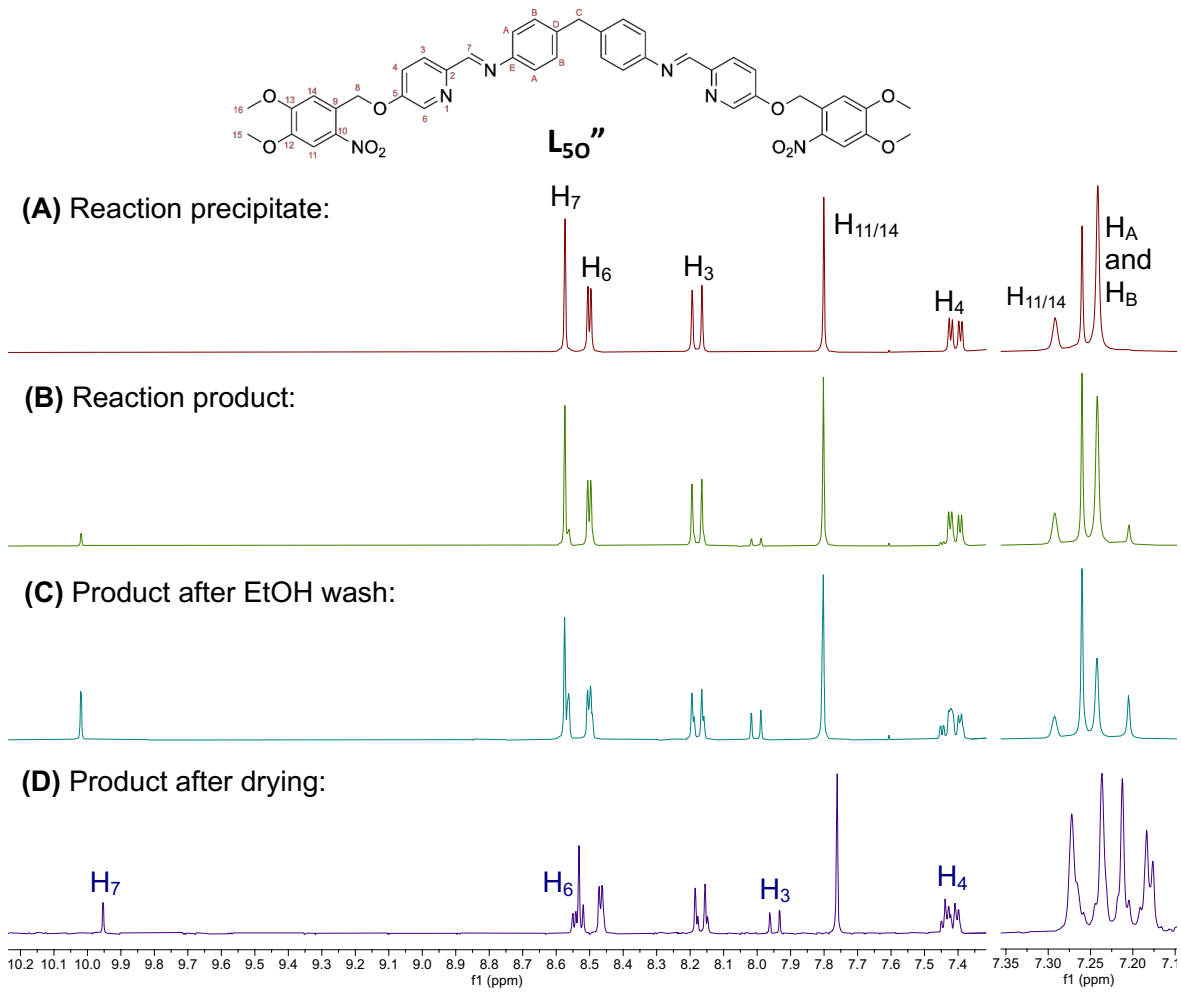

Figure 79: ^{1}H NMR (7.1-10.2 ppm, 300 MHz, Chloroform-d) of the reaction precipitate (A) taken directly from reaction mixture, (B) after reaction work up, (C) after washing with ethanol, and (D) (300 MHz, Methylene Chloride-d2) after drying overnight. The aldehyde peaks are assigned in purple (spectrum D) and the peaks between 7.10-7.35 have been magnified.

The colour change observed during the work up of the ligand may be caused by degradation as side-products were not observed in the reaction mixture precipitate. The appearance of the capped aldehyde suggests that the degradation is due to hydrolysis and not photocleavage of the cap from the ligand. The reaction was

repeated a final time under dark and inert conditions and the work up adapted as far as possible to reduce the exposure of the product to light and air. No colour change in the product was observed while handling and no side products are observed in the ^{1}H NMR spectrum (Figure 80). As with the aldehyde, the COSY NMR was used to distinguish between the benzyl protons (H_{11} and H_{14}).

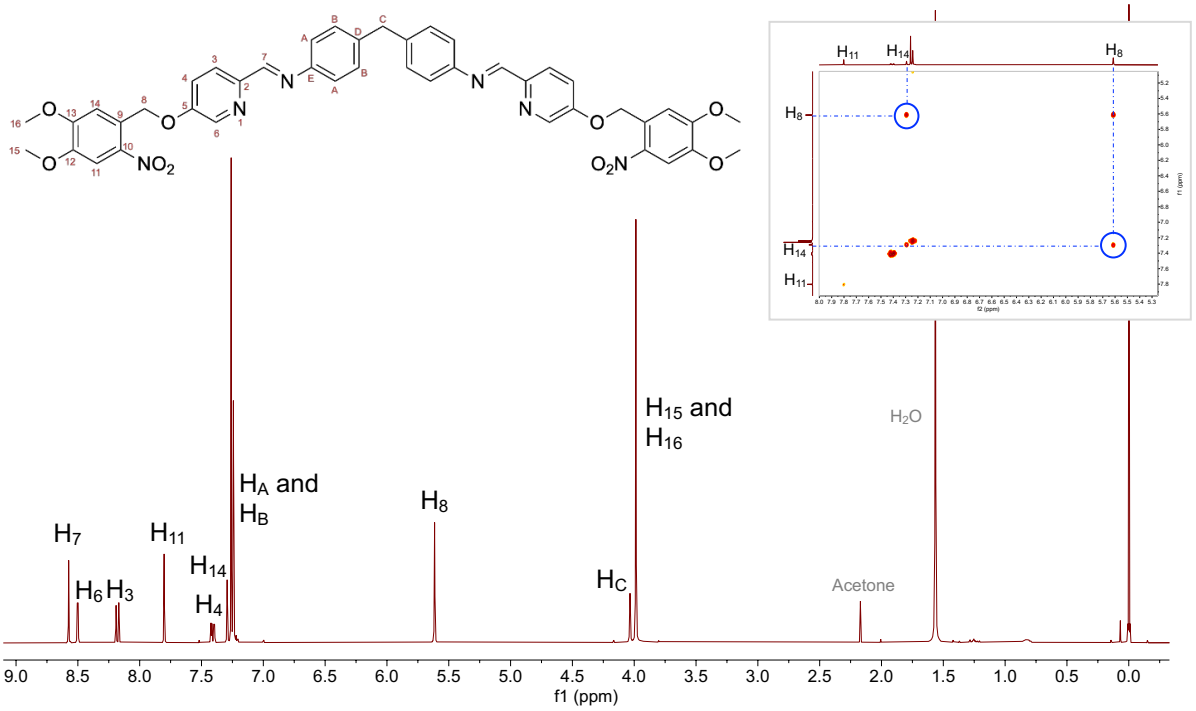

Figure 80: ^{1}H NMR (400 MHz, Chloroform-d) of L_{5O}". Inset: COSY spectrum (5-8 ppm) showing coupling between H_8 and H_{14} (blue circles).

The capped cylinders ($[Fe_2(L_{5O}")_3](PF_6)_4$ and $[Ni_2(L_{5O}")_3](PF_6)_4$) were synthesised by dissolving the capped ligand and desired metal chloride salt in methanol until a clear, coloured solution remains. Unlike the uncapped cylinder, the capped cylinder could be purified by anion exchange with ammonium hexafluorophosphate which was confirmed by the loss of colour from the solution upon isolation of the precipitate. The ^{1}H NMR spectrum of the hexafluorophosphate salt

(Figure 81) shows the broadening of phenyl protons (H_A and H_B), deshielding of the pyridine protons (H_3 and H_4) and shielding of the 6-position proton (H_6) similar to the uncapped cylinder. The protons of the cap (H_{11}, H_{14}, H_{15} and H_{16}) are distant from the metal binding motif so do not show large changes in chemical shift compared to the capped ligand.

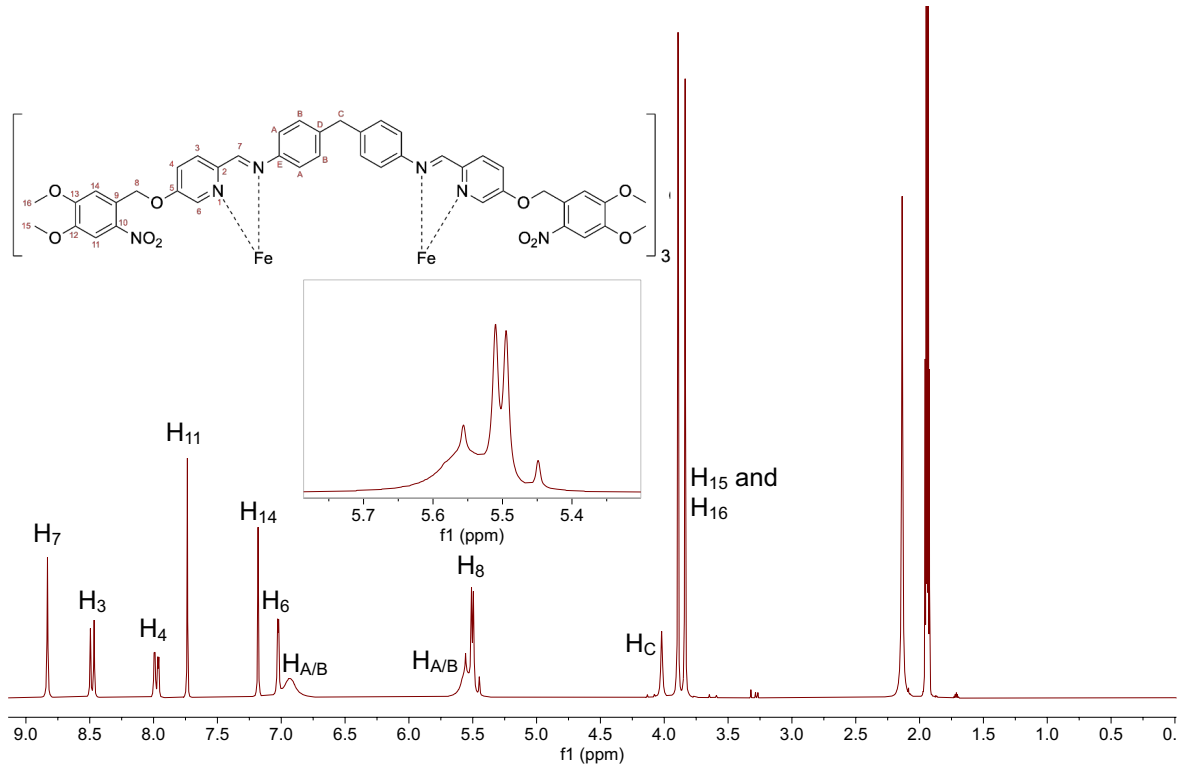

Figure 81: ^{1}H NMR (300 MHz, Acetonitrile-d$_3$) of [Fe$_2$(L$_{5O}$")$_3$](PF$_6$)$_4$. Inset: (5.3-5.8 ppm) highlighting the splitting of H$_8$.

The methyl protons of the cap (H_8) are split into two doublets with roofing angled towards each other. The coupling constant (J = 14 Hz) is characteristic of geminal coupling, suggesting the two protons are held into two different environments which is expected of a chiral helicate. Formation of the cylinder is further supported by the mass spectrum of the dark purple product (627 m/z, $[Fe_2(L_{5O}")_3]^{4+}$).

The formation of the nickel cylinder was followed by mass spectrometry which showed peaks assigned to the helicate (628, 838, and 849 m/z, for $[Ni_2(L_{5O}")_3]^{4+}$, $[Ni_2(L_{5O}")_3 - H]^{3+}$, and $[Ni_2(L_{5O}")_3 + Cl]^{3+}$, respectively) and the 5-capped species ($[Ni_2(L_{5O}")_2(L_{5O}') - H]^{3+}$) after 2.5 hours. The cylinder was extracted from the reaction mixture by anion exchange and the product analysed by mass spectrometry (Figure 82).

The appearance of the 5-capped in both spectra is unexpected as the alkylated aldehyde was purified by column chromatography before carrying forward. This species may be formed during the ionisation process or form due to photocleavage by ambient light. Following the success of a one-pot method for an alternative cylinder design (Chapter 5), the formation of the capped cylinders was also attempted by this method to see if formation of the 5-capped cylinder could be avoided. The capped aldehyde, MDA, and the chosen metal chloride salt were stirred in methanol at room temperature overnight before filtration to remove any unreacted starting materials. The cylinders were purified by anion exchange to a hexafluorophosphate salt and conversion back to a chloride using Dowex resin.

The ^1H NMR spectrum of the paramagnetic nickel cylinder was too broad to interpret. The ^1H NMR spectrum of the iron cylinder was recorded as both a hexafluorophosphate and chloride salt (Figure 83). The spectrum for the hexafluorophosphate salt is very similar to the spectrum recorded from the synthesis of the iron cylinder ($[Fe_2(L_{5O}")_3](PF_6)_4$) from the capped ligand ($L_{5O}"$). The doublet of doublets caused by the methylene bridge to the cap (H_8) become a singlet in the spectrum of the chloride salt, suggesting that the difference in environment felt by these protons is dependent on either the anion or solvent present.

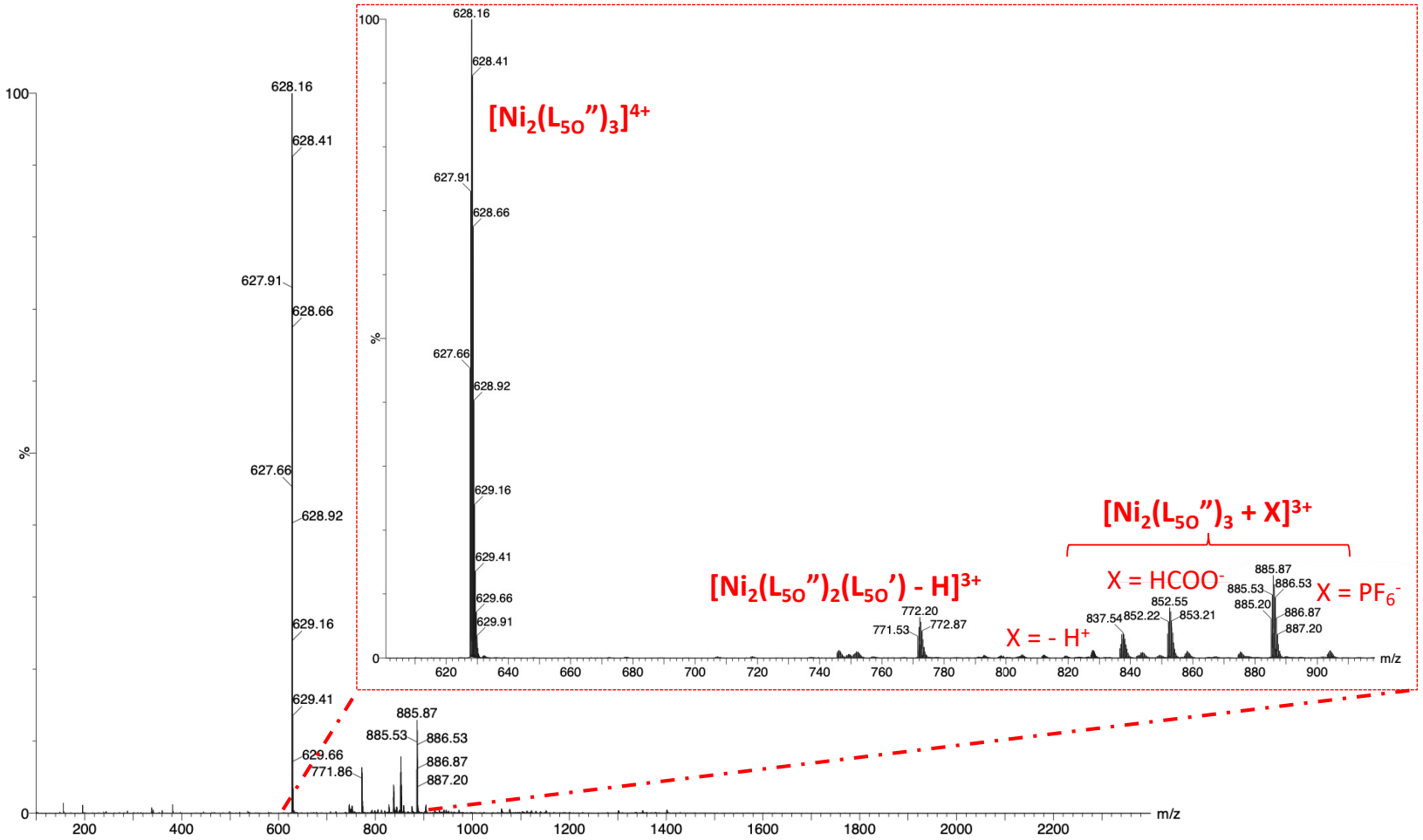

Figure 82: Mass spectrum (TOF ES+, MeCN) of $[Ni_2(L_{5O}")_3](PF_6)_4$.

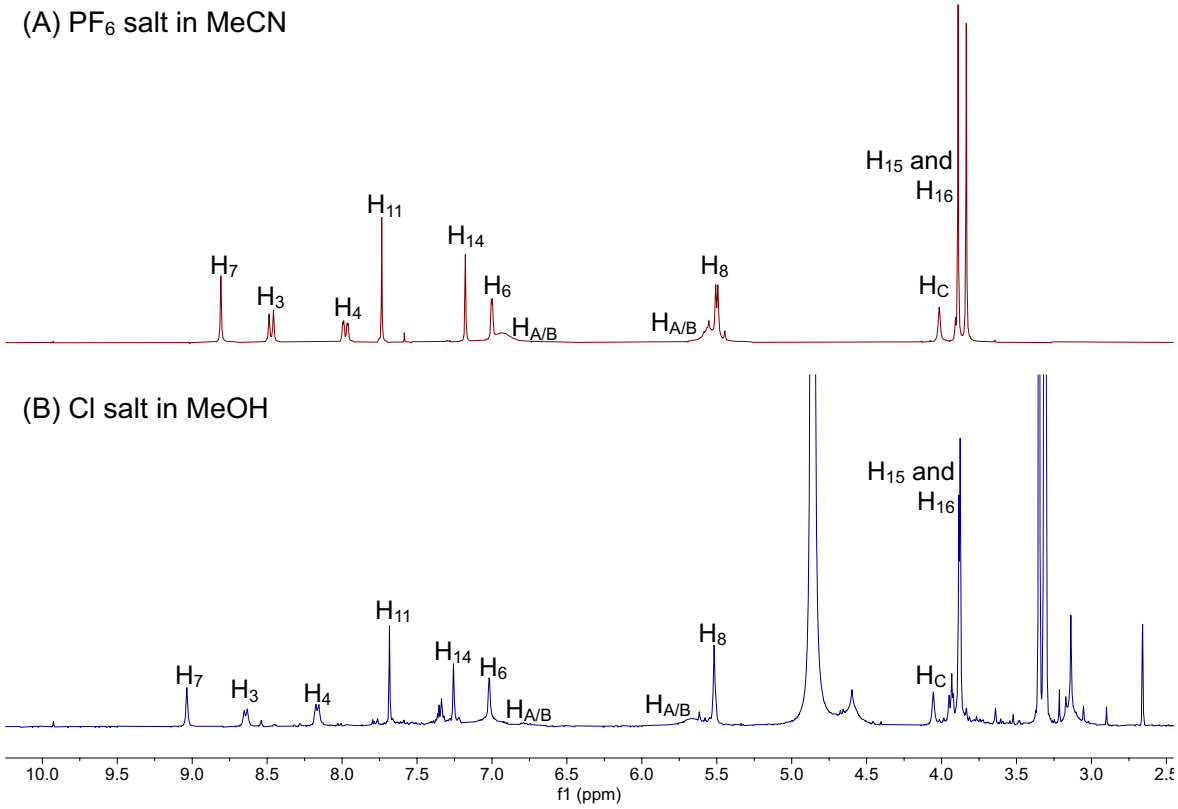

Figure 83: ^{1}H NMR of $[Fe_2(L_{5O}")_3]X_4$ (A) (300 MHz, Acetonitrile-d_3) X = PF_6, and (B) (400 MHz, MeOD) X = Cl.

The mass spectra of the chloride salts (Figure 84) show the fully capped cylinder ($[M_2(L_{5O}")_3]$) is present and a small peak is still observed for the 5-capped species ($[M_2(L_{5O}")_2(L_{5O}') - H]^{3+}$) as seen with the previous method.

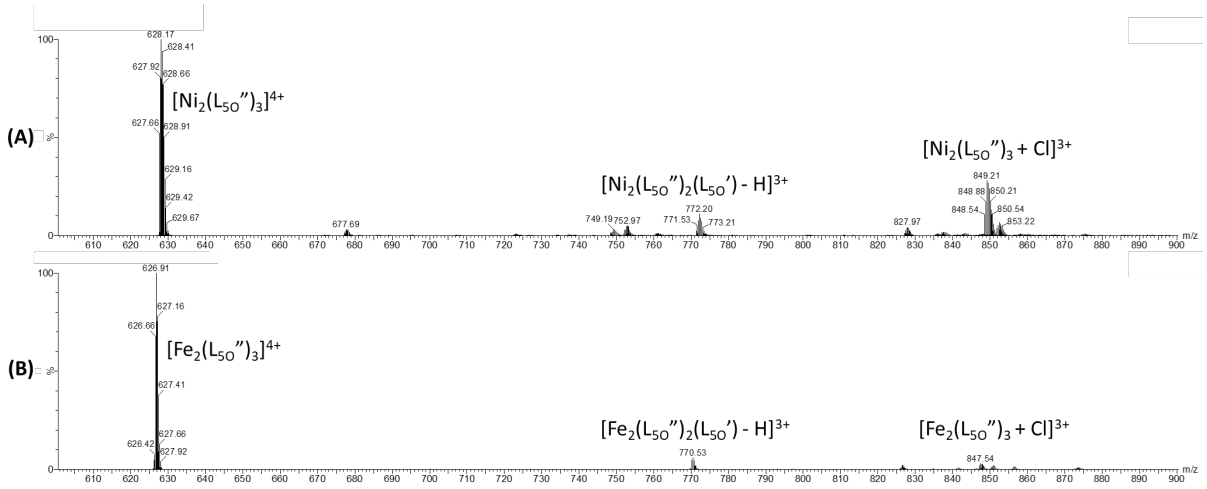

Figure 84: Mass spectrum (TOF ES+, MeOH) of (A) $[Ni_2(L_{5O}")_3]Cl_4$, and (B) $[Fe_2(L_{5O}")_3]Cl_4$.

The fully capped cylinders were successfully synthesized by two main methods, through the capped ligand (L_{5O}") and directly from the capped aldehyde (Ald_{5O}'). Both synthetic methods require the synthesis of the capped aldehyde which was purified from the uncapped aldehyde by silica gel column chromatography. The presence of uncapped species could therefore be due to light exposure during the synthesis process, which would be reduced by using completely dark conditions, and could indicate an increased reactivity of the cylinder towards light exposure compared to the previous design.

4.5. 5-oxypyridine based rotaxanes ($[M_2(L_{5O}")_3.CB10]Cl_4$)

Successful synthesis of both the uncapped ($[M_2(L_{5OH})_3]Cl_4$) and capped ($[M_2(L_{5OH})_3]Cl_4$) cylinders means both the capping and slipping mechanism are available for rotaxane formation (Figure 85). The slipping mechanism was preferred for the imidazole-based system as the rotaxane could be isolated with a higher purity through gentle heating under aqueous conditions, so the slipping mechanism was attempted first.

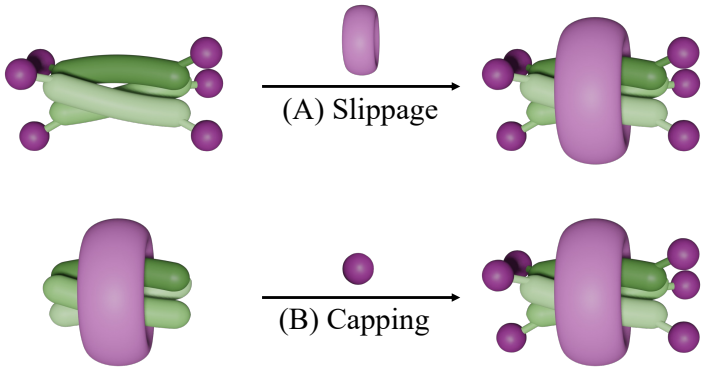

Figure 85: The slipping (A) and capping (B) mechanisms for rotaxane formation.

The iron capped cylinder ($[Fe_2(L_{5O}")_3]Cl_4$) was suspended in 20% deuterated methanol in deuterium oxide. The low methanol percentage helps the inorganic helicate to dissolved without disrupting the hydrophobic bonding between the metal complex and the macrocycle.

Deuterated methanol was used to dissolve the iron capped cylinder ($[Fe_2(L_{5O}")_3]Cl_4$) before dilution with deuterium oxide to encourage the hydrophobic bonding between the macrocycle and helicate. Solutions were stirred at both room temperature and 50°C and the ^1H NMR of each solution was recorded after 4 hours (Figure 86). Three additional peaks in each spectrum are assigned to CB10 due to their equal integrations which are 3.33 times the integration of the cylinder peaks confirming a one-to-one binding ratio of the cylinder to macrocycle. The cylinder protons have not shown a large change in splitting pattern compared to the cylinder alone or been separated into separate environments which implies that the rotaxane species retains the same symmetry. This is only possible for a one-to-one complex if the cylinder lies in the centre of the macrocyclic ring. The central methylene group and one of the phenyl protons (H_C and $H_{A//B}$, respectively) also show an upfield shift characteristic of encapsulation by CB10. The imine and the pyridine proton in the 3-

position (H_C and H_3, respectively) are deshielded as these protons point towards the carbonyl lined portals.

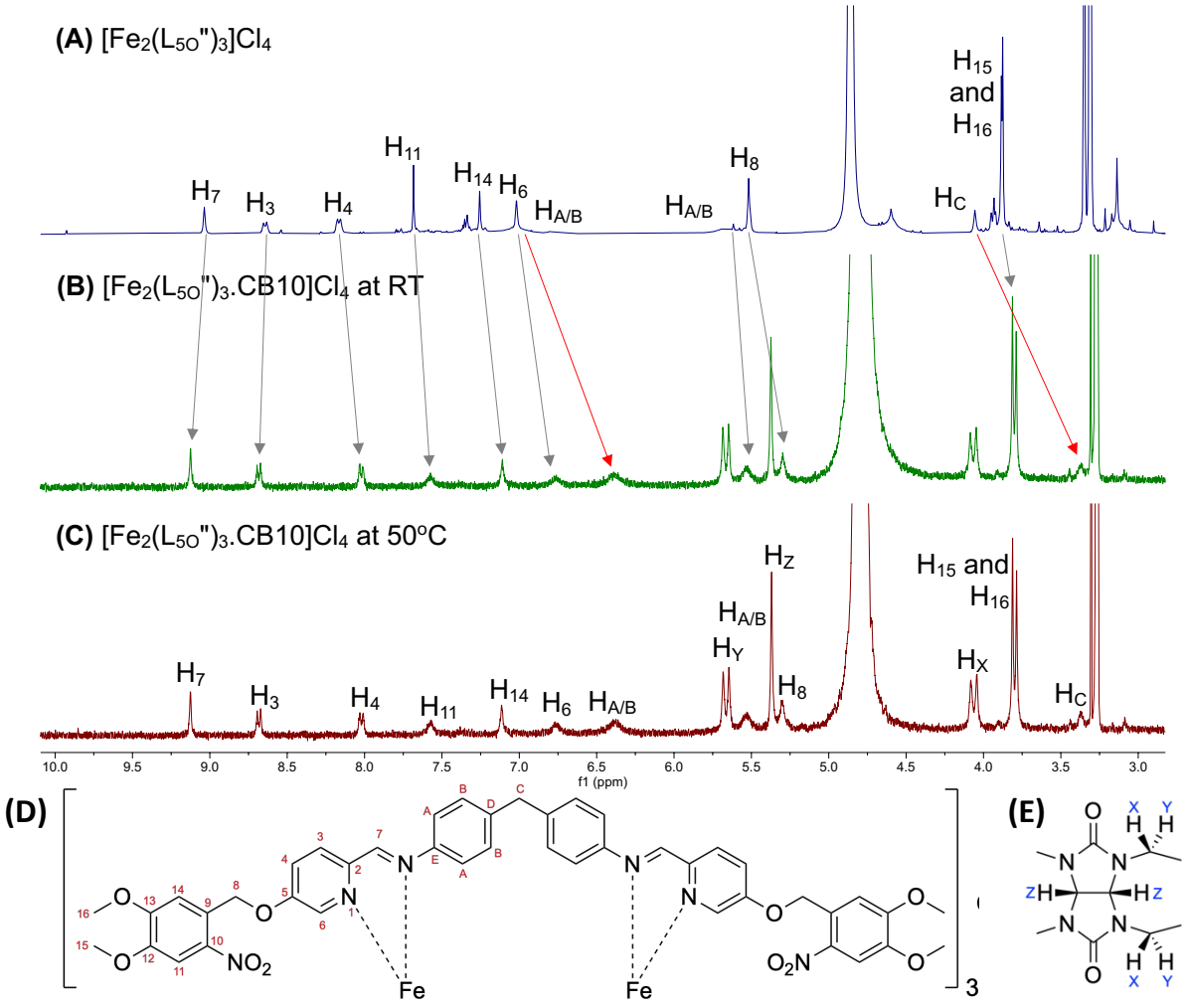

Figure 86: ^{1}H NMR (400 MHz) of (A) [Fe$_2$(L$_{5O}$")$_3$]Cl$_4$ in methanol-d$_4$, and [Fe$_2$(L$_{5O}$")$_3$.CB10]Cl$_4$ in 20% methanol-d$_4$ in deuterium oxide at (B) RT and (C) 50°C. Structures of reagents (D) [Fe$_2$(L$_{5O}$")$_3$]Cl$_4$ and (E) CB10 are shown below.

The formation of the one-to-one complex at room temperature implies that this structure is a *pseudo*rotaxane as no heat is required to overcome a steric barrier and is driven by the hydrophobic interaction between the cylinder and macrocycle. The reaction was repeated at 50°C when scaling up with both the iron and nickel capped cylinders to ensure that there would be no barrier to rotaxane formation.

The peak with the highest relative abundance in the mass spectra of both products is the 4+ charged rotaxane species (Figure 87 and Figure 88). In the iron spectrum there is a small peak for the 5-capped species (993 m/z, $[Fe_2(L_{5O}")_2(L_{5O}').CB10]^{4+}$) and the same species having lost an oxygen atom (990 m/z, $[Fe_2(L_{5O}")_2(L_{5OH}).CB10 - O]^{4+}$). It is possible that this species is formed by the loss of a terminal alcohol group, however it is unclear whether this would have occurred during the synthesis or ionisation of the cylinder. The nickel equivalent shows a larger variety of metal complex species including the 5-capped half ligand containing species (968 m/z, $[Fe_2(L_{5O}")_2(hL_{5O}').CB10]^{4+}$), the two metal, two ligand species (844 m/z, $[Ni_2(L_{5O}")_2.CB10]^{4+}$), and some larger species (m/z > 1300).

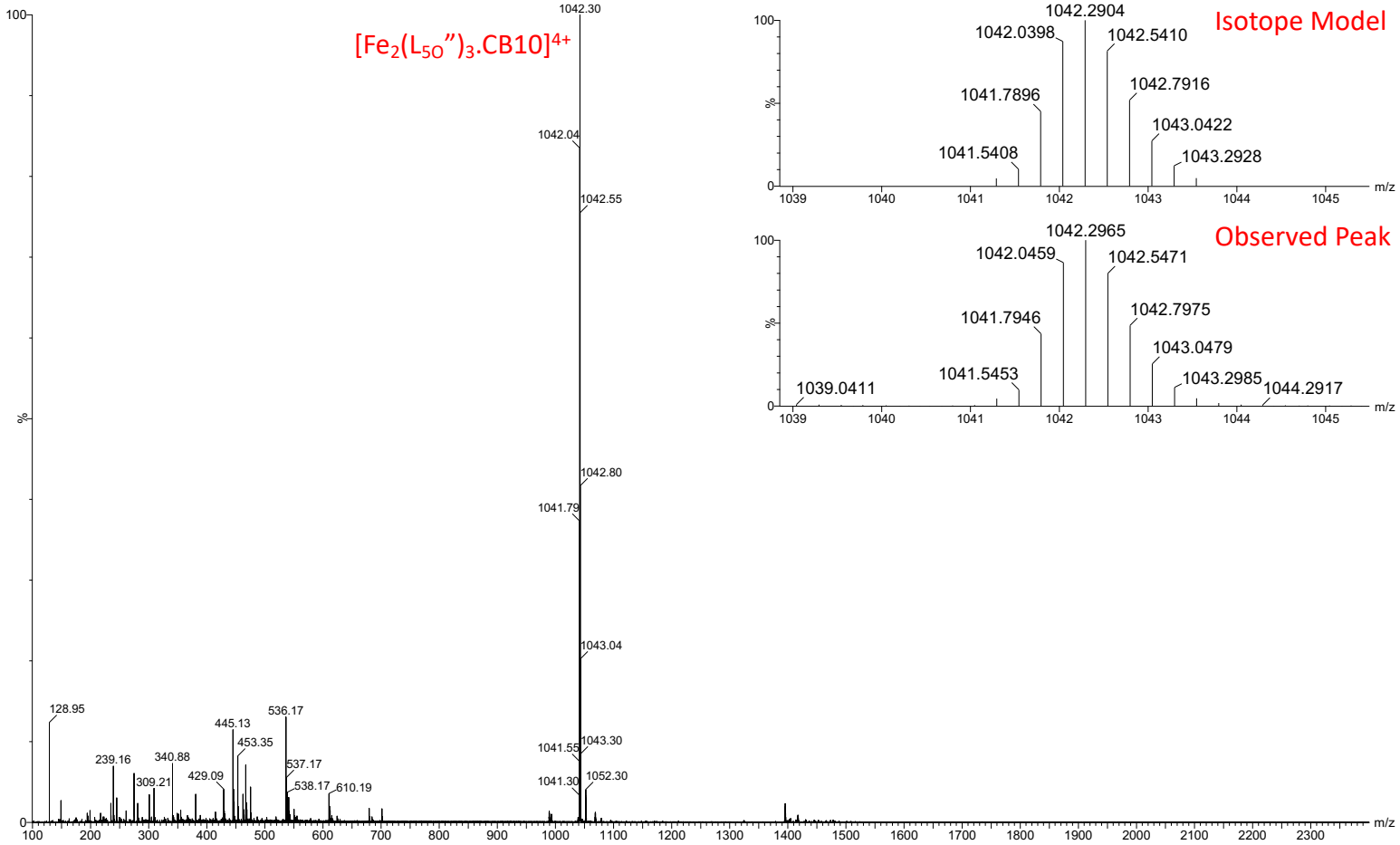

Figure 87: Mass spectrum (TOF ES+, H_2O) of $[Fe_2(L_{5O}")_3.CB10]Cl_4$. Inset: Comparison to the predicted isotope pattern.

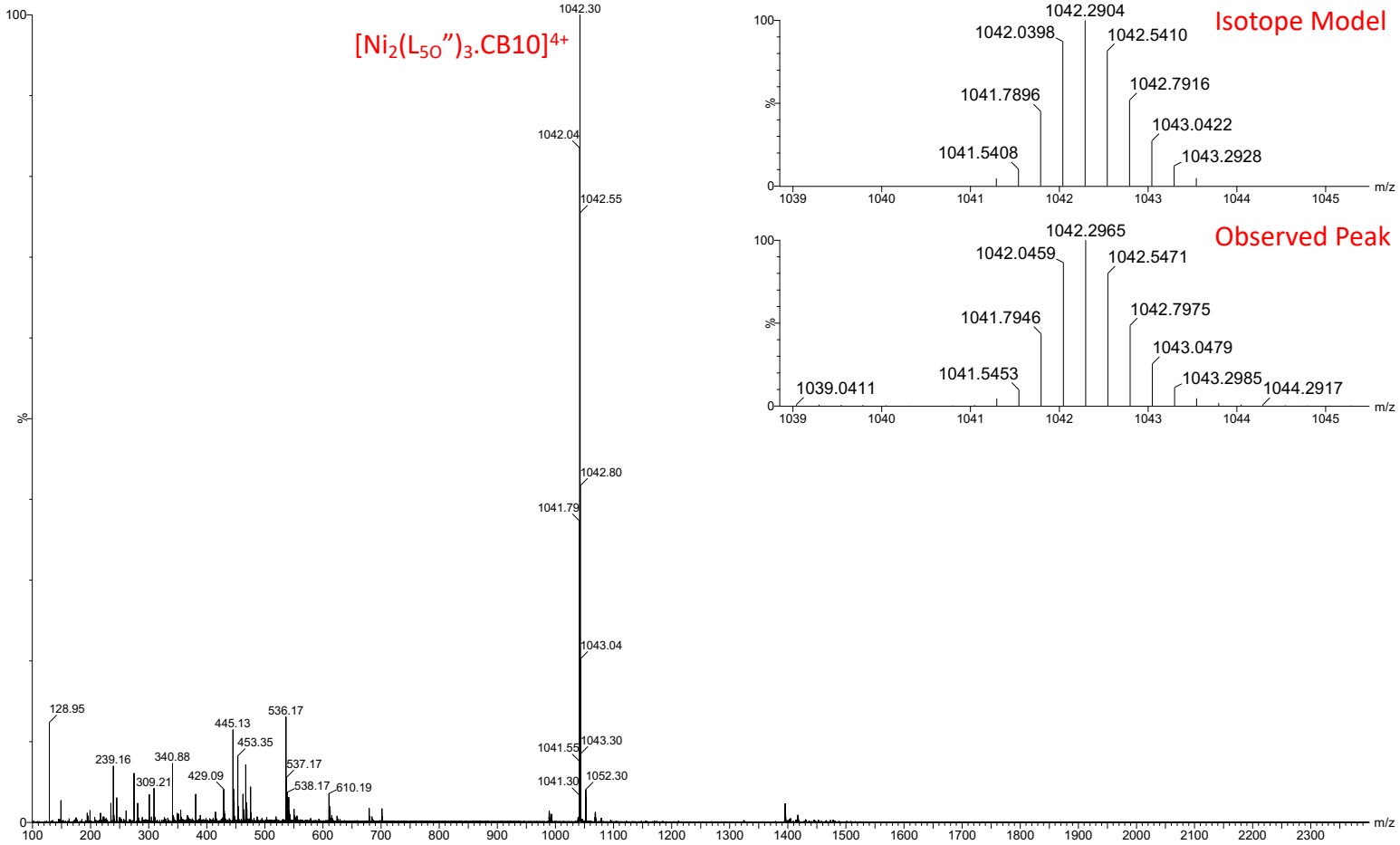

Figure 88: Mass spectrum (TOF ES+, H_2O) of $[Ni_2(L_{5O}")_3.CB10]Cl_4$. Inset: Comparison to the predicted isotope pattern.

4.6. Conclusions

In summary, both the iron and the nickel capped cylinders have been successfully complexed with CB10 via the slippage mechanism. These complexes will be referred to as rotaxanes for the remaining analysis although the CB10 ring is thermally, and not mechanically, locked in place. Initial evidence also suggests that this complex could be formed at room temperature, in which case the structure could more accurately be referred to as a *pseudo*rotaxane, however the room temperature reaction was never repeated on a larger scale to isolate a product for further analysis.

4.7. List of References

1 S. Swaminathan, M. Petriella, E. Deniz, J. Cusido, J. D. Baker, M. L. Bossi and F. M. Raymo, *J. Phys. Chem. A*, 2012, **116**, 9928–9933.

2 S. Shaban Ragab, S. Swaminathan, E. Deniz, B. Captain and F. M. Raymo, *Org. Lett.*, 2013, **15**, 3154–3157.

3 J. Malina, M. J. Hannon and V. Brabec, *Chem. Eur. J.*, 2007, **13**, 3871–3877.

4 A. Oleksy, A. G. Blanco, R. Boer, I. Usón, J. Aymamí, A. Rodger, M. J. Hannon and M. Coll, *Angew. Chem. Int. Ed.*, 2006, **45**, 1227–1231.

5 L. Cerasino, M. J. Hannon and E. Sletten, *Inorg. Chem.*, 2007, **46**, 6245–6251.

6 C. A. J. Hooper, L. Cardo, J. S. Craig, L. Melidis, A. Garai, R. T. Egan, V. Sadovnikova, F. Burkert, L. Male, N. J. Hodges, D. F. Browning, R. Rosas, F. Liu, F. V. Rocha, M. A. Lima, S. Liu, D. Bardelang and M. J. Hannon, *J. Am. Chem. Soc.*, 2020, **142**, 20651–20660.

7 A. Lavalette, F. Tuna, G. Clarkson, N. W. Alcock and M. J. Hannon, *Chem. Commun.*, 2003, 2666–2667.

8 P. Iqbal, M. Mayanditheuar, L. J. Childs, M. J. Hannon, N. Spencer, P. R. Ashton and J. A. Preece, *Materials*, 2009, **2**, 146–168.

9 G. I. Pascu, PhD Thesis, University of Birmingham, 2008.

10 C. D. J. Campbell, PhD Thesis, University of Birmingham, 2019.

11 A. Lavalette, J. Hamblin, A. Marsh, D. M. Haddleton and M. J. Hannon, *Chem. Commun.*, 2002, 3040–3041.

12 Sigma-Aldrich Products: 2,5-Pyridinedicarboxylic acid, https://www.sigmaaldrich.com/GB/en/product/aldrich/p63603, (accessed January 2024).

13 Sigma-Aldrich Products: 2,5-dibromopyrimidine, https://www.sigmaaldrich.com/GB/en/product/aldrich/740381, (accessed January 2024).

14 P. G. Avaji, C. H. Vinod Kumar, S. A. Patil, K. N. Shivananda and C. Nagaraju, *Eur. J. Med. Chem.*, 2009, **44**, 3552–3559.

15 J. J. P. Kramer, M. Nieger and S. Bräse, *Eur. J. Org. Chem.*, 2013, **2013**, 541–549.

16 M. J. Hannon, C. L. Painting, A. Jackson, J. Hamblin and W. Errington, *Chem. Commun.*, 1997, 1807–1808.

17 A. Alouane, R. Labruère, K. J. Silvestre, T. Le Saux, F. Schmidt and L. Jullien, *Chem. Asian J.*, 2014, **9**, 1334–1340.

5. 3- AND 4-OXYPYRIDINE BASED CYLINDERS

5.1. Alternative Cylinder Designs

The 5-oxypyridine based rotaxane ($[M_2(L_{5OH})_3]Cl_4$) detailed in Chapter 3 was shown to form at room temperature by slipping, suggesting that the product is a *pseudo*rotaxane. The capping groups in this design are positioned along the metal-metal axis which may increase the steric barrier to cylinder release, but a larger steric barrier is required to mechanically lock the macrocycle in place. For a classical rotaxane this would require a change of capping group, but for the supramolecular rotaxane the combined steric bulk of multiple capping groups is utilised and changing their relative position may therefore increase the barrier for release of the macrocycle. The 4-hydroxypyridine based systems investigated in this chapter move the caps to a position at a larger angle to metal-metal axis (Figure 89). This design aims to increase the combined steric bulk of the capping groups while maintaining their photoactivity and the 3WJ binding motif provided by the cylinder.

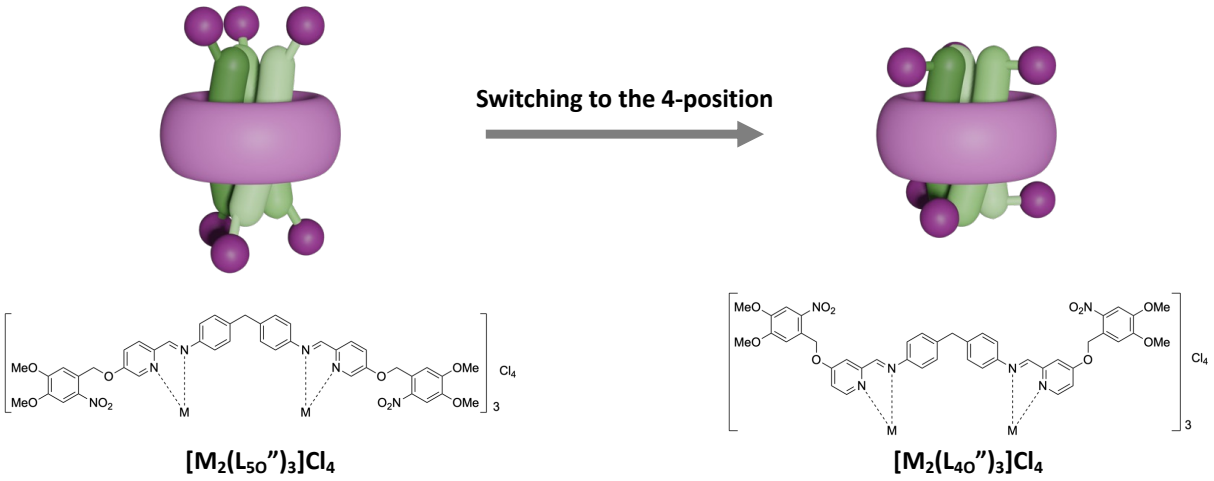

Figure 89: The change in rotaxane structure when capping in the 4-position.

An alternative design of cylinder is considered by placing the capping groups in the 3-position of the pyridine ring as the capping groups are directed back towards the centre of the cylinder and may hinder the 3WJ recognition site at the cylinder core (Figure 90). Prevention of 3WJ formation may therefore be achieved without the use of a macrocyclic ring making the structure reminiscent of a photo-protected pro-drug, as the activity of the cylinder is prevented in the presence of photocleavable group.

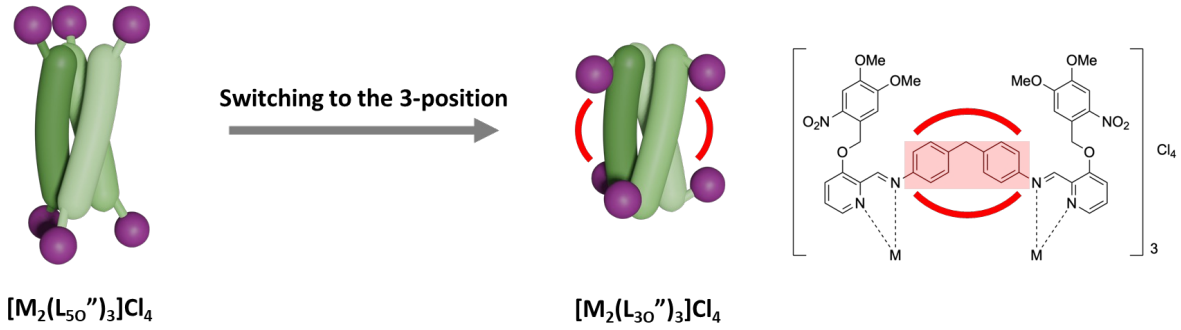

Figure 90: The change in cylinder structure when capping in the 3-position.

5.2. Synthesis of 4-hydroxypicolinaldehyde (Ald_{4OH})

Capping in the 4-position of the pyridine ring requires the 4-hydroxypicolinaldehyde, which was synthesised following a procedure published by A. Lumetzberger *et al*[1]. The reported synthesis (Scheme 6) starts from chelidonic acid, a pyrone with two carboxylic acid groups. Esterification of one of the acid groups (a, 74% yield) followed by removal of the other (b, 25% yield) produced the desired ethyl 4-oxo-4H-2-pyran-carboxylate. The low yielding removal of the unreacted carboxylic acid can be avoided by replacing the starting material with comanic acid (Scheme 7), which has

the same structure as chelidonic acid but does not possess the second carboxylic acid group.

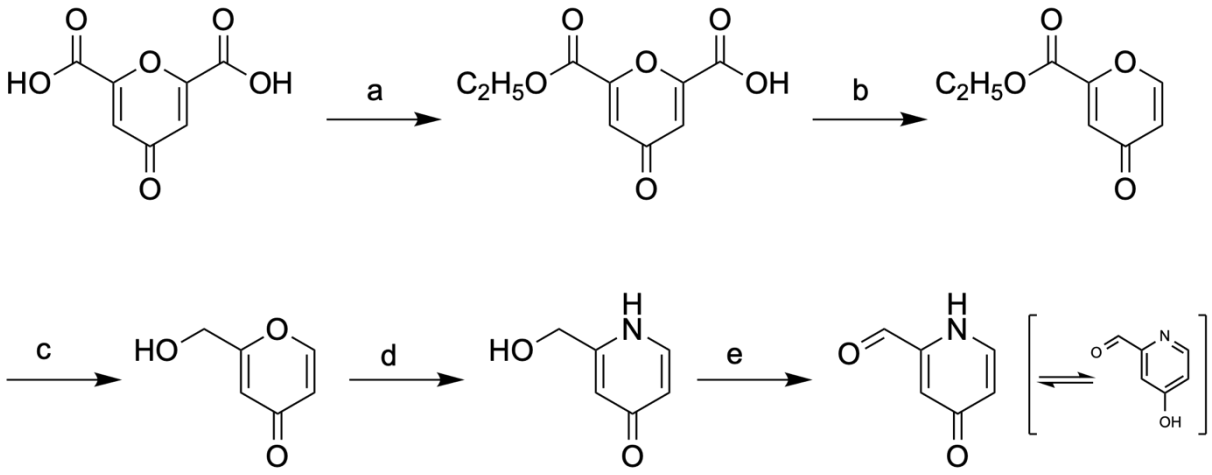

Scheme 6: Synthetic steps towards 4-hydroxypicolinaldehyde as detailed by A. Lumetzberger et al[1].

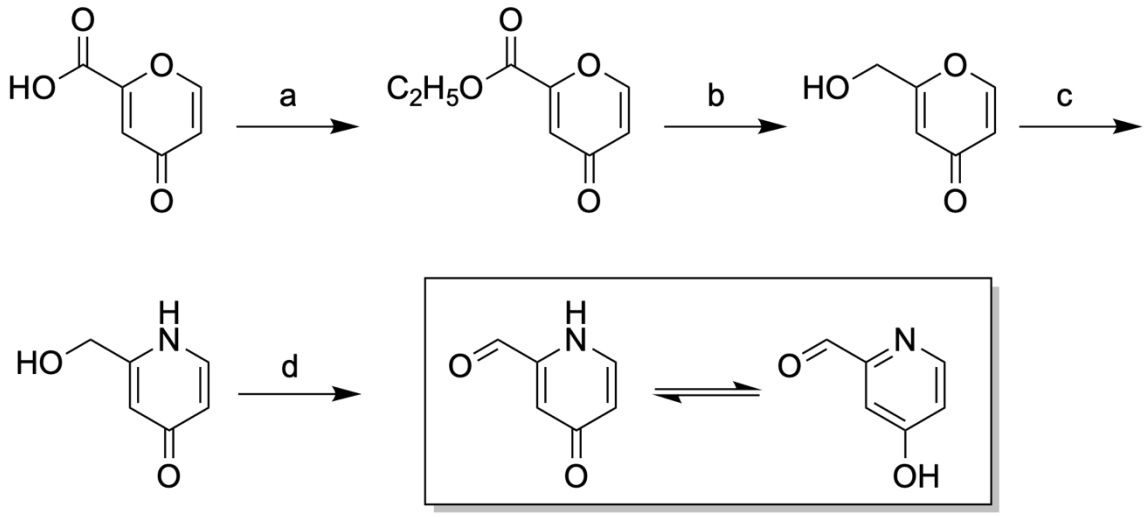

Scheme 7: Proposed synthesis of 4-hydroxypicolinaldehyde from comanic acid, modified from the method used by A. Lumetzberger et al.[1]*. Synthetic details: (a) 5% ethanolic sulphuric acid, 80°C, 20.5 hours; (b) $NaBH_4$, MeOH, -10°C, 2.5 hours; (c) NH_4CO_3, NH_3 aq., reflux, 90 mins; (d) MgO_2, MeOH, acetone, DCM, 60°C, 4 hours.*

Comanic acid is directly converted to the ethyl 4-oxo-4H-2-pyran-carboxylate by acid-catalysed esterification. An initial attempt in 5% ethanolic hydrochloric acid was

unsuccessful, so sulphuric acid was used as it has a lower water content. The reaction time was increased and the product extracted with ether to give an increased yield (58%) after column chromatography compared to the reported two-step process (19% total yield). The ^{1}H NMR spectrum of the product (Figure 91) matches the reported chemical shifts.

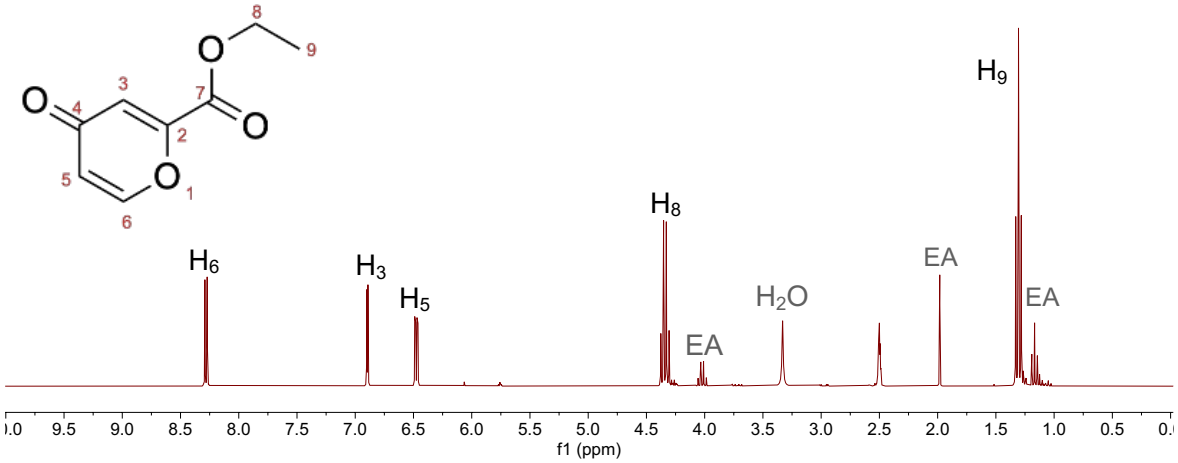

Figure 91: ^{1}H NMR (300 MHz, DMSO-d_6) of ethyl 4-oxo-4H-pyran-2-carboxylate.

The reaction scale was increased to account for lower yields in later steps of the synthesis protocol, however the column could not be scaled up due to the poor solubility of the crude product. The solvent system was changed to lower the retention factor of the product spot from 0.8 to 0.4 to make the product suitable for dry loading which increased the capacity of the column. A final yield of around 43% was achieved via this method on a scale 12 times less than the reported procedure[1]. Increasing the scale (from 0.014 mol to 0.071 mol) caused a decrease in yield (from 58% to 38%) so on a large scale the reported procedure may be preferred as although the yield is lower than achieved here (19% total yield), the scale of the reported reaction was much greater (6.45 mol).

The remaining synthetic steps were followed as reported with alterations made to the work up where necessary. The ester is reduced to an alcohol using sodium borohydride and purified by silica gel column chromatography before recrystallisation with ethanol and petroleum ether. The ^{1}H NMR spectrum of the product (Figure 92) matches the reported chemical shifts, however recrystallisation caused a 43% loss in yield and was deemed unnecessary for repeats of the reaction by recording the NMR spectrum before recrystallisation.

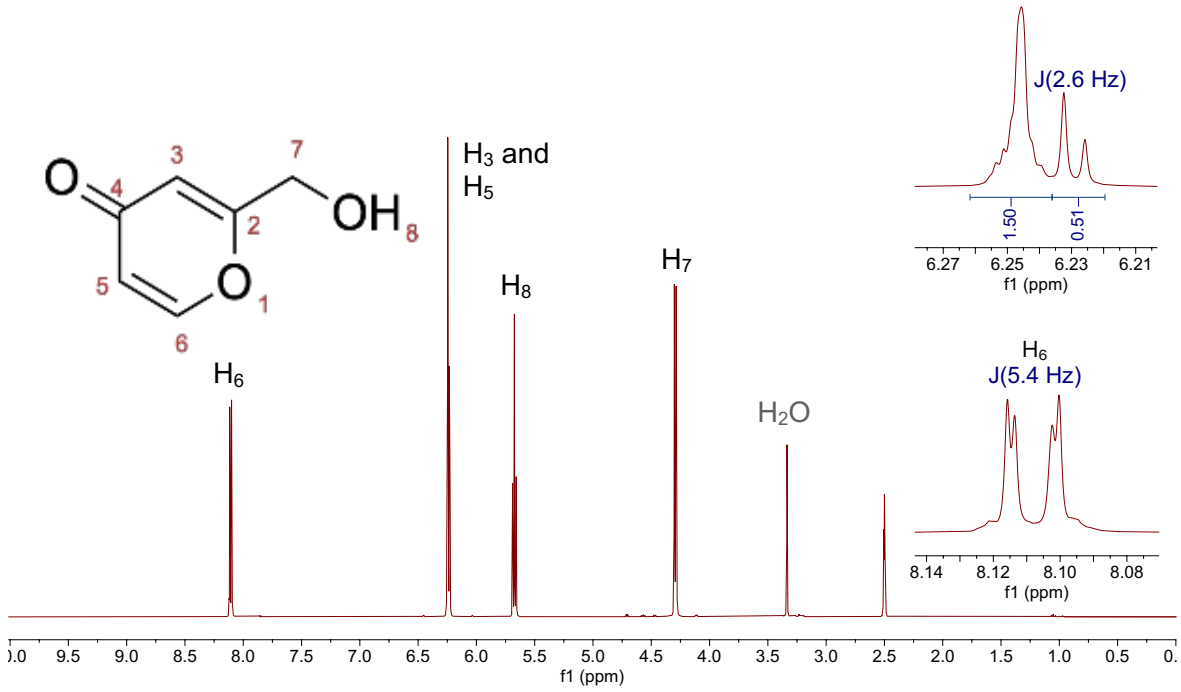

Figure 92: ^{1}H NMR (400 MHz, DMSO-d_6) of 2-hydroxymethyl-4H-pyran-4-one. Inset: The splitting pattern of the multiplets at 6.24 ppm (top) and 8.11 ppm (bottom) with manually measured J-values.

The pyrone ring is converted to pyridone via an addition of nucleophile, ring opening and ring closure, or ANRORC, mechanism (Figure 93)[2]. 2-hydroxymethyl-4H-pyran-4-one was dissolved in aqueous ammonium carbonate and ammonia solution and heated to reflux. Following the reported procedure[1] the reaction was stopped and

the pH adjusted. Removal of organic impurities was attempted by washing with 10% ethanol in ethyl acetate, followed by reflux of the concentrated aqueous layer with ethanol to isolate an organic layer. The final product was then recrystallised from ethanol.

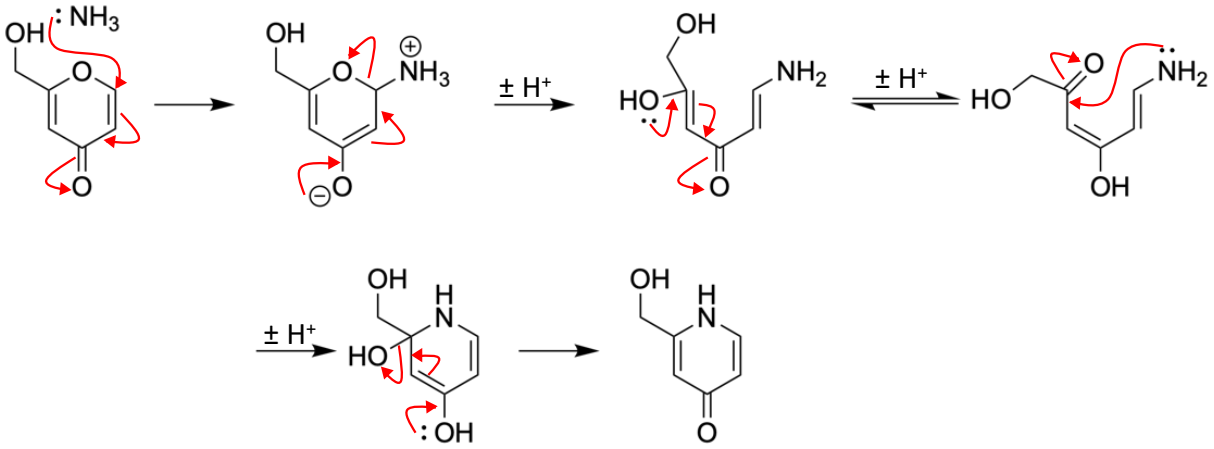

Figure 93: Proposed mechanism for the conversion of the pyrone to the pyridone ring[2].

This procedure was successfully followed on a small scale (2 mmol) to produce an off-white solid (0.3 mmol) with a 15% yield (compared to the 66% reported yield for 15.8 mmol scale)[1]. The exchange of the oxygen atom for nitrogen was confirmed by mass spectrometry (124 m/z, $[M - H]^-$). The ^1H NMR spectrum of the precipitate and filtrate of the recrystallisation were almost identical (Figure 94) so the products were recombined to maximise the amount of material for the final stage of the synthesis, increasing the yield to 26%.

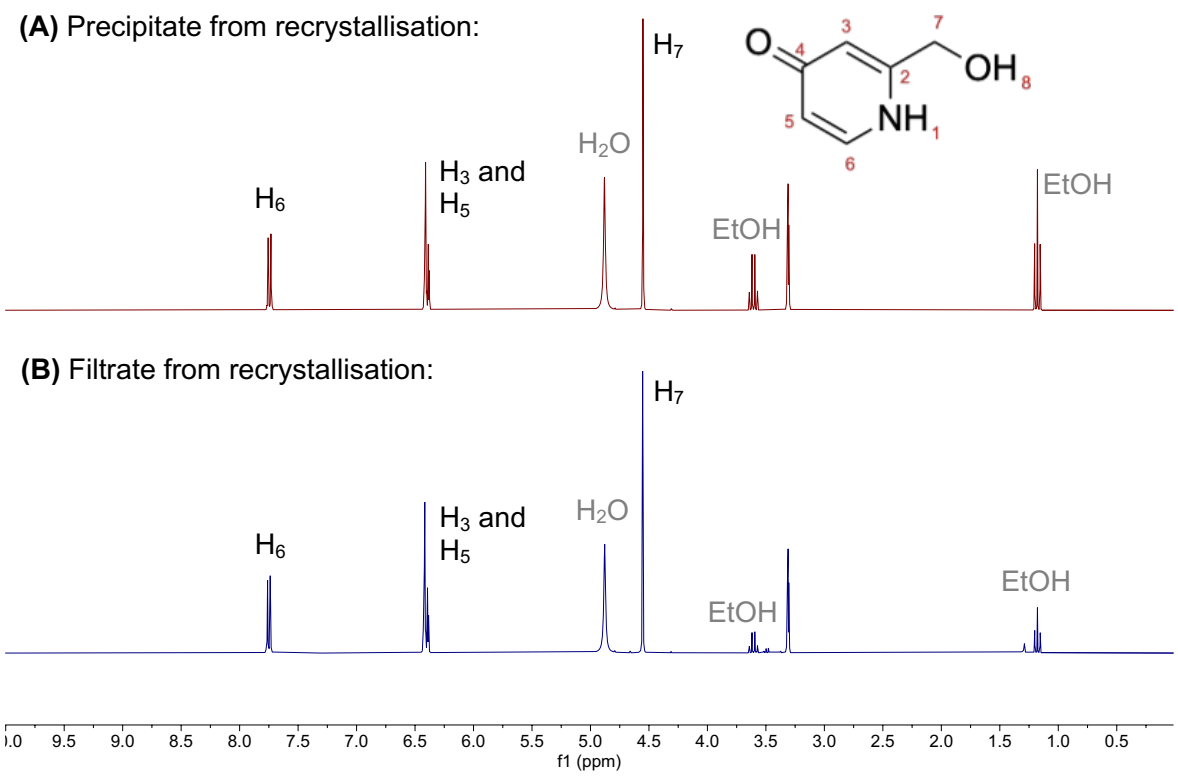

Figure 94: ^{1}H NMR (300 MHz, Methanol-d_4) of the recrystallisation (A) precipitate and (B) filtrate.

The final reflux in ethanol failed to separate into layers upon scaling up the reaction, which may be because the salt content was not high enough to promote separation. This step is required to remove the ammonium sulphate produced when the pH is adjusted, so the crude product was dissolved in water and washed with multiple organic solvents to extract the organic product. Filtration through Celite and recrystallisation from ethanol were also attempted but all methods were unsuccessful or caused a decrease in yield.

The reaction was repeated at a similar scale to the reported method[1] and the crude product purified by trituration with hot ethanol. The residue from the combined filtrates was recrystallised from ethanol and characterised by ^{1}H NMR (Figure 95)

which gave a broader spectrum than the small scale reaction but matched the reported chemical shifts[1].

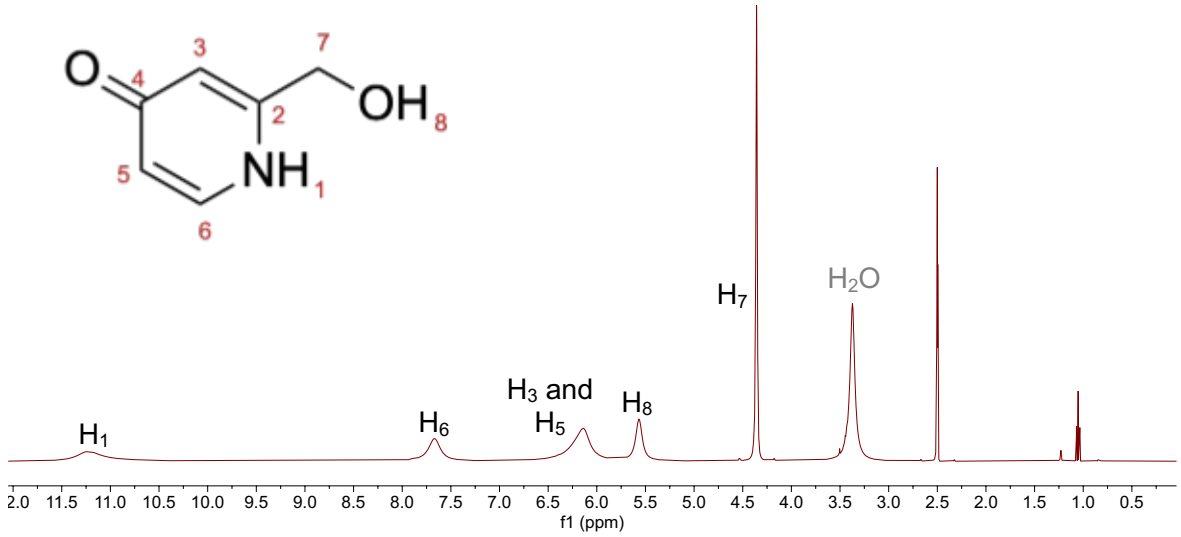

Figure 95: ^{1}H NMR (400 MHz, DMSO-d_6) of 2-(hydroxymethyl)pyridine-4(1H)-one.

The alcohol is oxidised to an aldehyde using manganese dioxide. Purification of the desired product was achieved by column chromatography with ethyl acetate giving a 30% yield (0.6 mmol reaction). The crude product was insoluble in ethyl acetate so was loaded on to the column in methanol which increased the solubility of the product in the mobile phase. In later, larger scale reactions (4 mmol) the first fraction was eluted with ethyl acetate before the methanol content was increase to 10% causing the elution of a yellow and red-brown band. The second fraction (a yellow band) was identified as the product by ^{1}H NMR (Figure 96) but was only isolated in a 11% yield.

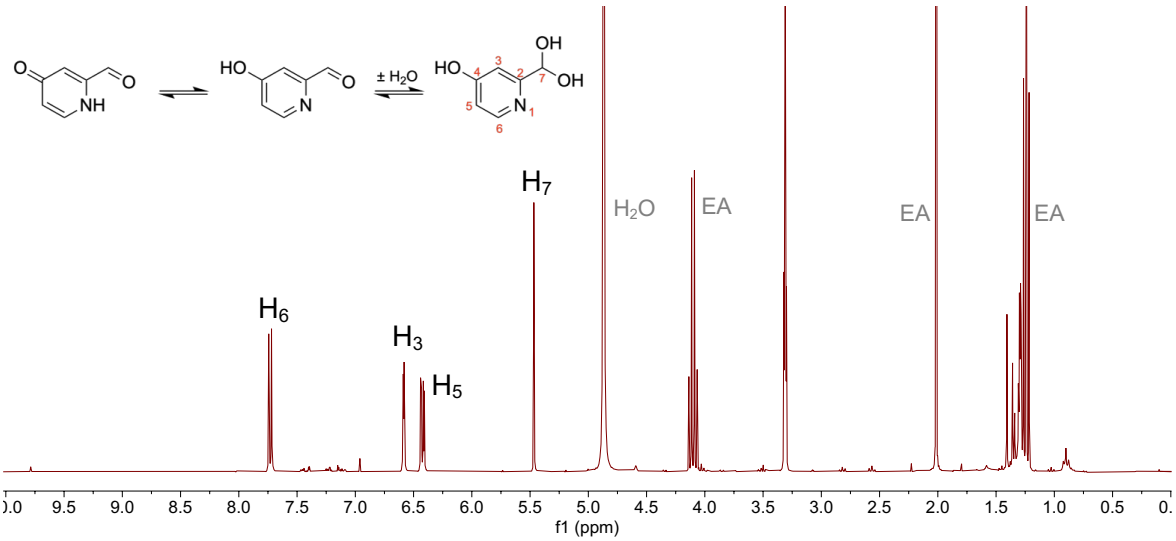

Figure 96: ^{1}H NMR (300 MHz, Methanol-d4) of 4-hydroxypicolinaldehyde.

The low yield may have been caused by hydrogen bonding to the silica column so alternative purification methods were considered. Trituration with both ethanol and DCM were unsuccessful because product was either poorly soluble (DCM) or other impurities were too soluble. One of these impurities was identified as the starting material by TLC which is very similar to the product meaning separation of the two would be difficult. Oxidation with manganese dioxide was repeated to remove the starting material from the crude mixture and increase the yield. By TLC the intensity of the spot for the starting material (R_f = 0.07) decreased while another spot (R_f = 0.47) increased in intensity. The product spot (R_f = 0.16) remained intense throughout the experiment making any changes difficult to see.

Recrystallisation of the crude from ethanol and ethyl acetate were unsuccessful. The crude was dissolved in methanol and added to excess ethyl acetate before filtering out any solid precipitate after it was noticed that an impurity did not move after TLC with 10% methanol in ethyl acetate. The solvent was removed from the filtrate to leave an oily brown solid and the amount of material to purify was successfully reduced by

52%. A shorter silica column was attempted as a final purification method. The crude (0.5 g) was loaded with methanol and run with ethyl acetate, however, only 38 mg of the product could be isolated. The ^{1}H NMR spectra of the crude and purified products show peaks of similar chemical shift, so the product is expected to be a major fraction of the crude and the low yield due to the purification method (Figure 97).

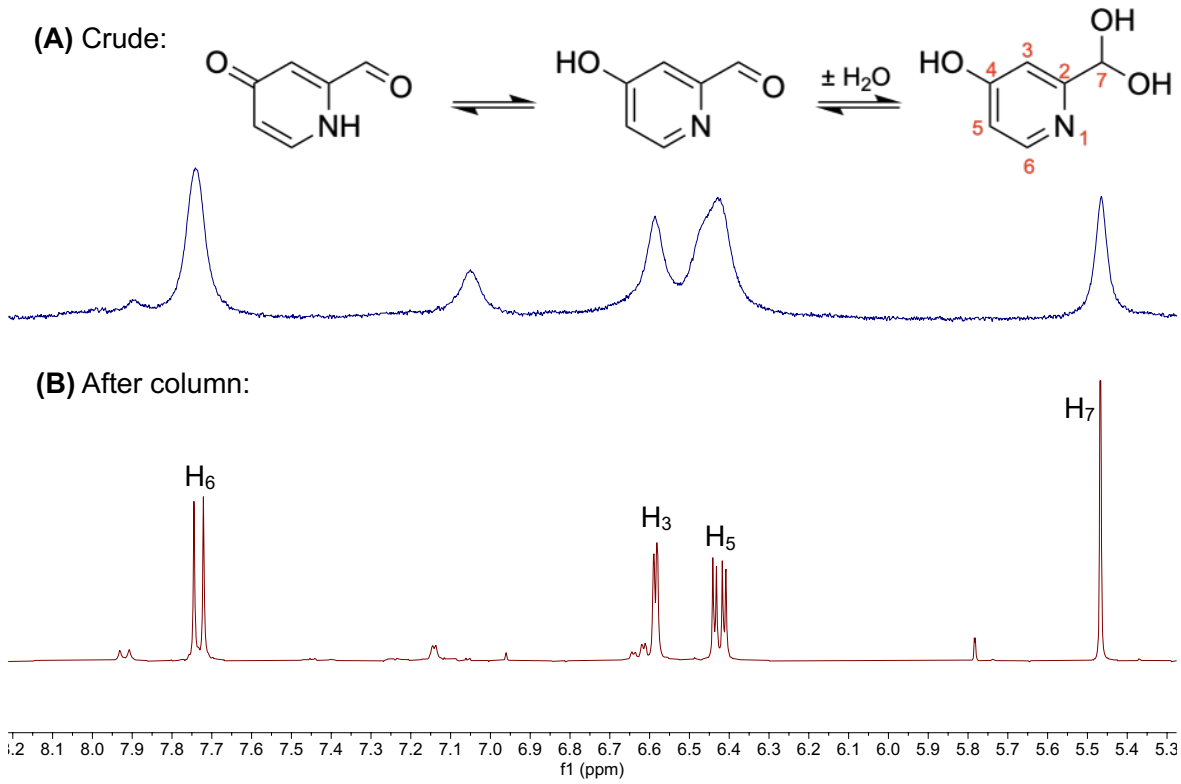

Figure 97: ^{1}H NMR (300 MHz, Methanol-d4) of the (A) crude product after second oxidation, and (B) purified product after column.

This final reaction step is reported with a high yield (71%), however this does not match the reported mass of the starting material and product (1.3 g, 10.4 mmol and 87.3 mg, 0.7 mmol respectively) which imply only a 7% yield, confirming that the product is difficult to purify.

It was concluded that the reaction scheme is successful but does not produce a great enough quantity to support the intended scale of further synthesis. The yield may be improved if an alternative method for the purification of the final product was used. In future, the use of flash column chromatography with alternative stationary phases, such as reverse phase or C18 silica, should be investigated. In Chapter 4, an aromatic alcohol (Ald_{5OH}) could be capped by alkylation and not a methylalcohol (Ald_{5OMe}). 2-(hydroxymethyl)pyridine-4-one may therefore selectively alkylate at the aromatic alcohol, which could then be oxidised to the aldehyde (Scheme 8), however this would not permit the synthesis of the uncapped cylinder.

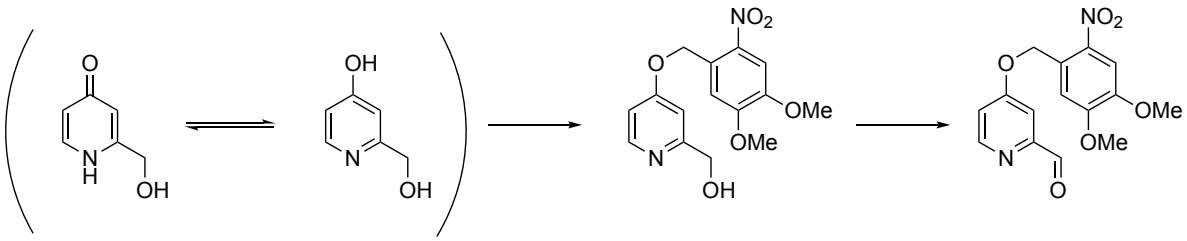

Scheme 8: An alternative synthesis of the capped 4-oxypicolinaldehyde.

5.3. 4-oxypyridine based systems

4-Hydroxypicolinaldehyde hydrochloride was purchased for the synthesis of both the uncapped and capped cylinders via their respective ligands (Scheme 9).

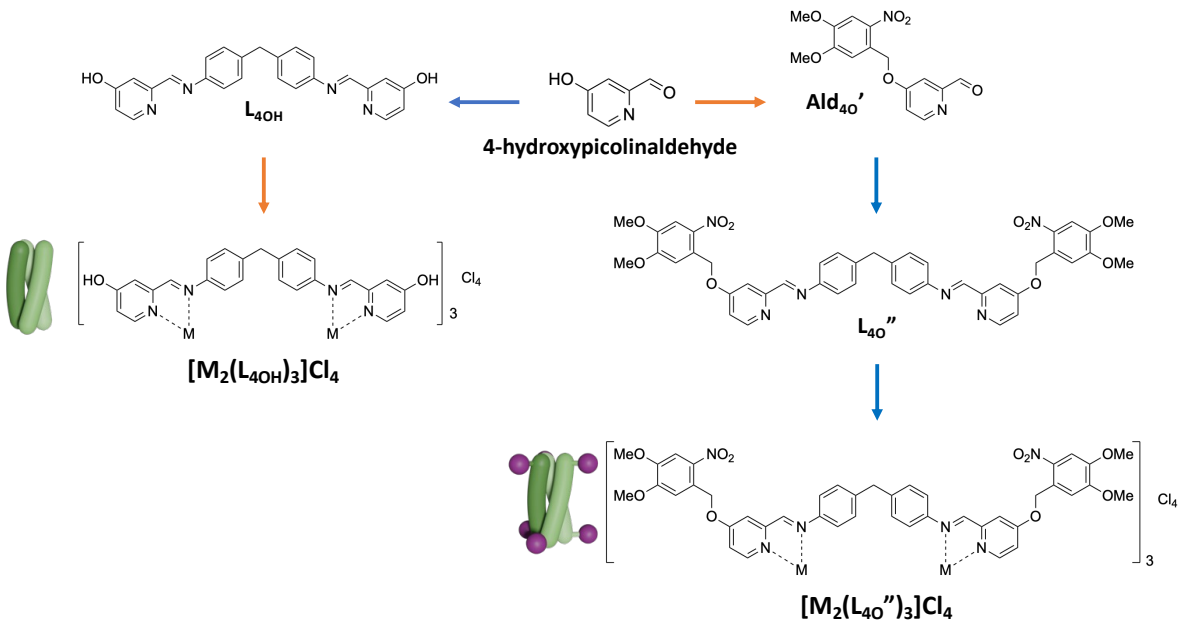

Scheme 9: Synthesis of $[M_2(L_{4OH})_3]Cl_4$ (orange arrows) and $[M_2(L_{4O}")_3]Cl_4$ (blue arrows).

5.3.1. 4-hydroxypyridine based cylinders ($[M_2(L_{4OH})_3]Cl_4$)

To form the uncapped ligand (L_{4OH}), 4-hydroxypicolinaldehyde hydrochloride and MDA were stirred in ethanol overnight at room temperature. A cream precipitate was collected by filtration in low yield (12%) and the precipitate and filtrate were compared by ^1H NMR (Figure 98). The largest peaks in the precipitate spectrum do not appear in the filtrate spectrum and can assigned to the ligand protons. Successful synthesis of the ligand is confirmed by mass spectrometry (407 m/z, $[L_{4OH} – H]^-$) which also has peaks assigned to the aldehyde (122 m/z, $[Ald_{4OH} – H]^-$) and half ligand (302 m/z, $[hL_{4OH} – H]^-$). A peak at 9.85 ppm indicates the presence of an aldehyde in both spectra and three additional peaks in the filtrate have the correct integration and coupling constants to suggest a structure based on the 4-hydroxypicolinaldehyde.

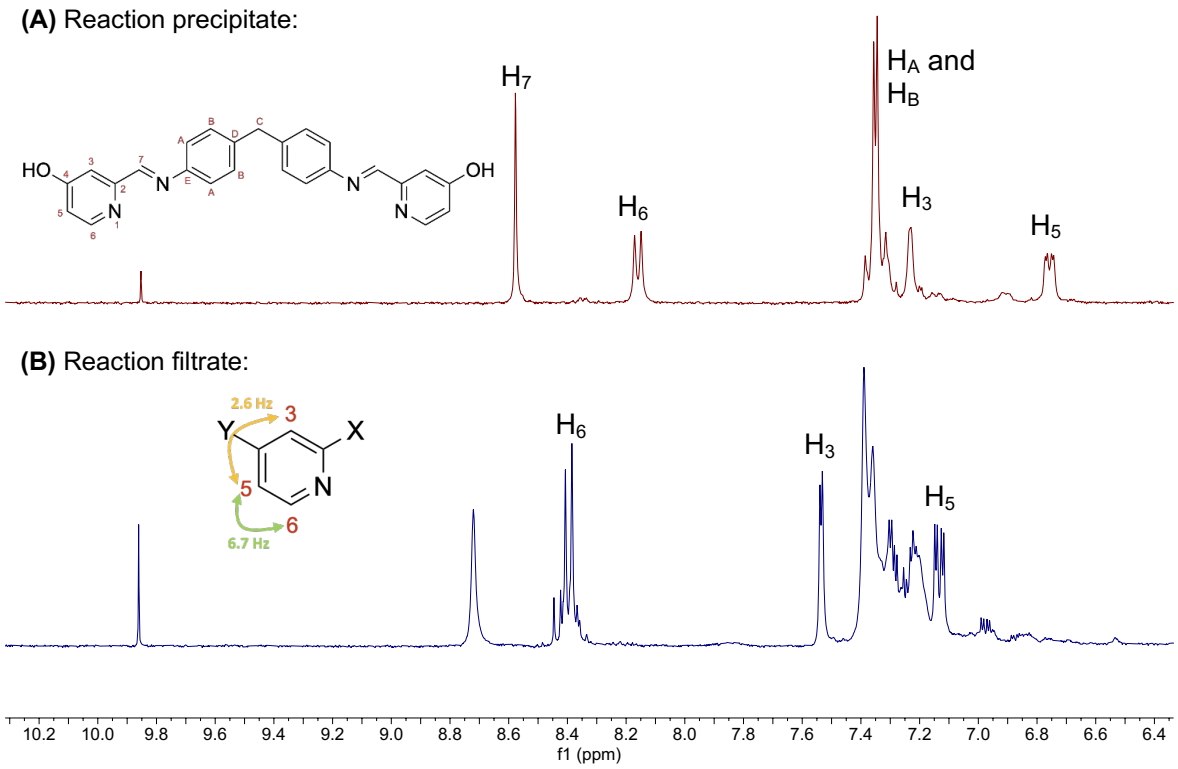

Figure 98: ^{1}H NMR (300 MHz, DMSO-d_6) of (A) the reaction precipitate and (B) the reaction filtrate after an overnight stir in ethanol. Structures of (A) L_{4OH} and (B) a 4-hydroxypyridine based species with observed J-values are shown.

The low yield and presence of an aldehyde suggested that the reaction had not finished and was therefore slower than the formation of the uncapped 5-hydroxypyridine ligand (L_{5OH}). The filtrate was resuspended in ethanol and heated to reflux to increase the reaction speed which caused the solution to turn dark orange. On cooling a dark brown precipitate was observed which was collected by filtration and found to be insoluble in DCM. This was not observed for similar reactions with the 3- and 5-substituted pyridines so degradation due to the use of the 4-hydroxypicolinaldehyde hydrochloride salt was considered as a possible cause.

The reaction was altered to first neutralise an aqueous solution of the 4-hydroxypicolinaldehyde hydrochloride salt (pH 1-2) with sodium hydrogen carbonate

solution. The solvent was removed and the residue was resuspended in ethanol with MDA to synthesise the ligand. Removal of the sodium chloride side product was not attempted to avoid the loss of the aqueous-soluble 4-hydroxypicolinaldehyde. The room temperature stir was stopped for analysis at 41 hours although the aldehyde was still observable by TLC. A precipitate was collected by filtration and washed with water to remove sodium chloride.

The ^{1}H NMR spectrum (Figure 99) in DMSO gave very broad peaks for the pyridine protons which could be caused by resonance with the pyridone form or protonation in solution. The small sharp peaks between 6 and 7 ppm and at 3.8 ppm could be due to the phenyl and methylene protons (H_F and H_G, and H_C, respectively) of the half ligand (hL_{4OH}). Peaks for both the half ligand (302 m/z, $[hL_{4OH} - H]^-$) and ligand (407 m/z, $[L_{4OH} - H]^-$) are present in the mass spectrum.

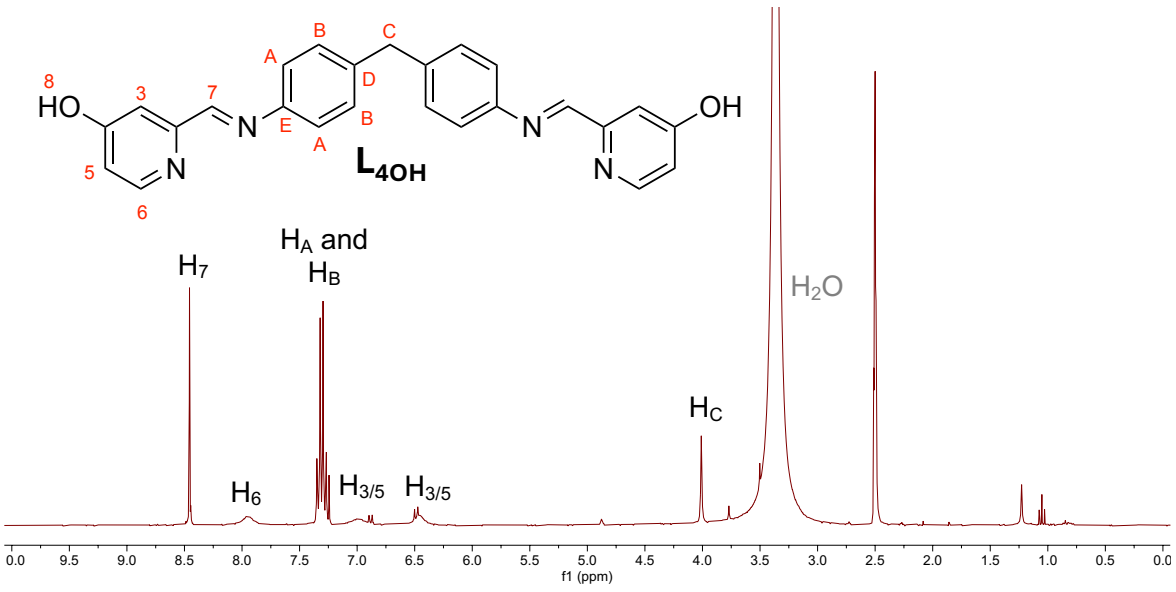

Figure 99: ^{1}H NMR (300 MHz, DMSO-d$_6$) of L_{4OH} after a 41 hour stir at room temperature.

To see if the reaction time could be reduced, the reaction was repeated and the precipitate investigated by ^{1}H NMR after an overnight stir in ethanol. Two sets of peaks

could be identified from the integration values in the spectrum, one of which was assigned to the ligand (L_{4OH}). The second set of peaks largely overlapped with the ligand peaks but included additional peaks (assigned in Figure 100A) which suggest a loss of symmetry characteristic of the half ligand. The reaction precipitate was subsequently recombined with the filtrate and heated to reflux for 24 hours. The ^{1}H NMR spectrum of the isolated precipitate (Figure 100B) indicates the ligand was successfully synthesised with only small amounts of the half ligand remaining.

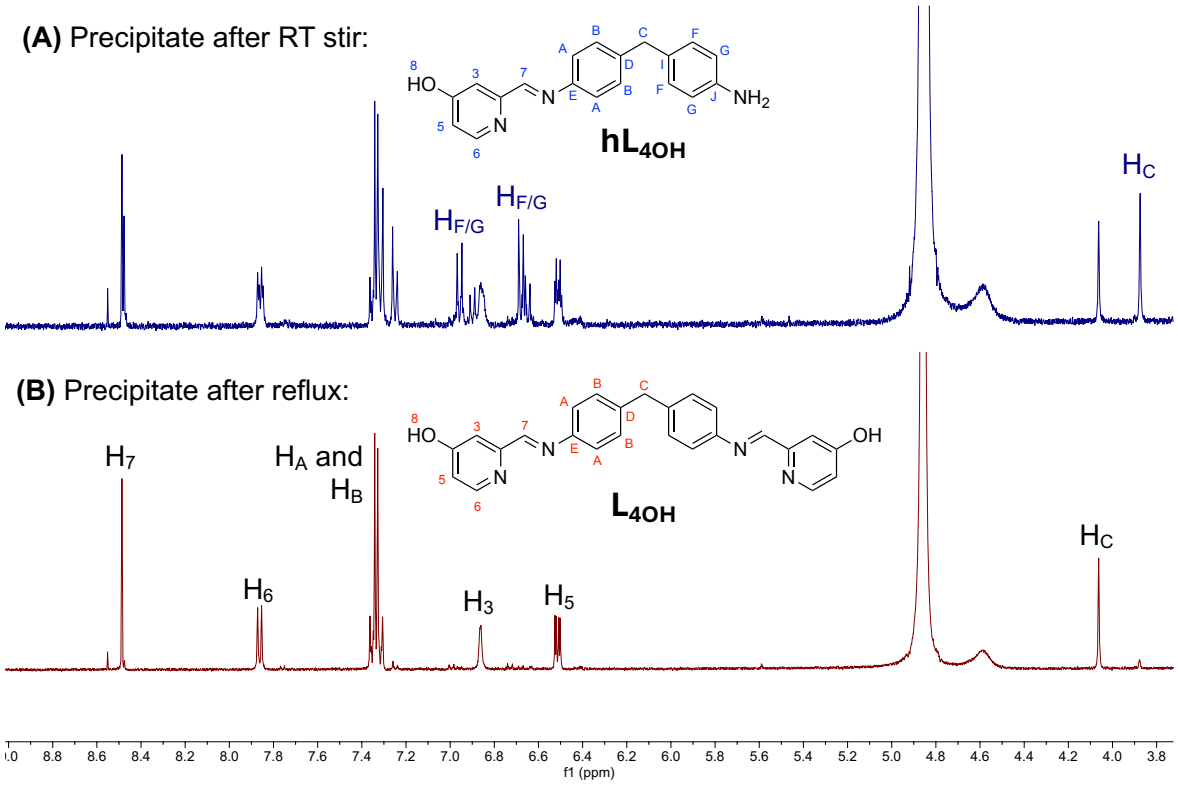

Figure 100: ^{1}H NMR (400 MHz, Methanol-d4) of the reaction precipitate after (A) an overnight stir at RT, and (B) overnight reflux. Structures of the (A) L_{4OH} and (B) hL_{4OH} are also shown.

The uncapped cylinders ($[M_2(L_{4OH})_3]Cl_4$) were synthesised by adding the methanolic metal chloride hydrate to a suspension of the ligand in methanol and stirring at room temperature until the ligand was almost completely dissolved. An excess of

the ligand was used to account for the presence of any half ligand so unreacted ligand was removed by filtration. Purification by anion exchange was not attempted due to the issues observed with the 5-hydroxypyrine base cylinders, so the filtrate concentrated before precipitating in diethyl ether.

Comparing the ^{1}H NMR spectra of the uncapped iron cylinder ($[Fe_2(L_{4OH})_3]Cl_4$) and the ligand shows the expected shifts of the pyridine proton peaks and the large upfield splitting of the phenyl peaks (Figure 101). Smaller peaks indicate the presence of the free ligand however this may be due to the presence of excess ligand or the breakdown of the cylinder in solution.

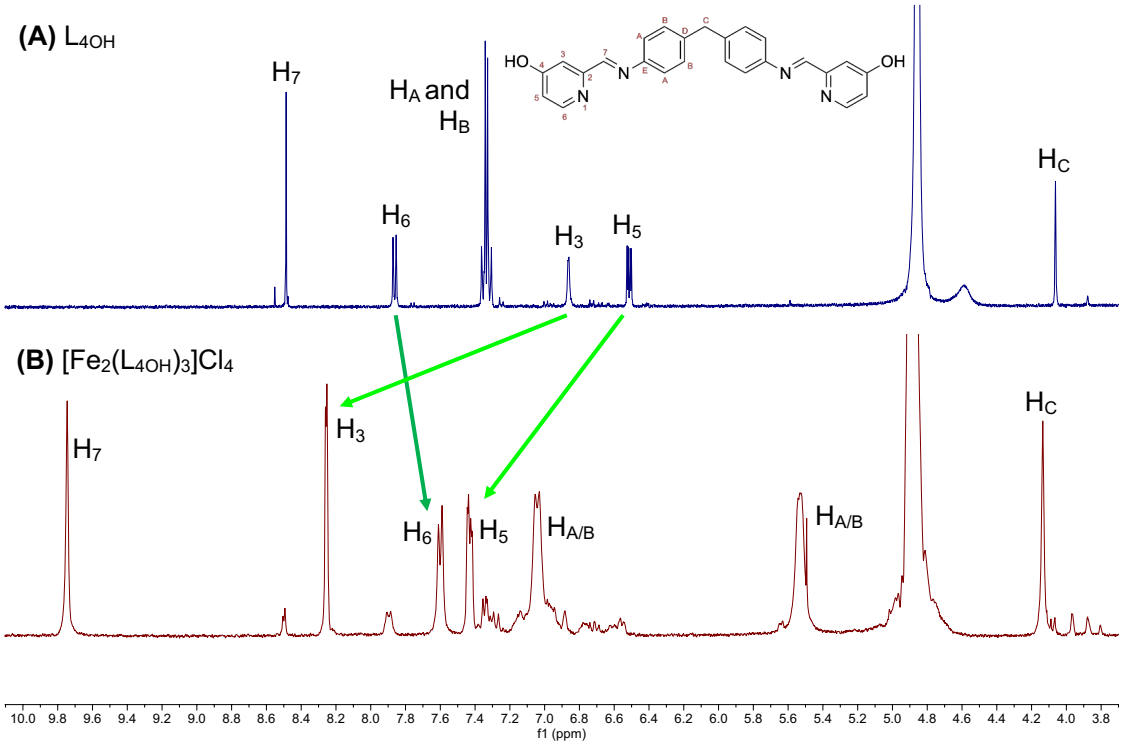

Figure 101: ^{1}H NMR (Methanol-d_4) of (A, 400 MHz) L_{4OH}, and (B, 300 MHz) $[Fe_2(L_{4OH})_3]Cl_4$.

Synthesis of the iron cylinder is confirmed in the mass spectrum (Figure 102), which also shows the presence of the two-metal, two-ligand species ($[Fe_2(L_{4OH})_2 - nH]^{(4-n)+}$), the ligand and the half ligand.

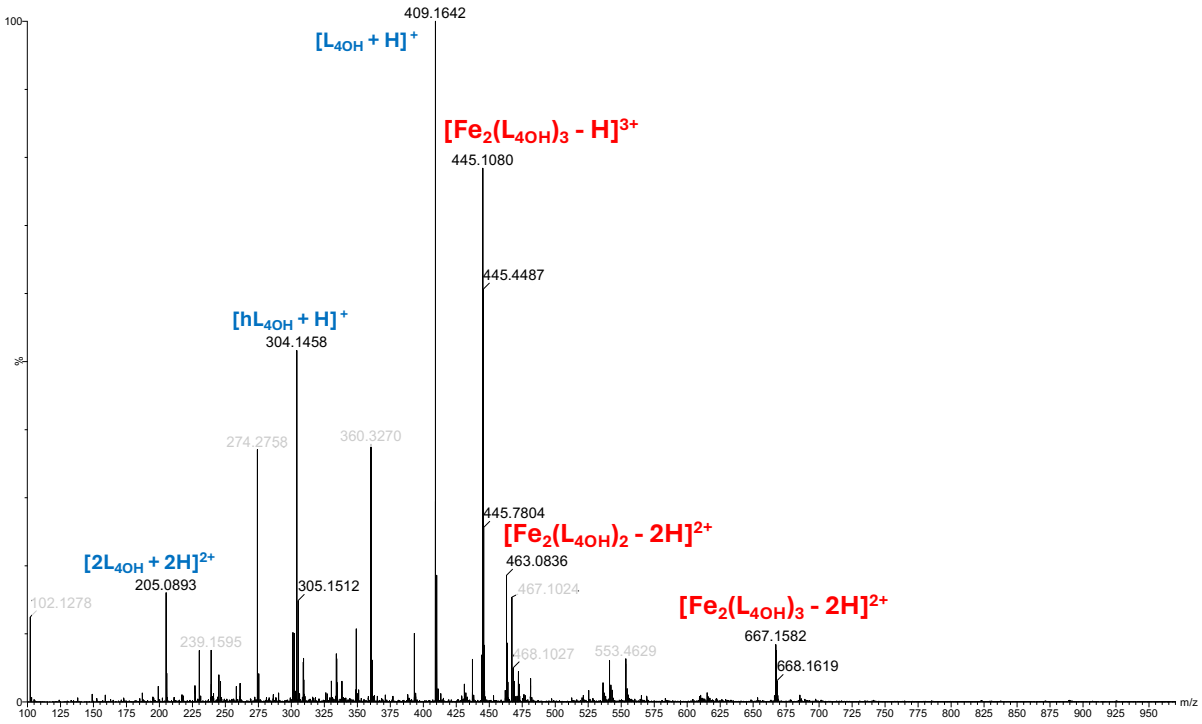

Figure 102: Mass spectrum (TOF ES+) of $[Fe_2(L_{4OH})_3]Cl_4$.

The ^{1}H NMR of the paramagnetic nickel cylinder in methanol is too broad to calculate reliable integration values so assignments are suggested based on comparison to the imidazole-based cylinders (Figure 103). The broad peak at 50 ppm could be assigned to the imine or pyridine protons (excluding H_6) and H_3 is suggested due to the distance from the metal centre.

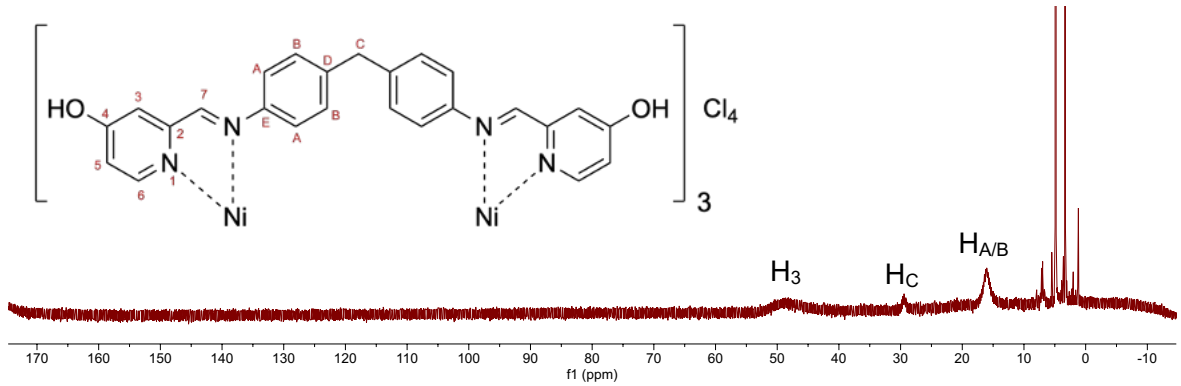

Figure 103: ^{1}H NMR (300 MHz, Methanol-d$_4$) of [Ni$_2$(L$_{4OH}$)$_3$]Cl$_4$.

The uncapped nickel cylinder is visible in the mass spectrum (Figure 104) along with the two-metal, two-ligand species ($[Ni_2(L_{4OH})_2 - nH]^{(4-n)+}$), ligand and half ligand observed in the iron cylinder spectrum. A small peak for the cylinder with one half ligand ($(Ni_2(L_{4OH})_2(hL_{4OH}) - H]^{3+}$) is also observed.

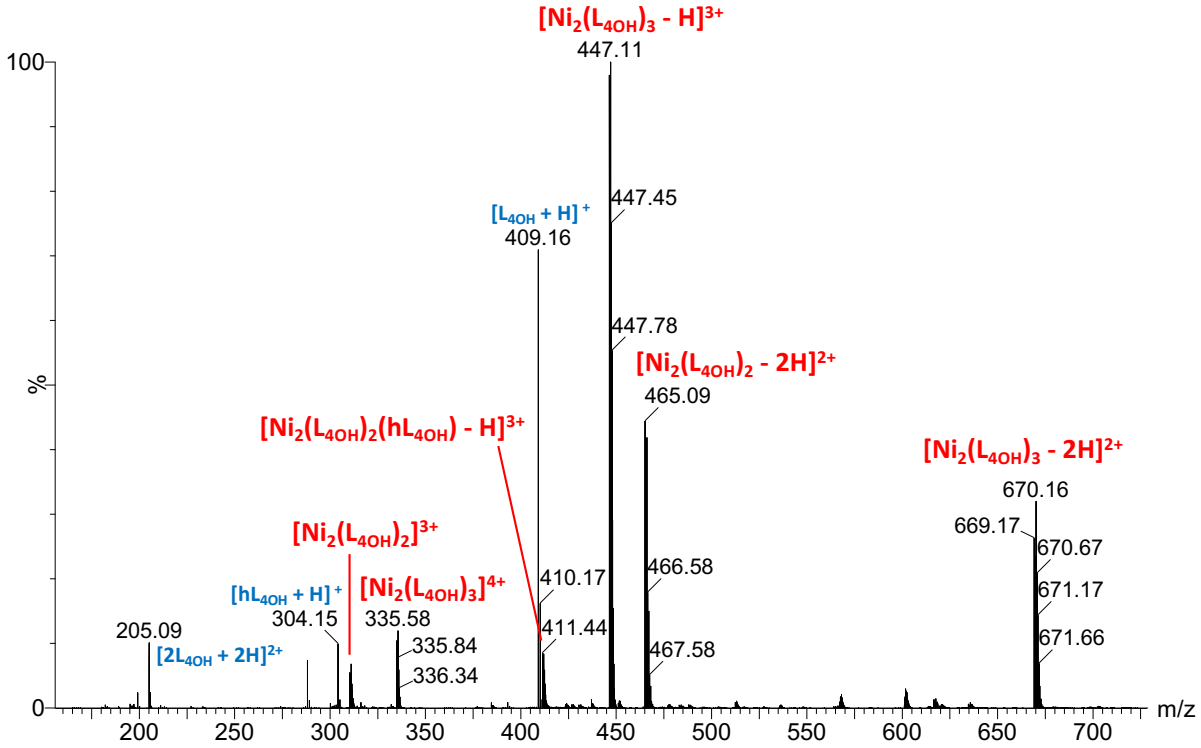

Figure 104: Mass spectrum (TOF ES+) of [Ni$_2$(L$_{4OH}$)$_3$]Cl$_4$.

The mass spectra of the final metal complex products demonstrate the successful synthesis of the cylinders however various organic ligand and alternative metal complexes were also observed. A small amount of the free ligand is observed in the NMR spectrum of the iron complex which could be caused by the lower purity of the complex, or the degradation of the complex in solution. Future experiments should check the stability of the complex in methanol (by UV-visible absorption or NMR) and consider finding an alternative method for cylinder purification.

5.3.2. Capped 4-oxypyridine based cylinders ($[M_2(L_{4O}")_3]Cl_4$

As with the 5-hydroxypyridine based cylinders, synthesis of the capped cylinder was attempted via the capped aldehyde and ligand. Initial experiments used 4-hydroxypicolinaldehyde synthesised in Section 5.2 for a synthesis based on a previously reported procedure (Scheme 10)[3].

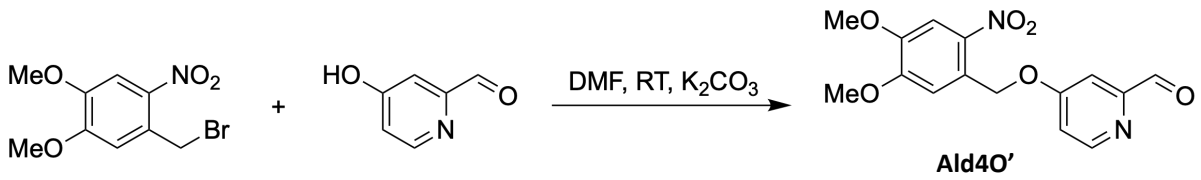

Scheme 10: Synthesis of Ald_{4O}'.

After 3 hours at room temperature the solvent was removed by separation. The crude product was purified by column chromatography to separate the unreacted DMNB-Br from another fraction (R_f = 0.95 and 0.75, respectively, DCM:ethyl acetate) which was identified as the product by ^1H NMR (Figure 105).

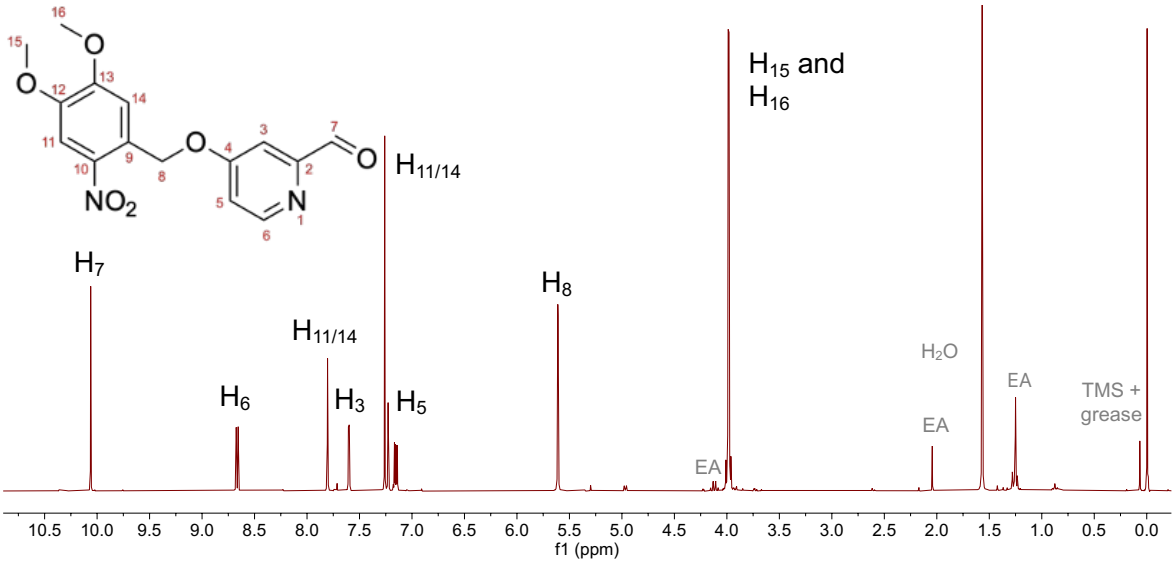

Figure 105: ^{1}H NMR (300 MHz, Chloroform-d) of Ald$_{4O}$'.

A high yield was desirable due to the limited supply of 4-hydroxypicolinaldehyde however the yield (56%) was lower than for the 5-hydroxypicolinaldehyde reaction. The reaction was repeated with 4-hydroxypicolinaldehyde hydrochloride, neutralised by an excess of the potassium carbonate base, and the reaction time extended overnight, however no significant changes between the TLC at 3 hours and after an overnight stir were observed. A reaction precipitate was collected by filtration before repeating the separation, and the product was found in the precipitate, organic and aqueous phases by TLC. All fractions were recombined in DMF, and dried under vacuo before the product was purified by column chromatography. Isolation of the product was confirmed by mass spectrometry (318 m/z, [Ald$_{4O}$]$^+$) and ^{1}H NMR (Figure 106), and achieved with a slightly lower yield (37%) at higher scale (0.50 mmol compared to 0.17 mmol).

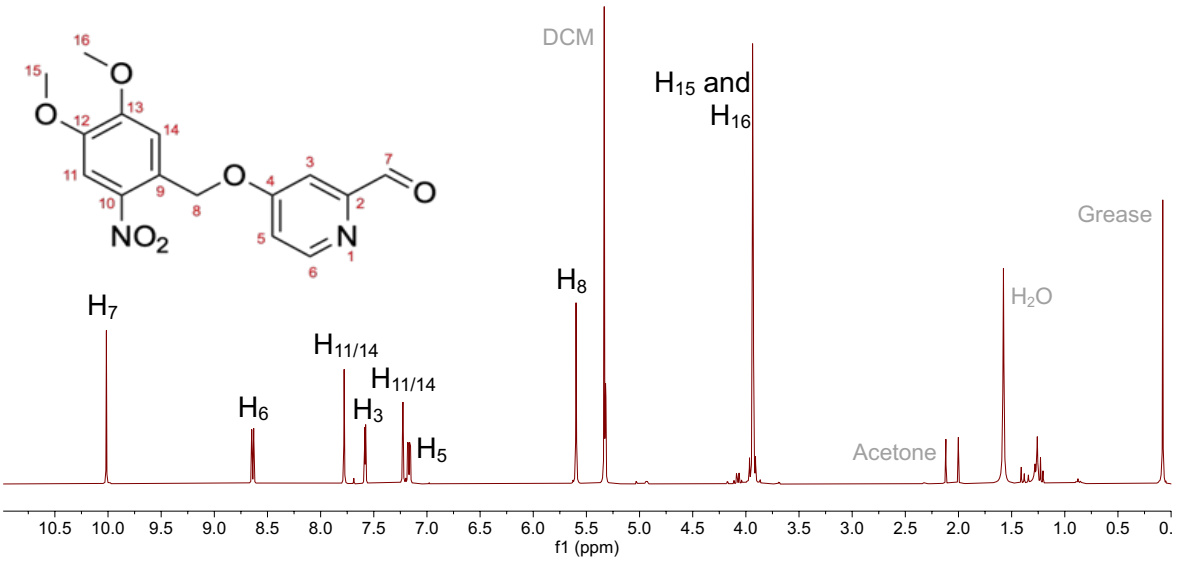

Figure 106: ^{1}H NMR (300 MHz, Methylene Chloride-d_2) of Ald_{4O}'.

A methanolic solution of the capped aldehyde and MDA was stirred at room temperature for 2 hours before a white precipitate was collected by vacuum filtration. The ^{1}H NMR spectrum of the precipitate (Figure 107A) showed the unreacted aldehyde was still present so the synthesis was repeated with an overnight stir. The major species present in the ^{1}H NMR spectrum of the white precipitate (Figure 107B) was the capped ligand (L_{4O}") however some other small peaks were also observed in the spectrum which suggest the presence of the unreacted aldehyde and half ligand. The mass spectrum indicated the presence of the ligand (799 m/z, $[L_{4O}" + H]^+$) along with the half ligand (499 m/z, $[hL_{4O}' + H]^+$) and various decapped species (604 m/z, $[L_{4O}' + H]^+$, 409 m/z, $[L_{4OH} + H]^+$, and 304 m/z, $[hL_{4OH} + H]^+$). The capped aldehyde (Ald_{4O}') was not observed, however the photocleavage product was visible (196 m/z, $[C_9H_{11}NO_4]^+$). The precipitate was washed with methanol to remove the observed impurities, however the ^{1}H NMR of the washed product (Figure 107C) indicates that this caused further degradation.

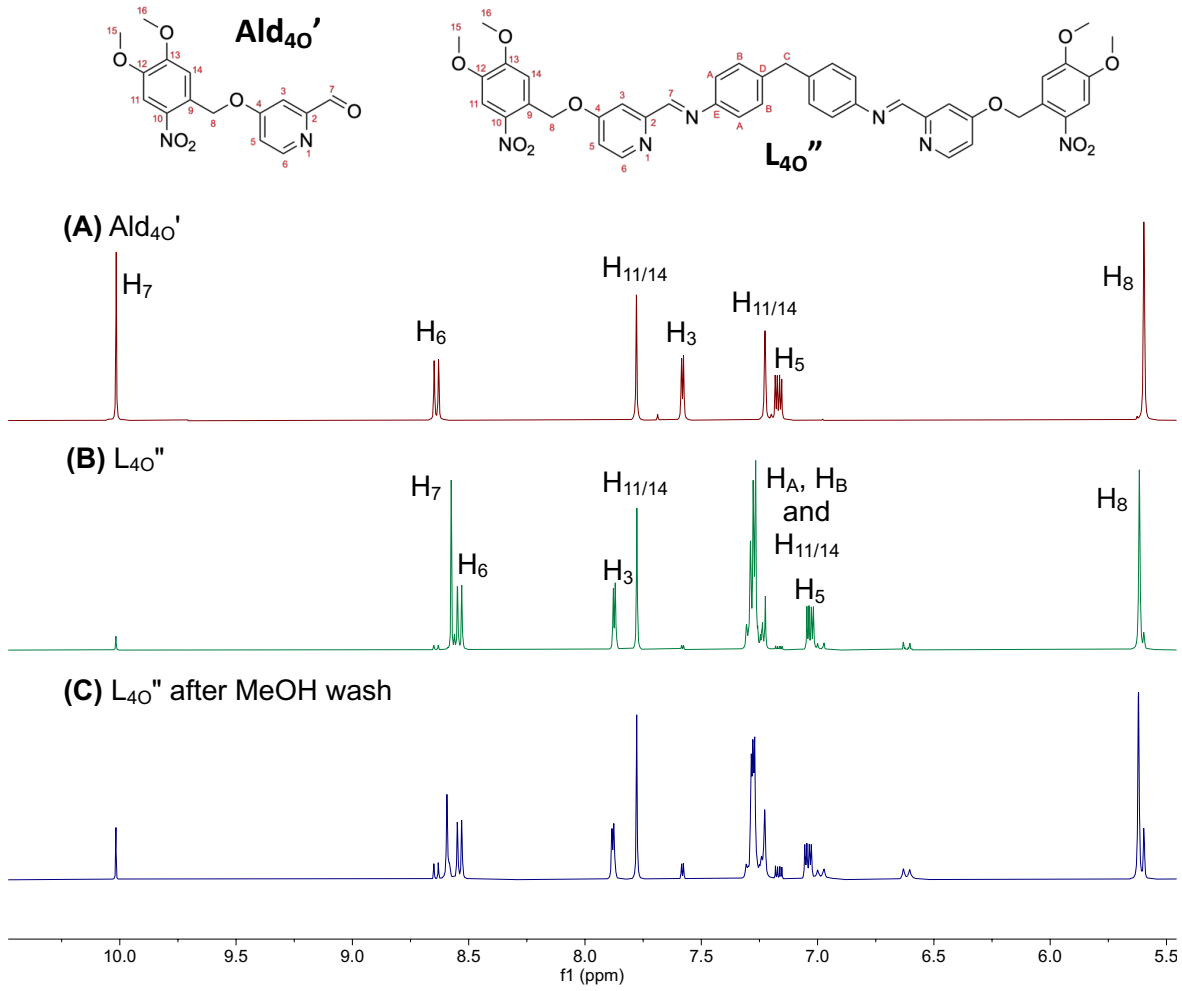

Figure 107: ^{1}H NMR (300 MHz, Methylene Chloride-d$_2$) of (A) Ald$_{4O}$', (B) L$_{4O}$" after overnight stir, and (C) L$_{4O}$" after methanol wash.

As the ligand was prone to degradation, alternative approaches to synthesise the capped cylinder were considered to minimise the exposure of the ligand to water, air and ambient light. A one-pot method avoids exposure of the ligand completely by synthesis of the capped cylinder directly from the capped aldehyde (Scheme 11). Metal templating may catalyse the ligand formation, and the lack of second metal binding motif in the half ligand (hL$_{4O}$') should favour co-ordination of the ligand (L$_{4O}$"), which also pushes the reaction forward. The one-pot method also benefits from a reduced work up, avoiding unnecessary losses in yield.

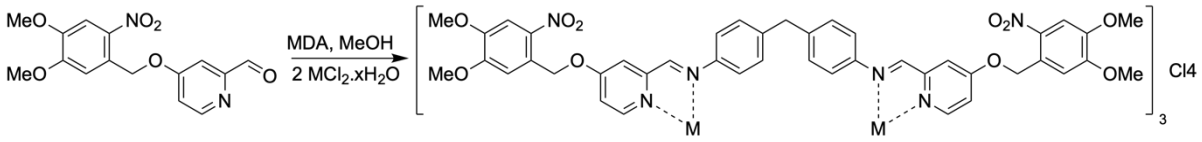

Scheme 11: One-pot method for the synthesis of $[M_2(L_{4O}")_3]Cl_4$.

The reaction was monitored by mass spectrometry (Figure 108) which shows an increase in the relative abundance of the capped cylinder (627 m/z, $[Fe_2(L_{4O}")_3]^{4+}$) over 24 hours. A peak for the 5-capped species is also observed (771 m/z, $[Fe_2(L_{4O}")_2(L_{4O}')]Cl_4$). Formation of the iron complex is also supported by a gradual colour change of the reaction solution to a clear, dark purple.

The reaction solution was filtered and the cylinder purified by anion exchange with ammonium hexafluorophosphate. A purple precipitate was collected by filtration in a 72% yield. The ^1H NMR spectrum of the cylinder (Figure 109) shows the characteristic shielding of the phenyl protons (H_A and H_B) by the inter-ligand π-stacking and the expected change in the chemical shifts of the pyridine protons (H_3, H_5, and H_6) due to metal coordination.

The hexafluorophosphate salt was converted to a chloride salt by stirring in methanol with Dowex beads. A purple solid was collected with a 71% yield from the Dowex conversion, leaving a 51% isolated yield from the reaction in total. Comparing the ^1H NMR spectrum of chloride salt to the capped ligand (Figure 110) shows the characteristic downfield shift of the imine (H_7) and pyridine protons (H_3 and H_5) due to the electron withdrawal caused by metal coordination, and upfield shift of the 6-position proton (H_6).

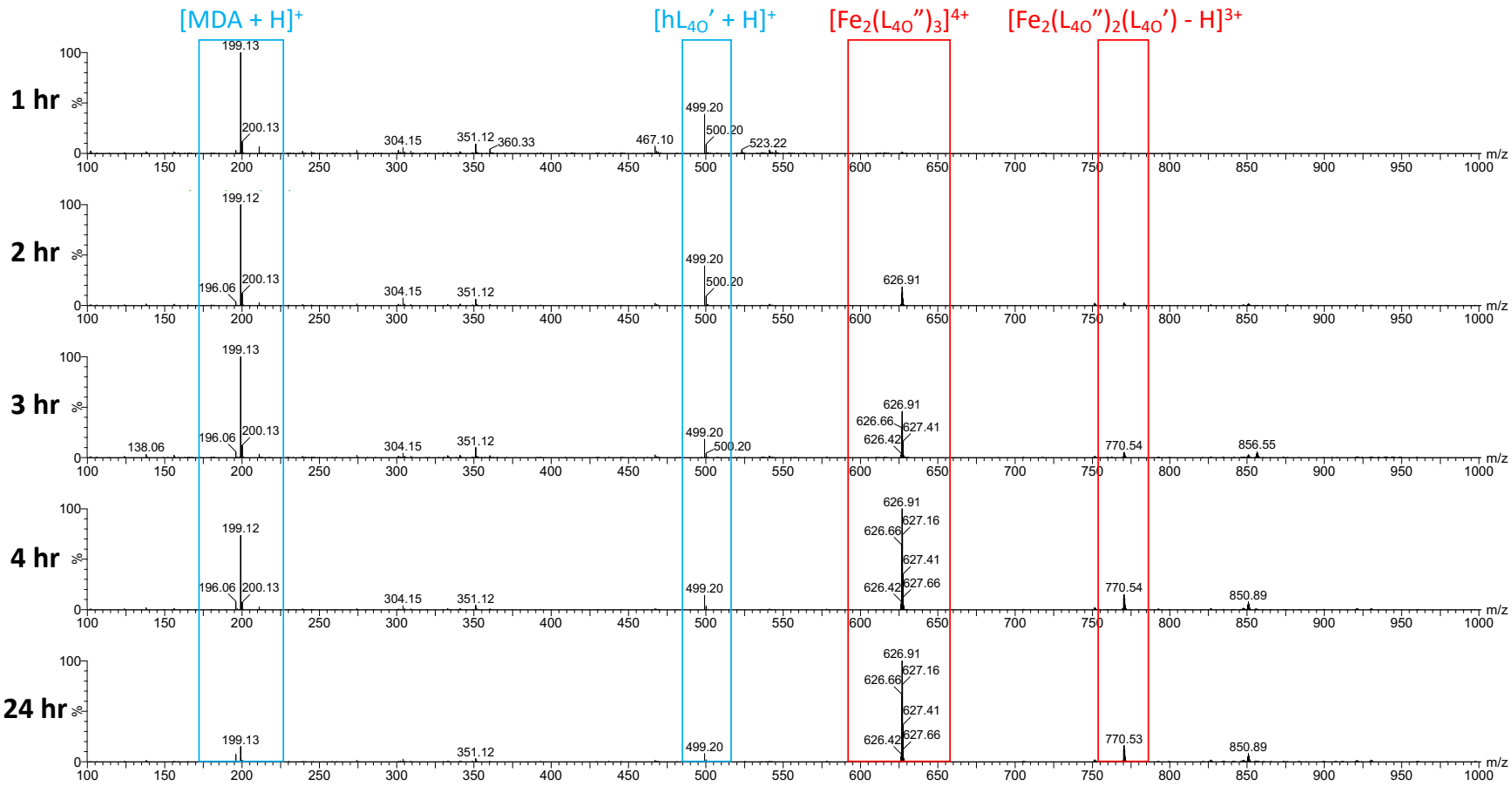

Figure 108: Mass spectra (TOF ES+, MeOH) of the one-pot reaction at different time points.

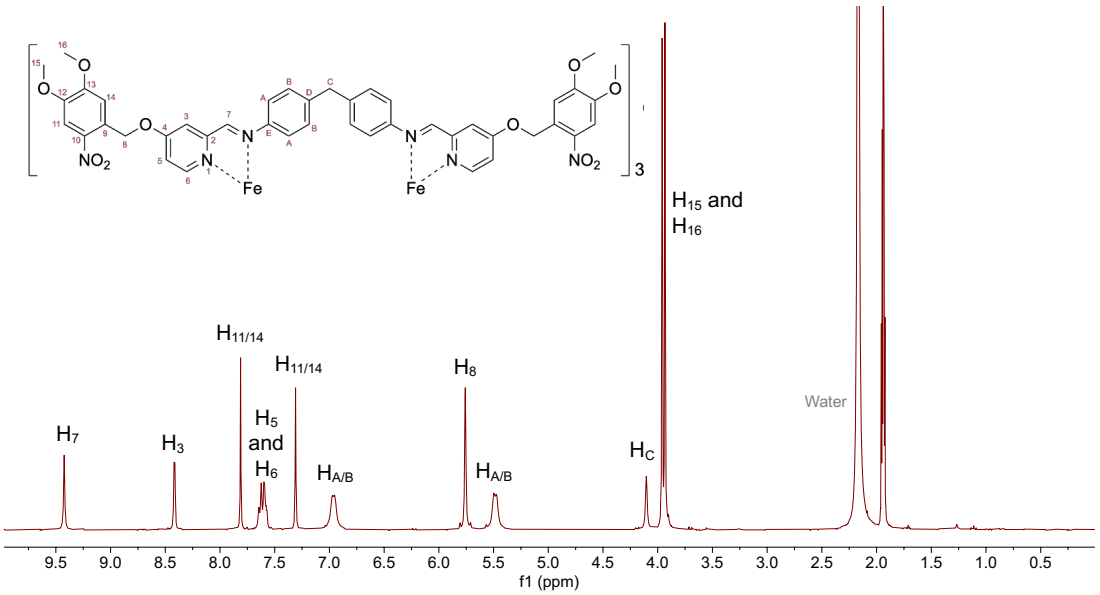

Figure 109: ^{1}H NMR (300 MHz, Acetonitrile-d$_3$) of [Fe$_2$(L$_{4O}$")$_3$](PF$_6$)$_4$.

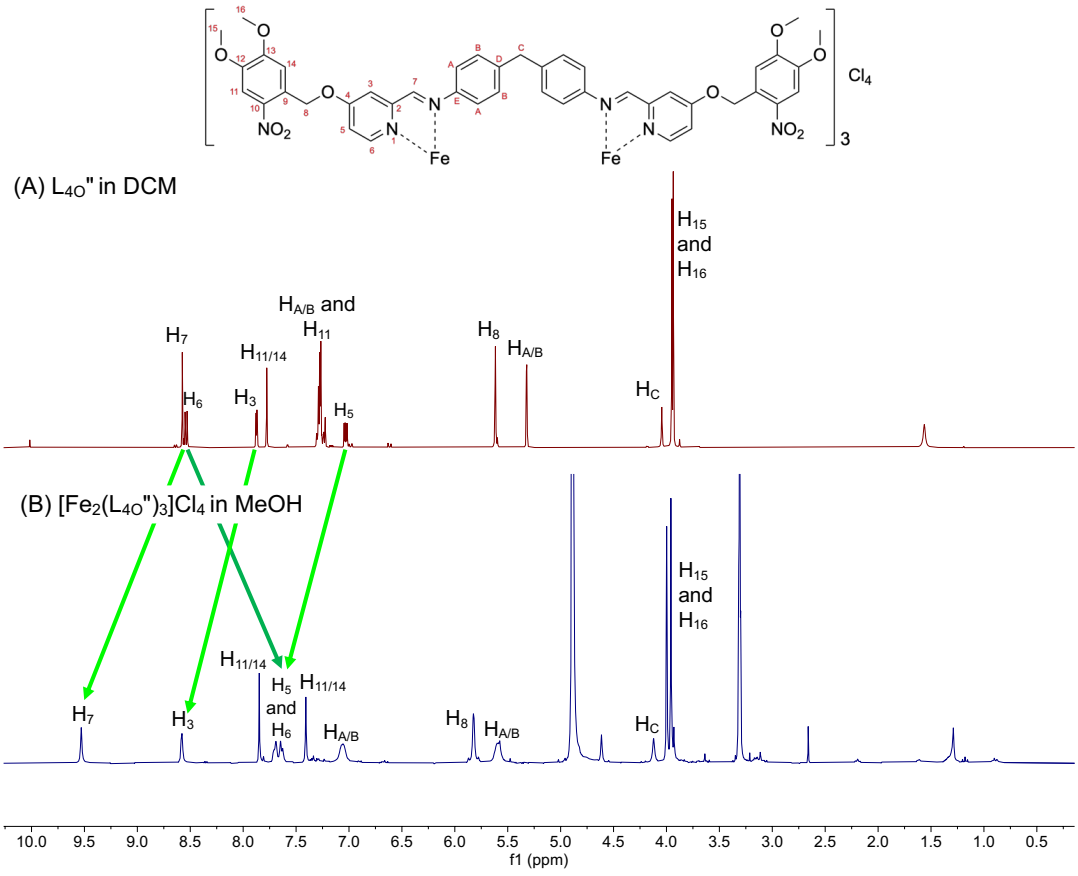

Figure 110: ^{1}H NMR (300 MHz) of (A) L$_{4O}$" (methylene chloride-d$_2$), and (B) [Fe$_2$(L$_{4O}$")$_3$]Cl$_4$ (methanol-d$_4$).

The reaction procedure was repeated for the nickel cylinder using nickel chloride hexahydrate. The nickel cylinder was soluble enough in acetonitrile (as a hexafluorophosphate salt, Figure 111A/C) and methanol (as a chloride salt, Figure 111B/D) for the NMR spectra to be recorded. Assignments were made in comparison to the uncapped nickel cylinder ($[Ni_2(L_{4OH})_3]Cl_4$) and the capped 5-oxypyridine based cylinder ($[Ni_2(L_{5O}")_3]Cl_4$). The central methylene (H_C), one of the phenyl peaks ($H_{A/B}$), and one of the pyridine protons (H_3) were assigned by comparison to the uncapped cylinder. Four sharp peaks between 3 and 9 ppm in the hexafluorophosphate salt spectrum could be assigned to the capping protons (H_8, H_{11}, H_{14}, H_{15} and H_{16}) by their integration values. The chloride salt has a similar spectrum with only the methyl-bridging protons (H_8) appearing at a slightly higher shift with a sharper peak. A very broad peak is observed underneath the spectrum between 3 and 5 ppm, however this was too broad for further investigation.

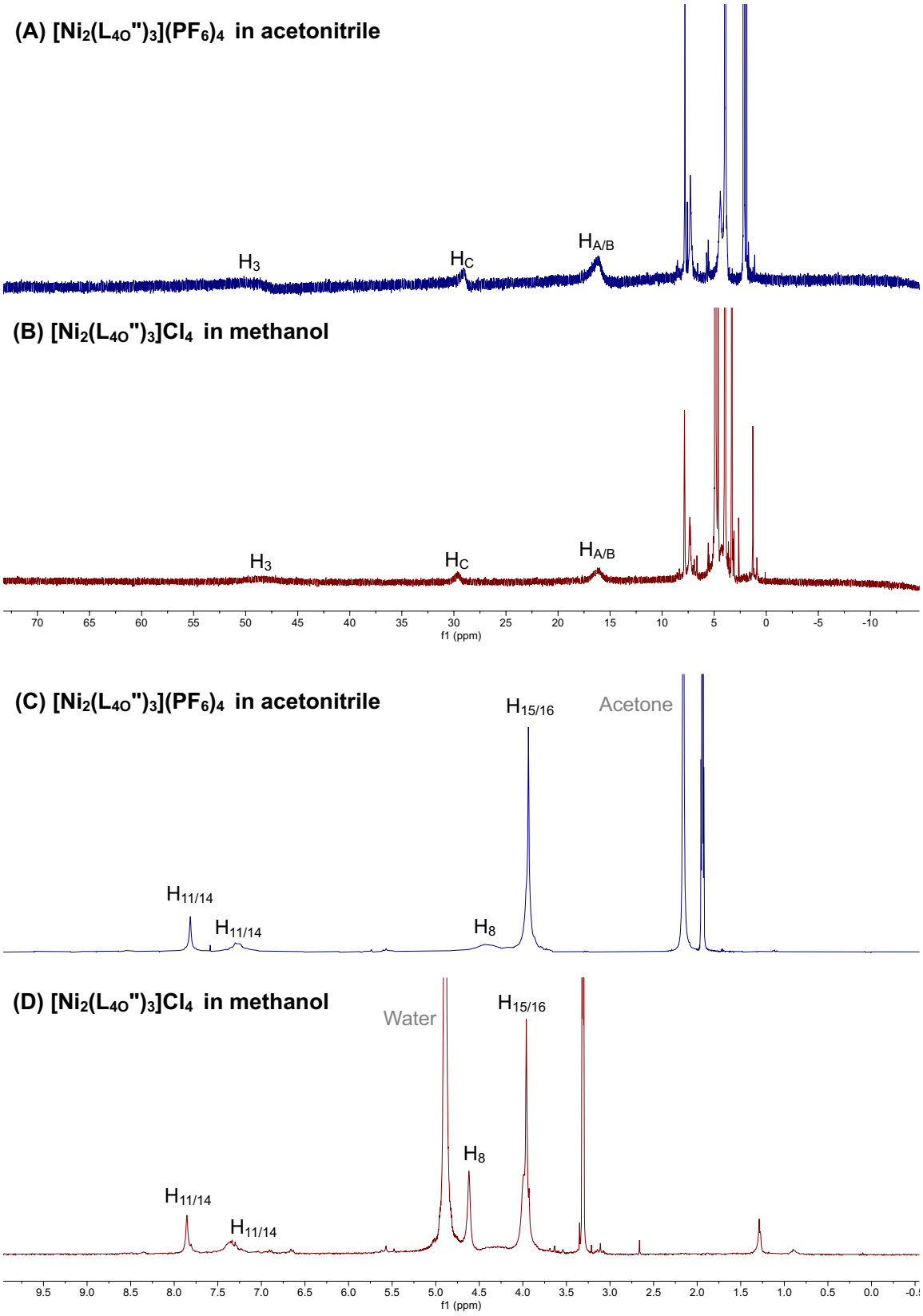

Figure 111: ^{1}H NMR (300 MHz) of (A and C, navy) $[Ni_2(L_{4O}")_3](PF_6)_4$ (Acetonitrile-d_3) and (B and D, maroon) $[Ni_2(L_{4O}")_3]Cl_4$ (Methanol-d_4).

The synthesis of the nickel cylinder is confirmed by the mass spectrum which shows the fully capped cylinder as a 4+ charged species and 3+ charged species with various counter ions (Figure 112). The 5-capped species is also observed which may be formed by photocleavage in ambient light (772 m/z, $[Ni_2(L_{4O}")_2(L_{4O}') - H]^{3+}$).

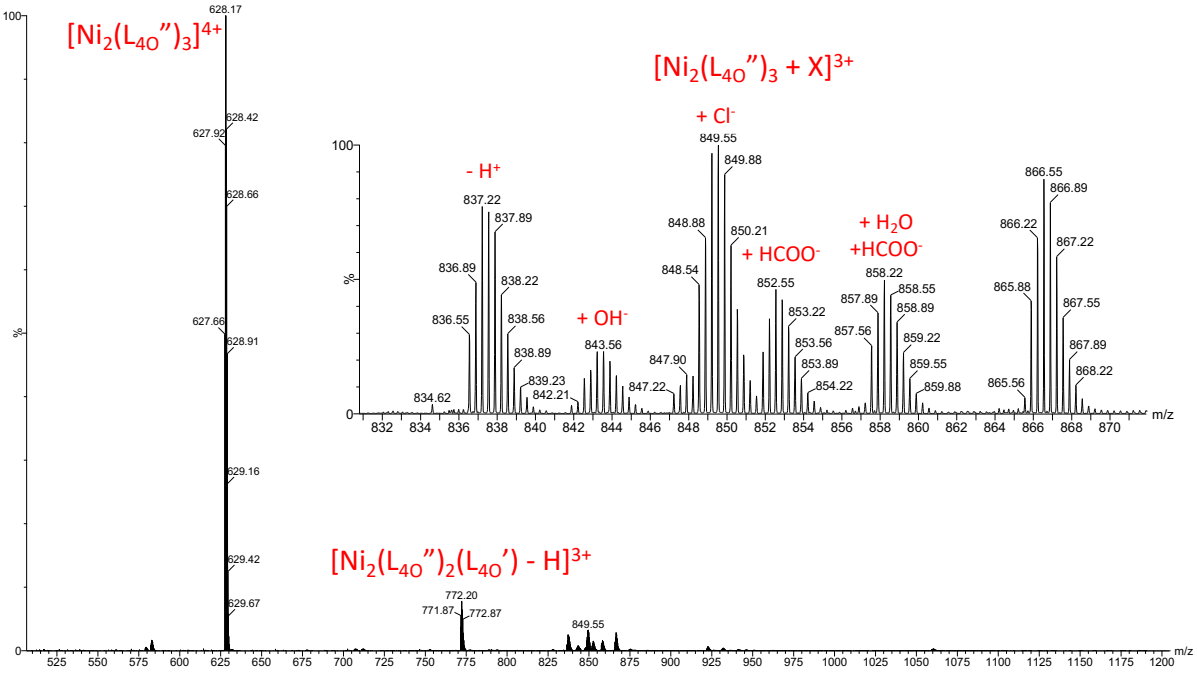

Figure 112: Mass spectrum (TOF ES+, MeOH) of $[NI_2(L_{4O}")_3]Cl_4$.

In summary, the iron and nickel capped cylinder are both successfully synthesised by via the capped ligand (L_{4O}"). The ^{1}H NMR spectra of both cylinders has been recorded, however the second phenyl proton of the nickel cylinder could not be seen (as with the uncapped cylinder) which may require a wider range of chemical shifts to be investigated (below –10 ppm).

5.3.3. 4-oxypyridine based rotaxane ($[M_2(L_{4O}'')_3.CB10]Cl_4$)

The 4-oxypyridine based cylinder was designed to increase the effective steric bulk of the capping groups compared to the 5-oxypyridine cylinder, providing the rotaxane with a larger barrier for dissociation of the CB10 ring. The slipping mechanism may not be possible, so the capping mechanism was investigated first.

As seen in previous attempts to cap imidazole-based iron cylinders, a loss of colour was observed after the addition of the base to the *pseudo*rotaxane solution ($[Fe_2(L_{4OH})_3.CB10]Cl_4$) suggesting the degradation of the iron cylinder at low pH. The nickel *pseudo*rotaxane ($[Ni_2(L_{4OH})_3.CB10]Cl_4$) solution did not lose colour after the addition of base.

Following the conditions optimised for the capping of the 3-hydroxypyridine cylinder (see Section 5.4.2) DMNB-Br (6 equivalents) was added portion-wise over 2 hours to a basic solution of the uncapped nickel cylinder ($[Ni_2(L_{4OH})_3]Cl_4$) with CB10 in 20% methanol in water at 50°C. The reaction was monitored by mass spectrometry (Figure 113) which indicated the presence of the *pseudo*rotaxane and singly capped complex (800 m/z, $[Ni_2(L_{4OH})_2(L_{4O}').CB10]^{4+}$) but the capping reaction showed no further progress over 2 hours. The relative abundance of the partially hydrolysed *pseudo*rotaxane complex, (725 and 966 m/z, $[Ni_2(L_{4OH})_2(hL_{4OH}).CB10 - n]^{(4-n)+}$) appears to decrease over time which could indicate a reduced stability. The remaining nickel containing complexes are the two-metal, two-ligand *pseudo*rotaxane species (865 m/z $[Ni_2(L_{4OH})_2.CB10 - H]^{3+}$) and the single metal hydrolysed species (858 m/z, $[Ni(hL_{4O}')(hL_{4OH}).CB10 - H]^{3+}$).

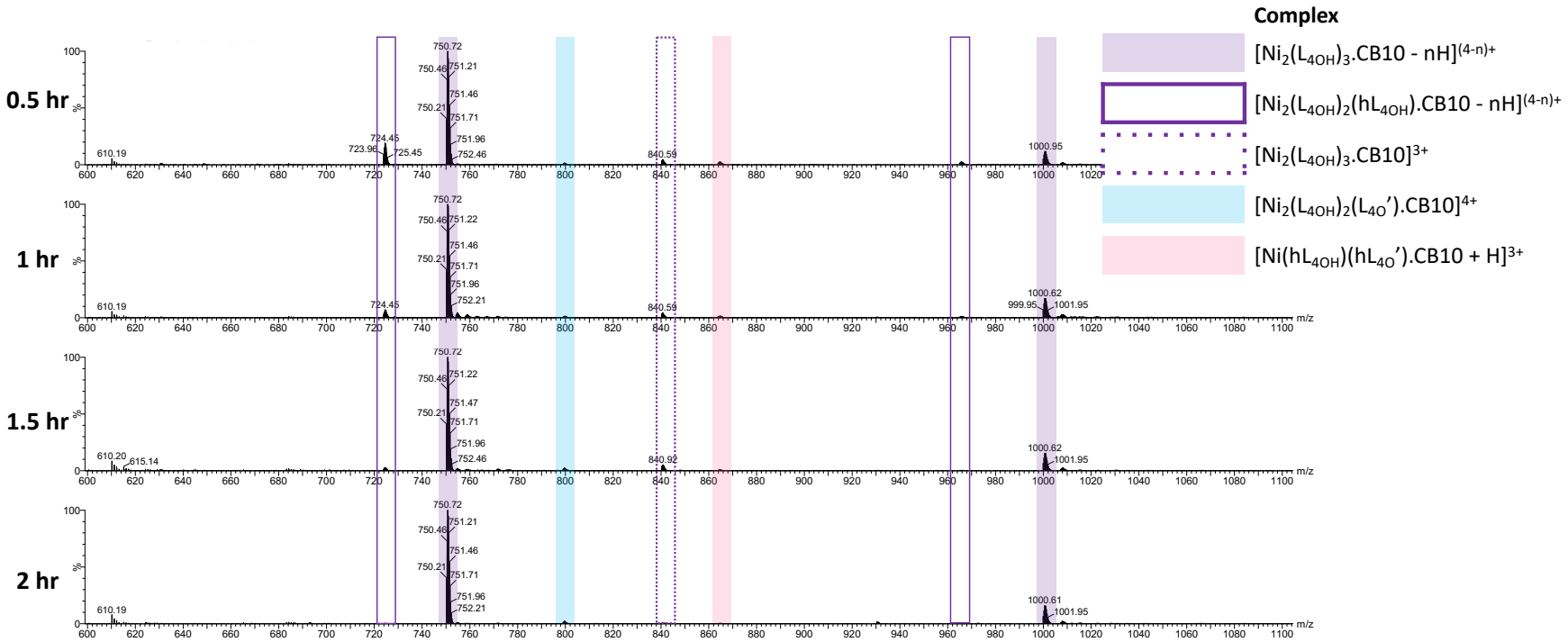

Figure 113: Mass spectra (TOF ES+, H_2O) of the $[Ni_2(L_{4OH})_3.CB10]Cl_4$ capping reaction.

The unthreaded cylinder is not observed which could be caused by a lower solubility in water or efficient binding between the host and guest. The reaction requires aqueous conditions at raised temperatures, and while the CB10 ring has been shown to increase the stability of the parent cylinder[4], it is possible that any unthreaded cylinders are hydrolysed, which is supported by an increasing peak for the free spacer unit (199 m/z, $[MDA + H]^+$).

As the capping method was unsuccessful, the slipping method was also attempted following the synthesis of the 5-oxypyridine rotaxane and slipping of the methylpyridine capped imidazole cylinder[5]. The nickel capped cylinder ($[Ni_2(L_{4O}")_3]Cl_4$) and CB10 were heated to 50°C in 20% methanol in water. The mass spectra of the solutions were recorded after the overnight reaction before the solvent was removed and the residue resuspended in water overnight to allow the rotaxane to dissolve. The filtrate was collected and the product isolated by freeze-drying.

The rotaxane peak (1044 m/z, $[Ni_2(L_{4O}")_3.CB10]^{4+}$) was observed in mass spectrum of the crude mixture, reaction product, and a residue which remained undissolved when the reaction residue was resuspended in water (Figure 114). Peaks can also be assigned to the free cylinder in the reaction mixture (628, 772, and 849 m/z, $[Ni_2(L_{4O}")_3]^{4+}$, $[Ni_2(L_{4O}")_2(HL_{4O}') - H]^{3+}$, and $[Ni_2(L_{4O}")_3 + Cl]^{3+}$, respectively), but these are largely removed by suspension of the reaction residue in water due to the reduced aqueous solubility of the cylinder compared to the rotaxane.

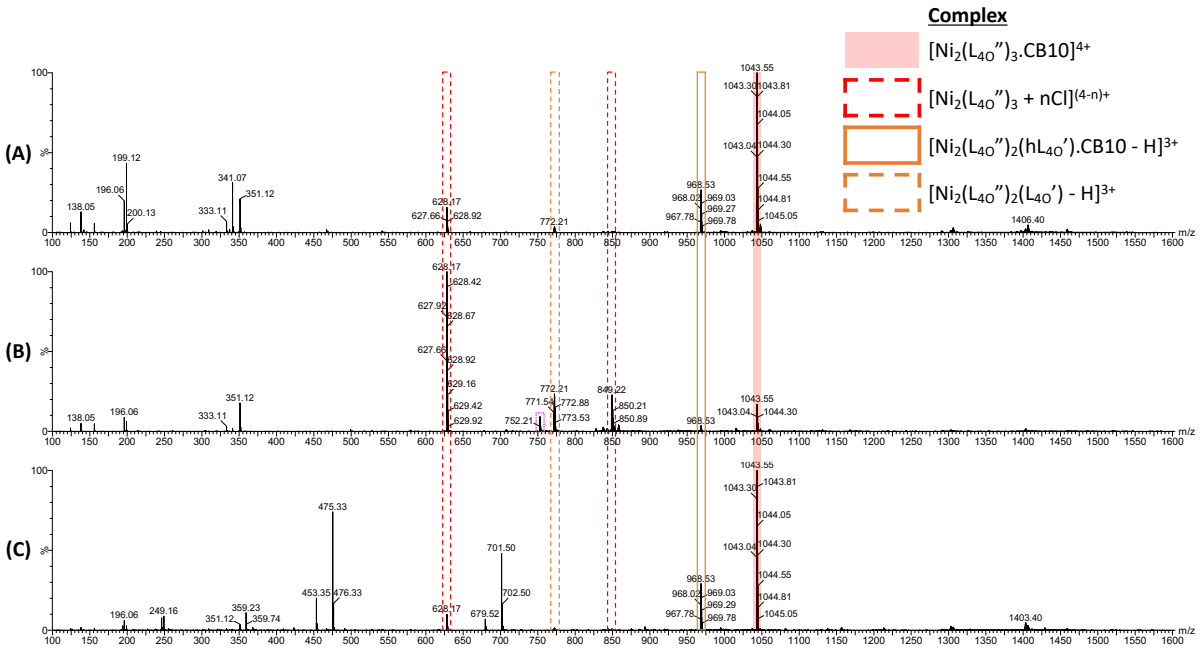

Figure 114: Mass spectrum (TOF ES+, H_2O) of (A) the crude reaction mixture, (B) the reaction residue after suspension in water, and (C) the reaction product.

The nickel based rotaxane was successfully synthesised by the slipping method, however isolation of the product requires optimisation. The low aqueous solubility of the rotaxane when suspended in water, and the highly static nature of the dried product caused a low isolated yield reported.

5.4. 3-oxypyridine based systems

As mentioned in Section 5.1, alkylation of a 3-hydroxypyridine based cylinder is expected to direct the capping group back towards the 3WJ recognition motif at the centre of the cylinder (Figure 90). In this position the capping groups may prevent the hydrophobic interaction between the CB10 ring and the cylinder and may mask the central phenyl junction binding motif, preventing junction formation.

5.4.1. 3-hydroxypyridine based cylinders

3-hydroxypicolinaldehyde is an inexpensive, readily available starting material which can be used directly for the synthesis of the uncapped ligand (L_{3OH}) by stirring with MDA in ethanol at room temperature for 26 hours. A bright yellow precipitate was collected by filtration (82% yield) and identified as the ligand by mass spectrometry (m/z = 409, $[L_{3OH} + H]^+$) and ^1H NMR (Figure 115).

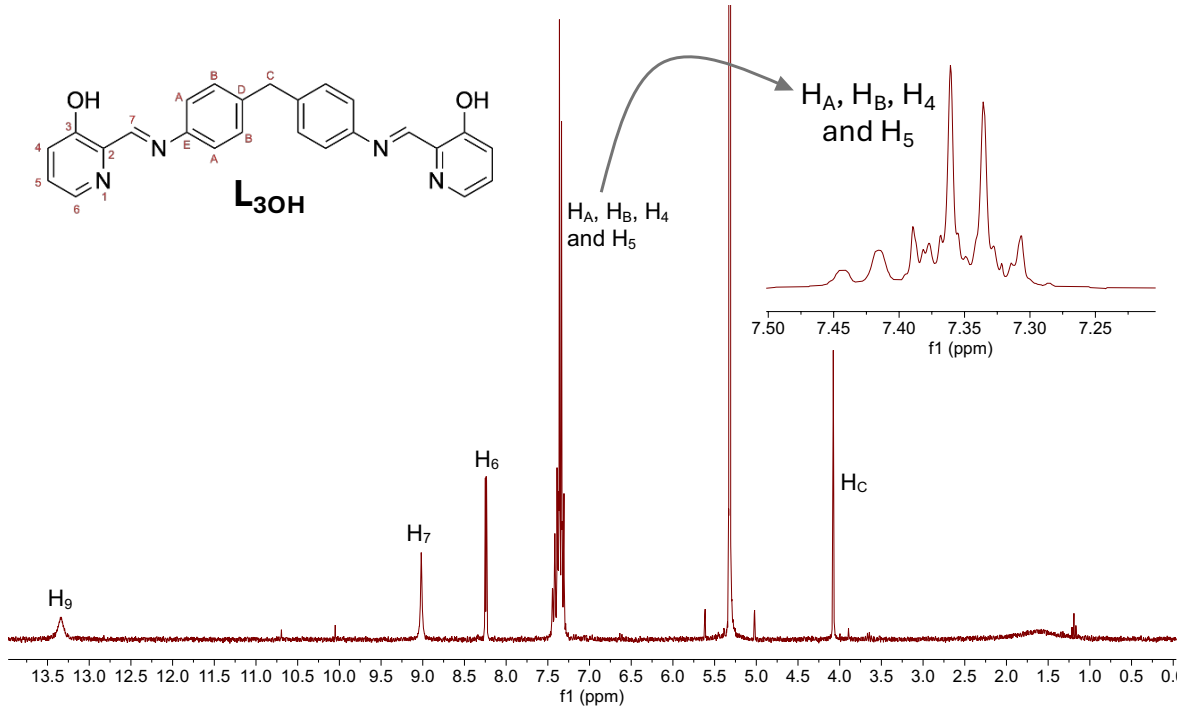

Figure 115: ^1H NMR (300 MHz, methylene chloride-d_2) of L_{3OH}. Inset: Magnification of the overlapping peaks at 7.35 ppm.

The phenyl (H_A and H_B) and two of the pyridine (H_4 and H_5) proton peaks overlap around 7.2-7.5 ppm so cannot be exactly assigned, however the expected number of peaks is also observed in the ^{13}C NMR spectrum (Figure 116). The single sp^3 carbon (C_c) is assigned to the peak with the lowest chemical shift and an even number of protons. Carbons with a single proton attached (C_A, C_B, C_4, C_5, and C_6) were assigned

by HSQC, however overlapping peaks in the ^{1}H NMR prevent the exact identification of each of the carbon peaks. The HSQC was recorded at too low a chemical shift to see coupling between H_7 and the attached carbon, however C_7 could be assigned as the final remaining carbon with a single proton attached. The remaining carbons (C_2, C_3, C_D, and C_E) are represented by four low intensity peaks, characteristic of carbons without an attached proton.

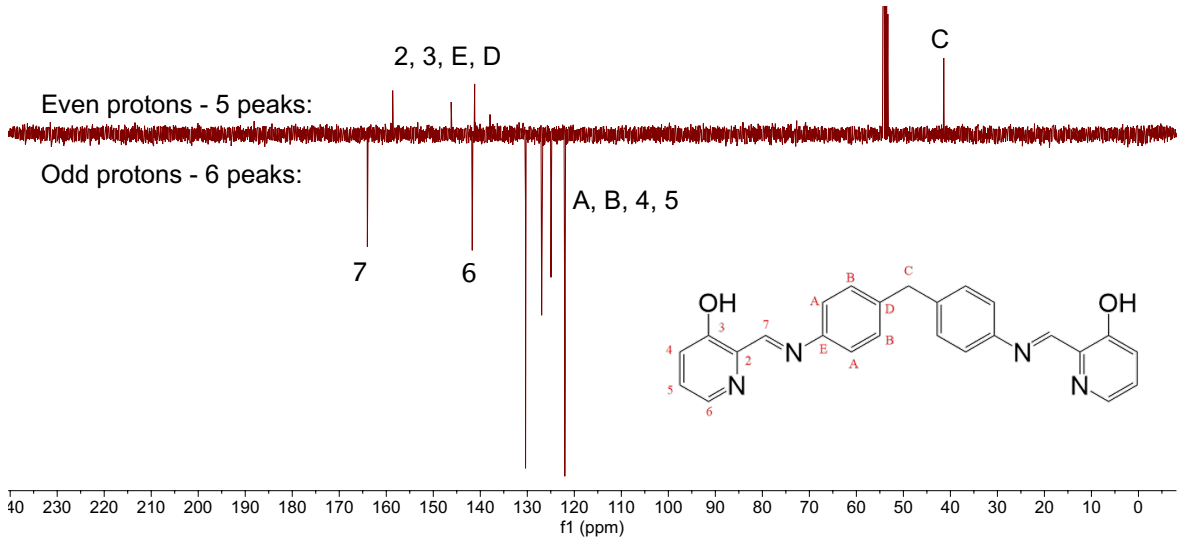

Figure 116: ^{13}C NMR (101 MHz, Methylene Chloride-d_2) of L_{3OH}.

To synthesise the uncapped cylinders ($[M_2(L_{3OH})_3]Cl_4$, M = Fe/Ni), the ligand was stirred with the desired metal chloride hydrate salt in methanol to a clear, coloured solution was observed. The solution was filtered and concentrated to precipitate in diethyl ether and the chloride salt collected by filtration.

The ^{1}H NMR spectrum of the iron complex (Figure 117) was too broad for splitting patterns to be observed, so assignments were made by comparison to the 4- and 5-hydroxy complexes. The methylene (H_C) proton peak is around 4 ppm across all the iron species, and the imine proton is a sharp peak with high chemical shift (H_7).

The pyridine proton in the 6 position (H_6) is always shielded in the electron cloud of the metal in the helicate structure, whereas the other pyridine protons (H_4 and H_5) are deprotected upon metal coordination. Broad peaks in the baseline have been assigned to the phenyl protons ($H_{A/B}$), however it is not possible to calculate the integration value for these peaks. The splitting of these peaks into two environments could be explained by inter-ligand π-stacking of the phenyl rings, which is normally averaged into one by fast ring spinning on the NMR timescale.

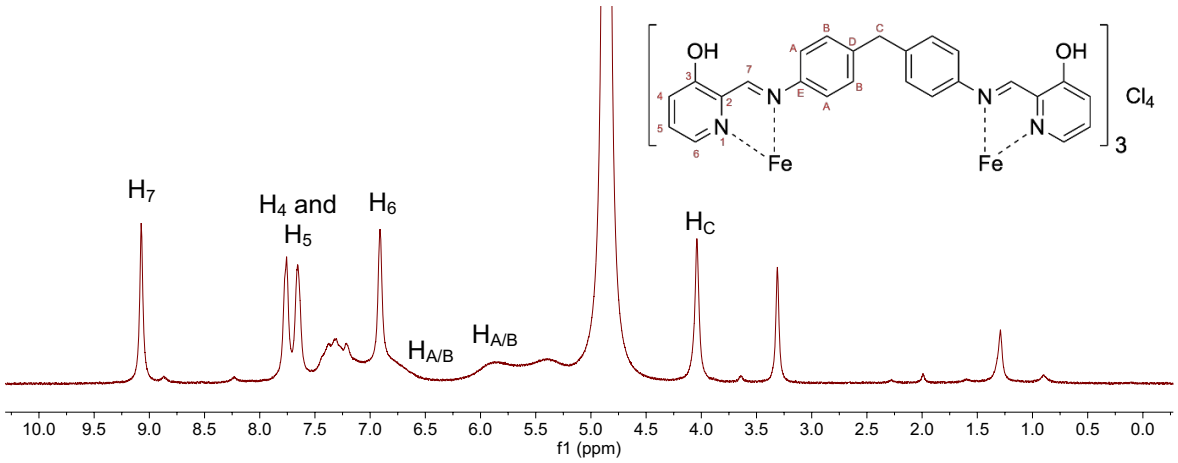

Figure 117: ^{1}H NMR (400 MHz, Methanol-d$_4$) of [Fe$_2$(L$_{3OH}$)$_3$]Cl$_4$.

The mass spectrum of the iron cylinder ([$Fe_2(L_{3OH})_3$]Cl_4, Figure 118) shows that the synthesis was successful with the mono-, di- and tri-cationic cylinder species observed, as well as the two-ligand species, two-metal species. Similar species were seen in the mass spectrum nickel cylinder ([$Ni_2(L_{3OH})_3$]Cl_4, Figure 119).

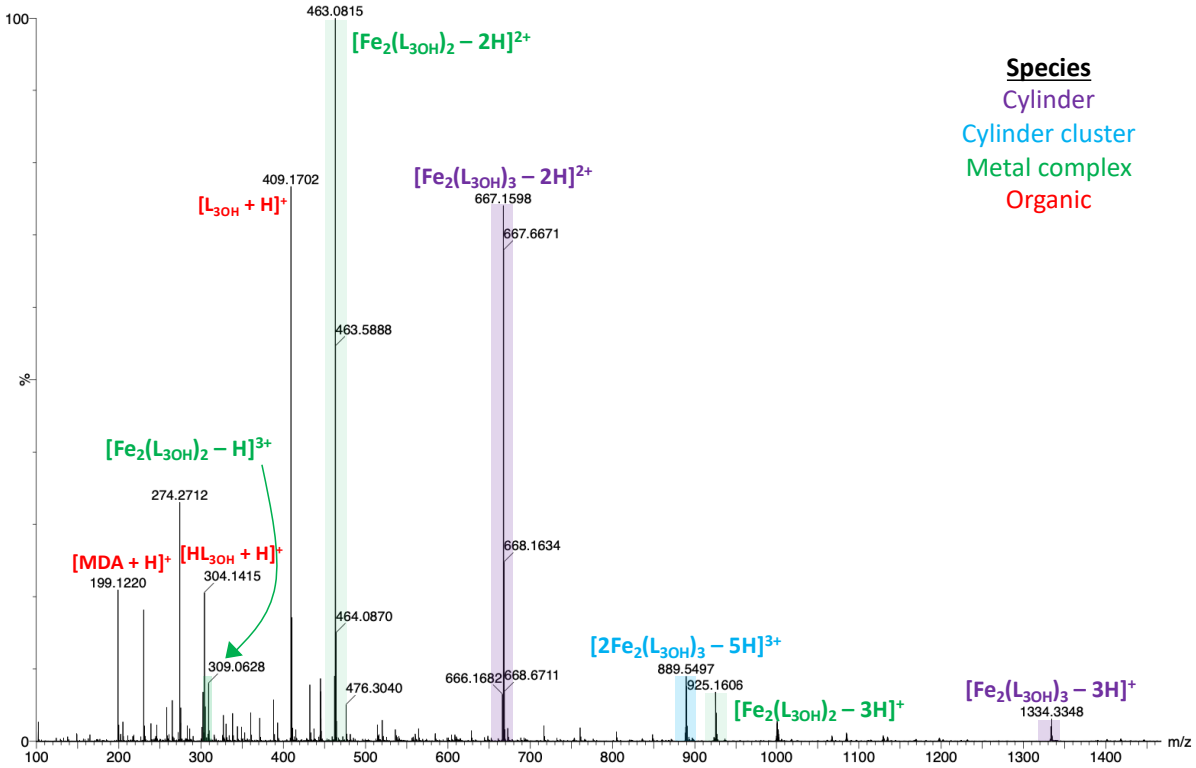

Figure 118: Mass spectrum (TOF ES+, MeOH) of $[Fe_2(L_{3OH})_3]Cl_4$.

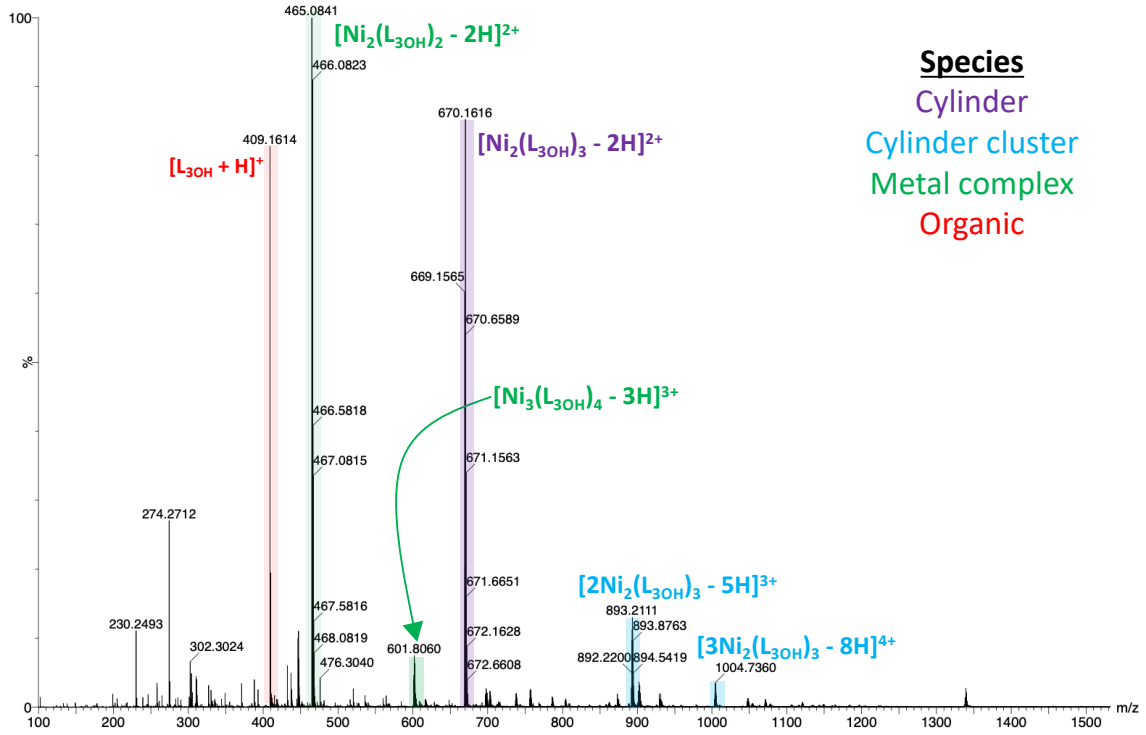

Figure 119: Mass spectrum (TOF ES+, MeOH) of $[Ni_2(L_{3OH})_3]Cl_4$.

Both mass spectra show the appearance of clusters of cylinders where multiple cylinders are analysed together, which could be due to hydrogen bonding between the terminal alcohol groups. The mass spectrum of the nickel complex also has a peak corresponding to the three metal, four ligand species ($[Ni_3(L_{3OH})_4]Cl_4$) which was also observed in the mass spectrum of the nickel 5-hydroxypyridine cylinder.

5.4.2. Capped 3-oxypyridine based cylinders ($[M_2(L_{3O}'')_3]Cl_4$)

Synthesis of the capped cylinder was attempted via the capped aldehyde and ligand. Alkylation of 3-hydroxypicolinaldehyde was achieved using similar conditions to the previously investigated hydroxypicolinaldehydes, following the procedure reported by A. Alouane *et al.* (Scheme 12)[3].

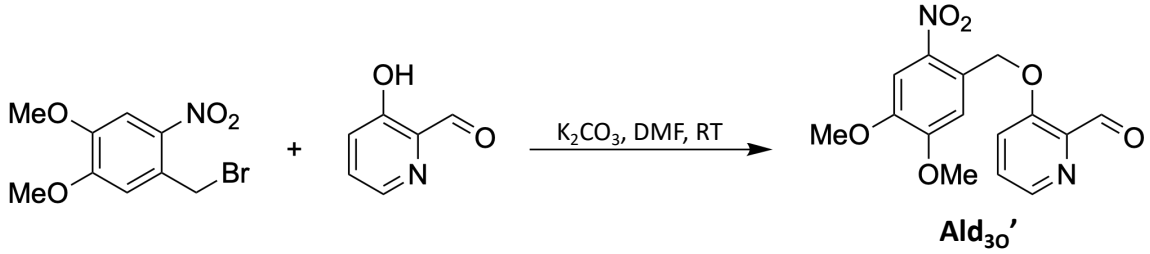

Scheme 12: Synthesis of Ald3O'.

3-Hydroxypicolinadelhyde, DMNB-Br and potassium carbonate were stirred in DMF for 3 hours before filtering to collected an off-white precipitate (68% yield) which was characterised by mass spectrometry (m/z = 319, $[M + H]^+$) and ^1H NMR (Figure 120). The product precipitated from the reaction solution with no uncapped aldehyde impurities so no further purification was required. TLC analysis of the reaction solution suggested that some unreacted aldehyde and DMNB-Br were still present so the reaction time should be extended if repeated.

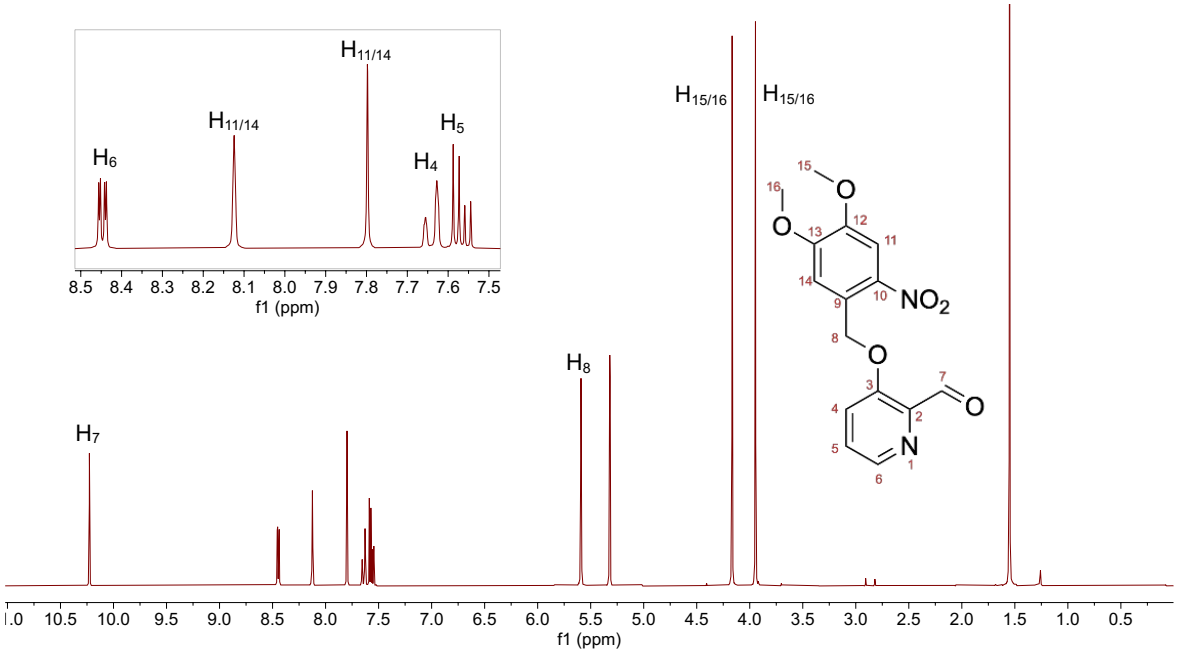

Figure 120: ^{1}H NMR (300 MHz, methylene chloride-d_2) of Ald_{3O}'.

An overnight reflux of the capped aldehyde (Ald_{3O}') with 4,4'-methylenedianiline in ethanol afforded the capped 3-oxypyridine based ligand (L_{3O}") as a pale-yellow powder which precipitated from the reaction solution in a 94% yield. The ligand was characterised by mass spectrometry (409 m/z, $[L_{3OH} + H]^+$) and ^{1}H NMR (Figure 121) which was assigned using the integration values and expected splitting patterns. The methylene bridge (H_8) and methoxy protons of the cap ($H_{15/16}$), and the central methylene unit (H_C) could all be assigned by their lower chemical shifts (< 6 ppm) and integration values. The imine proton (H_7) is a sharp singlet and the pyridine protons have characteristic coupling values which allows their identification (J_{H4-5} = 8.5 Hz, J_{H4-6} = 1.3 Hz, and J_{H5-6} = 4.5 Hz). The phenyl protons of the cap ($H_{11/14}$) appear as sharp singlet peaks and the phenyl protons of the spacer moiety appear as a multiplet ($H_{A/B}$) with higher integration in the aromatic region.

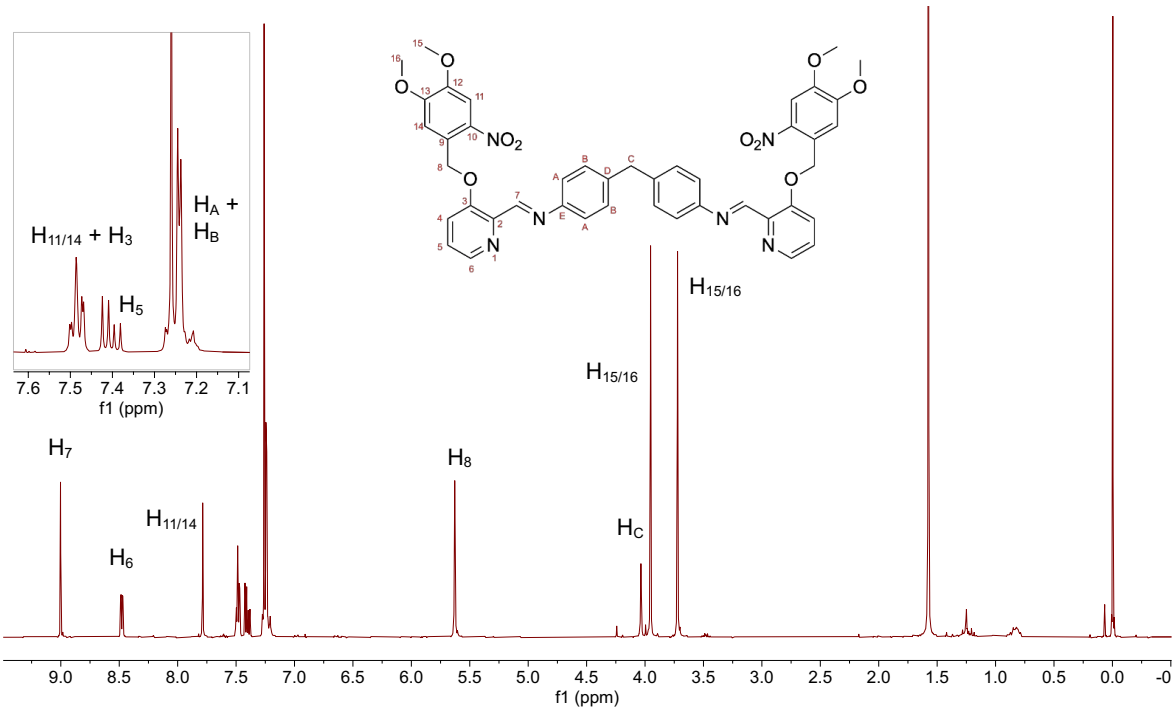

Figure 121: ^{1}H NMR (300 MHz, chloroform-d) of L_{3O}".

Iron chloride tetrahydrate and the capped ligand were dissolved in methanol and heated to reflux for 2 hours to synthesise the capped iron cylinder ($[Fe_2(L_{3O}")_3]Cl_4$). The cylinder was isolated by precipitation in diethyl ether and characterised by ^{1}H NMR (Figure 122). The pyridine protons can be identified via the coupling constant (H_4-H_5 = 8.8 Hz, H_5-H_6 = 5.4 Hz) and show the characteristic shifts (downfield for H_4 and H_5,upfield for H_6) caused by metal coordination. The imine proton (H_7) is assigned to a singlet peak at lower chemical shift than observed for the previous capped oxy-pyridine based cylinders. The benzyl protons of the cap (H_{11} and H_{14}) are assigned to two sharp peaks relatively unaffected by metal binding compared to the ligand whereas the methylene bridge protons (H_8) are diastereotopic in the cylinder complex and so are split into two roofed doublets with geminal coupling constants (J = 11.3 Hz). The phenyl protons ($H_{A/B}$) are assigned to broad peaks of unknown integration value in the baseline of the spectrum, similar to the uncapped ligand (Figure 117).

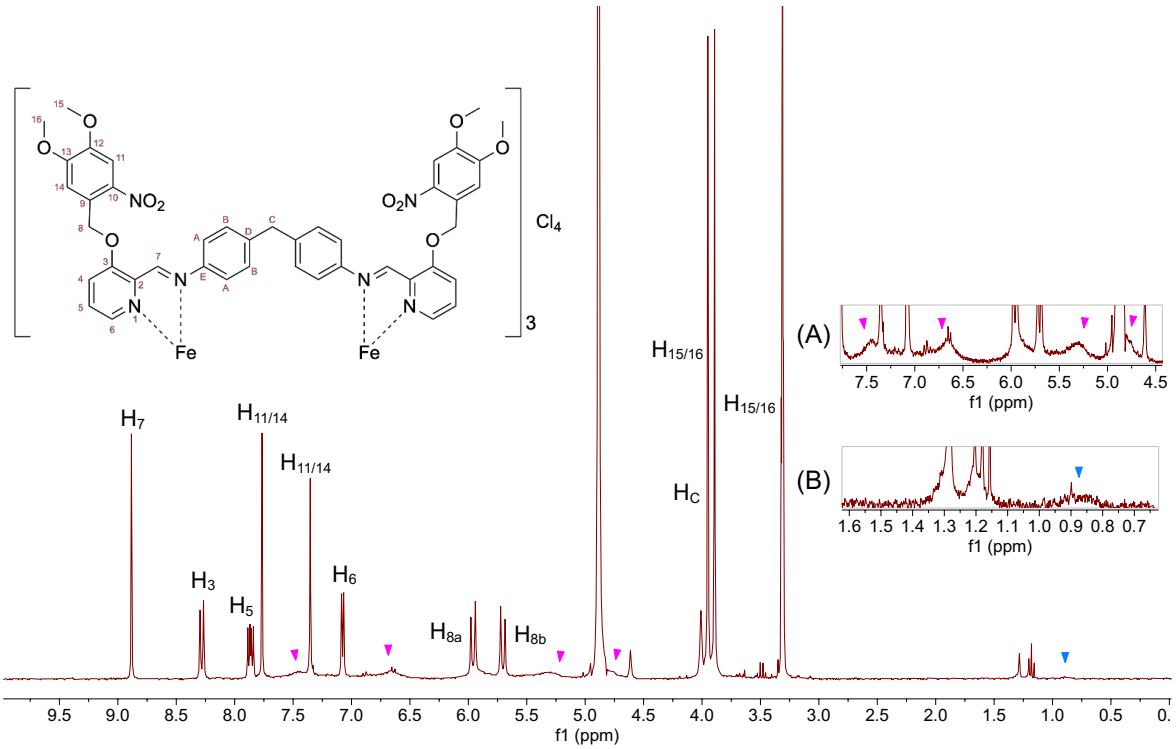

Figure 122: ^{1}H NMR (300 MHz, Methanol-d4) of $[Fe_2(L_{3O}'')_3]Cl_4$. Inset: Broad peaks highlighted by coloured arrows in the baseline between (A) 4.5 and 7.5 ppm, and (B) 0.6 and 1.6 ppm.

The structure is confirmed by the mass spectrum (Figure 123) which shows the fully capped cylinder has been formed along with the 5-capped species which may have formed due to photocleavage in ambient light. Other organic peaks which appear in the mass spectrum with a high relative abundance are background ions[6].

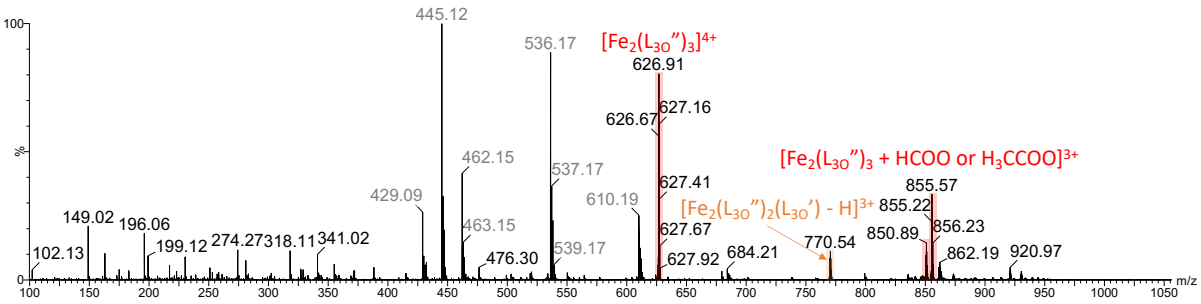

Figure 123: Mass spectrum (TOF ES+, MeOH) of $[Fe_2(L_{3O}'')_3]Cl_4$.

This process was repeated with the nickel chloride hexahydrate to form the nickel cylinder. After stirring overnight at reflux, the reaction mixture was filtered and the filtrate concentrated to precipitate in diethyl ether. This gave an orange powder product which displayed an unexpected variety of differently capped species in the mass spectrum (Figure 124). Regularly spaced peaks could be categorised into a 4+ charged and two 3+ charged series which almost match the series expected for the sequential loss of the photocleavable caps. The difference between the expected and observed peaks was identified as the addition of a methyl group. The mass spectrum was repeated in water instead of methanol to ensure that the observed peaks were not an artifact caused by replacement of the alcohol group upon ionisation. It is hypothesised that the DMNB caps are replaced by methyl groups in the presence of nickel (Figure 125).

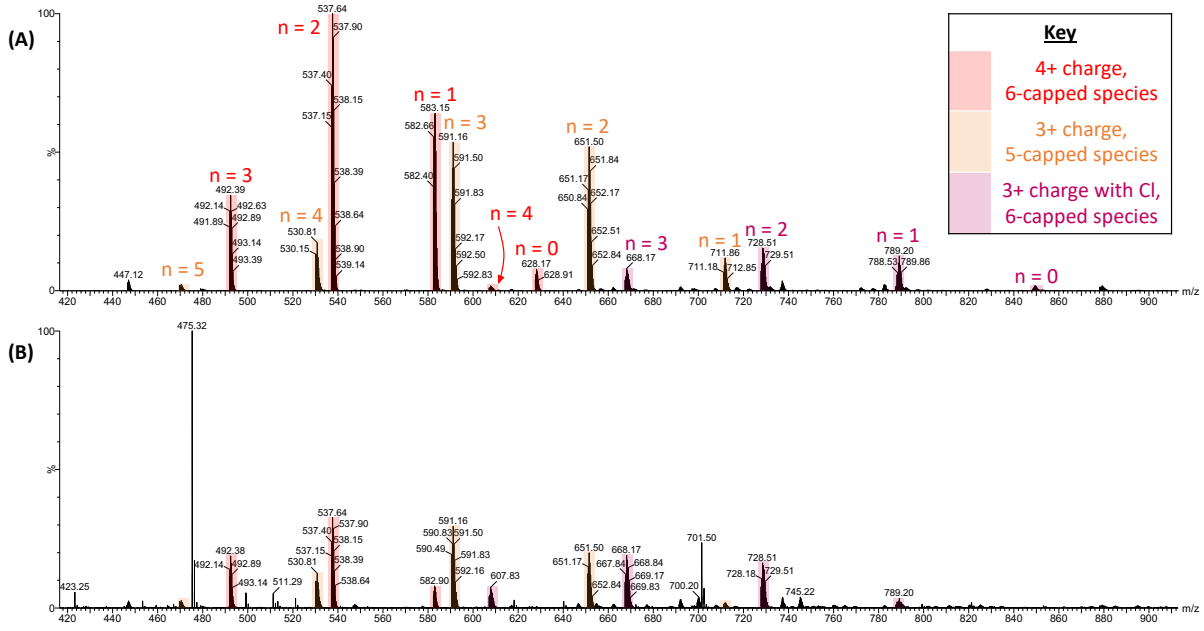

Figure 124: Mass spectra (TOF ES+, MeOH) of the product formed from two repeats (A and B) of complexing the capped ligand (L_{3O}") with nickel. Colour indicates the charge and overall number of caps (see key) and "n" refers to the number of caps which are CH_3 groups instead of DMNB.

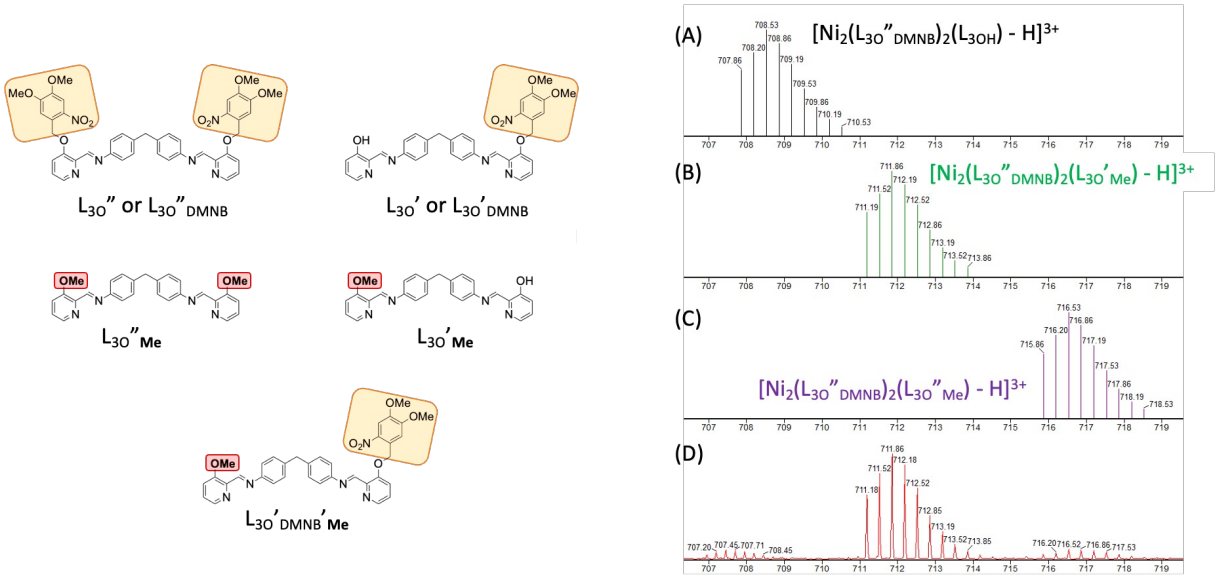

Figure 125: Possible ligand structures with different capping groups (left) and (right,D) part of the mass spectrum (TOF ES+, MeOH) of the product of the cylinder formation from the capped ligand with the calculated isotope patterns for (A) $[Ni_2(L_{3O}"_{DMNB})_2(L_{3OH}) - H]^{3+}$,(B) $[Ni_2(L_{3O}"_{DMNB})_2(L_{3O}'_{Me}) - H]^{3+}$, and (C) $[Ni_2(L_{3O}"_{DMNB})_2(L_{3O}"_{Me}) - H]^{3+}$.

This change in capping was not observed for the equivalent reaction with iron chloride or the formation of the nickel 4- and 5-hydroxypyridine cylinders. The specificity to the 3-oxypyridine could be due to the altered position of the alcohol group offering an alternative binding site for metal ions (Figure 126).

Expected coordination site: Alternative coordination site:

Figure 126: Alternative metal coordination by 3-hydroxypyridine.

Post-assembly modification of the 3-hydroxypyridine based cylinder offers an alternative route to the capped cylinder ($[Ni_2(L_{3O}")_3]Cl_4$) in which the nickel ions are

already coordinated so should not be free to react with the capping groups (Scheme 13).

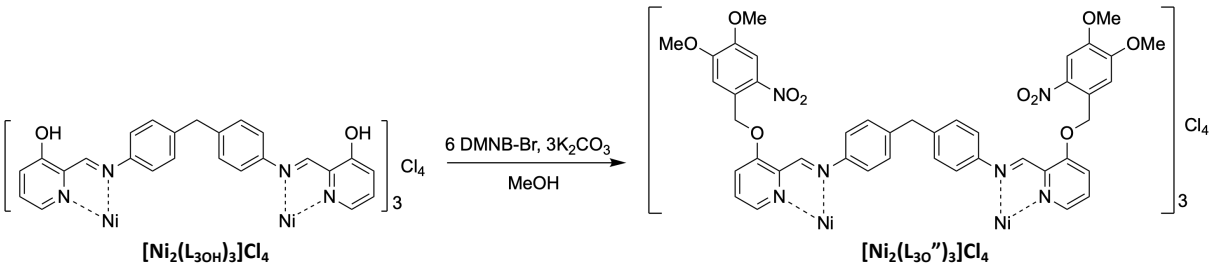

Scheme 13: Post-assembly modification of [$Ni_2(L_{3O}")_3Cl_4$) to form [$Ni_2(L_{3O}")_3Cl_4$).

An initial attempt was made using and excess of the alkylating agent (DMNB-Br, 9 equivalents) and base (K_2CO_3, 4.3 equivalents). The reaction was monitored by mass spectrometry (see Table 2 for assignments) over more than 19 hours (Figure 127). A range of partially capped cylinders were identified (between 0 and 4 caps) with different charges, but species where the cap was replaced by the methyl group were not observed indicating that this method did not give the unexpected side reaction as the formation from the ligand and was a viable route to the capped cylinder. The relative abundance of each differently capped cylinder does not change between the 2 and 20 hour spectra, with the singly capped species being the most prominent peak for both the 3+ and 2+ series despite an excess of DMNB-Br being used. An attempt to precipitate the partially capped cylinder product from solution via anion exchange to the hexafluorophosphate was unsuccessful as a precipitate did not appear to form.

Caps	Cylinder	Rotaxane
0	$[M_2(L_{OH})_3]$	$[M_2(L_{OH})_3.CB10]$
1	$[M_2(L_O')(L_{OH})_2]$	$[M_2(L_O')(L_{OH})_2.CB10]$
2	$[M_2(L_O'')(L_{OH})_2]$	$[M_2(L_O'')(L_{OH})_2.CB10]$
3	$[M_2(L_O')_3]$	$[M_2(L_O')_3.CB10]$
4	$[M_2(L_O'')_2(L_{OH})]$	$[M_2(L_O'')_2(L_{OH}).CB10]$
5	$[M_2(L_O'')_2(L_O')]$	$[M_2(L_O'')_2(L_O').CB10]$
6	$[M_2(L_O'')_3]$	$[M_2(L_O'')_3.CB10]$

Table 2: Key for the mass spectra assignments.

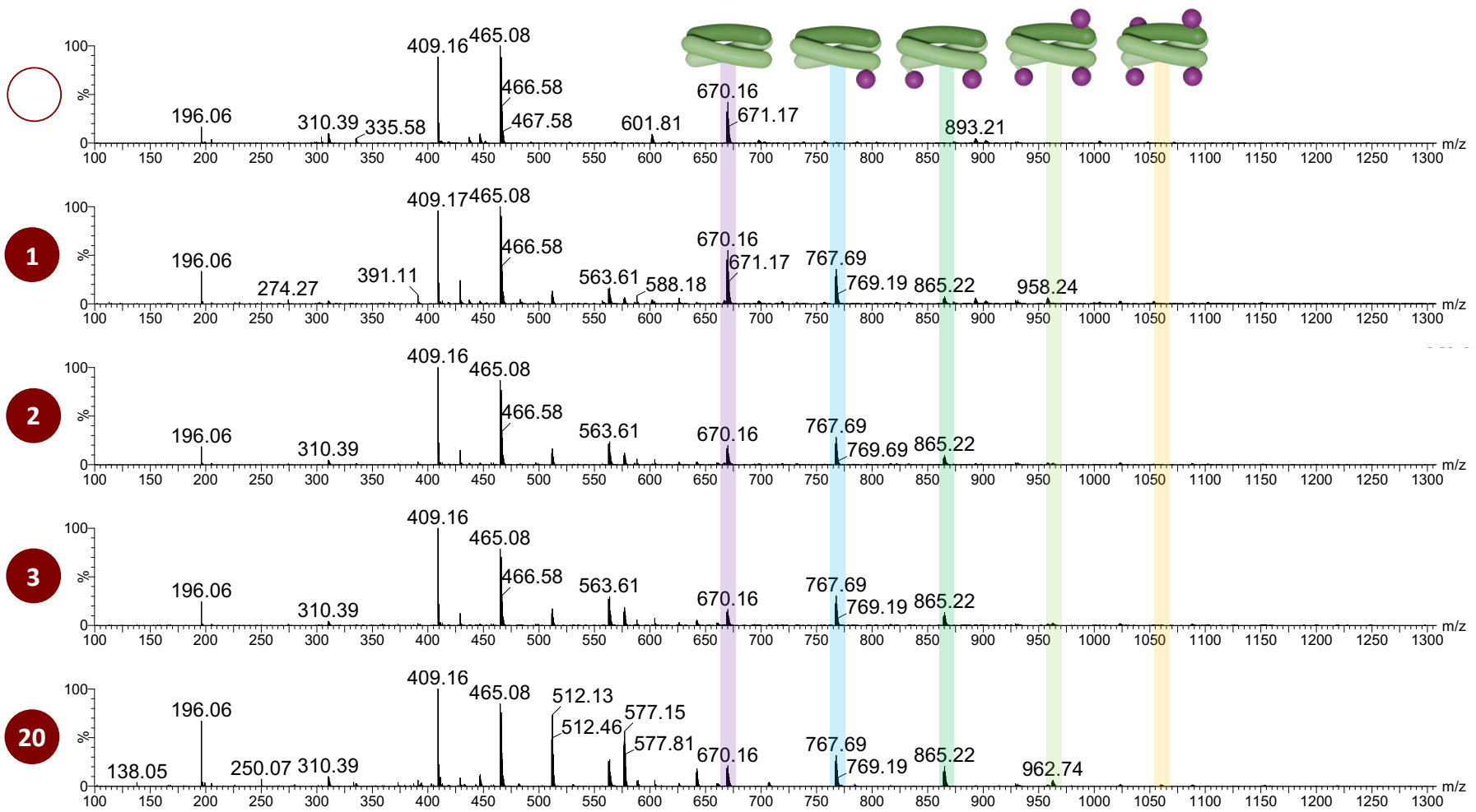

Figure 127: Mass spectra (TOF ES+, MeOH) of nickel cylinder capping reaction at different time points.

The alkylation reaction appears to stop soon after the reflux has started which could be due to a competing reaction of the starting materials. The DMNB-Br is known to undergo a photocleavage reaction in response to light, however the reaction was done under dark conditions. A similar degradation may occur due to the use of a base or application of heat to the reaction, which is suggested by the appearance of a peak for the photocleavage product (196 m/z, $[C_9H_9NO_4 + H]^+$). The synthesis was therefore adjusted to include the portion-wise addition of DMNB-Br to prevent the degradation of the reagent before alkylation of the cylinder.

Additions of 1.5 equivalents of the alkylating agent to the cylinder solution were made half-hourly until 6 equivalents of the cap had been added. The solvent system was also changed to 20% aqueous methanol in which the *pseudo*rotaxane can form, so it may be possible to form a rotaxane with the alternative hydroxypyridine cylinders by capping. Within the first 2 hours, where only 6 equivalents of DMNB-Br and 4 equivalents of the base have been used, the 6-capped species is observed in the mass spectrum (Figure 128 and Figure 129). Hourly additions of 1 excess equivalent of the alkylating agent were made for a total of 3 hours (9 total equivalents) to see if the reaction could be pushed to completion. No obvious change in the mass spectrum was observed between 2 and 5 hours suggesting that the alkylating agent is not the limiting factor (Figure 130).

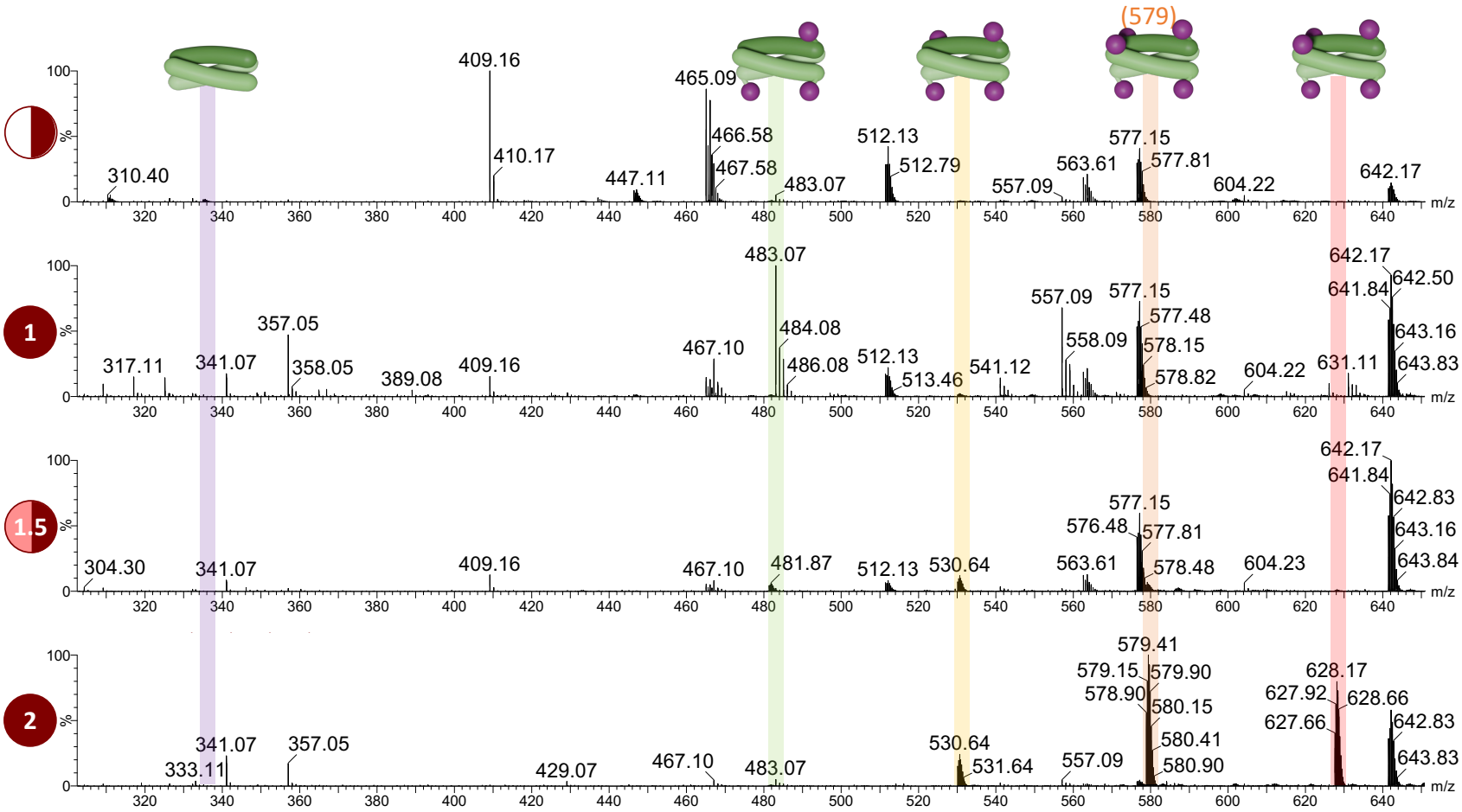

Figure 128: Mass spectra (TOF ES+, MeOH:H_2O, 300-650 m/z) of the capping reaction (20% MeOH, portion-wise addition of alkylating agent) at different time points (hours indicated in circles). The 4+ species are highlighted in colours corresponding to the number of caps each species possess.

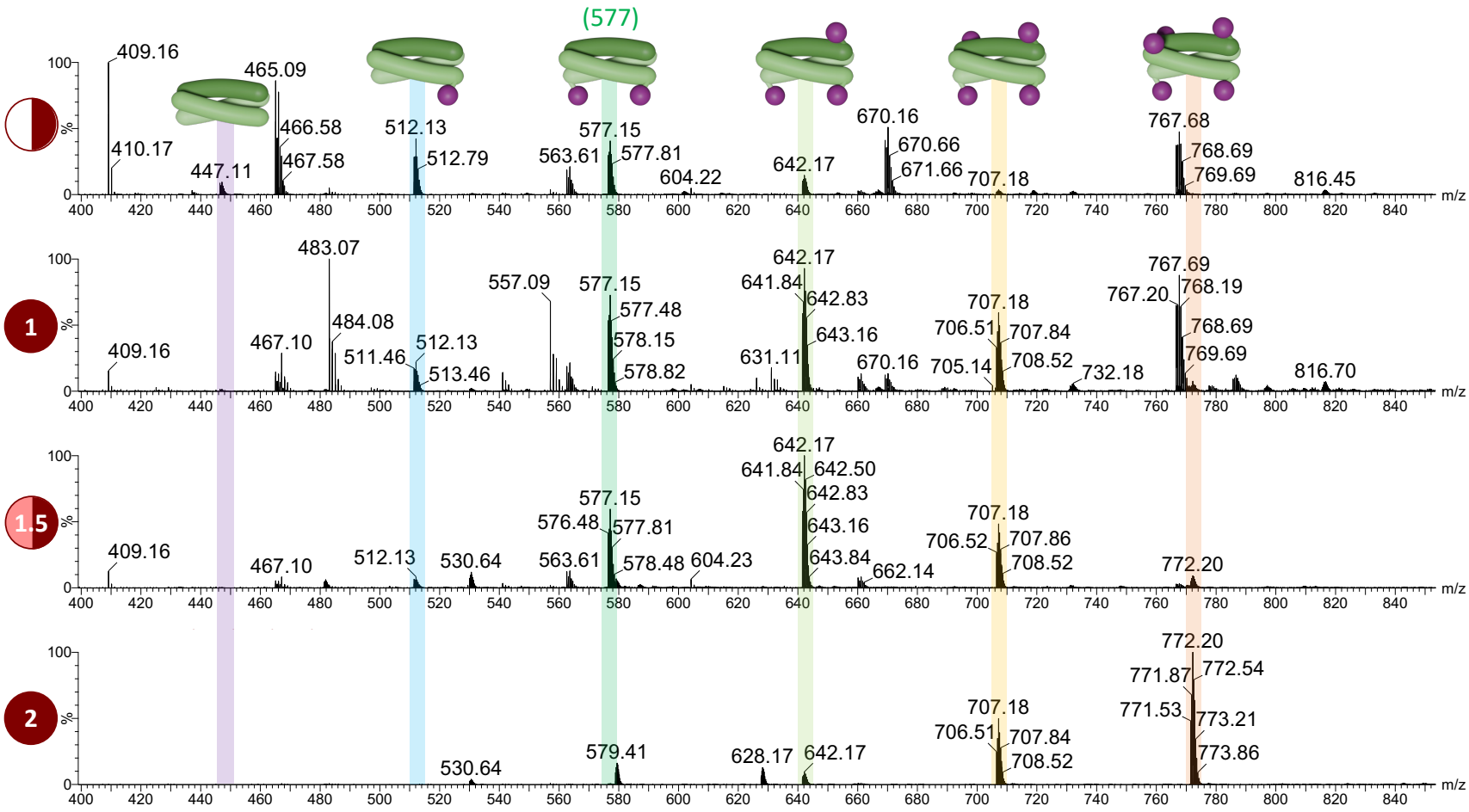

Figure 129: Mass spectra (TOF ES+, MeOH:H_2O, 400-850 m/z) of the capping reaction (20% MeOH, portion-wise addition of alkylating agent) at different time points. The 3+ species are highlighted.

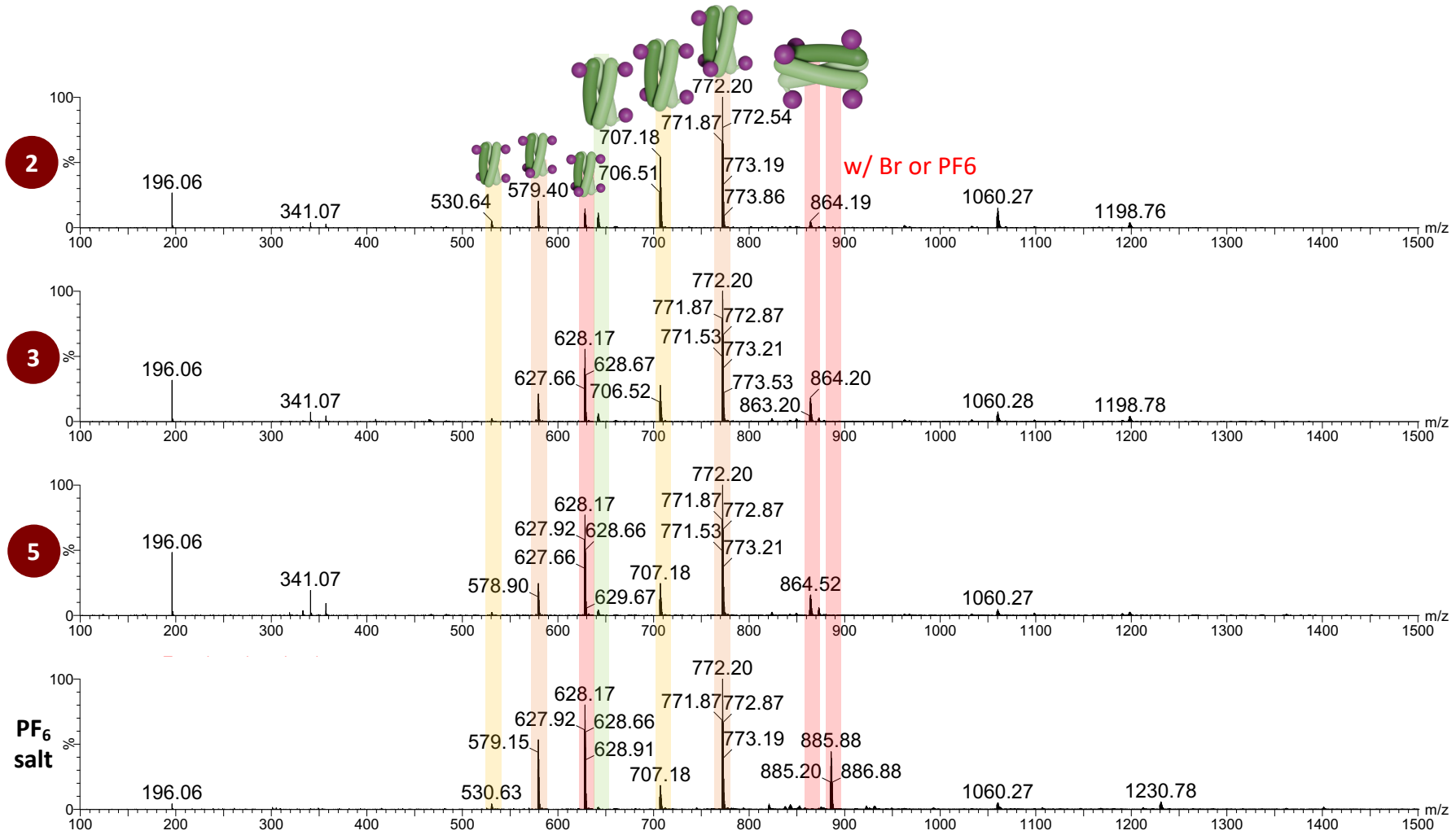

Figure 130: Mass spectra (TOF ES+, MeOH:H_2O) of the capping reaction (20% MeOH, portion-wise addition of alkylating agent) at different time points, followed by the mass spectrum (TOF ES+, MeCN) of the hexafluorophosphate product. The cylinder species are highlighted in colours corresponding to the number of caps each species possess.

Release of hydrobromic acid from degradation of the excess DMNB-Br could neutralise the base, preventing the deprotonation of the alcohol for nucleophilic attack. 3 equivalents of potassium carbonate (6 equivalents of a base, B^-) per cylinder are required for the deprotonation of every alcohol for alkylation. The pH of the reaction solution was recorded as pH 4 after the final addition of excess alkylating agent so an additional 1.5 equivalents of the base were added. The mass spectrum taken at 5 hours does not show a significant difference to the previous spectra, so the reaction was allowed to continue overnight and the capped cylinder was precipitated by anion exchange to the hexafluorophosphate salt and isolated. Both the 6-capped 3+ and 5-capped 2+ species are observed in the final mass spectrum with a hexafluorophosphate anion. A small peak for the 4-capped species is also present.

Multiple repeats of the reaction were attempted with varying amounts of the alkylating agent (7-18 equivalents), timings of the additions, and using water only as the solvent, and the reactions were monitored by mass spectrometry as above. Repeating the reaction in water gave similar results to the reaction in 20% methanol, so the use of 20% methanol was continued for the increased solubility of the uncapped cylinder starting reagent.

Using a large excess of the alkylating agent (18 equivalents, 3 times the 6 required equivalents) was attempted to increase the rate of reaction so that the product could be isolated before any possible degradation. This included addition of the 18 equivalents directly to the cylinder solution (“direct addition”) and halving the time between portion-wise additions (1.5 equivalents every 15 minutes, then 3 equivalents every 30 minutes, up to 18 total equivalents, “portion-wise addition”). A final attempt included the same portion-wise addition of 1.5 equivalents every 15 minutes, with an

additional 12 equivalents added directly to the solution after 1 hour with an additional 4 equivalents of the base (“portion-wise addition with excess base”). Direct addition gave predominantly the 5- and 6-capped species in less than 60 minutes but showed no further increase of the 6 capped peak by mass spectrometry (Figure 131). The two portion-wise addition reactions (with and without excess base) showed the presence of the 3-6 capped cylinders after 60 minutes but gave very similar results to the direct addition after 2 and 3 hours. The addition of excess base did not appear to push the reaction further towards the fully capped species.

When scaling up the reaction, additions of 1.5 equivalents were made every 15 minutes for 1 hour followed by the addition of 6 further equivalents of alkylating agent, and 4 further equivalents of base. The product was purified by anion exchange but showed a lower degree of capping overall (Figure 132A), possibly due to insufficient mixing which had been observed in previous attempts. A medium scale reaction was therefore attempted with additions of 1.5 equivalents of the alkylating agent every 30 minutes. The reaction was followed by mass spectrometry with further additions of the alkylating agent (1 equivalent at 30, 60 and 90 minutes after the initial 6 equivalents were added), base (after 3 excess equivalents of alkylating agent) and again alkylating agent (1 equivalent) were made to see if the reaction could be pushed to yield the fully capped cylinder as the product, exclusively. The helicate products were isolated by anion conversion to give product containing between 4 and 6 capped cylinders by mass spectrometry (Figure 132B).

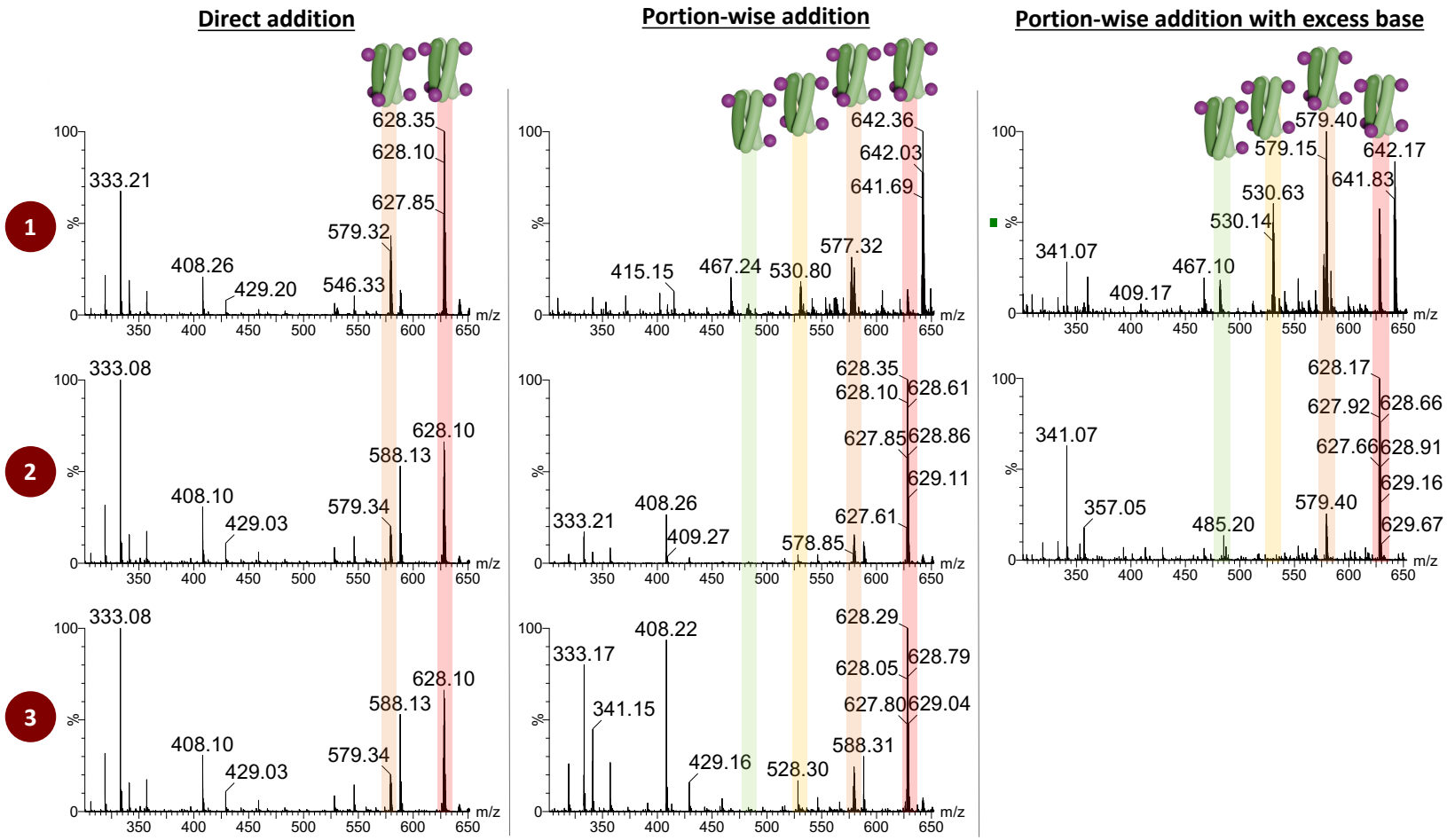

Figure 131: Mass spectra (TOF ES+, MeOH:H_2O) of various capping reactions with 18 equivalents of the alkylating agent at different time points (1, 2, and 3 hours, as indicated in circles. The 4+ species are highlighted in colours corresponding to the number of caps each species possess.

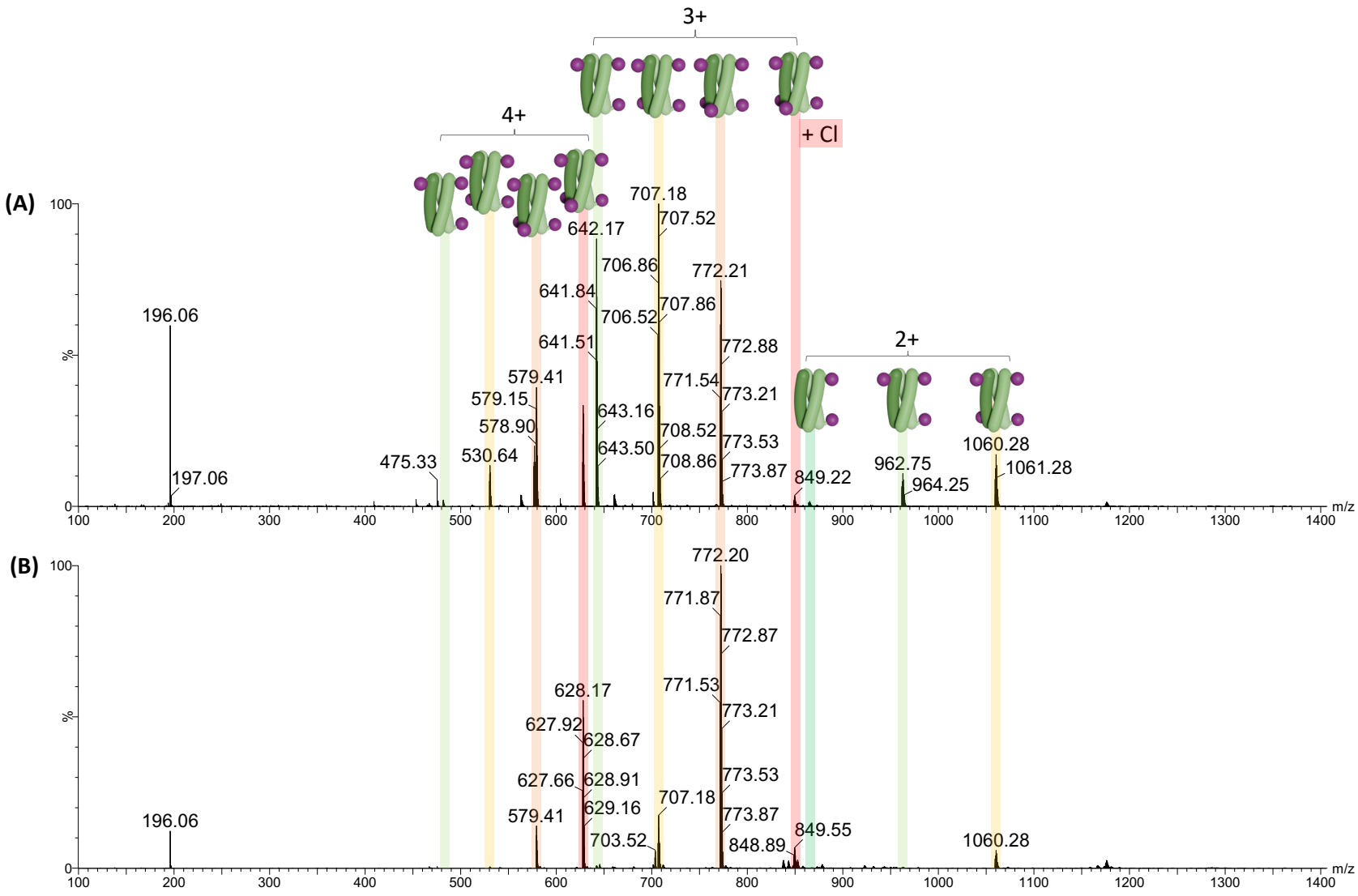

Figure 132: Mass spectra (TOF ES+, MeOH) of the scaled up capping reactions with (A) 15 minute and (B) 30 minute intervals between additions. The cylinders are highlighted in colours corresponding to the number of caps each species possess.

5.5. Conclusions

The capped iron cylinder ($[Fe_2(L_{3O}")_3]Cl_4$) was successfully synthesised via the capped ligand ($L_{3O}"$) similar to the 4- and 5-oxypyridine equivalents, however when metal complexation was attempted with nickel, capping groups were replaced with methylated species. Synthesis of the capped nickel cylinder ($[Ni_2(L_{3O}")_3]Cl_4$) was instead attempted via a capping method, starting from the uncapped nickel cylinder ($[Ni_2(L_{3OH})_3]Cl_4$). The final product gave a helical product with between 4-6 caps for a larger scale reaction, and only 5 and 6 capped species for smaller scale reactions. The reaction could not be optimised to exclusively produce the fully capped cylinder by mass spectrometry, however this is also not achieved for the synthesis of the cylinder via the capped ligand, which could suggest that ambient light exposure or heat is causing the appearance of lesser capped species. The capping reaction is therefore deemed equally useful for the production of the capped species, especially on a small scale.

5.6. List of References

1 A. Lumetzberger, W. Löwe, M. Weber and P. Luger, *J. Heterocycl. Chem*., 2007, **44**, 155–159.

2 S. A. Usachev, B. I. Usachev and V. Y. Sosnovskikh, *Chem. Heterocycl. Comp.*, 2017, **53**, 1294–1301.

3 A. Alouane, R. Labruère, K. J. Silvestre, T. Le Saux, F. Schmidt and L. Jullien, *Chem. Asian J.*, 2014, **9**, 1334–1340.

4 C. A. J. Hooper, L. Cardo, J. S. Craig, L. Melidis, A. Garai, R. T. Egan, V. Sadovnikova, F. Burkert, L. Male, N. J. Hodges, D. F. Browning, R. Rosas, F. Liu, F. V. Rocha, M. A. Lima, S. Liu, D. Bardelang and M. J. Hannon, *J. Am. Chem. Soc.*, 2020, **142**, 20651–20660.

5 J. S. Craig, PhD Thesis, University of Birmingham, 2023.

6 ESI+ Common Background Ions, https://www.waters.com/webassets/cms/support/docs/bkgrnd_ion_mstr_list.pdf, (accessed January 2024).

6. PHOTOCLEAVAGE OF OXYPYRIDINE BASED COMPLEXES

6.1. Photocleavage Studies

As with the imidazole-based cylinders (Chapter 3), photocleavage was investigated primarily by UV-visible spectroscopy and mass spectrometry. These techniques were chosen as UV-visible spectroscopy can quantitatively measure changes to the overall solution between irradiations without affecting the sample. This is complimented by mass spectrometry which is used to identify the species contributing to this overall effect.

6.1.1. 5-hydroxypyridine based cylinders

6.1.1.1. Absorbance

The absorbance spectrum for the uncapped ($[M_2(L_{5OH})_3]Cl_4$), capped ($[M_2(L_{5O}")_3]Cl_4$) and rotaxanated ($[M_2(L_{5O}")_3.CB10]Cl_4$) species was recorded for both the iron and nickel cylinders.

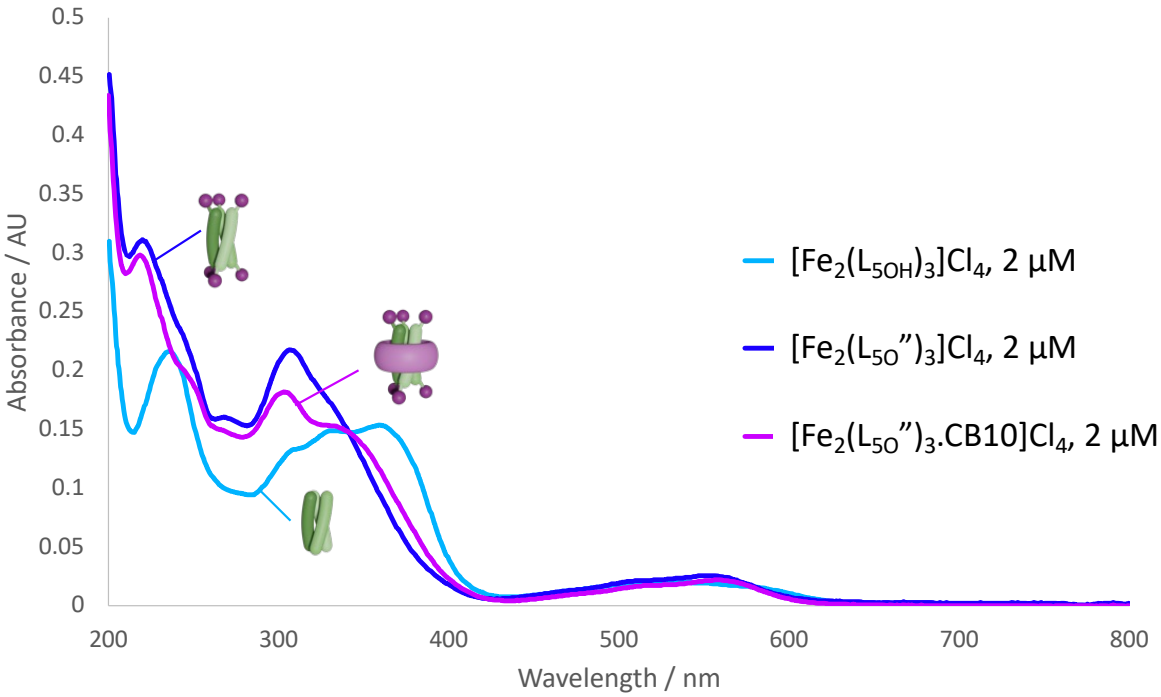

Figure 133: UV-visible absorbance of $[Fe_2(L_{5OH})_3]Cl_4$, $[Fe_2(L_{5O}")_3]Cl_4$ and $[Fe_2(L_{5O}")_3.CB10]Cl_4$ in 2 µM methanolic (cylinders) or aqueous (rotaxane) solutions.

All iron species (Figure 133) show a peak in absorbance between 500-600 nm caused by the metal to ligand charge transfer band (MLCT) indicating similar metal coordination between each species. At shorter wavelengths (200-400 nm) the absorbance of the uncapped ($[Fe_2(L_{5OH})_3]Cl_4$) and capped ($[Fe_2(L_{5O}")_3]Cl_4$) cylinders differs as the uncapped cylinder has less intense absorbance peaks at slightly longer wavelengths than the capped cylinder. There are only small differences between the capped cylinder and the rotaxanate ($[Fe_2(L_{5O}")_3.CB10]Cl_4$) indicating that the absorbance is primarily dependent on the complex and not the macrocyclic ring.

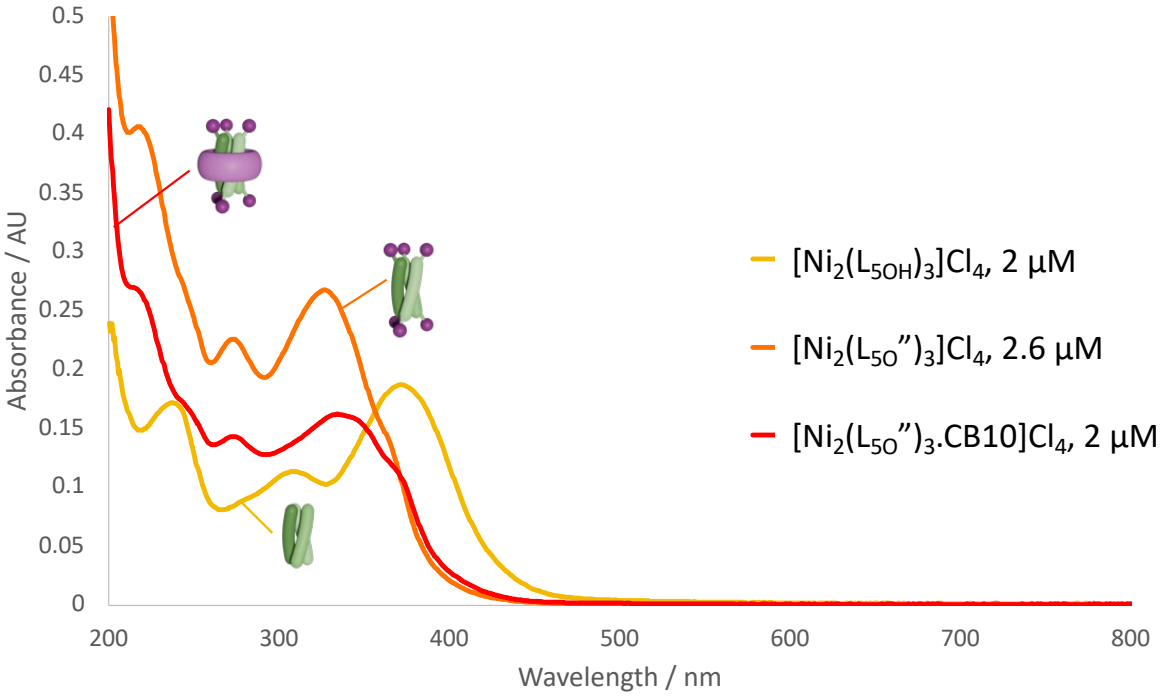

Figure 134: UV-visible absorbance of $[Ni_2(L_{5OH})_3]Cl_4$, $[Ni_2(L_{5O}")_3]Cl_4$ and $[Ni_2(L_{5O}")_3.CB10]Cl_4$ in methanolic (cylinders) or aqueous (rotaxane) solutions.

A similar trend is observed for the nickel species (Figure 134) as the uncapped cylinder ($[Ni_2(L_{5OH})_3]Cl_4$) has peaks at slightly longer wavelengths when compared to the capped cylinder ($[Ni_2(L_{5O}")_3]Cl_4$) and the addition of the macrocycle does not cause a significant difference in the absorbance of the rotaxane in comparison with the capped cylinder.

The absorbance coefficient (epsilon value, ε) was assessed for each species which requires the measurement of the absorbance at different sample concentrations. A linear relationship observed between absorbance and concentration for the capped cylinders and rotaxanes, following the Beer-Lambert Law, however the absorbance of the uncapped cylinders changes with concentration (Figure 135).

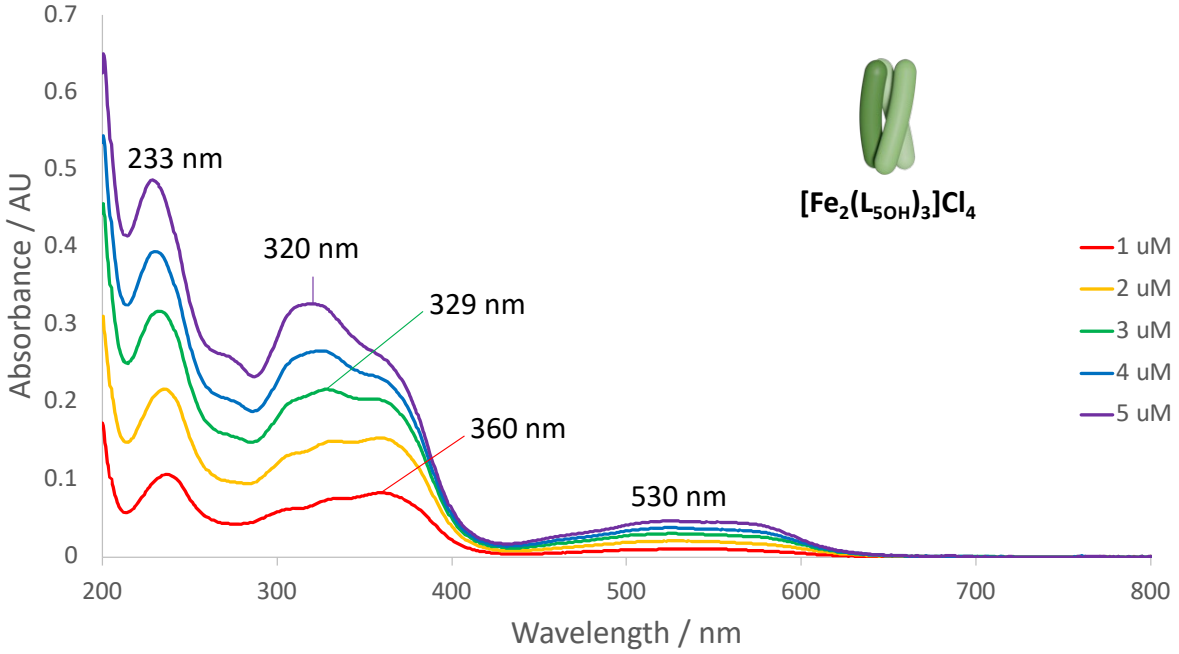

Figure 135: Averaged UV-visible spectrum of $[Fe_2(L_{5OH})_3]Cl_4$ at different concentrations in MeOH.

The absorbance maximum at the shortest wavelength for the uncapped iron cylinder ($[Fe_2(L_{5OH})_3]Cl_4$ shows a gradual blue shift (to shorter wavelength) with increasing concentration from 237 nm to 229 nm (at 1 μM and 5 μM, respectively). Between 300 and 400 nm the low concentration absorbance maximum is at 360 nm with two shouldering peaks observed at shorter wavelengths. The contribution of these shouldering peaks increases with concentration until they are larger than the peak at 360 nm, changing the maximum absorbance to 329 nm at 3 μM and then 320 nm by 5 μM. The peak at 530 nm is too broad to accurately assign a maximum absorbance.

A similar effect is observed for the absorbance of the uncapped nickel cylinder ($[Ni_2(L_{5OH})_3]Cl_4$, Figure 136). The absorbance maximum at the shortest wavelength shows a blue shift from 237 nm to 225 nm with increasing concentration (1 μM to 8 μM, respectively). Similarly the absorbance at 366 nm shifts to 370 nm (1 μM to 5 μM, respectively) as the peak sharpens with increasing concentration. Peaks at 276 nm

and 345 nm (measured at 8 μM) increase in intensity with increasing concentration overwhelming the peak at 306 nm (measured at 1 μM).

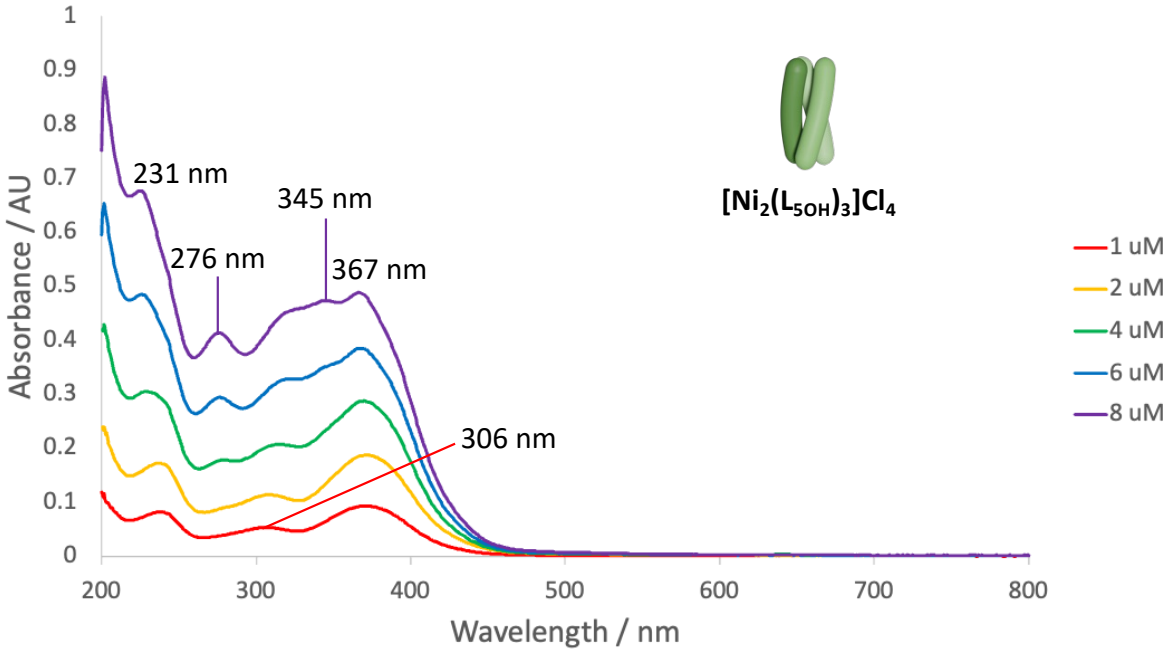

Figure 136: Average UV-visible spectrum of $[Ni_2(L_{5OH})_3]Cl_4$ at different concentrations in MeOH.

Complete degradation of the sample would cause a decrease in the absorbance while precipitation would cause an increase of noise in the spectrum due to scattering caused by particles in solution, neither of which is observed. Concentration dependent changes in complex characteristics can be due to aggregation or interaction between individual complexes. This change is only observed for the uncapped species containing free alcohol groups at the ends of the helicates which may be capable of hydrogen bonding between the cylinders.

These changes are not entirely dependent on concentration as Figure 135 and Figure 136 show the average of three scans, however the intensity of the peaks in each of the averaged spectra is not consistent. This is more pronounced for the nickel species due to the increased maximum concentration (8 μM against 5 μM). Changes

in the absorbance spectrum are therefore due to both the concentration and additional factors such as time allowed for the sample to dissolve, which was not controlled.

6.1.1.2. Photocleavage of the iron complexes

A 2 μM solution of each species was irradiated at 5 minute time intervals for 30 minutes, after which intervals were increased to 10 minutes. After each irradiation, the sample was mixed using a pipette and a small amount of the solution was taken for mass spectrometry. The absorbance of the sample was measured before continuing to irradiate the sample. Mass spectra in this Chapter have been assigned following the key in Table 3.

Caps	Cylinder	Rotaxane
0	$[M_2(L_{OH})_3]$	$[M_2(L_{OH})_3.CB10]$
1	$[M_2(L_O')(L_{OH})_2]$	$[M_2(L_O')(L_{OH})_2.CB10]$
2	$[M_2(L_O'')(L_{OH})_2]$	$[M_2(L_O'')(L_{OH})_2.CB10]$
3	$[M_2(L_O')_3]$	$[M_2(L_O')_3.CB10]$
4	$[M_2(L_O'')_2(L_{OH})]$	$[M_2(L_O'')_2(L_{OH}).CB10]$
5	$[M_2(L_O'')_2(L_O')]$	$[M_2(L_O'')_2(L_O').CB10]$
6	$[M_2(L_O'')_3]$	$[M_2(L_O'')_3.CB10]$

Table 3: Key for assignments in mass spectra (M = Fe/Ni).

The uncapped iron cylinder ($[Fe_2(L_{5OH})_3]Cl_4$, Figure 137A) shows a small decrease in absorbance over 60 minutes, but no change in the wavelengths being absorbed. This could suggest a small decrease in the concentration of the cylinder however it should also be considered that the uncapped cylinder absorbance is dependent on other factors as discussed previously (Figure 135). The overall decrease in peak height was measured at the three main peaks in the spectrum (235 nm, 332 nm, and 523 nm), which showed a decrease of less than 10% over the one hour irradiation period (6%, 6%, and 7% respectively). Peaks assigned to the

uncapped cylinder ($[Fe_2(L_{5OH})_3]Cl_4$) are visible in the mass spectrum throughout the 60 minutes of irradiation time (Figure 138).

The absorbance peaks of the capped cylinder ($[Fe_2(L_{5O}")_3]Cl_4$, Figure 137B) decrease in intensity while a new set of absorbance peaks increase in intensity with increasing irradiation time. The new peaks appear at longer wavelengths than peaks of the capped cylinder, and after 60 minutes the most intense peak between 300 and 400 nm switches from the peak at 306 nm to a peak at 326 nm. The peak at 221 nm also shows a gradual red shift to 232 nm after 60 minutes of irradiation. After irradiating the absorbance spectrum more closely resembles the uncapped cylinder (Figure 133) than the capped cylinder. The mass spectrum of the iron capped cylinder before irradiation shows the fully capped cylinder is present (627 m/z, $[Fe_2(L_{5O}")_3]^{4+}$), however after 60 minutes of irradiation the lesser capped species (1-5 caps) are observed, particularly as 3+ charged species (Figure 139, Figure 140, and Figure 141). The peaks in the 5 and 30 minute spectra are not visible due to organic peaks appearing in both which have a high relative abundance.

The absorbance of the rotaxane ($[Fe_2(L_{5O}")_3.CB10]Cl_4$, *Figure 137*C) also shows a decrease in absorbance over the 60 minutes of irradiation which varies between the peaks. There is a 30% decrease in the height of the peak at 303 nm but only a 12% decrease in the height of the peak at 329 nm. The fully capped iron rotaxane is present in the mass spectrum prior to irradiation (1042 m/z, $[Fe_2(L_{5O}")_3.CB10]^{4+}$) and species with fewer caps with increasing irradiation time (Figure 142). The decapped pseudo-rotaxane is observed after 30 minutes of irradiation (749 m/z, $[Fe_2(L_{5OH})_3.CB10]^{4+}$).

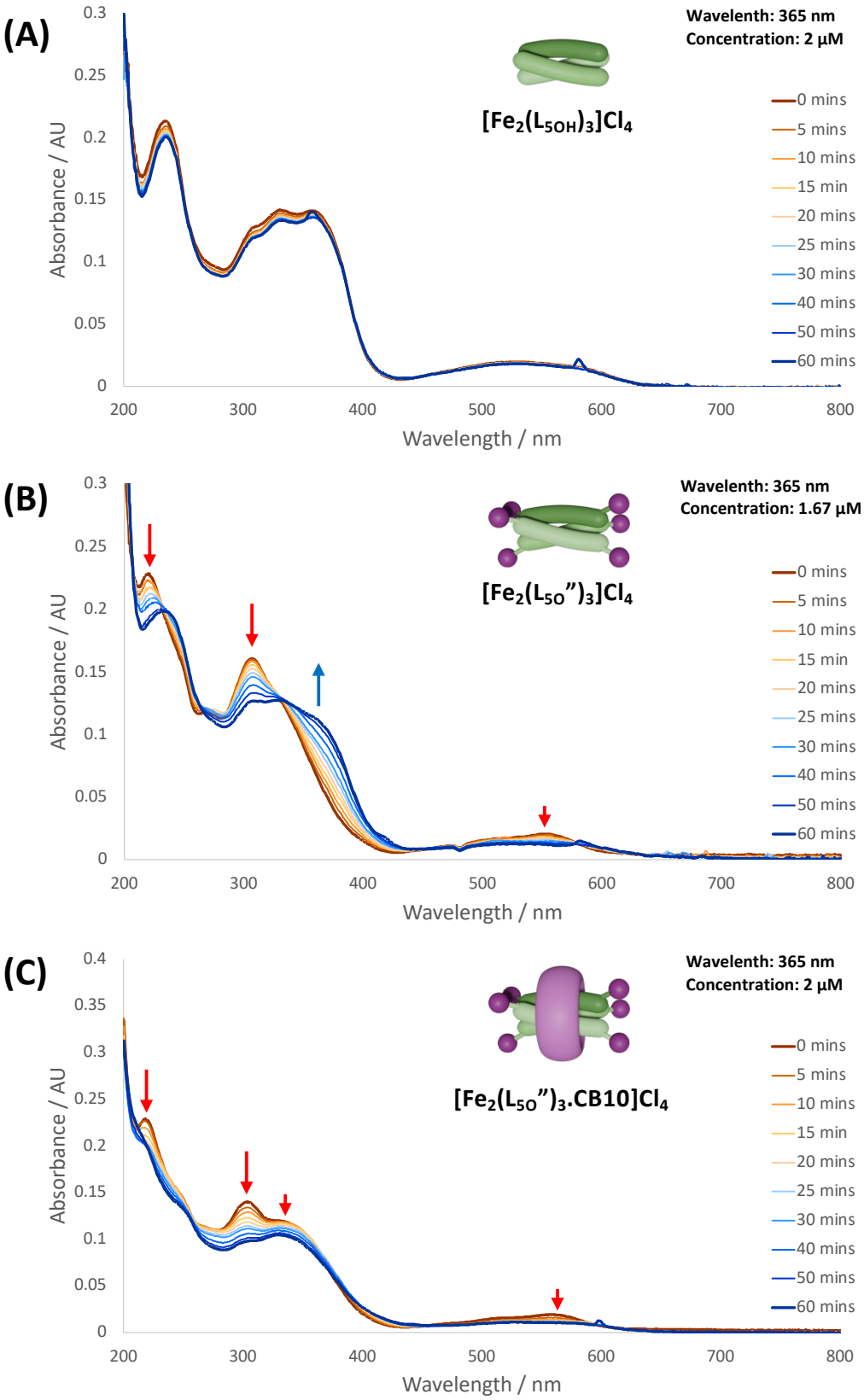

Figure 137: UV-visible absorbance of the (A) $[Fe_2(L_{5OH})_3]Cl_4$, (B) $[Fe_2(L_{5O''})_3]Cl_4$, and (C) $[Fe_2(L_{5O''})_3.CB10]Cl_4$ in 2 µM methanolic (cylinders) or aqueous (rotaxane) solutions after increasing irradiation times.

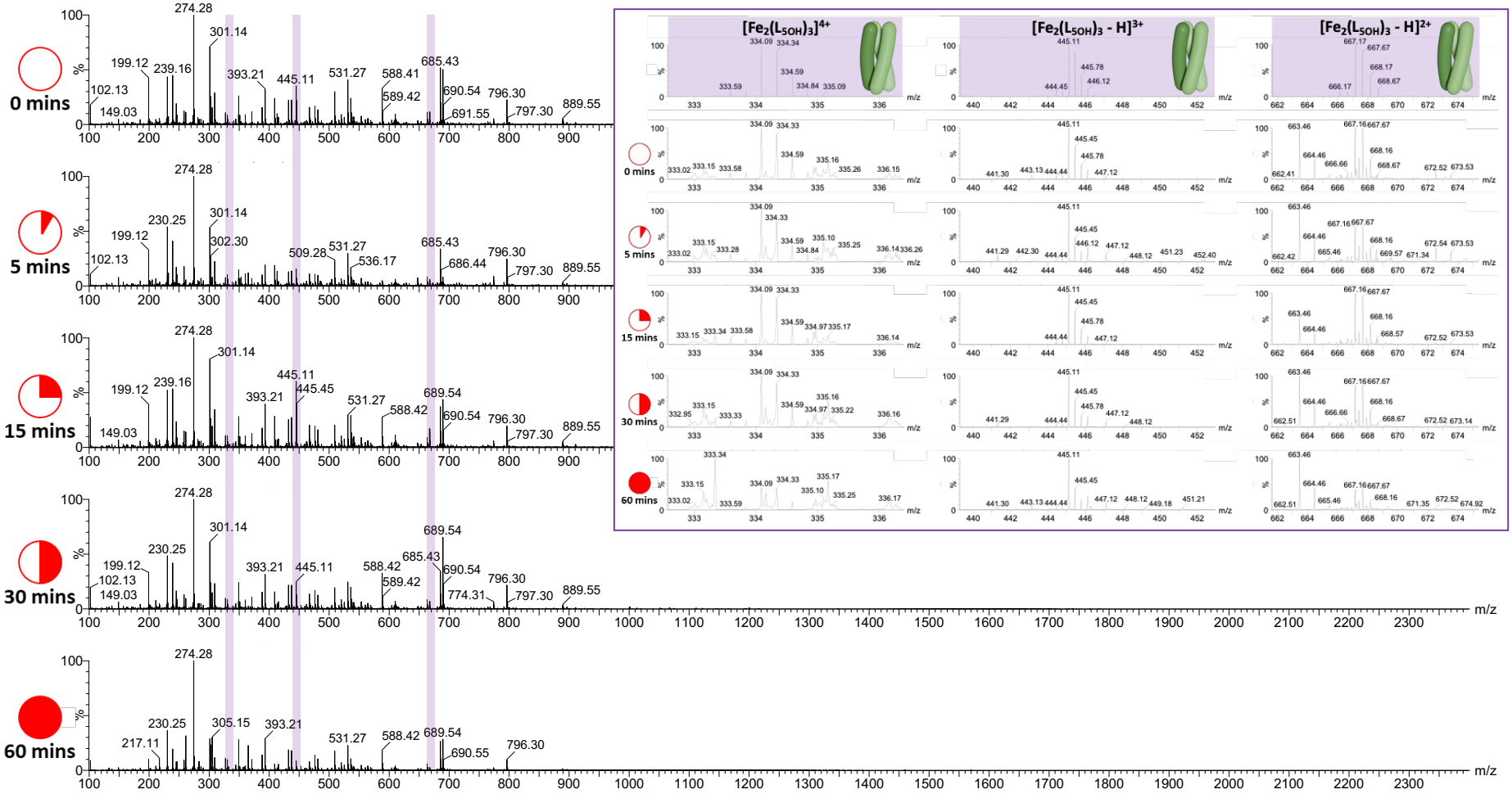

Figure 138: Mass spectra (TOF ES+, MeOH) of $[Fe_2(L_{5OH})_3]Cl_4$ over 60 minutes of irradiation highlighting the differently charged species, and inset image showing each of the highlighted peaks compared to their isotope patterns.

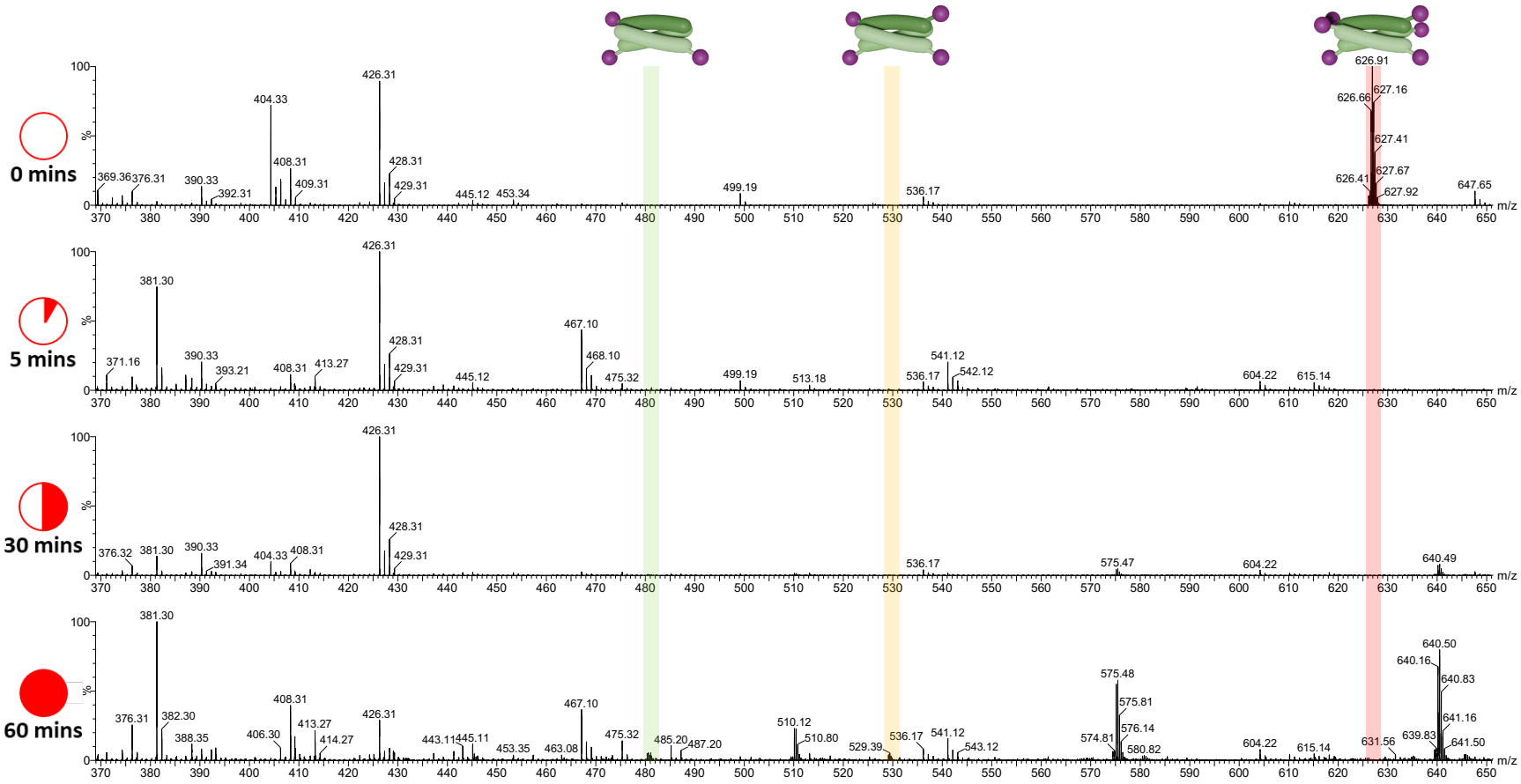

Figure 139: Mass spectra (TOF ES+, MeOH, 370-650 m/z) of $[Fe_2(L_{5O}")_3]Cl_4$ over 60 minutes of irradiation highlighting the 4+ charged species.

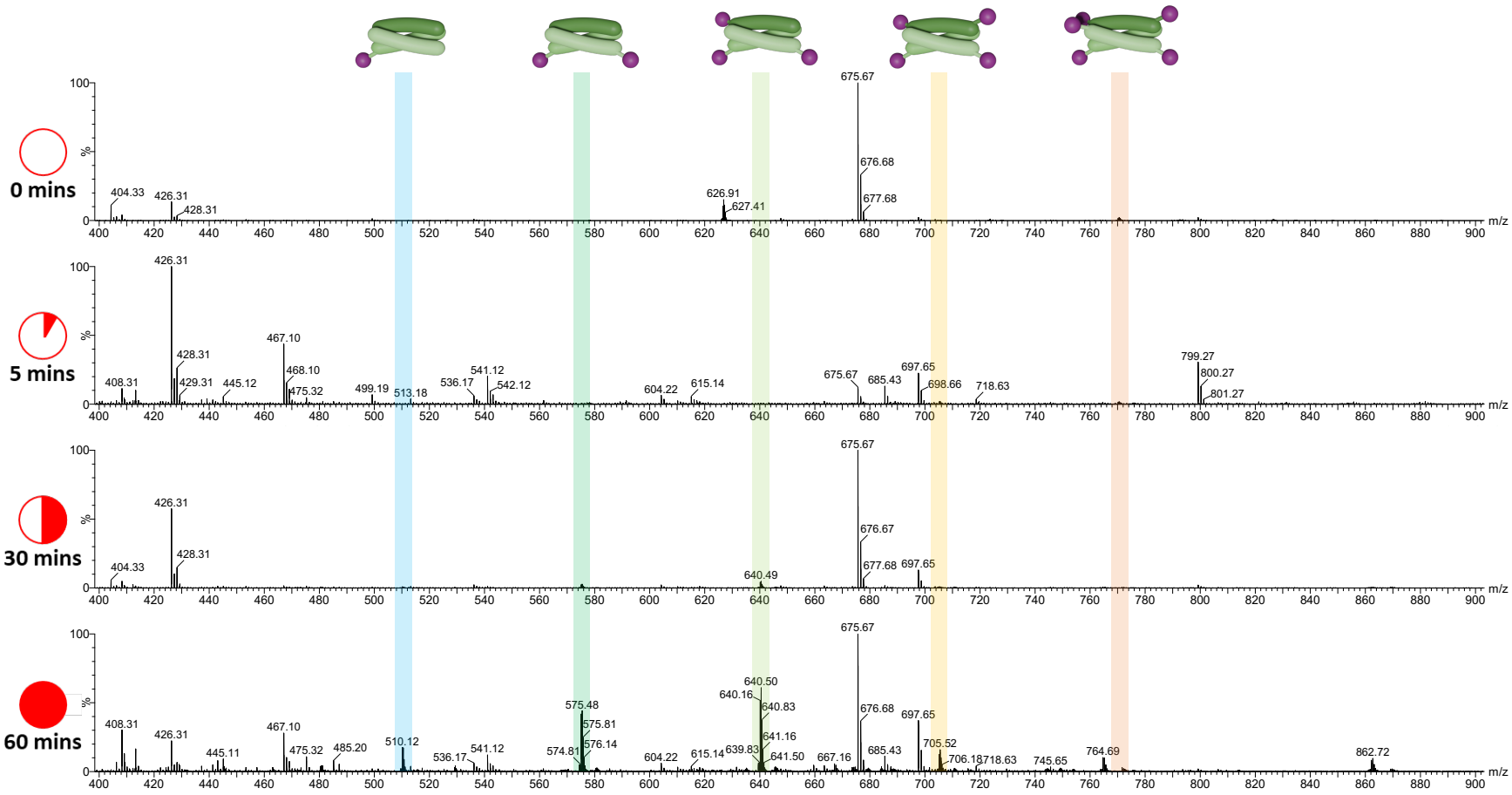

Figure 140: Mass spectra (TOF ES+, MeOH, 400-900 m/z) of the $[Fe_2(L_{5O}")_3]Cl_4$ over 60 minutes of irradiation highlighting the 3+ charged species.

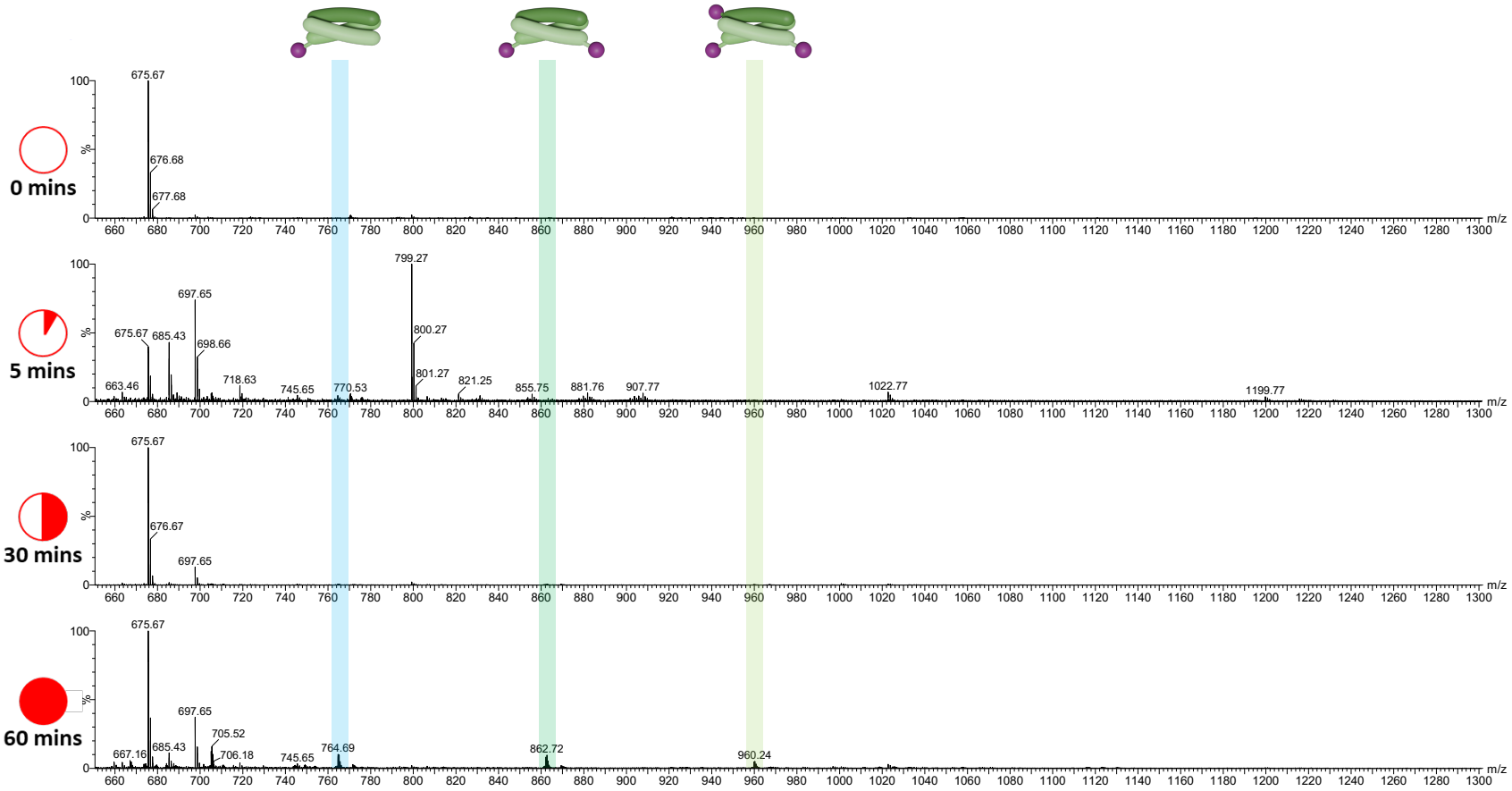

Figure 141: Mass spectra (TOF ES+, MeOH, 650-1300 m/z) of $[Fe_2(L_{5O}")_3]Cl_4$ over 60 minutes of irradiation highlighting the 2+ charged species.

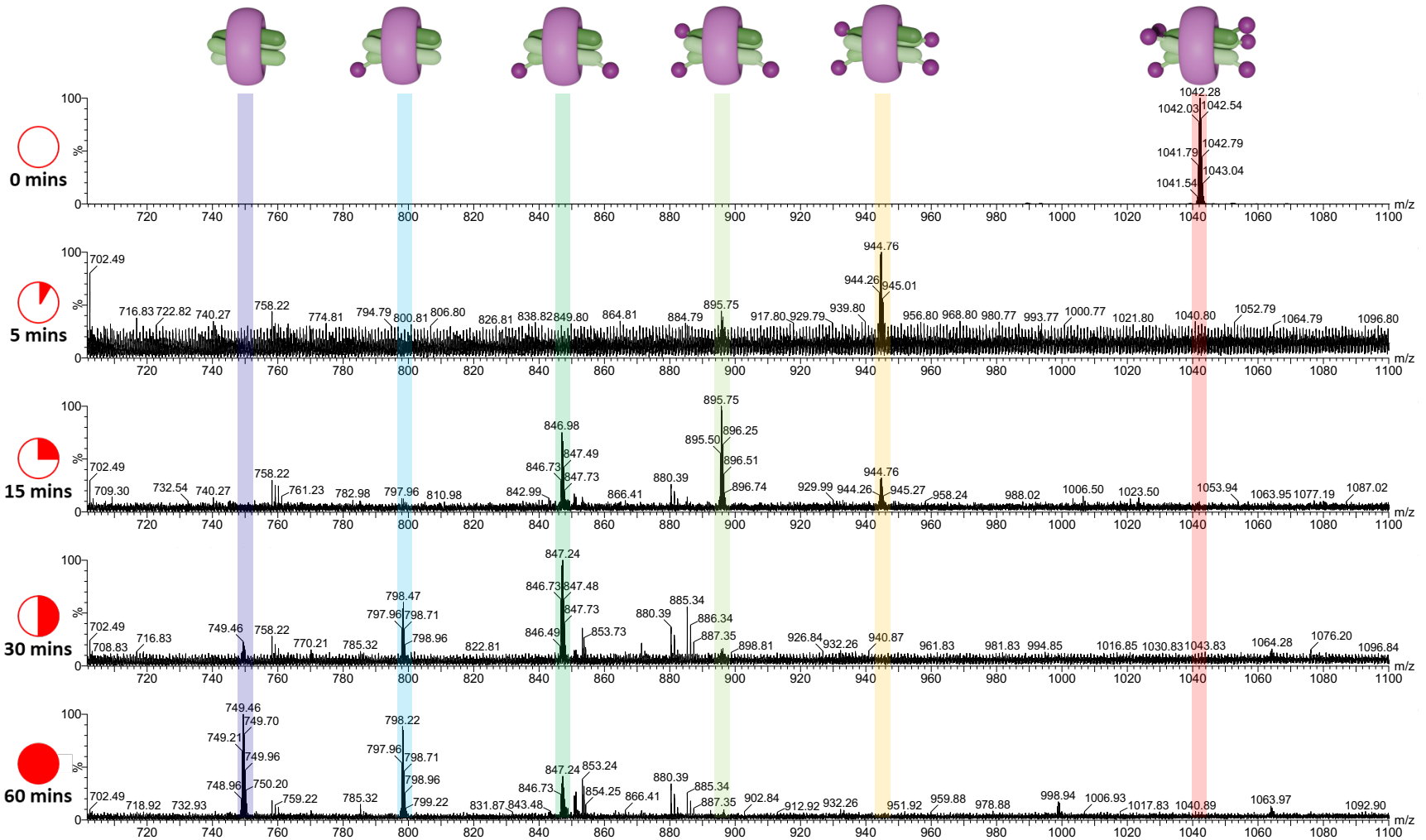

Figure 142: Mass spectra (TOF ES+, MeOH, 700-1100 m/z) of $[Fe_2(L_{5O}")_3.CB10]Cl_4$ over 60 minutes of irradiation highlighting the 4+ charged species.

From the absorbance and mass spectrometry results, the photocleavage is successful for both the capped cylinder and rotaxane. The uncapped cylinder ($[Fe_2(L_{5OH})_3]Cl_4$) shows as small decrease in absorbance over 60 minutes of irradiation, but remained present in the mass spectrum throughout. This suggests that a small amount of degradation is observed for the uncapped cylinder.

The absorbance spectrum of the capped cylinder ($[Fe_2(L_{5O}")_3]Cl_4$) shows the decrease in intensity of the capped cylinder peaks and the appearance of new peaks. This suggests the decreasing concentration of the capped cylinder while the concentration of a new species increases. Mass spectrometry indicates that this change is due to the increasing concentration of species with fewer caps (1-5), implying that the photocleavage reaction has been successful.

The expected photocleavage product of the rotaxane ($[Fe_2(L_{5O}")_3.CB10]Cl_4$) is the *pseudo*rotaxane ($[Fe_2(L_{5OH})_3.CB10]Cl_4$) so in future experiments the absorbance spectrum of the *pseudo*rotaxane should be recorded for comparison. The absorbance shows an overall decrease which is uneven at different wavelengths. The increasing intensity of a smaller peak underneath the decreasing 329 nm peak may cause the overall slower decrease. The success of the photocleavage reaction is confirmed by mass spectrometry which shows the relative abundance of species with fewer caps increases with increasing irradiation time.

6.1.1.3. Photocleavage of the nickel complexes

The photocleavage of the nickel complexes was investigated using the same method as the iron complexes, using both UV-visible absorbance and mass spectrometry to follow the sample solutions.

The uncapped cylinder ($[Ni_2(L_{5OH})_3]Cl_4$) shows a small decrease in absorbance over time (8, 8, and 7% at 237, 308, and 371 nm, respectively) with the largest decrease in absorbance occurring over the first 5 minutes in each case (Figure 143A). The 3+ and 2+ charged uncapped cylinder species are present in the mass spectrum throughout the 60 minute irradiation period (Figure 144).

The capped cylinder ($[Ni_2(L_{5O}")_3]Cl_4$) shows a decrease in the peaks at 219, 273, and 327 nm but also an increase in new peaks at 239 and 365 nm corresponding to the formation of a new product (Figure 143B). These peaks appear at wavelengths close to those observed for the uncapped cylinder (237 and 371 nm, respectively). The fully capped cylinder is present as both a 4+ and 3+ charged species (with various counter ions) in the mass spectrum before irradiation (Figure 145, Figure 146, and Figure 147). The 5-capped 3+ ($[Ni_2(L_{5O}")_2(L_{5O}')]Cl_4$), and 4-capped 2+ ($[Ni_2(L_{5O}")_2(L_{5OH})]Cl_4$) species are also observed. With increasing irradiation time, lesser capped species appear in the spectrum which is most obvious for the 3+ charged series (Figure 146). The completely uncapped species is not visible in the 4+ and 3+ series, but is visible after 15 minutes in the 2+ series.

The nickel rotaxane ($[Ni_2(L_{5O}")_3.CB10]Cl_4$) shows an overall decrease in absorbance at the 237 and 335 nm peaks which is accompanied by a red shift in the absorbance of both peaks. A similar effect is observed for a small shoulder peak observed below 250 nm. The nickel rotaxane mass spectra differs from the previous spectra as both the fully capped rotaxane (1043 m/z, $[Ni_2(L_{5O}")_3.CB10]^{4+}$) and the 5-capped rotaxane with one half ligand (969 m/z, $[Ni_2(L_{5O}")_2(hL_{5O}').CB10]^{4+}$) are present in the 0 minute spectrum (Figure 148 and see 9.1.1, Figure 163). The gradual decrease in the number of caps can be followed for both species (Figure 148, Figure 149 and Figure 163).

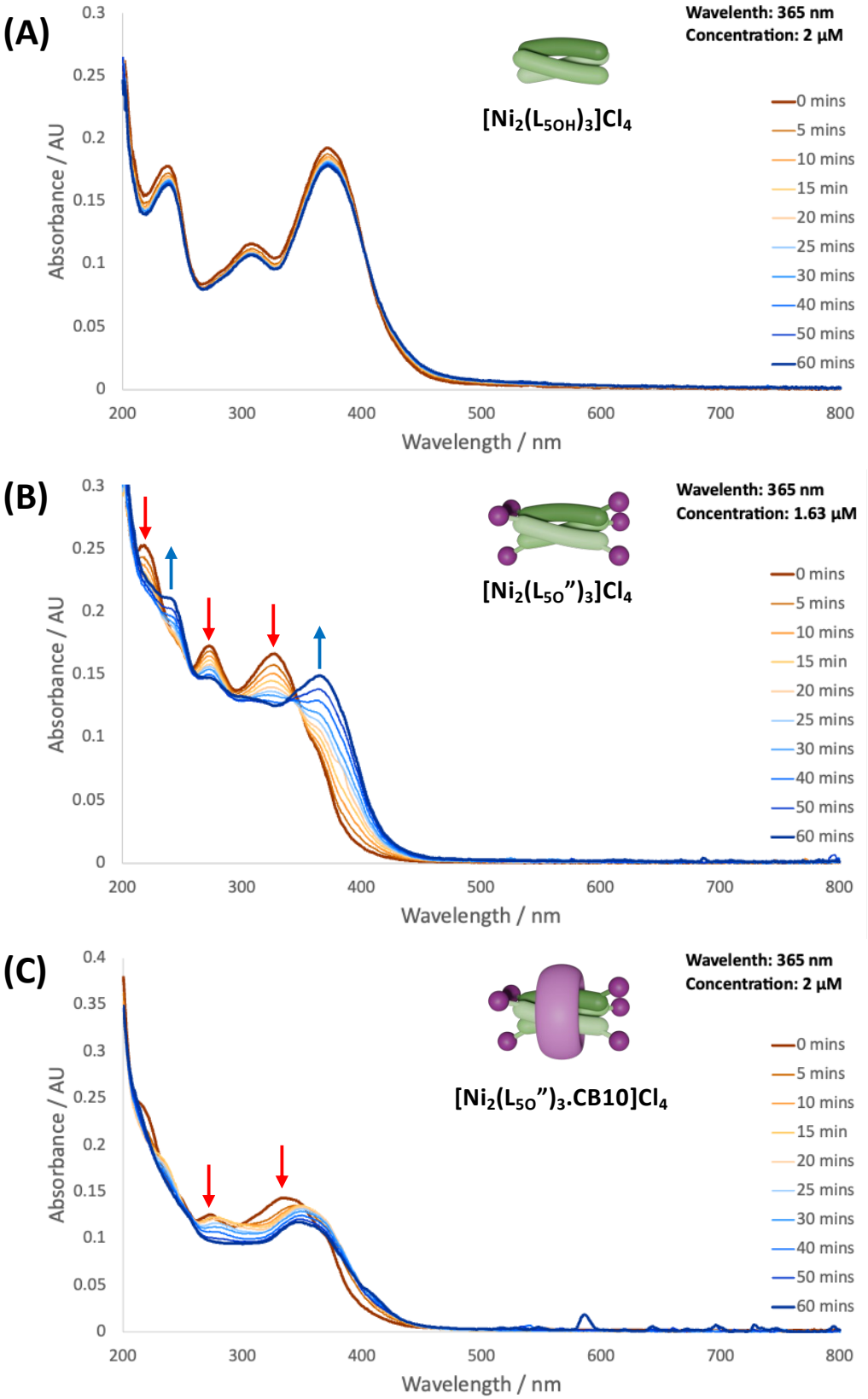

Figure 143: UV-visible absorbance of the (A) $[Ni_2(L_{5OH})_3]Cl_4$ (2 µM), (B) $[Ni_2(L_{5O''})_3]Cl_4$ (1.63 µM), and (C) $[Ni_2(L_{5O''})_3.CB10]Cl_4$ (2 µM) in methanolic (cylinders) or aqueous (rotaxane) solutions after increasing irradiation times.

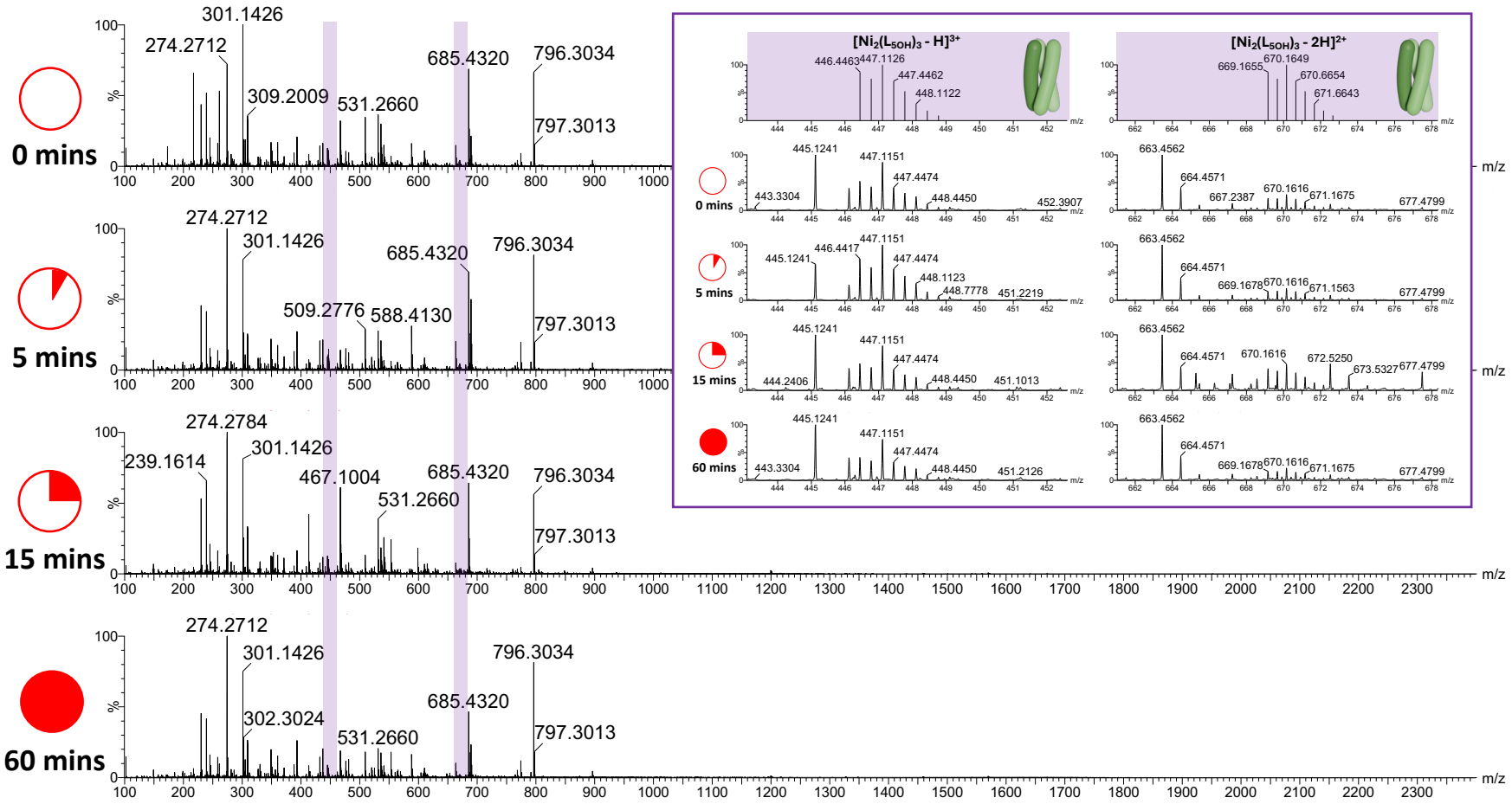

Figure 144: Mass spectra (TOF ES+, MeOH) of $[Ni_2(L_{5OH})_3]Cl_4$ over 60 minutes of irradiation highlighting the differently charged cylinder species, and compared to their isotope patterns (inset).

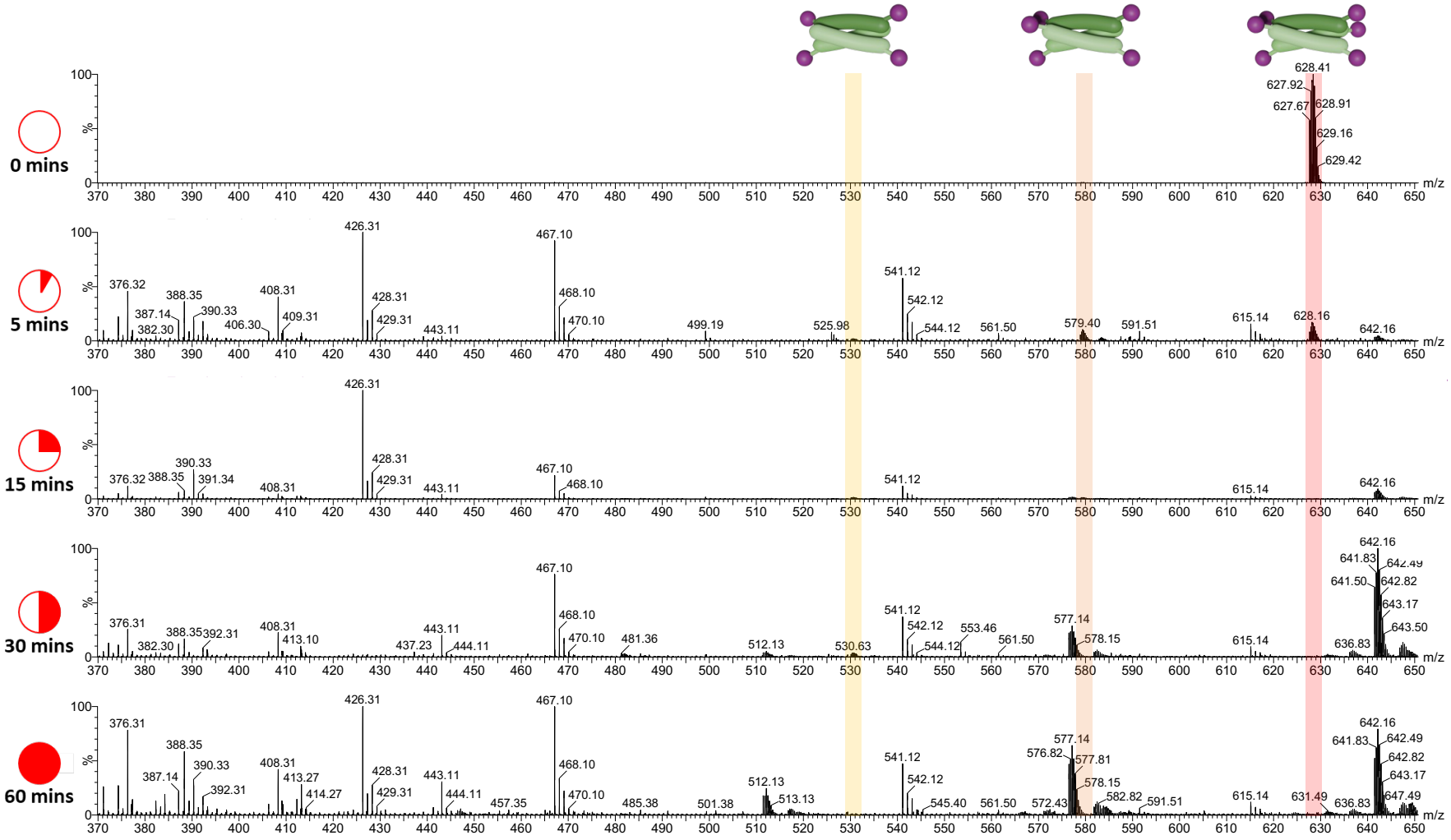

Figure 145: Mass spectra (TOF ES+, MeOH, 370-650 m/z) of $[Ni_2(L_{5O}")_3]Cl_4$ over 60 minutes of irradiation highlighting the 4+ charged species.

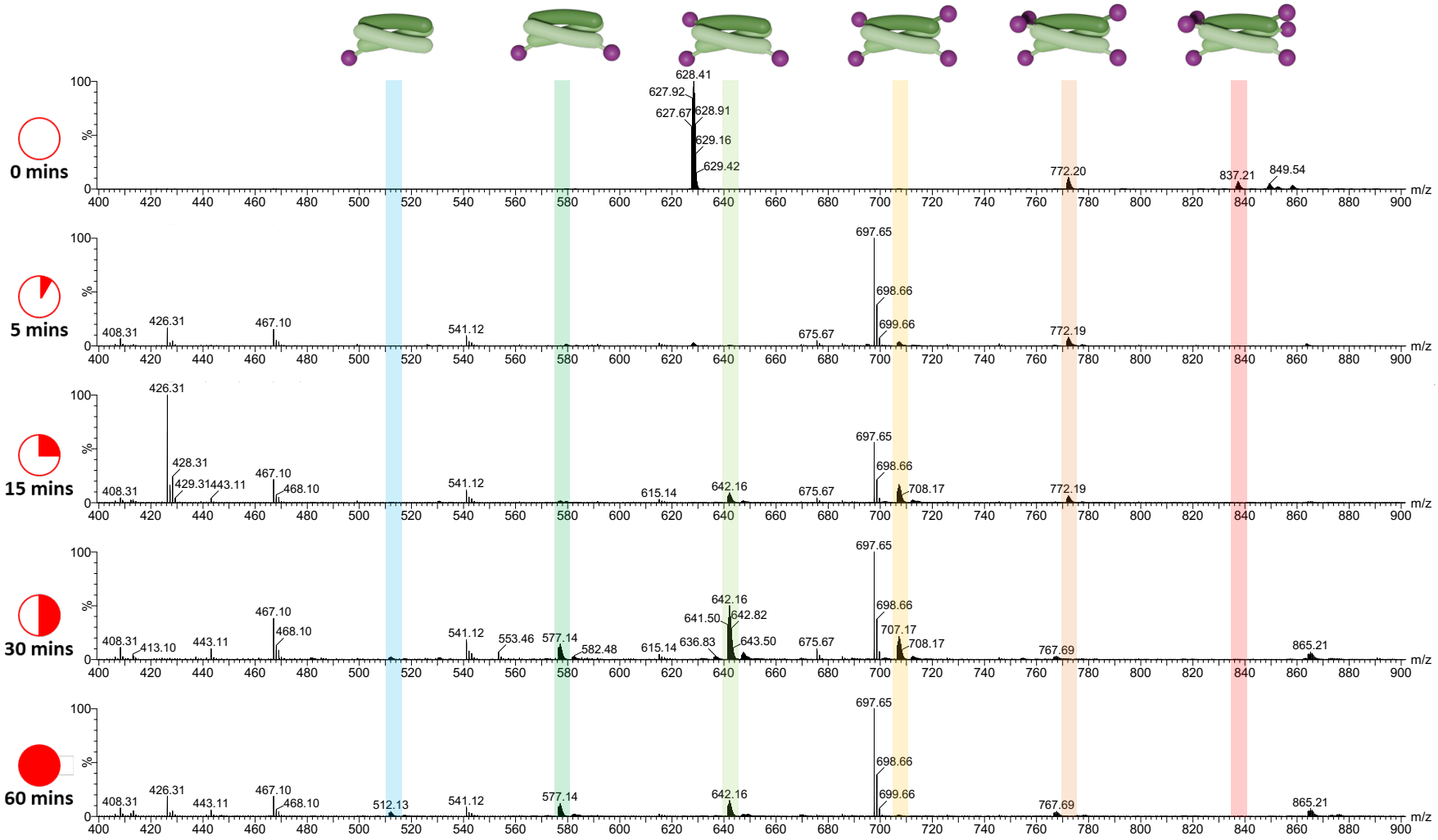

Figure 146: Mass spectra (TOF ES+, MeOH, 400-900 m/z) of $[Ni_2(L_{5O}")_3]Cl_4$ over 60 minutes of irradiation highlighting the 3+ charged species.

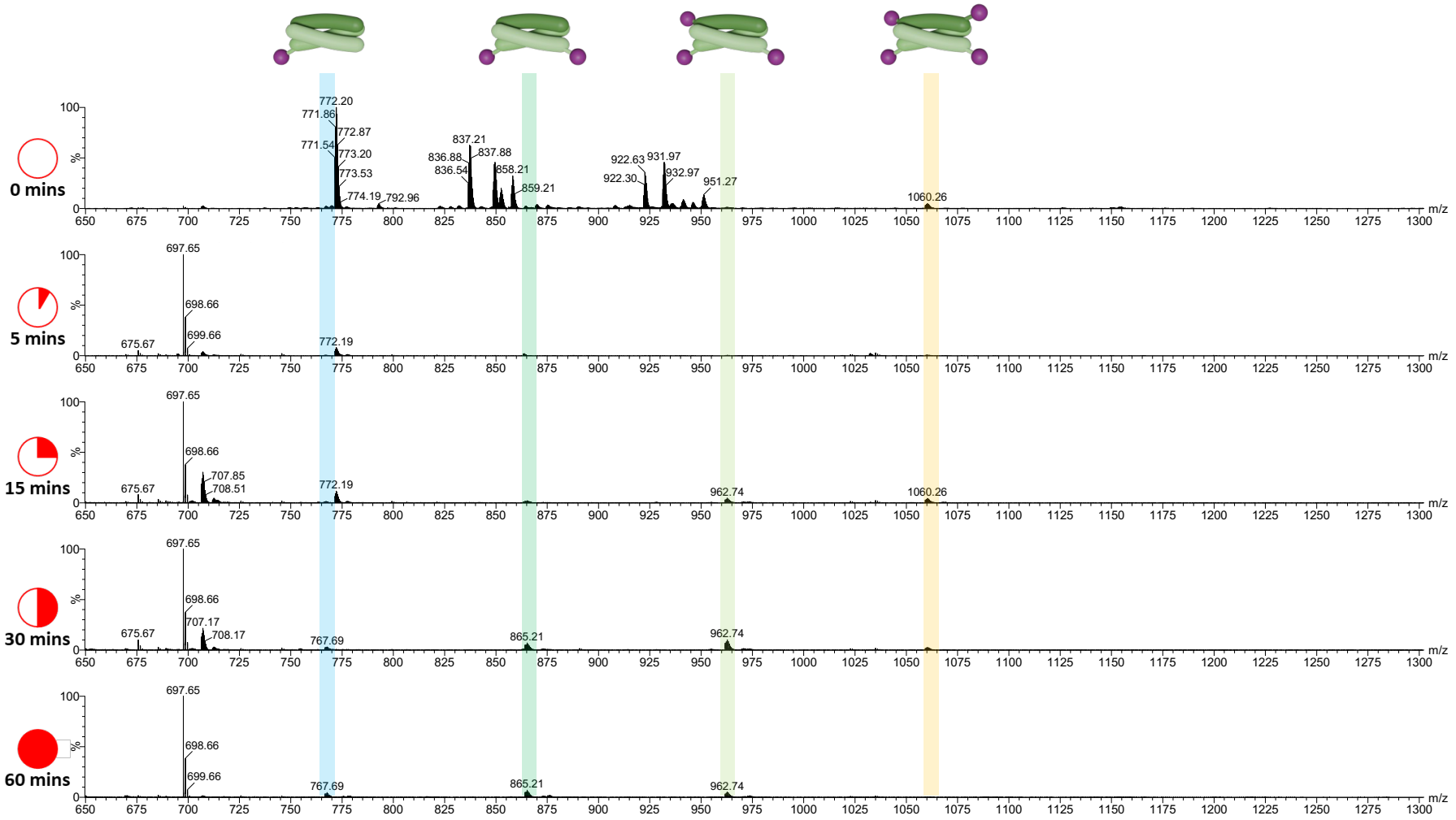

Figure 147: Mass spectra (TOF ES+, MeOH, 650-1300 m/z) of $[Ni_2(L_{5O}")_3]Cl_4$ over 60 minutes of irradiation highlighting the 2+ charged species.

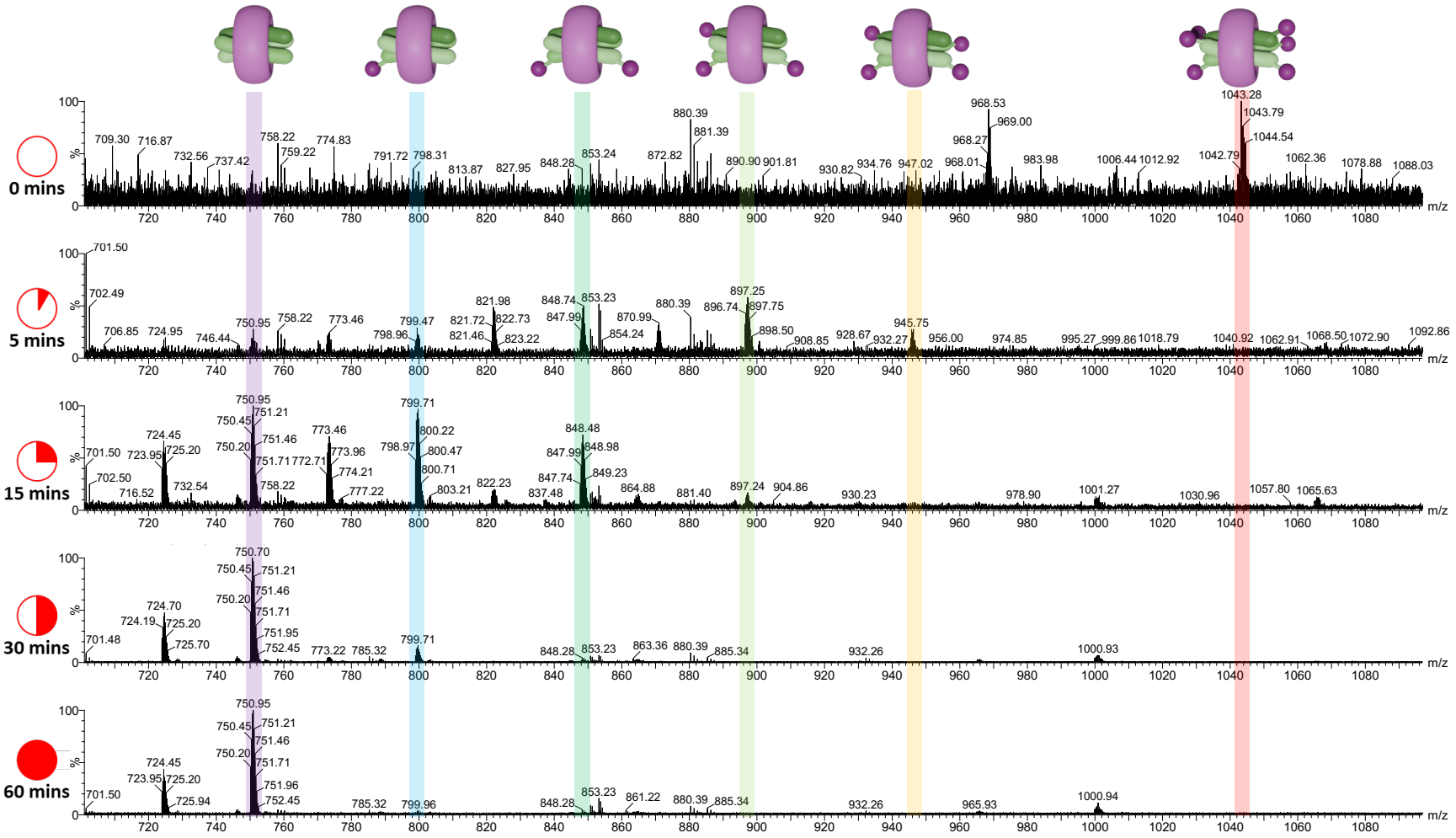

Figure 148: Mass spectra (TOF ES+, MeOH, 700-1100 m/z) of $[Ni_2(L_{5O}")_3.CB10]Cl_4$ over 60 minutes of irradiation highlighting the 4+ charged species. See also 9.1.1, Figure 163.

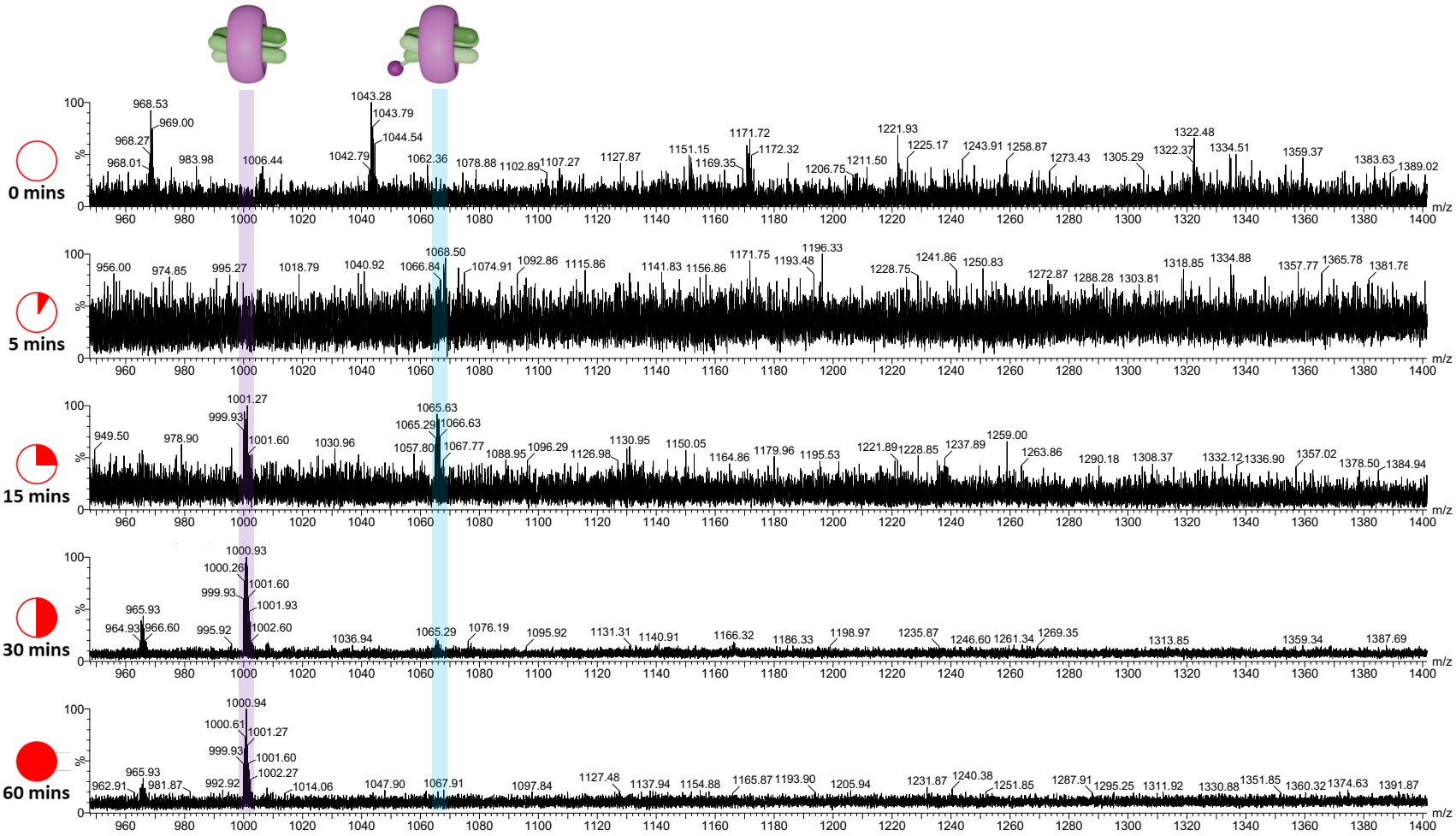

Figure 149: Mass spectra (TOF ES+, MeOH, 950-1400 m/z) of $[Ni_2(L_{5O}")_3.CB10]Cl_4$ over 60 minutes of irradiation highlighting the 3+ charged species.

Similar to the iron equivalent, the nickel uncapped cylinder ($[Ni_2(L_{5OH})_3]Cl_4$) shows a small decrease (less than 10%) in absorbance intensity over 60 minutes which could indicate degradation in solution over this time period, however the uncapped cylinder remains present in the mass spectrum. The absorbance spectrum of the capped cylinder ($[Ni_2(L_{5O}")_3]Cl_4$) shows the appearance of new peaks of similar wavelength to the uncapped cylinder suggesting that the photocleavage reaction has been successful. This was confirmed by mass spectrometry as an increase in the abundance of lesser capped species is observed over the 60 minutes of irradiation.

The rotaxane ($[Ni_2(L_{5O}")_3.CB10]Cl_4$) shows an overall decrease in absorbance similar to the iron species, and mass spectrometry has been used to confirm that this is caused by the successful photocleavage of the capping groups. Species containing more than one half ligand (hL_{5O}^X) are not observed throughout the irradiation time. This could suggest that irradiation does not cause the hydrolysis and that these species originate from the 5-capped rotaxane observed before irradiation began, however it is also possible that species containing two half ligands are unstable in solution. Compared to the capped cylinder, which shows multiple species present after 60 minutes of irradiation, the uncapped *pseudo*rotaxane species has the highest relative abundance after 60 minutes of the rotaxane irradiation.

6.1.2. Photocleavage of the 4-hydroxypyridine complexes

The nickel cylinders and rotaxane were used to study the photocleavage of the 4-hydroxypyridine based cylinders as the iron rotaxane could not be isolated. The methods used to investigate the photocleavage are not affected by the paramagnetic nature of the nickel cylinder, which is preferred for gel electrophoresis studies, so

photocleavage of the iron cylinder would not be expected to provide any further information.

The absorbance of the uncapped cylinder ($[Ni_2(L_{4OH})_3]Cl_4$) around 240 nm does not change in intensity (remaining within 3% of the original peak height), however after 5 minutes of irradiation, the peak is red-shifted from 239 nm to 242 nm (Figure 150A). The peak at 316 nm shows an 9% decrease in intensity compared to the absorbance of the cylinder before irradiation was applied. The mass spectrum (Figure 151) of the solution demonstrates that the uncapped cylinder is present throughout the irradiation process as the 4+, 3+ or 2+ species (336, 447, and 670 nm, for $[Ni_2(L_{4OH})_3]^{4+}$, $[Ni_2(L_{4OH})_3]^{3+}$, and $[Ni_2(L_{4OH})_3]^{2+}$, respectively). The two metal, two ligand species is also observed (465 nm, $[Ni_2(L_{4OH})_2]^{2+}$) and has a higher relative abundance with increased irradiation time.

The capped cylinder ($[Ni_2(L_{4O}")_3]Cl_4$) shows a decrease in the absorbance intensity of the peak at 231 nm (7%) which is accompanied by a red shift in the absorbance maximum to 234 nm with increasing irradiation time (Figure 150B). The absorption minima at 210 nm and 270 nm both show an increase in absorption and a large red shift of 9 and 13 nm, respectively. Photocleavage is not expected to cause the large change in absorbance observed for the 5-oxypyridine based cylinder (Figure 143B) as the absorbance spectrum of the capped cylinder of the 4-oxypyridine series is very similar to the uncapped cylinder. The mass spectrum (Figure 152) of the capped cylinder shows a gradual increase in abundance of the 5-capped (579 and 772 nm, $[Ni_2(L_{4O}")_2(L_{4O}')]^{4+}$ and $[Ni_2(L_{4O}")_2(L_{4O}')]^{3+}$) and 4-capped species (531 and 707 nm, $[Ni_2(L_{4O}")_2(L_{4OH})]^{4+}$and $[Ni_2(L_{4O}")_2(L_{4OH})]^{3+}$, respectively) with increasing irradiation time up to 20 minutes. Samples which had been irradiated over 20 minutes were not

detected by the mass analyser and so only the reference (Leucine Enkephalin, 556 m/z, $[M+ H]^+$) and background ions were observed in the spectrum (the 60 minute spectrum has been included as an example). The least capped species in the spectrum after 20 minutes still has 4 caps however this is similar to the capped 5-oxypyridine cylinders in which the lowest number of caps is the 3-capped after 15 minutes (Figure 146 and Figure 147), before more caps are removed to produce the single capped species after 60 minutes of irradiation.

The absorbance of the rotaxane ($[Ni_2(L_{4O}")_3.CB10]Cl_4$) shows a decrease in the sharp peak at 228 nm, and a broad decrease in absorbance around 316 nm (Figure 150C). An overall 24% decrease in absorbance at 228 nm is accompanied by a red shift to 230.5 nm after 15 to 20 minutes of irradiation, which then shows a blue shift back to 228 nm after 60 minutes. The peak at 308.5 nm is red shifted to 315.5 nm after 60 minutes of irradiation. The broad decrease in absorbance is calculated to be 11% at 315.5 nm. The mass spectrum of the rotaxane structure before irradiation (Figure 153 and see 9.1.2, Figure 164) shows the 6-capped and 5-capped species without and with a half ligand (1043 m/z, $[Ni_2(L_{4O}")_3.CB10]^{4+}$, 995 m/z, $[Ni_2(L_{4O}")_2(L_{4O}').CB10]^{4+}$, and 968 m/z, $[Ni_2(L_{4O}")_2(hL_{4O}').CB10]^{4+}$, respectively). Species with fewer caps are observed in the mass spectrum with increasing irradiation time until only the uncapped *pseudo*rotaxane (751 m/z, $[Ni_2(L_{4OH})_3.CB10]^{4+}$ and 1000 m/z, $[Ni_2(L_{4OH})_3.CB10]^{3+}$) and the equivalent species with one half ligand (724 m/z, $[Ni_2(L_{4OH})_2(hL_{4OH}).CB10]^{4+}$) remain after 60 minutes of irradiation. Also visible in the spectrum is the 3+ charged two-ligand, two-metal series which starts with the 3-capped species observed after 15 minutes (1060 m/z, $[Ni_2(L_{5O}")(L_{5O}')]^{3+}$) and finishes with the uncapped species (864 m/z, $Ni_2(L_{5OH})_2]^{3+}$) at 0 minutes.

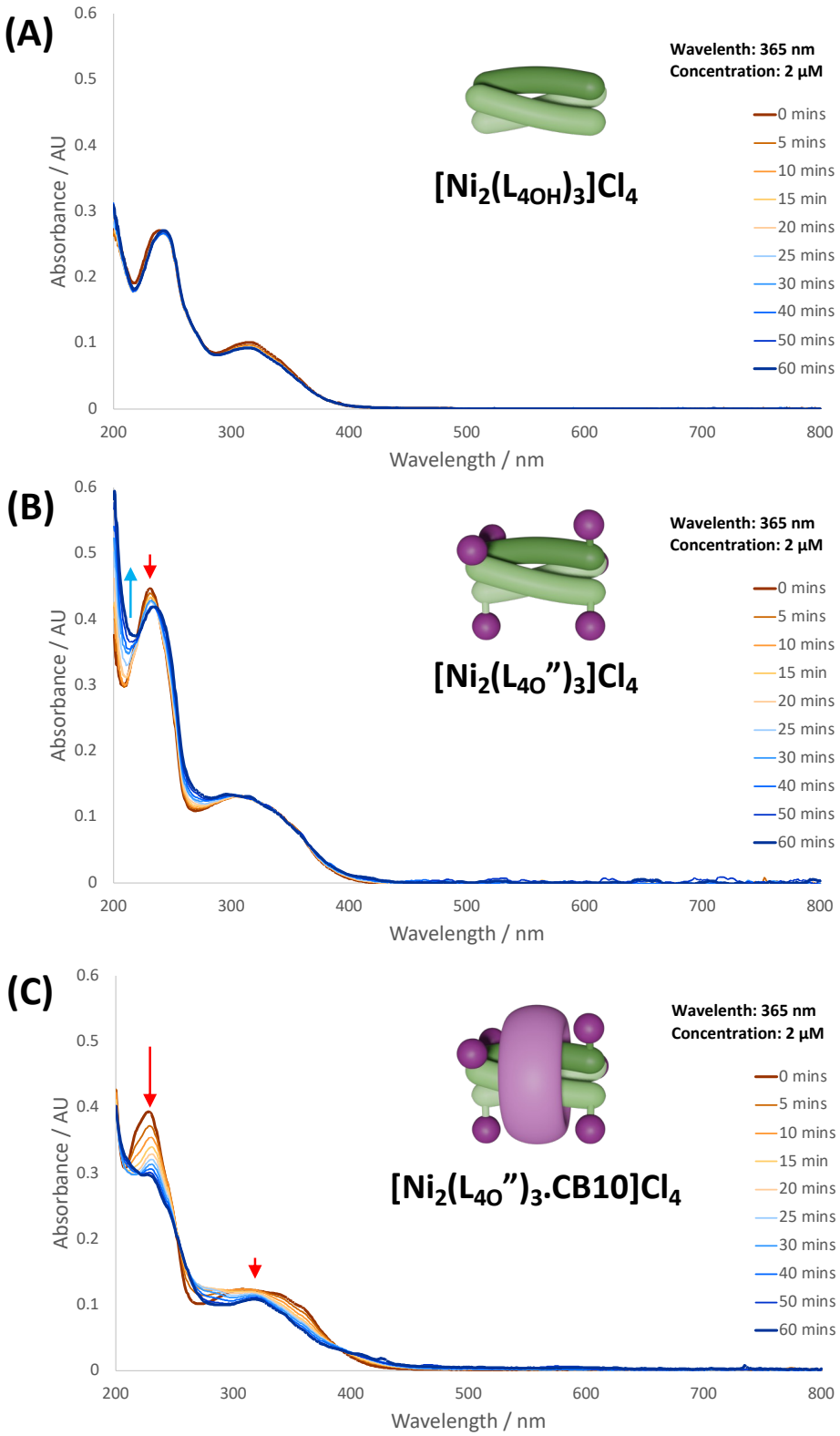

Figure 150: UV-visible absorbance of the (A) $[Ni_2(L_{4OH})_3]Cl_4$, (B) $[Ni_2(L_{4O''})_3]Cl_4$, and (C) $[Ni_2(L_{4O''})_3.CB10]Cl_4$ in methanolic (cylinders) or aqueous (rotaxane) solutions (2 µM) after increasing irradiation times.

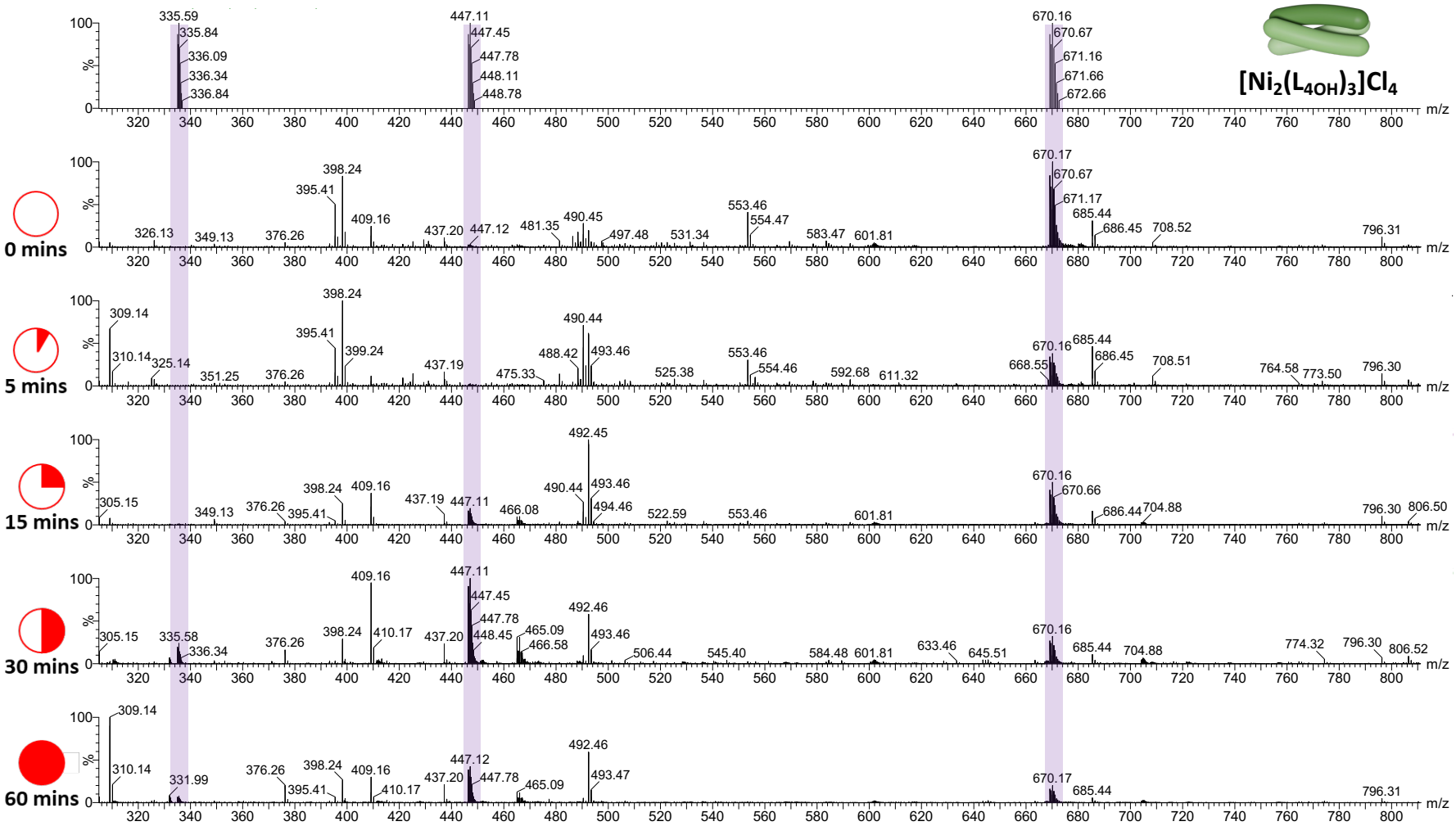

Figure 151: Mass spectra (TOF ES+, MeOH, 310-800 m/z) of $[Ni_2(L_{4OH})_3]Cl_4$ over 60 minutes of irradiation highlighting the 4+, 3+ and 2+ charged species.

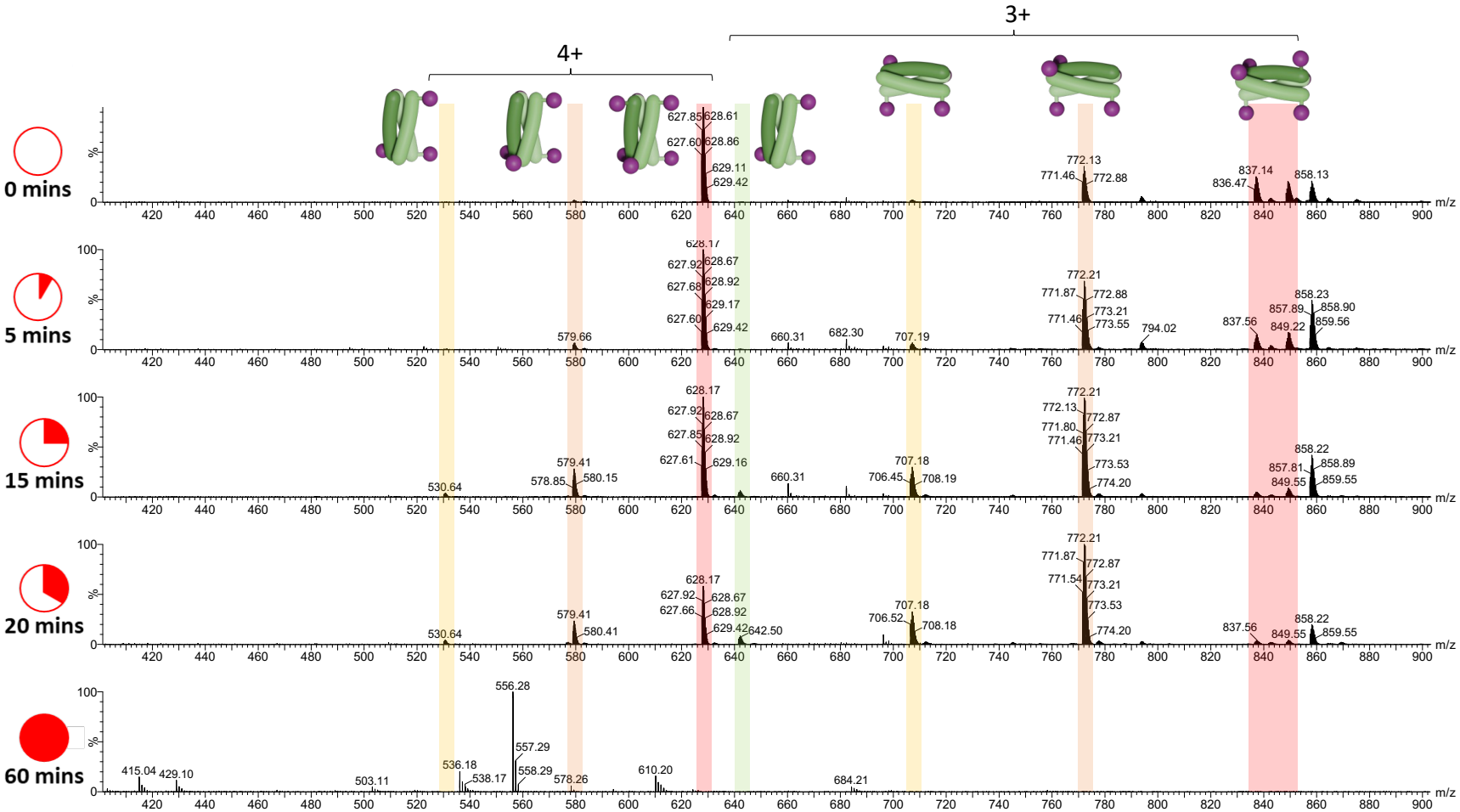

Figure 152: Mass spectra (TOF MS ES+, MeOH, 400-900 m/z) of $[Ni_2(L_{4O}")_3]Cl_4$ over 60 minutes of irradiation highlighting the 4+ and 3+ charged species.

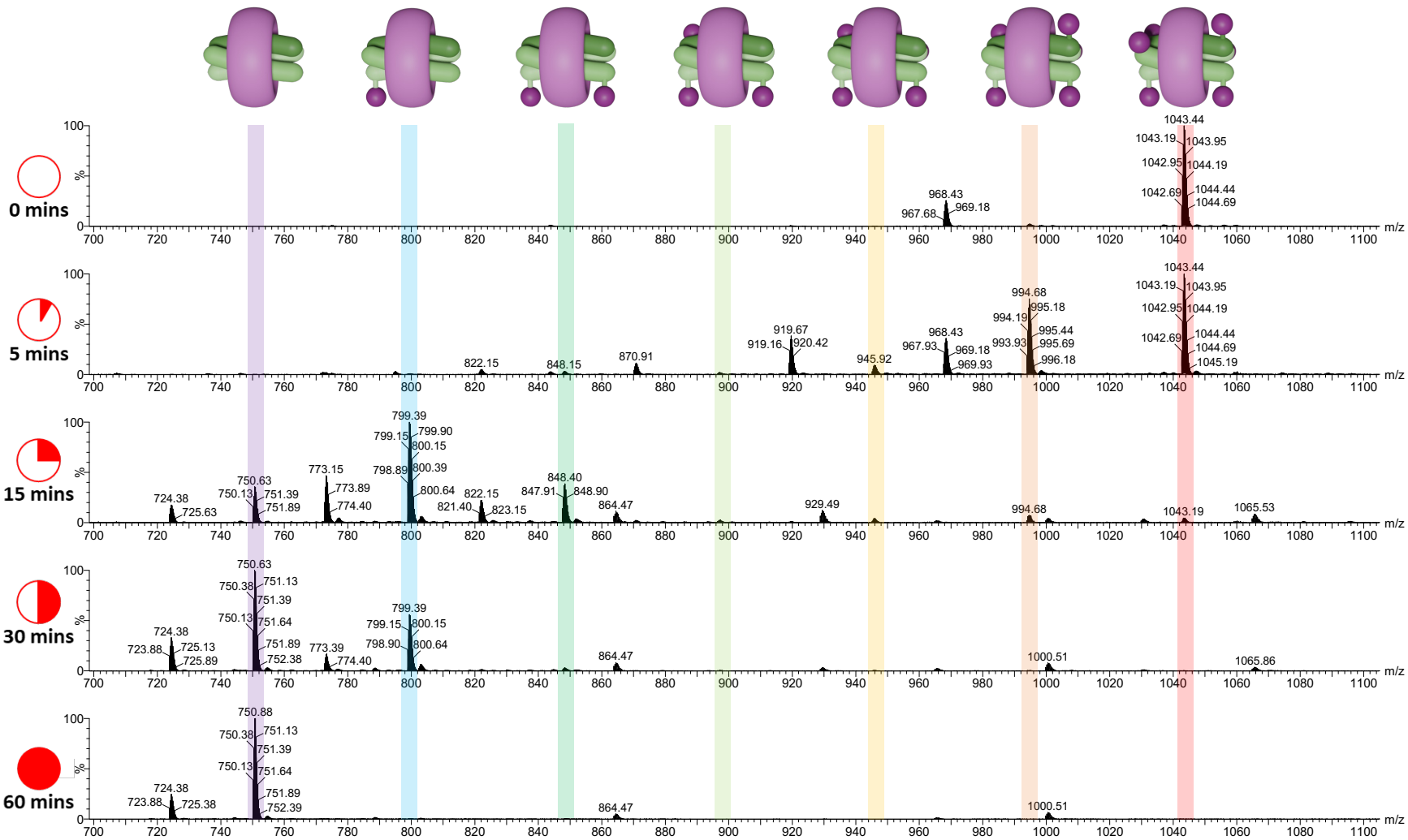

Figure 153: Mass spectra (TOF ES+, MeOH, 700-1100 m/z) of $[Ni_2(L_{4O}")_3.CB10]Cl_4$ over 60 minutes of irradiation highlighting the 4+ charged species. See also 9.1.2, Figure 164.

The mass spectra confirm that photocleavage is successful, as with the 5-oxypyridine equivalent cylinders. The small decrease in the absorbance spectrum of the uncapped cylinder could indicate degradation of the cylinder, as with the 5-oxypyridine series, but the intact cylinder is still observed in all mass spectra across the irradiation period. The rotaxane shows larger decreases in the absorbance spectrum upon increasing irradiation and the mass spectra suggest that this is caused by decapping of the rotaxane. Species with fewer caps appear with increasing irradiation time, leaving the uncapped *pseudo*rotaxane after 60 minutes.

The changes in the absorbance spectrum with increasing irradiation are similar for the 4- and 5-oxypryidine based nickel uncapped cylinder and rotaxane, however the 4-oxypyridine capped cylinder shows a smaller change in absorbance compared to the 5-oxypyridine equivalent, with no peaks specific to the reaction product appearing over time which could be due to the similiarity between the absorbance of the capped and uncapped cylinders. The mass spectrum after 15 minutes is very similar to that of the 5-oxypryidine capped cylinder after the same irradiation time suggesting that the photocleavage is similar between both species.

6.1.3. Photocleavage of the 3-oxypyridine cylinders

Issues with the synthesis of the capped 3-oxypyridine based nickel cylinder meant the photocleavage was recorded using the iron capped cylinder which was readily prepared from the capped ligand. Analysis by mass spectrometry was attempted but the metal complex species could not be identified in the spectra due to an abundance of organic species.

The absorbance of the uncapped cylinder ($[Fe_2(L_{3OH})_3]Cl_4$, Figure 154A) does not appear affected by increasing irradiation time. The maximum decrease measured at each of the absorbance maxima (236, 328, 398 and 592 nm) was less than 6% (4%, 5%, 2% and 6% respectively) and the decrease in intensity did not appear consistent with increasing irradiation time. The low absorbance means than any changes in intensity are low. Small errors in the absorbance measurements may therefore cause large differences in the results which could mask an overall decrease with time. Alternatively, small changes in the spectra could be due to errors caused by external factors such as poor mixing.

The capped cylinder ($[Fe_2(L_{3O}")_3]Cl_4$, Figure 154B) shows a decrease in absorbance at all of the peaks, and an increase in absorbance between the peaks. The shortest wavelength peak at 245 nm shows a 10% decrease in absorbance and a small blue shift (244 nm) over 60 minutes of irradiation. The broad peak at 314.5 nm also shows a decrease in absorbance (16% over 60 mintues) and the peak maxima appears to change suddenly between 15 and 20 minutes of irradiation to a maxima at 317.5 nm. A broad peak between 450 and 650 nm shows an overall decrease in intensity (29% measured at 584 nm).

The changes in the absorbance spectra for the 3-oxypyridine based cylinders are similar to those observed for the 5- and particularly the 4-oxypyridine. All show much greater changes in the absorbance spectrum for the capped cylinder than for the uncapped cylinder, which is expected to be due to the photocleavage of the capped species. For the 4- and 5-oxypyridine cylinders this has been confirmed by tracking the differently capped species observed in the mass spectrum of the irradiated sample at

different irradiation time points, however this information is not available for this experiment.

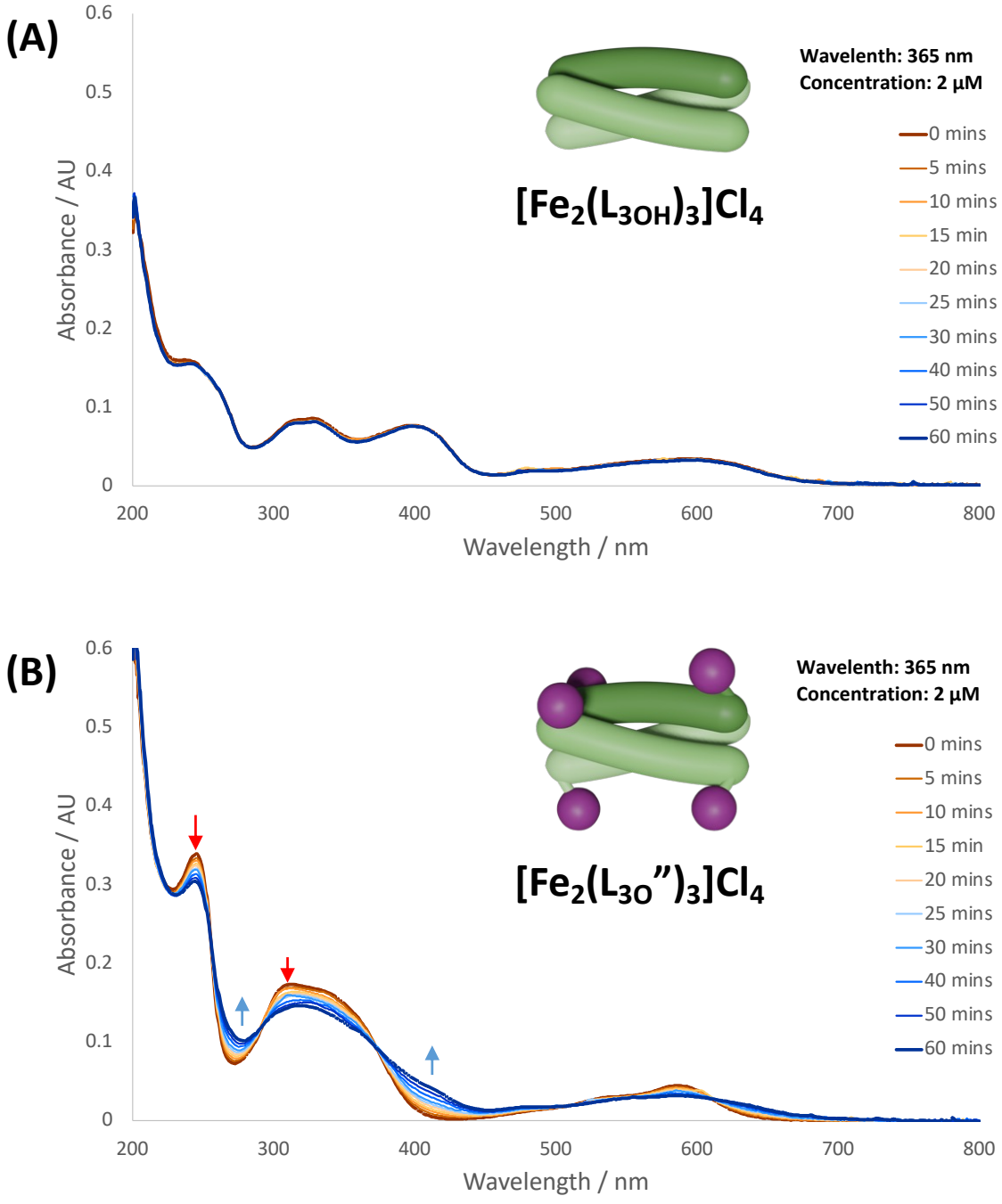

Figure 154: UV-visible absorbance of the (A) $[Fe_2(L_{3OH})_3]Cl_4$), and (B) $(Fei_2(L_{3O}")_3]Cl_4$) in methanolic solutions (2 µM) after increasing irradiation times.

6.1.4. Photocleavage Summary

Photocleavage of the oxypyridine-based cylinders was confirmed by following the change in absorbance by UV-visible spectroscopy and the species present in the mass spectrum of a sample over increasing irradiation time up to 60 minutes. The absorbance spectrum of the uncapped cylinders showed only small decreases in the peak maxima (less than 10%) over 60 minutes of irradiation, and the mass spectra of the 4- and 5-hydroxypyridine cylinders suggests that the uncapped cylinder is present throughout.

The capped cylinder samples showed greater changes in both absorbance and in the species present in the mass spectra with increasing irradiation. While the 3- and 4-oxypyridine based cylinders both show a decrease in the absorbance maxima with increasing irradiation time, the 5-oxypyridine cylinders (both iron and nickel) also show the emergence of new peaks corresponding to the formation of a new product. The success of the photocleavage reaction is evidenced by the appearance of helicate species with decreasing numbers of peaks with increasing irradiation time. Peaks corresponding to the singly capped species for the 5-oxypyridine species are observed after 60 minutes of irradiation and the 3-capped species is observed for the 4-oxypyridine species after just 20 minutes of irradiation.

The rotaxanes showed a gradual decrease in absorbance with increasing irradiation time, however there was no appearance of new peaks forming for a reaction product as observed for the capped 5-oxypyridine cylinders. Mass spectrometry was used to confirm that the photocleavage was successful and appears more efficient for the rotaxanes than for the capped cylinders, demonstrated by the appearance of the uncapped *pseudo*rotaxane in between 5 and 30 minutes.

For a more complete comparison of the photocleavage of the oxypyridine based cylinders, the photocleavage of the capped 4-oxypyridine cylinder ($[Ni_2(L_{4O}")_3]Cl_4$) should be repeated to obtain the mass spectra at the longer time points (up to 60 minutes). The photocleavage of the capped 3-oxypyridine cylinders should also be repeated to record the mass spectrum. To avoid issues with the mass spectrometry, the concentration of the samples could be doubled. This would keep the absorbance below 1 AU, to keep the absorbance measurements accurate, but should increase the concentration of the metal complexes in solution for monitoring by mass spectrometry. It should be taken into account that changing the concentration of the solution will affect both the photocleavage reaction efficiency and the absorbance of the uncapped cylinders as observed previously (Figure 135).

6.2. Junction Binding

After the success of the photocleavage reaction was confirmed for the 5-oxypyridine cylinders by UV-Visible absorbance and mass spectrometry, gel electrophoresis was employed to investigate the 3WJ binding properties of the cylinders and rotaxanes.

Following the same protocol as used for the imidazole-based cylinders, the 3WJ binding of the nickel 5-oxypyridine cylinders and rotaxane was investigated by PAGE. The concentration of the 3WJ was maintained and the concentration of the cylinder species present was increased from 0.5 equivalents to 4 equivalents per junction.

Samples incubated with the uncapped 5-hydroxypyridine based cylinder ($[Ni_2(L_{5OH})_3]Cl_4$) gave a 3WJ band which increases in intensity with increasing concentration but is less intense than the 3WJ band formed by the parent cylinder

(Figure 155, wells 7-10). By enhancing the contrast of the image, a very faint band is observed for the capped cylinder (Figure 155, wells 11-14), and for the rotaxane (Figure 155, wells 15-18). The final well contains a sample of the rotaxane after 60 minutes of irradiation from the previous photocleavage experiment, however no band is observed.

A reduction in the fluorescence intensity of the single stranded band is observed for the parent and uncapped cylinder species at high concentration which is due to the formation of the junction. A similar reduction in intensity is also observed for the capped cylinder and rotaxane despite the low intensity of the 3WJ band which could suggest that these complexes affect the DNA sample without the formation of the 3WJ. The lack of fluorescent residue in the wells suggests this reduction in intensity is not due to precipitation of the DNA.

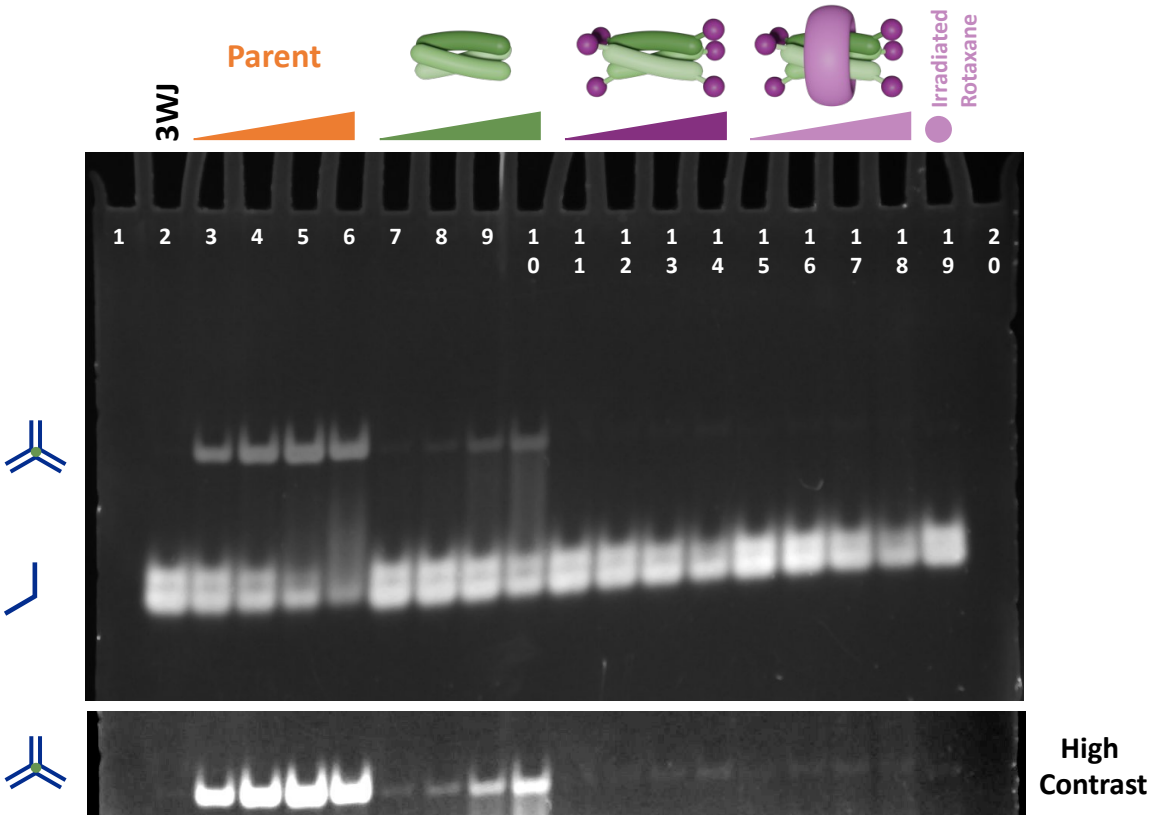

Figure 155: Gel electrophoresis study of 3WJ formation in the presence of increasing concentration of cylinders (0.5, 1, 2, and 4 μM). Wells: (1,20) running dye; (2) 3WJ stock solution; (3-6) $[Ni_2L_3]Cl_4$; (7-10) $[Ni_2(L_{5OH})_3]Cl_4$; (11-14) $[Ni_2(L_{5O}")_3]Cl_4$; (15-18) $[Ni_2(L_{5O}")_3.CB10]Cl_4$; (19) $[Ni_2(L_{5O}")_3.CB10]Cl_4$ after 60 minutes of irradiation. The 3WJ band is shown at higher contrast below.

It was concluded that the 5-hydroxypyridine cylinder forms and stabilises the 3WJ at room temperature. The release of the uncapped cylinder from the capped cylinder and rotaxane by photocleavage should therefore be visible by gel electrophoresis. The 5-oxypyridine complexes were irradiated simultaneously in black-walled cuvettes for 0, 15, 30, and 60 minutes as aqueous solutions (2 μM, diluted from a 1 mM methanolic stock for the cylinders). A sample of each solution was then taken and added to a 3WJ sample so that there was one equivalent of irradiated cylinder per junction. The rotaxane was also irradiated in the presence of the 3WJ by making a solution of cylinder and junction (both 1 μM) in a tris-base and boric acid (TB) buffer and taking samples after 0, 15, 30, and 60 minutes of irradiation.

None of the complexes give a clear band for the formation of the junction (Figure 156). Increasing the contrast of the image displays very faint 3WJ bands for the uncapped cylinder at 15, 30 and 60 minutes. The most intense bands observed at the higher contrast are the rotaxane samples after 60 minutes of irradiation (irradiated alone and in the presence of DNA, wells 15 and 19). These are accompanied by less intense 3WJ bands after 30 minutes of irradiation in each case.

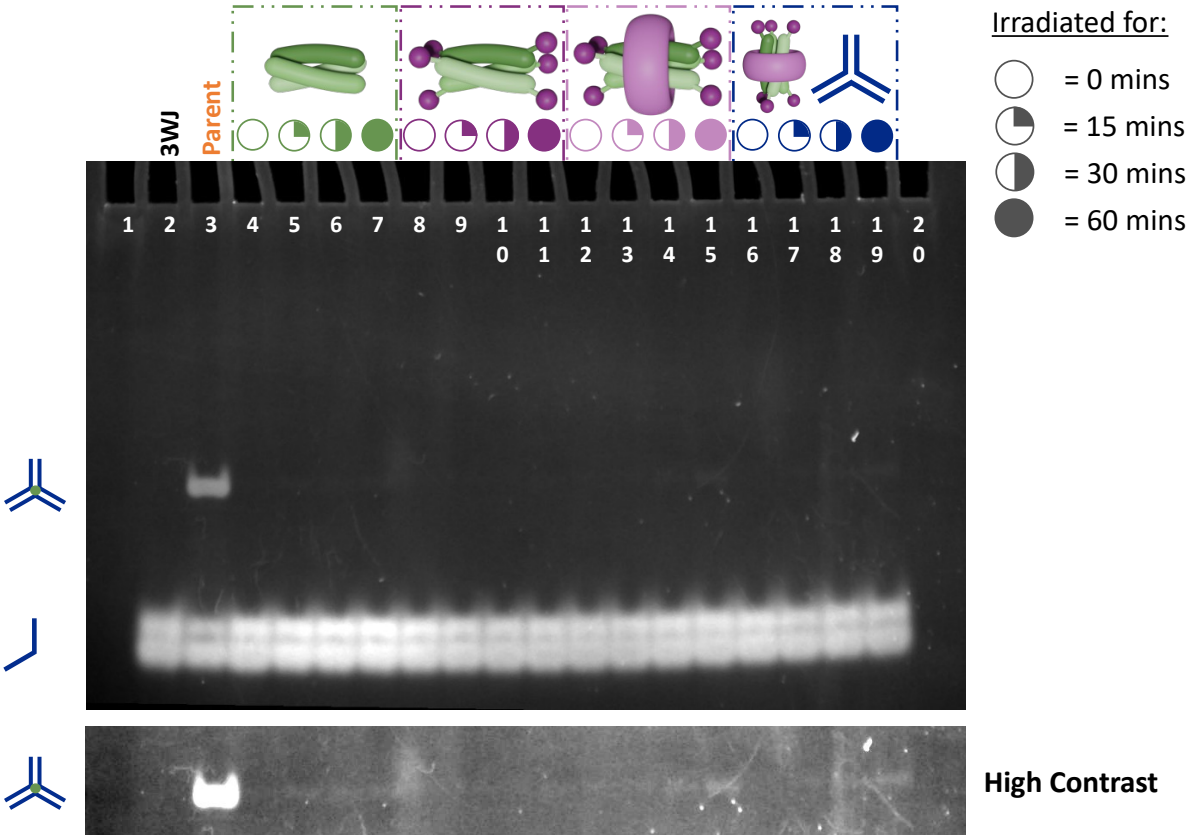

Figure 156: Gel electrophoresis study of 3WJ formation in the presence of cylinders (1 μM) after increasing irradiation times (0, 15, 30 and 60 minutes). Wells: (1,20) running dye; (2) 3WJ stock solution; (3) $[Ni_2L_3]Cl_4$; (4-7) $[Ni_2(L_{5OH})_3]Cl_4$; (8-11) $[Ni_2(L_{5O}")_3]Cl_4$; (12-15) $[Ni_2(L_{5O}")_3.CB10]Cl_4$; (16-19) $[Ni_2(L_{5O}")_3.CB10]Cl_4$ irradiated in the presence of the 3WJ. The 3WJ band is shown at higher contrast below.

Although the concentration was the same (2 μM), irradiation of the metal complexes in preparation for gel electrophoresis requires different conditions to the initial photocleavage experiments. Samples were irradiated simultaneously in reduced

volume cuvettes which decreases the surface area exposed to the irradiation source. Gel electrophoresis is also done under aqueous conditions, so the methanolic cylinder solutions (1 mM) were diluted in water instead of methanol. A final experiment was designed to follow the photocleavage of the cylinder samples under these new conditions before gel electrophoresis. The UV-visible absorbance of the cylinders and rotaxane was taken at 0, 30, and 60 minutes of irradiation, and samples were taken at each time point for mass spectrometry and gel electrophoresis. Although the fluorescence of the bands was very low in the previous gel, the concentration of cylinders in the electrophoresis samples was not increased in favour of maintaining the 2 μM concentration used for irradiation.

The change in solvent means that the absorbance spectra of the cylinders can not be directly compared to the spectra taken in methanol. The absorbance spectra of the uncapped cylinder (Figure 157A) shows a rapid decrease in absorbance over the first 30 minutes of irradiation at both the 226 nm and 361 nm (28% and 29%, respectively) followed by an additional smaller decrease over the next 30 minutes (2% and 3%, respectively). The overall shape of the absorbance spectrum does not change which could indicate degradation of the cylinder.

The absorbance of the capped cylinder shows a more gradual change in the absorbance spectrum (Figure 157B). The absorbance at 217, 271, and 326 nm decreases by 29%, 17%, and 31% respectively and the peak at 271 nm is red shifted to 275 nm over 60 minutes of irradiation. The peak at 326 nm (0 minutes) has a shoulder peak at higher wavelength (around 360 nm) which increases in intensity while the absorbance at 326 nm decreases, suggesting the formation of a product species. The mass spectra of the irradiated samples show an increasing peak for organic

contaminants including the plasticiser diisooctyl phthalate (391, 413 and 429 m/z)[1] which reduce the relative abundance of the metal containing peaks (Figure 158). Before irradiation the peak for the fully capped and 5-capped cylinders are observed (628 m/z and 772 m/z, respectively). After 30 minutes of irradiation the 5-capped cylinder is also visible as a 4+ charged species, and a peak for the 4-capped species also appears (579 m/z and 707 m/z respectively) suggesting that the photocleavage is occurring. The further removal of capping groups is not observed after 60 minutes of irradiation.

The absorbance spectrum of the rotaxane (Figure 157C) before irradiation shows three main absorbance maxima at 214, 273, and 333 nm, similar to the capped cylinder. There is a large decrease in absorbance at 214 and 333 nm after 30 minutes of irradiation (9% and 11%, respectively) followed by a smaller decrease between 30 and 60 minutes (1% and 3%). This change in absorbance is smaller than observed for the capped cylinder (10-15% compared to 15-30%). Both peaks at 272 and 333 nm show a red shift to 277 and 340 nm respectively over 60 minutes. As with the capped cylinder, a shoulder peak to the 333 nm peak could indicate the formation of a new species in solution. The mass spectrum (Figure 159 and 9.1.3, Figure 165) of the rotaxane before irradiation shows the expected 4+ charged peak (1044 m/z) along with the half-ligand containing species (969 m/z, $[Ni_2(L_{5O}")_2(hL_{5O}').CB10]^{4+}$). The two-metal, two-ligand species is observed (844 m/z, $[Ni_2(L_{5O}")_2.CB10]^{4+}$) suggesting that only species with the maximum number of caps are present. A peak at 944 m/z with high charge could not be identified and is only present in the 0 minute spectrum. The metal species in the 30 minute spectrum are too low abundance for accurate identification, however the 60 minute spectrum displays a range of helicate-CB10 complexes with

between 0 and 4 caps. A similar spread is observed for the species containing one half ligand, with peaks for the 0 to 3 capped species visible. Although it has not been highlighted in Figure 159, the same pattern is observed for the two-metal, two-ligand species. The mass spectra overall suggest that the photocleavage has been successful for the rotaxanated species, however the reaction has not been pushed as far as in the original photocleavage experiment (Figure 148), where the uncapped *pseudo*rotaxane was the peak with the highest relative abundance.

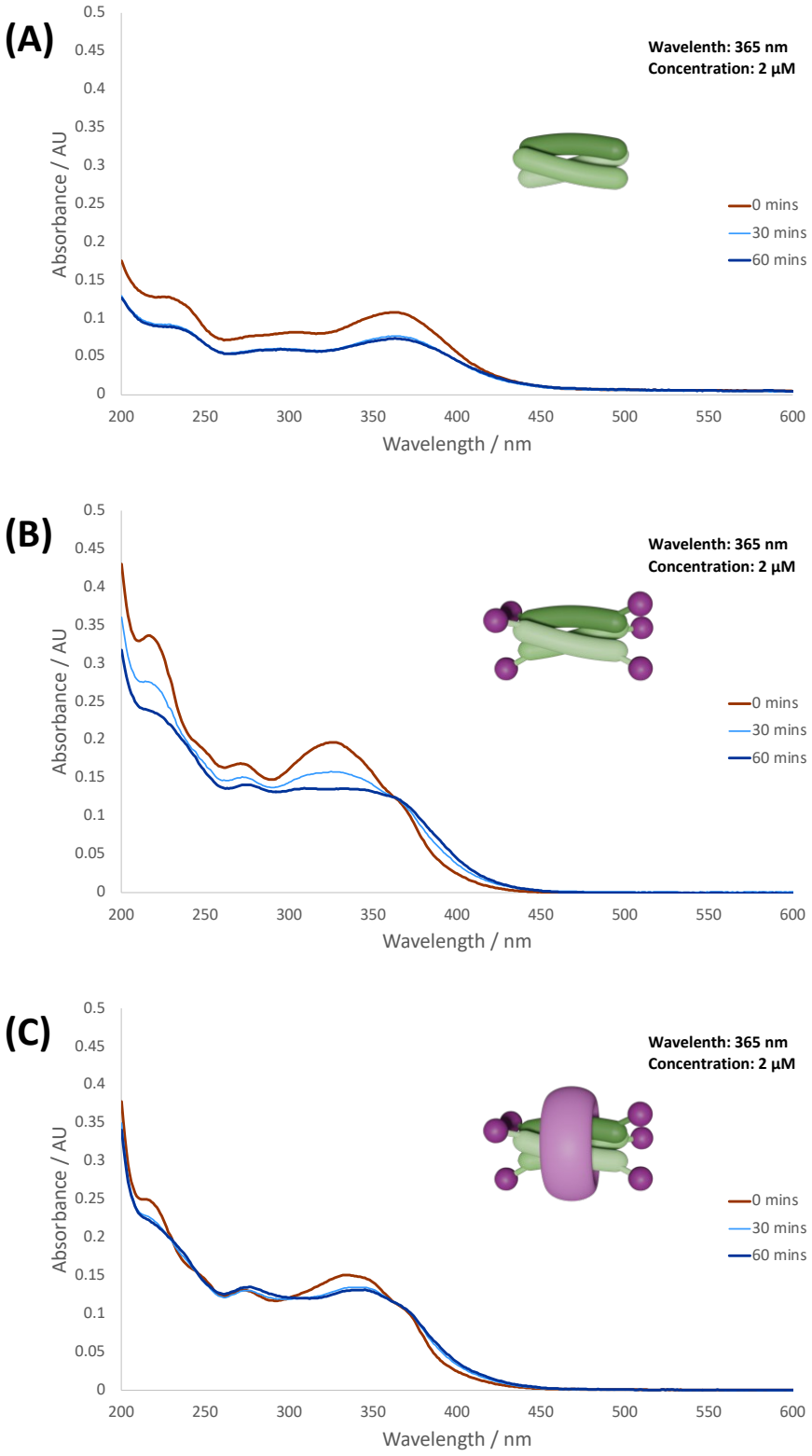

Figure 157: UV-visible absorbance of the (A) uncapped ($[Ni_2(L_{5OH})_3]Cl_4$), (B) capped ($[Ni_2(L_{5O''})_3]Cl_4$), and (C) rotaxanated ($[Ni_2(L_{5O''})_3.CB10]Cl_4$, 2 µM) nickel cylinder species in methanolic (cylinders) or aqueous (rotaxane) solutions after different accumulated irradiation times.

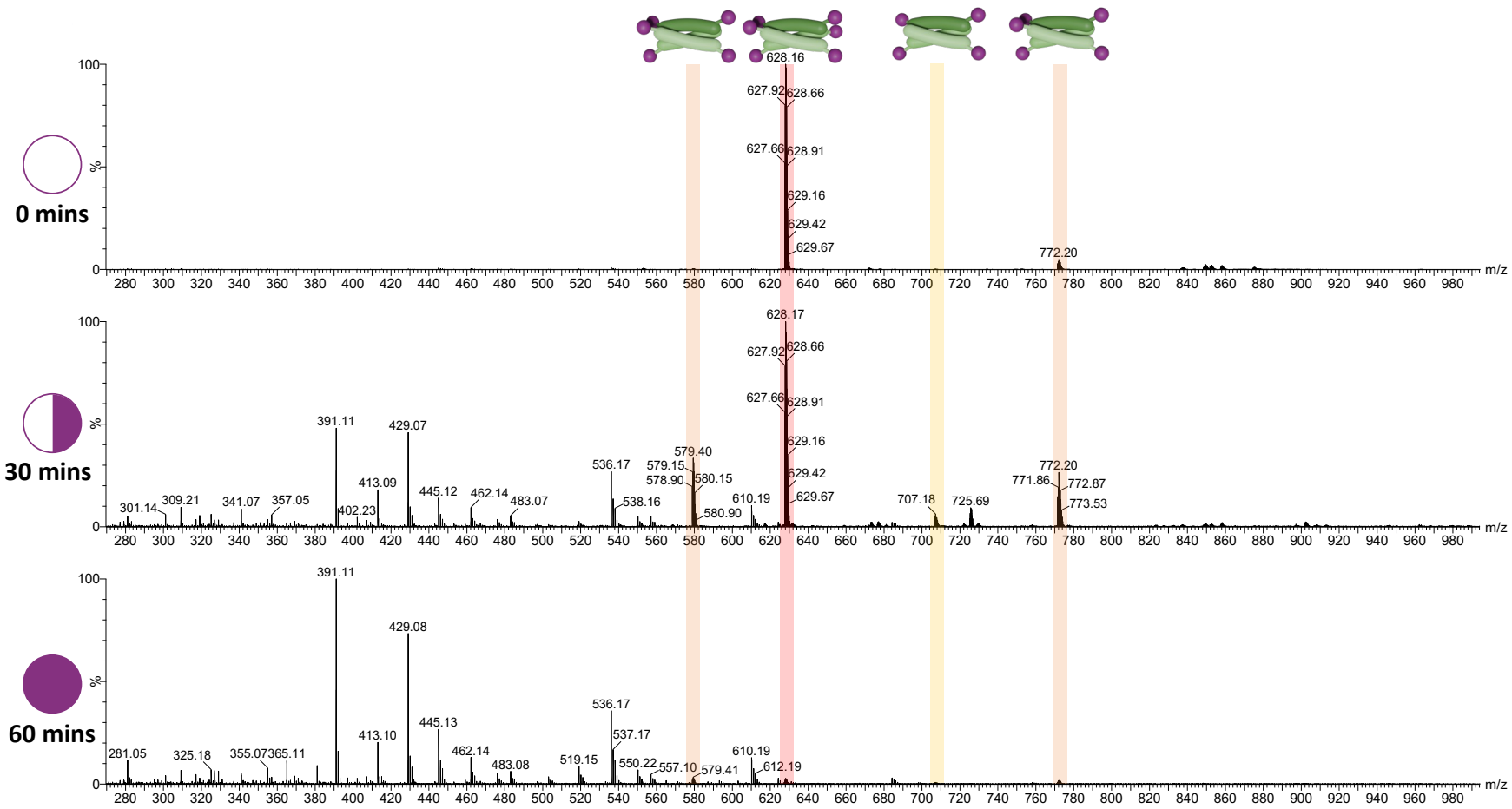

Figure 158: Mass spectrum (TOF ES+, H_2O, 280-980 m/z) of the capped cylinder ($[Ni_2(L_{5O}")_3]Cl_4$) at increasing irradiation time points (0, 30, and 60 mins).

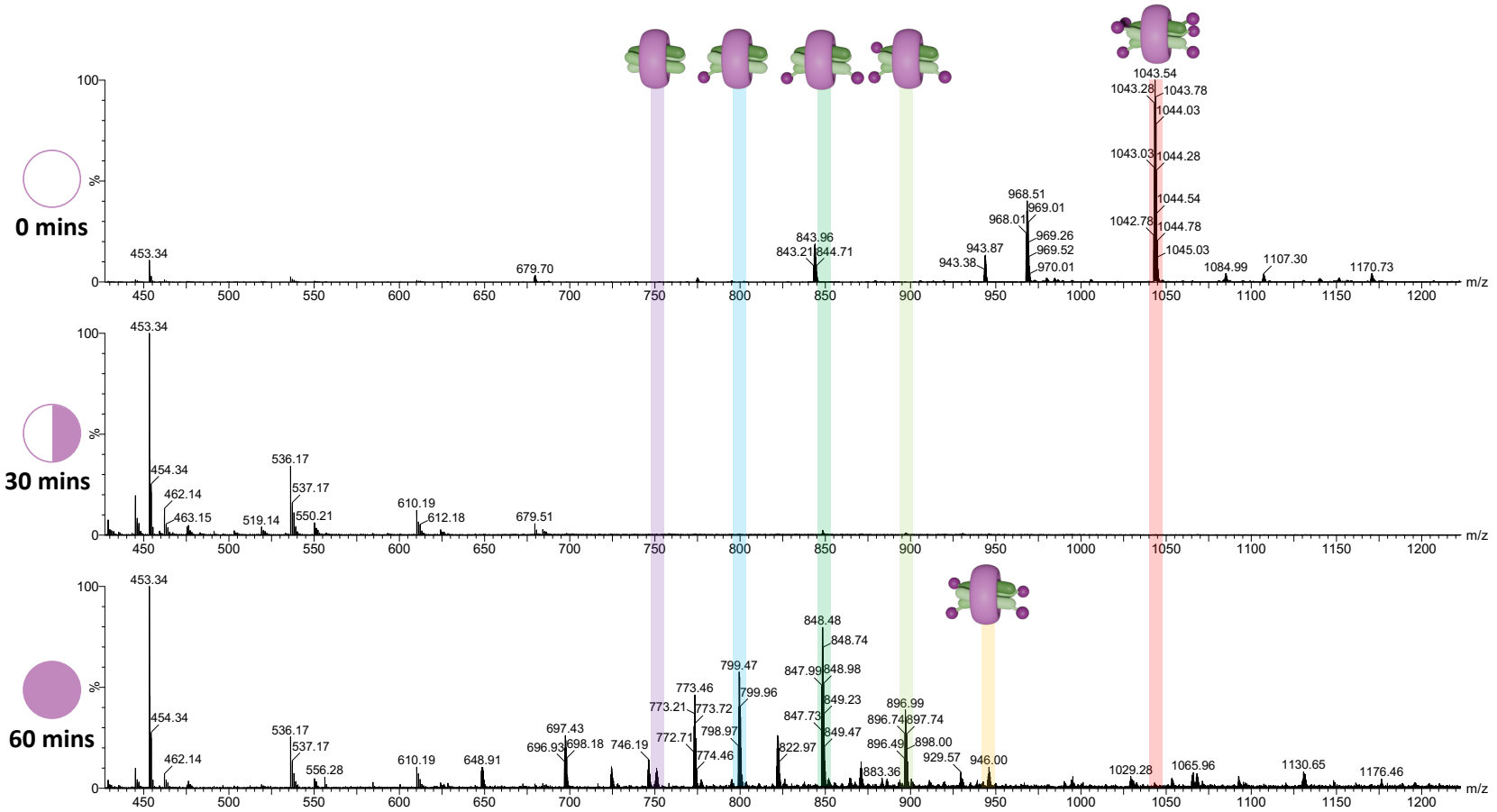

Figure 159: Mass spectrum (TOF ES+, H_2O, 280-980 m/z) of the 5-oxypyridine rotaxane ($[Ni_2(L_{5O}")_3.CB10]Cl_4$) at increasing irradiation time points (0, 30, and 60 mins). See also 9.1.3, Figure 165.

After the irradiation was completed, samples of the cylinders and the rotaxane at each time point (0, 30, and 60 mins) were incubated with the 3WJ DNA solution. Two further samples were made for each of the complexes containing the junction DNA. One of these was kept in the dark as a control and the other was irradiated for 60 minutes. These samples were then incubated as usual and used directly for gel electrophoresis.

Uneven staining of the gel with SYBR gold masks some of the 3WJ bands, particularly for the uncapped and capped cylinder (Figure 160). For clear results this gel should be repeated, however the negative and positive controls (wells 2 and 3, respectively) suggest that the gel has run correctly and so the visible wells have been used as an indicator of preliminary results.

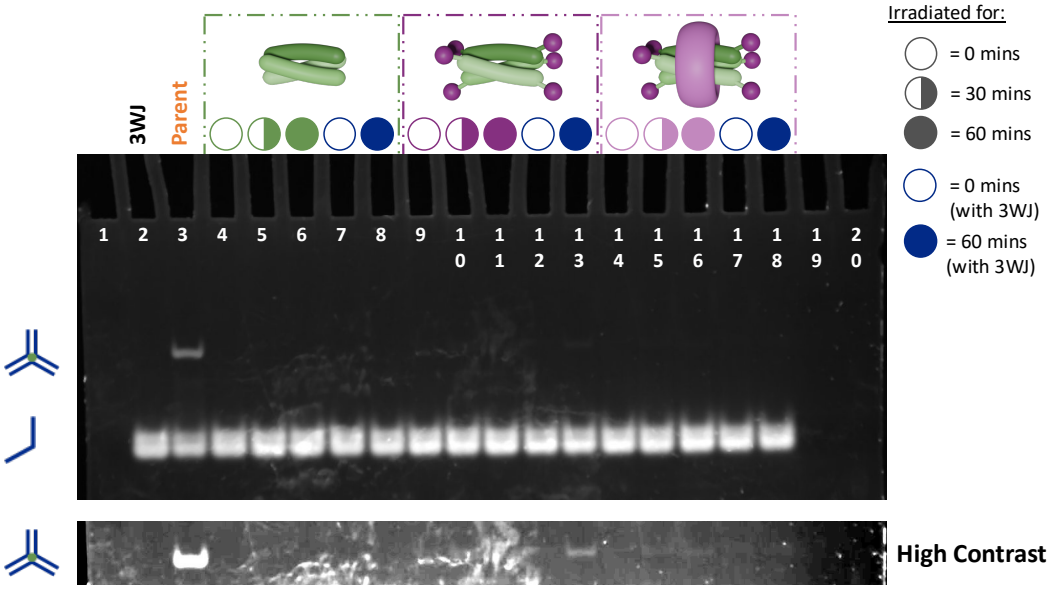

Figure 160: Gel electrophoresis study of 3WJ formation in the presence of cylinders (1 μM) after increasing irradiation times (0, 30 and 60 minutes) and before and after irradiation in the presence of the 3WJ. Wells: (1,20) running dye; (2) 3WJ DNA alone; (3) $[Ni_2L_3]Cl_4$; (4-6) $[Ni_2(L_{5OH})_3]Cl_4$; (9-12) $[Ni_2(L_{5O}")_3]Cl_4$;; (15-17) $[Ni_2(L_{5O}")_3.CB10]Cl_4$; and complexes irradiated with 3WJ (7, 8) $[Ni_2(L_{5OH})_3]Cl_4$; (13, 14) $[Ni_2(L_{5O}")_3]Cl_4$; (18-19) $[Ni_2(L_{5O}")_3.CB10]Cl_4$. The 3WJ band is shown at higher contrast below.

The fluorescence is very low for each sample and so the 3WJ band has been displayed at high contrast. The rotaxane samples are not masked by the staining artifact and show a faint band for junction formation after 30 and 60 minutes of irradiation. No band is observed for the sample which has not been irradiated. When combined with the mass spectrometry and absorbance results it can be concluded that this band is formed due to the release of lesser-capped cylinders from the rotaxane structure. No band is observed for the rotaxane in the presence 3WJ DNA, and it is possible that a very faint band is present for the rotaxane after 60 minutes, however the experiment should be repeated to confirm these results.

The capped cylinder irradiated for 60 minutes in the presence of the DNA shows the most intense 3WJ band. As the other capped cylinder samples are masked by the staining artifact, it is not possible to compare to the 0 minute control, or the cylinder samples irradiated not in the presence of the junction DNA.

Given these preliminary results, this experiment could be improved by increasing the concentration of the metal complex samples used. From the absorbance, the concentration of the irradiated samples could be doubled (4 μM) which should increase the intensity of the 3WJ band, as observed in the first study (Figure 155). Taking a larger sample at each time point for mass spectrometry should increase the relative abundance of the metal complexes in the mass spectrum, which would aid the interpretation of the results.

Overall, the first experiment indicates that the uncapped cylinder ($[Ni_2(L_{5OH})_3]Cl_3$) has retained the ability to form the 3WJ, although this seems reduced in comparison to the parent cylinder. The lack of junction formation in the second experiment is

therefore unexpected, but could be due to the decrease in concentration indicated by the decreased intensity observed in the absorbance spectrum.

The capped cylinder ($[Ni_2(L_{5O}")_3]Cl_3$) shows reduced cylinder binding compared to the uncapped equivalent which is in contrast to the previous example of rotaxanated cylinders, in which the methyl pyridine cap appeared to increase the binding of the imidazole-based cylinder[2]. While the second experiment, where the cylinder was irradiated before incubation with DNA, suggested no increase in junction formation with irradiation time, the final experiment showed that junction formation was successful when the complex was irradiated in the presence of DNA.

The rotaxane ($[Ni_2(L_{5O}")_3.CB10]Cl_3$) also showed very little junction formation in the initial experiment. Formation of the junction here is not expected as the macrocyclic ring should sterically block interactions between the DNA and cylinder. It is possible that the small amount of junction formation is due to release of the helicate from the cylinder under the incubation conditions (37°C). The second experiment identified an increase in the junction formation for the rotaxane both when irradiated prior to incubation with the DNA, and when irradiated in the presence of the DNA. These results were not observed as clearly in the final experiment, however the absorbance and mass spectra were able to confirm that photocleavage is successful under these conditions.

6.3. Stability

The absorbance of the uncapped hydroxypyridine-based cylinders appears to decrease with increasing irradiation despite no change being expected. The decrease was exaggerated when the nickel uncapped cylinder was irradiated under aqueous

conditions for gel electrophoresis causing triple the decrease in intensity compared to the irradiation in methanol over 60 minutes. In addition, the gel electrophoresis experiments show varied results for the 3WJ formation by the uncapped cylinder. The stability of the complexes was examined under organic and aqueous conditions to aid the interpretation of these results.

The UV-visible absorbance of the 4- and 5-oxypyridine complexes was recorded over 24 hours to assess the stability of the cylinders in methanol, and both the cylinders and rotaxanes in water. These solvents were chosen as the gel electrophoresis studies, and any biological studies of these structures, would require the complexes to be dissolved in aqueous media. The absorbance in methanol has been recorded to check that the cylinders are stable in their stock solutions (1 mM), and to ensure changes in absorbance observed in the photocleavage experiments are not due to cylinder degradation.

The 5-oxypyrine complexes have an absorbance maxima at a very short wavelength (< 250 nm) which was masked by noise in most samples, so these peaks have not been considered in this discussion. The absorbance spectrum of the uncapped 5-hydroxypyridine based cylinder ($[Ni_2(L_{5OH})_3]Cl_4$) shows a larger decrease in intensity in water (Figure 161A, 362 nm, 33%), than in methanol (Figure 161B, 19% at 310 nm and 15% at 369 nm) over 24 hours. For the sample in methanol, a large proportion of the overall decrease in intensity occurs within the first four hours of monitoring (15% at 310 nm and 12% at 369 nm).

The absorbance intensity of the capped cylinder ($[Ni_2(L_{5O}")_3]Cl_4$) decreases in water (Figure 161C, 272 nm, 13%, and 327 nm, 16%) whereas the absorbance in

methanol is unchanged over 24 hours, remaining within 2% of the average absorbance at both 275 and 332 nm (Figure 161D).

The absorbance spectra of the ($[Ni_2(L_{5O}")_3.CB10]Cl_4$) rotaxane differs from the cylinders as a decrease in absorbance intensity is observed over the first 3 hours (334 nm, 5%) after which the absorbance appears to plateau until the last few hours (20-24 hours) which shows another small decrease (Figure 161E). A similar initial decrease followed by a plateau after 6 hours is observed at 272 nm. The maximum decrease in absorbance intensity compared to the 0 minute absorbance reading is at 1 hour (5%) and 24 hours (5%) for the peaks at 272 and 334 nm, respectively.

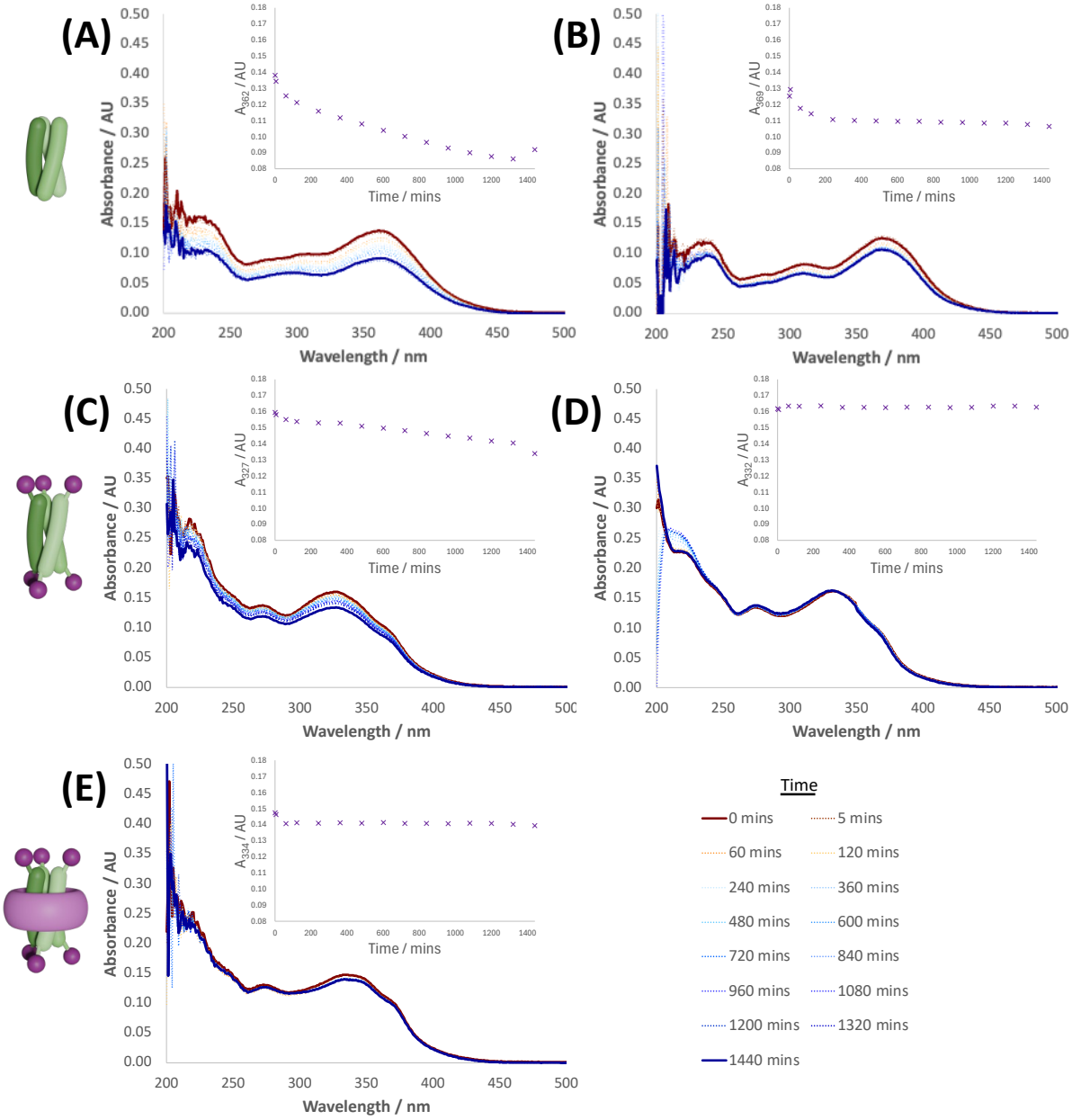

Figure 161: UV-visible absorbance (200-500 nm) of the 5-oxypyridine complexes over 24 hours: (A) $[Ni_2(L_{5OH})_3]Cl_4$ in water (inset: absorbance at 362 nm over 24 hours), and (B) methanol (inset: absorbance at 369 nm over 24 hours); (C) $[Ni_2(L_{5O''})_3]Cl_4$ in water (inset: absorbance at 327 nm over 24 hours), and (D) methanol (inset: absorbance at 332 nm over 24 hours); and (E) $[Ni_2(L_{5O''})_3.CB10]Cl_4$ in water (inset: absorbance at 334 nm over 24 hours).

The stability of the 4-oxypyridine cylinders and rotaxane was also investigated. The uncapped cylinder ($[Ni_2(L_{4OH})_3]Cl_4$) in water shows the largest decrease in absorption over 24 hours across all complexes (Figure 162A). The absorbance intensity decreases by 73% at 315 nm over 24 hours, and by 59% at 238 nm, which is

accompanied by a red shift to 247 nm. In methanol the absorbance intensity of the maxima remains within 2% of the absorbance at the 0 minute time point (Figure 162B). The absorbance maxima at 315 nm decreases in intensity by 12% within the first 12 hours, at which point the absorbance appears to plateau.

The capped cylinder ($[Ni_2(L_{4O}")_3]Cl_4$) in water shows a decrease in absorbance intensity which is largest in the first 12 hours after the experiment was started (Figure 162C). The peak at 230 nm shows a 9% decrease in absorption intensity over the first 12 hours, giving a total decrease of 11% after 24 hours. Similarly, the absorbance at 304 nm decreases by 12% over 12 hours, and 13% over 24 hours. In contrast, the absorbance maxima of the complex in methanol (Figure 162D) stays within 2% of the average absorbance at both 230 and 305nm. The peak at 230 nm shows an increase in absorbance over 19 hours which then decreases rapidly up to 24 hours while the peak at 305 nm shows an overall increase in absorbance.

The absorbance of the rotaxane ($[Ni_2(L_{4O}")_3.CB10]Cl_4$) in water shows the largest change over the first 90 minutes, after which the rate of change is decreased. The peak at 306 nm decreases in intensity by 7% in the first 90 minutes, but only by 7% over 24 hours, while the peak at 229 nm decreases by 6% over 90 minutes, and 8% overall.

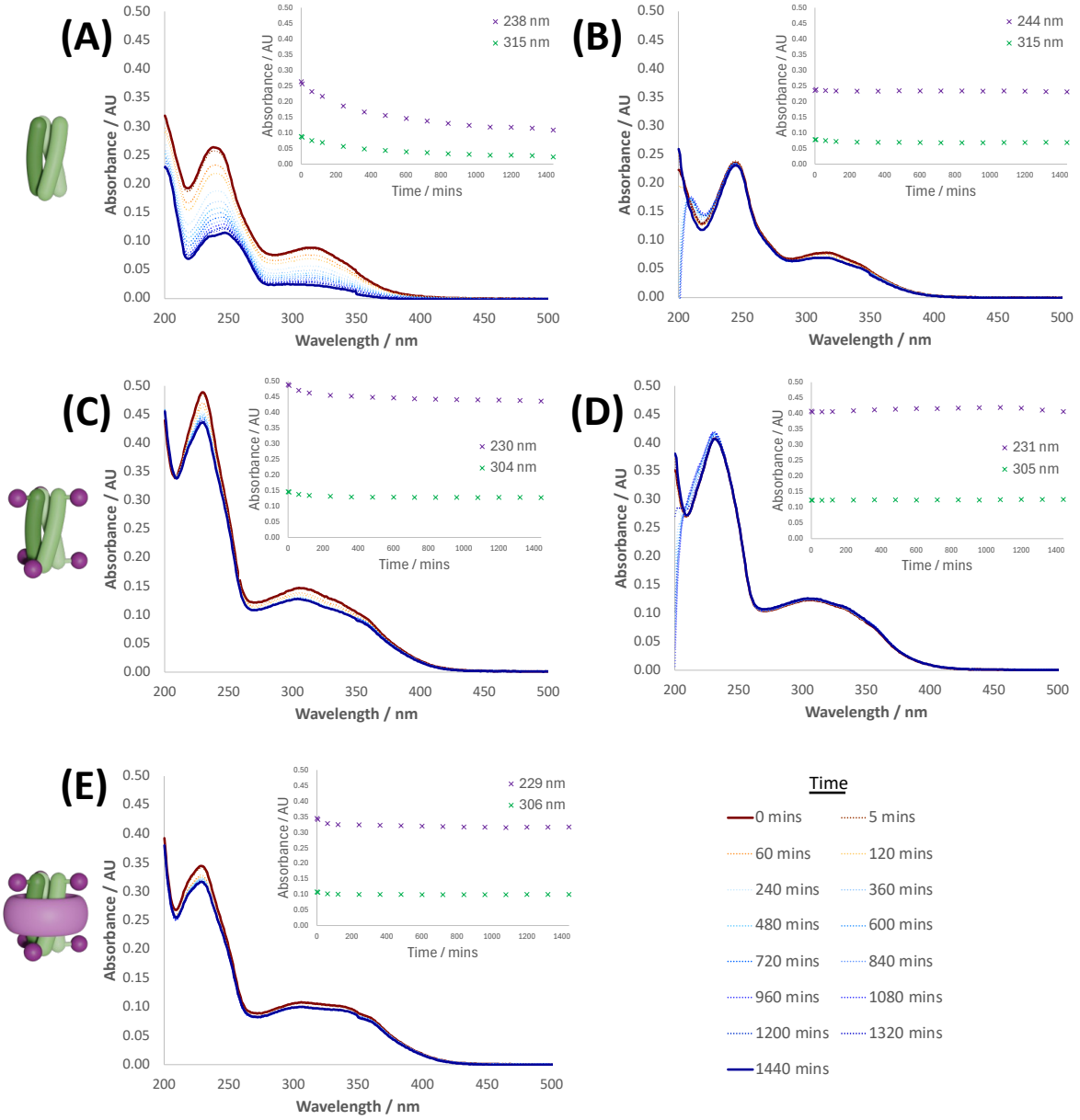

Figure 162: UV-visible absorbance (200-500 nm) of the 4-oxypryidine complexes over 24 hours: (A) $[Ni_2(L_{4OH})_3]Cl_4$ in water (inset: absorbance over 24 hours at 238 and 315 nm), and (B) methanol (inset: absorbance over 24 hours at 244 and 315 nm); (C) $[Ni_2(L_{4O}")_3]Cl_4$ in water (inset: absorbance over 24 hours at 230 and 304 nm), and (D) methanol (inset: absorbance over 24 hours at 231 and 305 nm); and (E) $[Ni_2(L_{4O}")_3.CB10]Cl_4$ in water (inset: absorbance over 24 hours at 229 and 306 nm).

Both the 4- and 5-oxypyridine complexes showed similar changes in absorbance over 24 hours. The 4-oxypyridine solutions were made directly before recording the absorbance whereas the 5-oxypyridine samples were diluted from stock solutions made 2 days prior so some degradation may have occurred before the first

absorbance measurement was recorded. The uncapped cylinders show a much larger decrease in absorbance under aqueous conditions than in methanolic solution which indicates a decreased concentration and therefore some degradation of the helicates. This difference is largest for the 4-hydroxypyrinde based cylinders, which shows a large decrease in the absorbance in water (73%) compared to a relatively small decrease (12%) in methanol over 24 hours. In either case, solutions for analysis should be made directly before use to ensure degradation of the sample is minimised.

A similar result is observed for the capped cylinders although the decrease in absorbance is much smaller in water, and the complexes appear stable in methanol, suggesting that they can be stored as methanolic stock solutions without degrading.

The rotaxanes show less than a 10% decrease in absorbance in aqueous solution suggesting that the CB10 ring stabilises the cylinder under these conditions. This is in agreement with experiments comparing the stability of the parent *pseudo*rotaxane ($[Fe_2L_3.CB10]Cl_4$) to the parent cylinder ($[Fe_2L_3]Cl_4$) which showed enhanced stability of the iron parent in water[2].

The rotaxanes have shown relatively low aqueous solubility and dissolve slowly in water, so stock solutions were prepared in advance for some studies. Instability in solution of the complexes, and poor aqueous solubility of the rotaxanes may have therefore impacted the results of the PAGE studies and should be considered in future experiments.

6.4. Conclusions

Photocleavage of the 4- and 5-oxypryidine based complex has been confirmed by UV-visible absorbance spectroscopy and mass spectrometry, and preliminary

absorbance studies of the iron 3-oxypyridine complexes also suggest photocleavage may occur.

Taking the 5-oxypyridine complexes as an example of this class of cylinder and rotaxane, gel electrophoresis studies were used to demonstrate that the uncapped cylinder retains the 3WJ formation ability of the parent cylinder although this is somewhat reduced when compared to the parent. The results also suggest that both the capping groups and CB10 ring impede 3WJ formation which should allow the photocleavage of the complexes to be investigated by gel electrophoresis, however the irradiation conditions should be optimised for a clear result.

All cylinders investigated appear more stable in methanol than water, while the CB10 ring of the rotaxane appeared to stabilise the capped cylinder axle under aqueous conditions. The increased degradation under aqueous conditions could suggest hydrolysis of the ligand at the imine bond as a key degradation pathway. The uncapped cylinders showed the greatest amount of degradation over 24 hours and it was concluded that sample solutions should be made directly before use.

The results of the stability study should also be considered when interpreting the results of the photocleavage and gel electrophoresis studies. While the uncapped *pseudo*rotaxane was observed from the photocleavage of the rotaxane, the uncapped cylinder was more difficult to observe from the photocleavage of the cylinder. This may reflect the stability of the uncapped species, with the uncapped cylinder being stabilised by the CB10 ring, rather than the efficiency of the photocleavage.

The formation of the 3WJ observed by gel electrophoresis may also be affected by this instability. Instability of the uncapped cylinder over extended periods of time may explain the varied results for junction formation and explain the decreased

fluorescence intensity when compared to the parent cylinder. The uncapped cylinder may also be stabilised in the presence of hosts such as CB10 or the junction, so irradiation of complexes in the presence of these species may increase the junction formation observed as the uncapped cylinder is protected from degradation. The irradiation of the complexes alone and in the presence of DNA for gel electrophoresis should therefore be repeated.

6.5. List of References

1 ESI+ Common Background Ions, https://www.waters.com/webassets/cms/support/docs/bkgrnd_ion_mstr_list.pdf, (accessed January 2024).

2 C. A. J. Hooper, L. Cardo, J. S. Craig, L. Melidis, A. Garai, R. T. Egan, V. Sadovnikova, F. Burkert, L. Male, N. J. Hodges, D. F. Browning, R. Rosas, F. Liu, F. V. Rocha, M. A. Lima, S. Liu, D. Bardelang and M. J. Hannon, *J. Am. Chem. Soc.*, 2020, **142**, 20651–20660.

7. CONCLUSIONS AND FUTURE WORK

This thesis aimed to develop a method to control the previously explored 3WJ binding of a supramolecular helicate known as a cylinder[1–3]. Use of a cylinder as the axle of a supramolecular rotaxane had previously been shown to prevent junction binding, so this work investigated the release of the cylinder from the mechanically interlocked system in response to an external stimulus[4,5]. This thesis explored the synthesis, photocleavage and 3WJ binding of various supramolecular rotaxanes.

Chapter 2 details the successful synthesis of the nickel 2-imidazole based rotaxane ($[Ni_2(L_{Im2})_3.CB10]Cl_4$) by both the slipping and capping mechanism. Capping the 2-imidazole cylinder gave a mixture of partially capped side products which could be confused with photocleavage products during further analysis. The aqueous conditions of the slipping reaction caused some hydrolysis of the cylinder ligands, however this route to the supramolecular rotaxane was preferred as the synthesis of partially capped side products was avoided. The iron capped cylinder ($[Fe_2(L_{Im2}")_3.CB10]Cl_4$) could not be synthesised by either route so clear NMR spectra of these cylinder species could not be recorded. Similar to the iron cylinder, the cobalt 4-imidazole cylinder ($[Co_2(L_{Im4})_3]Cl_4$) retains sharp peaks in the paramagnetic NMR[6], so may provide a better model for NMR analysis in future.

The photocleavage and junction binding of the nickel imidazole complexes was investigated in Chapter 3. The UV-visible absorbance decreases for both the capped cylinder and rotaxane with increasing irradiation time, however the mass spectra did not indicate the formation of 4,5-dimethoxy-2-nitrosobenzaldehyde or the lesser capped species beyond the 4-capped cylinder, so photocleavage of the complexes

could not be confirmed. If repeating the photocleavage experiments, the volume taken for mass spectrometry should be increased to ensure there is enough sample for analysis, and the number of time points decreased to avoid large changes in the volume for subsequent irradiations. PAGE demonstrated that the uncapped and capped cylinders were able to stabilise 3WJs, however irradiation of the capped cylinder and rotaxane showed no change in the fluorescence intensity of the junction band. The conditions under which these samples are irradiated (in water, smaller volumes) differ from the photocleavage experiments, so the absorbance and mass spectra should be recorded before incubation with the DNA to see if similar changes are observed. Although the uncapped imidazole-based cylinder was able to stabilise 3WJs, release of the cylinder from the rotaxane was unsuccessful under the irradiation conditions used.

Chapters 4 and 5 present the synthesis of pyridine-based cylinders with alcohol groups in the 3-, 4- and 5-position. For the 5-oxypyridine, both the iron and nickel uncapped ($[M_2(L_{5OH})_3]Cl_4$), capped ($[M_2(L_{5O''})_3]Cl_4$), and rotaxanated ($[M_2(L_{5O''})_3.CB10]Cl_4$) helicate species have been successfully synthesised. Formation of the encapsulated complex at room temperature implies that the DMNB capping groups are not large enough to mechanically lock the CB10 ring in place, suggesting that this species is a *pseudo*rotaxane.

The 4-oxypyridine cylinder was designed to increase the combined steric bulk of the capping groups by repositioning them at a larger angle to the metal-metal axis. Synthesis of the 4-hydroxypicolinaldehyde reagent was achieved following a previously reported procedure[7] however purification on a scale large enough to carry forward for future reactions was unsuccessful. The uncapped cylinder ($[M_2(L_{4OH})_3]Cl_4$)

was synthesised however alternative purification methods should be considered in the future as anion exchange was not possible and small peaks in the ^{1}H NMR spectrum of the iron cylinder suggest that the free ligand may still be present. The capped cylinder ($[M_2(L_{4O}")_3]Cl_4$) was synthesised directly from the capped aldehyde (Ald_{4O}') following observations that the capped ligand ($L_{4O}"$) may be unstable. The one-pot method produced the capped cylinder in high yield and purity and was later used as an alternative method to form the capped 5-oxypyridine based cylinder. Post-assembly modification of the nickel *pseudo*rotaxane ($[Ni_2(L_{4OH})_3.CB10]Cl_4$) to form the rotaxane ($[Ni_2(L_{4O}")_3]Cl_4$) via a capping method was unsuccessful however, formation of the nickel rotaxane was achieved by a slipping reaction. This gave a low isolated yield due to the low aqueous solubility of the rotaxane and static nature of the product. To improve the yield of the rotaxane, different purification methods should be considered such as anion exchange.

3-hydroxypicolinaldehyde is a commercially available reagent so the 3-oxypyridine based uncapped ($[M_2(L_{3OH})_3]Cl_4$) and capped iron ($[Fe_2(L_{3O}")_3]Cl_4$) cylinders were the most easily accessible of the oxypyridine cylinder series. Unlike the other cylinders which could be synthesised from their respective ligands, the capped nickel cylinder ($[Ni_2(L_{3O}")_3]Cl_4$) could only be synthesised via post-assembly modification of the uncapped cylinder. Investigating the rotaxanation of these complexes by slipping may indicate how the change in position of the caps affects threading of the cylinder.

Chapter 6 demonstrates the successful photocleavage of the 4- and 5-oxypyridine complexes by UV-visible spectroscopy and mass spectrometry. While the uncapped nickel cylinders showed only small decreases in absorbance over a 60-

minute irradiation period, the capped and rotaxanated nickel cylinders show larger changes in the absorbance which are due to the formation of lesser-capped species as observed in the mass spectra. The absorbance spectra of both the nickel and iron capped 5-oxypyridine cylinders demonstrate the appearance of product peaks with increasing intensity during the irradiation period. Photocleavage of the 3-oxypyridine based-cylinders was also investigated by UV-visible absorbance spectroscopy and preliminary results are comparable to the 4- and 5-oxypyridine cylinders.

The 3WJ binding of the nickel 5-oxypyridine complexes was also investigated by PAGE. Preliminary results suggest that the uncapped cylinder ($[Ni_2(L_{5OH})_3]Cl_4$) can stabilise the junction but with a reduced efficiency compared to the nickel parent cylinder ($[Ni_2L_3]Cl_4$). Photocleavage of the nickel species prior to incubation with the 3WJ DNA gave a very weak increase in the junction formation of the rotaxane and irradiation of the species in the presence of DNA showed an increased binding for the capped cylinder in one gel, and rotaxane in another. The variation in results is possibly due to the instability of the uncapped cylinders, and to a lesser degree the capped cylinders, in aqueous solution as indicated by the large decrease in intensity of the absorbance spectrum over 24 hours.

To further understand the results of the PAGE studies, the effect of the sample preparation method on the complexes should be investigated. Photocleavage of the complexes should be repeated under aqueous conditions, and the stability of the cylinders in aqueous solutions at 37°C should be monitored. Investigating the stability and junction binding of the *pseudo*rotaxane ($[Ni_2(L_{5OH})_3.CB10]Cl_4$) would also be beneficial, as encapsulation of the uncapped cylinder by CB10 may increase the stability of the complex. Competition between the macrocycle and junction for cylinder

binding may also be highlighted, which would aid the interpretation of rotaxane junction binding results. PAGE studies should be repeated with an increased concentration of the cylinders to increase the junction formation. Although a one-to-one binding ratio is expected, increasing the intensity of the 3WJ band may allow smaller changes between the binding of the different complexes to be reported. Once optimised, the junction binding of the 3- and 4-oxypyridine complexes should also be investigated and compared.

This thesis explores just one (light) of a variety of possible external triggers for the release of cylinders from a supramolecular rotaxane. The general design of the supramolecular rotaxane explored during this thesis is attractive as the complex can be altered to respond to alternative triggers by exchanging the capping group used. To expand this area of trigger sensitive rotaxanes, a screening process for each potential capping group should be implemented to ensure that the capping group being used can be removed from the terminal aromatic group of the cylinder. For example, investigating the photocleavage of the capped 2-imidazolecarboxaldehyde (Ald_{Im2}') from Chapter 2 would likely have been unsuccessful due to the imidazole ring being a poor leaving group for the photocleavage reaction indicating that this combination of imidazole-based cylinder and capping group was unsuitable for the desired purpose before the synthesis of the rotaxane.

Comparable experimental data for different pre-existing helicate structures would also aid the design of future rotaxane systems. The structure of the cylinder released from the rotaxane for junction binding (the uncapped cylinder) is altered from the cylinder encapsulated in the cucurbituril (the capped cylinder) by removal of the capping groups. This may cause a difference in the properties of the released cylinder

to be unsuitable for 3WJ binding. Compiling a database containing the characteristics of different helicates, such as their absorbance, aqueous solubility, and stability, would indicate which cylinders have features which are most suitable for the intended purpose. It is particularly important to include structures which show poor characteristics such as low solubility and stability as these are less likely to have been published and would prevent similar issues arising in future studies. Including gel electrophoresis experiments to measure the 3WJ binding of each cylinder would also allow a structure activity relationship to be investigated and may highlight the importance of specific features for structural recognition through comparison.

A method for the separation of the metal complex helicates would be invaluable for the continued investigation of supramolecular rotaxanes. Optimisation of HPLC for cylinder separation would allow both the purification and quantitative analysis of differently capped cylinders in solution. This would permit the preparation of supramolecular complexes via post-assembly modification and could also characterise the mechanical bond as the number of caps required to maintain the interlocked structure could be identified. HPLC could also be used to monitor and compare the efficiency of decapping different designs of cylinder by alternative external triggers.

This thesis concludes that the release of cylinders from supramolecular rotaxanes by sequential removal of capping groups can be controlled by an external trigger. This concept could be used to control the formation of 3WJ structures in future studies.

7.1. List of References

1 M. J. Hannon, C. L. Painting, A. Jackson, J. Hamblin and W. Errington, *Chem. Commun.*, 1997, 1807–1808.

2 A. Oleksy, A. G. Blanco, R. Boer, I. Usón, J. Aymamí, A. Rodger, M. J. Hannon and M. Coll, *Angew. Chem. Int. Ed.*, 2006, **45**, 1227–1231.

3 L. Cerasino, M. J. Hannon and E. Sletten, *Inorg. Chem.*, 2007, **46**, 6245–6251.

4 C. A. J. Hooper, L. Cardo, J. S. Craig, L. Melidis, A. Garai, R. T. Egan, V. Sadovnikova, F. Burkert, L. Male, N. J. Hodges, D. F. Browning, R. Rosas, F. Liu, F. V. Rocha, M. A. Lima, S. Liu, D. Bardelang and M. J. Hannon, *J. Am. Chem. Soc.*, 2020, **142**, 20651–20660.

5 C. A. J. Hooper, MRes Thesis, University of Birmingham, 2020.

6 F. Tuna, M. R. Lees, G. J. Clarkson and M. J. Hannon, *Chem. Eur. J.*, 2004, **10**, 5737–5750.

7 A. Lumetzberger, W. Löwe, M. Weber and P. Luger, *J. Heterocycl. Chem.*, 2007, **44**, 155–159.

8. EXPERIMENTAL DETAILS

8.1. General

Commercially available reagents and consumables have been supplied by Sigma-Aldrich, Fisher Scientific, Merck Life Science, VWR International, Scientific Laboratory Supplies, Alfa Aesar, Acros Organics, and Cambridge Bioscience. Silica plates were used for TLC. Alfa Aesar chloride-form Dowex ion exchange resin (1 x 8, 200-400 mesh) has been used throughout. CB10 was synthesised and supplied by the Liu research group from The State Key Laboratory of Refractories and Metallurgy, School of Chemistry and Chemical Engineering, Wuhan University of Science and Technology, Wuhan.

^{1}H and ^{13}C NMR spectra where recorded using a Bruker AVIII 300 MHz spectrometer (5 mm BBFO probe), a Bruker AVANCE NEO 400 MHz NMR spectrometer (5 mm BBFO “smart” probe), and a Bruker AVIII 400 MHz NMR spectrometer (5 mm ^{1}H-^{13}C DUL probe). NMR spectra have been processed using MestReNova (v14.0.0-23239) software. Where possible the residual solvent peak has been used as a reference peak and chemical shifts normalised according to previously reported values[1]. The carbon atoms of each synthesised structure have been numbered (in red) and where protons would be attached these assume the same number as the attached carbon. Spectra have been assigned using the chemical shifts, splitting patterns, J-values and by comparison to literature where available.

C. Hooper recorded mass spectra using a Waters Synapt G2-S with an Advion Triversa Nanomate attachment and a Thermofisher Scientific LCQ-Fleet (low resolution spectra). Other mass spectra were recorded by the analytical staff at the

University of Birmingham using Waters Synapt G2-S with an Advion Triversa Nanomate attachment, a Waters Xevo G2-XS, a Bruker MircOToF QII and an Orbitrap Exploris GC. Spectra were analysed using MassLynx (v4.2) software. The inbuilt MassLynx isotope pattern calculator has been used where possible to confirm assignments, along with enviPat isotope pattern calculator[2]. Common electrospray (ES) background were identified using a list produced by Waters[3]. For assignments, "M" is the structure displayed at the beginning of the section for organic molecules. For inorganic complexes, "M" excludes any anions shown in the structure at the start of the section. Anions will be indicated in the structure where necessary.

8.2. Synthesis of the Imidazole based cylinders

8.2.1. 2-imidazole based ligand (L_{Im2})

Based on the synthesis by F. Tuna *et al.*[4].

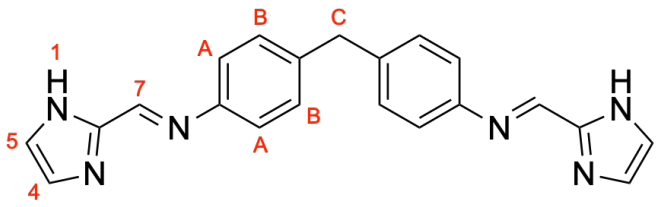

4,4'-methylendianiline (0.79 g, 3.98 mmol) and 2-imidazolecarboxaldehyde (0.77 g, 8.00 mmol) were put under an inert atmosphere. Methanol (35mL) was added and stirred for 10 minutes. Two drops of glacial acetic acid are then added and the mixture was refluxed for 2 h at 80°C. An off-white precipitate was collected by filtration, washed with methanol and dried in vacuo (1.18 g, 3.34 mmol, 84% yield).

^{1}H NMR (300 MHz, DMSO-d_6): δ 13.05 (s, 1H, H_1), 8.40 (s, 1H, H_7), 7.35 – 7.18 (m, 6H, H_A, H_B, H_4, and H5), 3.98 (s, 1H, H_C).

MS (TOF ES+, DCM/MeOH): m/z = 178.09 ($[M + 2H]^{2+}$), 277.15 ($[hL_{Im2} + H]^+$), 355.17 ($[M + H]^+$).

8.2.2. 4-imidazole based ligand (L_{Im4})

Based on the synthesis by F. Tuna *et al.*[4].

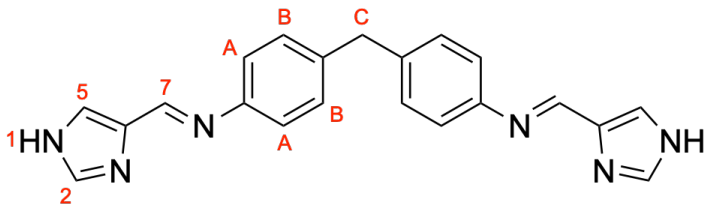

4,4'-methylendianiline (0.79 g, 3.98 mmol) and 4-imidazolecarboxaldehyde (0.77 g, 8.00 mmol) are stirred in methanol (30 mL) for 10 min; two drops of glacial acetic acid are then added and the mixture is refluxed for 2 h. An off-white solid should precipitate and is collected by filtration, washed with methanol (1.09 g, 3.08 mmol, 77% yield).

^{1}H NMR (400 MHz, DMSO-d_6) δ 12.77 (s, 1H, H_1), 8.43 (s, 1H, H_2), 7.81 (br s, 1H, H_5), 7.31 – 7.21 (m, 2H, $H_{A/B}$), 7.20 – 7.07 (m, 2H, $H_{A/B}$), 3.95 (s, 1H, H_C).

MS (TOF ES+, DCM): m/z = 178.09 ($[M + 2H]^{2+}$), 277.15 ($[hL_{Im4} + H]^+$), 287.13 ($[C_{18}H_{15}N]^+$), 355.17 ($[M + H]^+$), 377.15 ($[M + Na]^+$), 709.33 ($[2M + H]^+$).

8.2.3. 2-imidazole iron cylinder ($[Fe_2(L_{Im2})_3](BF_4)_4$)

Based on the work of F. Tuna *et al.*[4] and M. Pascu[5].

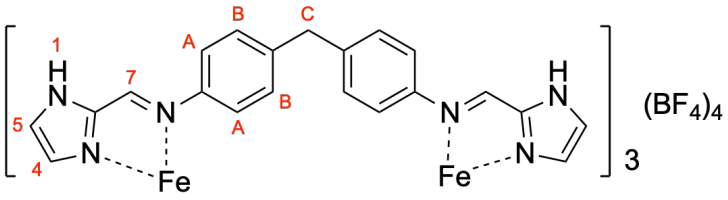

Iron(II) tetrafluoroborate hexahydrate (0.14 g, 0.38 mmol) was dissolved in acetonitrile (15 mL) and added to the 2-imidazole ligand (L_{Im2}, 0.20 g, 0.56 mmol) in acetonitrile (10 mL) under argon atmosphere. The solution was stirred for 1 hour at room temperature before removing the solvent under vacuo. The residue was redissolved in acetonitrile (minimal), precipitated in diethyl ether (400 mL) and filtered to collect the precipitate. The solvent was removed from the coloured filtrate and the residue redissolved in minimal acetonitrile to reprecipitate in diethyl ether (400 mL). The suspension was filtered and the dark purple precipitates combined (0.29 g, 0.19 mmol, 100% yield).

^{1}H NMR (300 MHz, Acetonitrile-d_3) [Paramagnetic] δ 124.16 (s, 1H, H_4), 71.17 (s, 1H, H_7), 65.28 (s, 1H, H_1), 56.40 (s, 1H, H_5), 22.11 (s, 1H, H_C), 17.80 (s, 2H, $H_{A/B}$), 0.63 (s, 2H, $H_{A/B}$).

MS (TOF ES+, MeCN): m/z = 355.17 ($[L_{Im2} + H]^+$), 409.59 ($[Fe_2(L_{Im4})_2 – 2H]^{2+}$), 586.16 ($[M– 2H]^{2+}$).

8.2.4. 2-imidazole nickel cylinder ($[Ni_2(L_{Im2})_3]Cl_4$)

Based on the work of F. Tuna *et al.*[4] and M. Pascu[5].

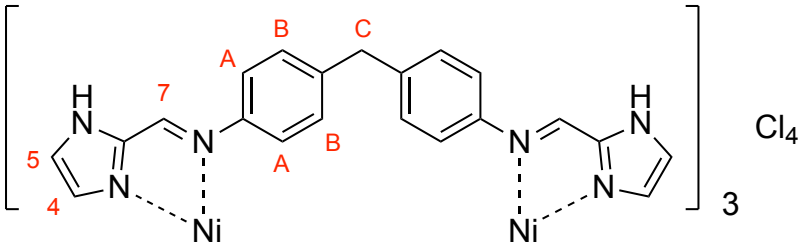

Nickel(II) chloride hexahydrate (0.19 g, 0.80 mmol) was dissolved in methanol (10 mL) and added to the 2-imidazole ligand (0.43 g, 1.20 mmol) suspended in methanol (40 mL) while stirring under inert atmosphere. The solution was stirred for 1 hour at room temperature before filtering under vacuo. Ammonium hexafluorophosphate (0.65 g, 4.0 mmol) was added and the solution was allowed to precipitate at 4°C for 2 days. The precipitate was collected by vacuum filtration and washed with cold methanol to yield an orange product (0.63 g, 0.36 mmol).

MS (TOF ES+, MeCN): m/z = 178.09 ($[L_{Im2} + 2H]^{2+}$), 274.39 ($[Ni_2(L_{Im2})_2 – H]^{3+}$), 294.09 ($[M]^{4+}$), 355.17 ($[L_{Im2} + H]^{+}$), $]^{+}$), 287.13 ($[C_{18}H_{15}N]^{+}$), 411.09 ($[Ni_2(L_{Im2})_2 – 2H]^{2+}$), 588.17 ($[M - 2H]^{2+}$).

The precipitate was then suspended in methanol (50 mL) with excess Dowex resin and stirred for 1 hour. The solution was filtered, the precipitate washed with methanol (25 mL) and the solvent removed from the filtrate to yield an orange powder (0.37 g, 0.28 mmol, 70% yield).

MS (TOF ES+, MeCN): m/z = 178.09 ($[L_{Im2} + 2H]^{2+}$), 274.39 ($[Ni_2(L_{Im2})_2 – H]^{3+}$), $]^{+}$), 287.13 ($[C_{18}H_{15}N]^{+}$), 294.59 ($[M]^{4+}$), 355.17 ($[L_{Im2} + H]^{+}$), 393.11 ($[M - H]^{3+}$), 411.08 ($[Ni_2(L_{Im2})_2 – 2H]^{2+}$), 588.17 ($[M - 2H]^{2+}$), 821.16 ($[Ni_2(L_{Im2})_2 – 3H]^{+}$).

8.2.5. 4-imidazole iron cylinder ($[Fe_2(L_{Im4})_3]Cl_4$)

Based on the work of F. Tuna *et al.*[4].

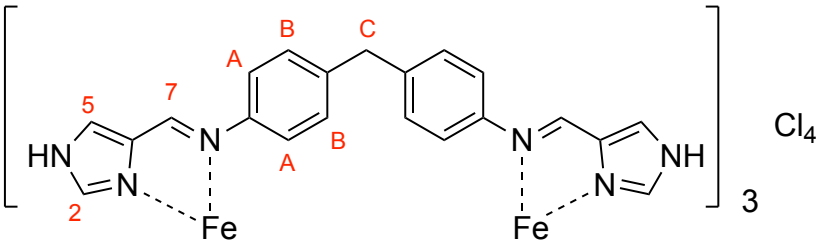

Iron(II) chloride tetrahydrate (0.10 g, 0.48 mmol) and the 4-imidazole ligand (0.28 g, 0.79 mmol) were stirred in methanol (20 mL) for 40 minutes at room temperature before filtering through celite. Ammonium hexafluorophosphate (excess, 400 mg) was added to the filtrate and the solution was allowed to precipitate at 4°C for 4 days. The precipitate was collected by vacuum filtration and washed with cold methanol (15 mL). The orange crude product was suspended in methanol (20 mL) and stirred with Dowex resin for 1 hour until the solution appeared a clear orange. The solution was filtered, washed with methanol (minimal) and the solvent removed to yield a dark orange solid (0.25 g, 0.19 mmol, 80% yield).

^{1}H NMR (300 MHz, Methanol-d_4) [Paramagnetic] δ 157.35 (s, 1H, H_2), 41.91 (s, 1H, H_7), 37.21 (s, 1H, H_5), 25.29 (s, 1H, H_C), 14.69 (s, 2H, $H_{A/B}$), -5.67 (s, 2H, $H_{A/B}$).

MS (TOF ES+, MeOH): m/z = 178.09 ($[L_{Im4} + 2H]^{2+}$), 277.14 ($[hL_{Im4} + H]^{+}$), 355.17 ($[L_{Im4} + H]^{+}$), 391.12 ($[M - H]^{3+}$), 409.09 ($[Fe_2(L_{Im4})_2 - 2H]^{2+}$), 586.17 ($[M - 2H]^{2+}$), 817.17 ($[Fe_2(L_{Im4})_2 - 3H]^{+}$).

8.2.6. 4-imidazole nickel cylinder ($[Ni_2(L_{Im4})_3]Cl_4$)

Based on the work of F. Tuna *et al*[4].

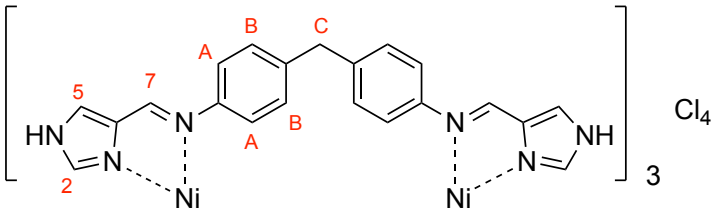

Nickel(II) chloride hexahydrate (0.10 g, 0.40 mmol) was dissolved in methanol (20 mL) and added to the 4-imidazole ligand (L_{Im4}, 0.21 g, 0.60 mmol) suspended in methanol (20 mL). The solution was stirred for 30 minutes at room temperature before ammonium hexafluorophosphate (excess) was added. The solution was allowed to precipitate at 4°C for 3 days before the precipitate was collected by vacuum filtration and washed with methanol (minimal). The filtrate was filtered again and the precipitate was washed with methanol (10 mL). The combined precipitates were resuspended in MeOH (20 mL) and converted to the chloride salt by Dowex conversion. The green solution was filtered to remove the Dowex beads and the solvent was removed from the filtrate to yield a pale green powder (0.12 g, 0.09 mmol, 45% yield).

MS (TOF ES+, MeOH): m/z = 178.09 ($[L_{Im2} + 2H]^{2+}$), 274.40 ($[Ni_2(L_{Im2})_2 – H]^{3+}$), 277.14 ($[hL_{Im4} + H]^{+}$), 287.13 ($[C_{18}H_{15}N]^{+}$), 295.08 ($[M]^{4+}$), 355.17 ($[L_{Im2} + H]^{+}$), 393.10 ($[Ni_2(L_{Im2})_3 – H]^{3+}$), 411.09 ($[Ni_2(L_{Im2})_2 – 2H]^{2+}$), 588.16 ($[M - 2H]^{2+}$), 821.17 ($[Ni_2(L_{Im4})_2 – 3H]^{+}$).

8.2.7. Attempted synthesis of the 2-imidazole nickel cylinder via capping ($[Ni_2(L_{Im2}"_{DMNB})_3](PF_6)_4$)

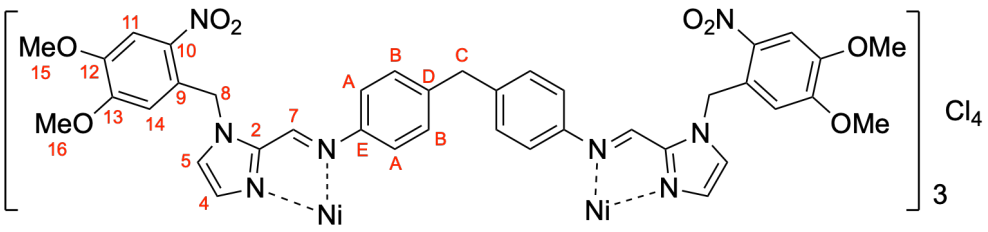

$[Ni_2(L_{Im2})_3]Cl_4$ (0.030g, 0.02 mmol) was suspended in deionised water (20 mL) and added to DMNB-Br (0.056 g, 0.20 mmol) under inert atmosphere. Aqueous potassium carbonate (0.01 g in 1 mL) was added and the mixture was heated to reflux for 13 hours. A cloudy yellow solution was cooled to room temperature and water removed under vacuo until less than 1 mL remained. Methanol (40 m) was added and the solution filtered through a 0.45 µm Millipore filter to remove a green precipitate. Methanolic ammonium hexafluorophosphate (0.15 g) was added to the filtrate and the complex allowed to precipitate. The precipitate was collected by vacuum filtration from an orange solution.

8.2.8. Attempted synthesis of the capped 4-imidazole nickel cylinder ($[Ni_2(L_{Im4}"_{DMNB})_3]Cl_4$)

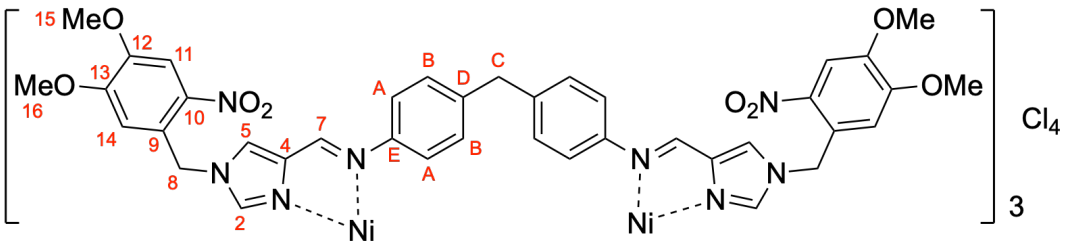

$[Ni_2(L_{Im4})_3]Cl_4$ (0.015 g, 0.011 mmol) and DMNB-Br (0.027 g, 0.099 mmol) were suspended in water (10 mL) under inert atmosphere. Potassium carbonate (0.005 g,

0.033 mmol) dissolved in water (2 mL) was added and the suspension heated to reflux for 21 hours. The solution was allowed to cool to room temperature before filtering through a 0.45 μm filter to remove a brown precipitate. A pale green solution was investigated by mass spectrometry.

8.2.9. Attempted synthesis of the 2-imidazole based nickel rotaxane ($[Ni_2(L_{Im2}'')_3.CB10](PF_6)_4$)

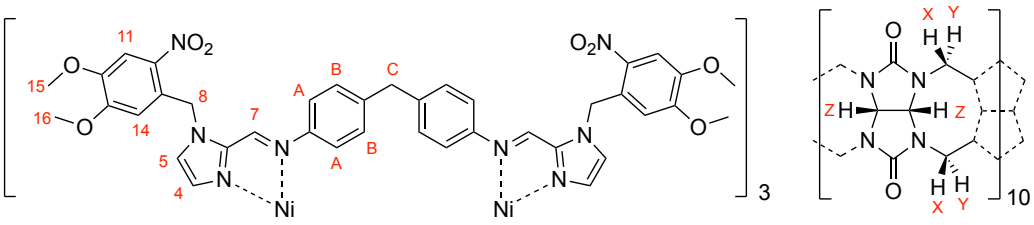

$[Ni_2(L_{Im2})_3]Cl_4$ (0.007 g, 0.005 mmol) and CB10 (0.008 g, 0.005 mmol) were suspended in degassed, deionised water (15 mL). Aqueous potassium carbonate (0.004 g in 1 mL) was added to form a cloudy solution. DMNB-Br (0.017 g, 0.06 mmol) was added before the mixture was heated to reflux (100°C) for 24 hours. The solution was cooled to room temperature and filtered under *vacuo*. NH_4PF_6 (excess) was added to the filtrate and the product allowed to precipitate for 3 days. A solid was collected by filtration and washed with water (4 mL) and diethyl ether to dry giving an orange powder product (0.004 g, 0.001 mmol, 27%).

8.2.10. Capped 2-imidazolecarboxaldehyde (Ald_{Im2}')

Based on the work of V. Sadovnikova[6].

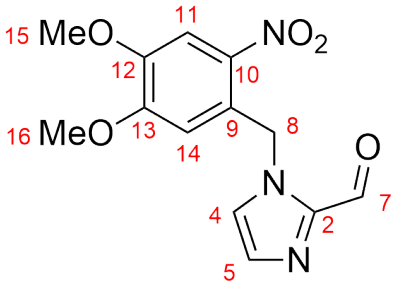

2-imidazolecarboxaldehyde (0.19 g, 2.0 mmol) was suspended in acetonitrile and potassium carbonate (0.55 g, 4.0 mmol) in water (3.5 mL) was added. DMNB-Br (0.55 g, 2.0 mmol) was suspended in degassed acetonitrile (15 mL) under dark and inert conditions and added to the 2-imidazole carboxaldehyde solution. The solution was heated to reflux (80°C) for 19 hours before cooling to room temperature and the solvent was removed under vacuo until less than 3 mL remained. The orange oil was redissolved in DCM (10 mL) and washed with brine (2 x 5 mL). The organic phase was collected and dried over $MgSO_4$ before the solvent was removed under vacuo to leave a crude yellow oil which crystallised on standing.

The crude product was purified by column chromatography (silica gel, 10% ethyl acetate in chloroform, 1% methanol added during elution) to yield an orange-yellow solid product in two fractions (0.41 g, 1.4 mmol, 71% yield).

^{1}H NMR (300 MHz, Chloroform-*d*): δ 9.82 (d, *J* = 1.0 Hz, 1H, H_7), 7.72 (s, 1H, $H_{11/14}$), 7.37 (d, *J* = 0.9 Hz, 1H, $H_{4/5}$), 7.29 – 7.27 (m, 1H, $H_{4/5}$), 6.26 (s, 1H, $H_{11/14}$), 5.99 (s, 2H, H_8), 3.94 (s, 3H, $H_{15/16}$), 3.74 (s, 3H, $H_{15/16}$).

MS (TOF ES+): m/z = 292.15 ($[M + H]^+$), 310.16 ($[M + H_2O + H]^+$), 314.13 ($[M + Na]^+$), 324.18 ($[M + MeOH + H]^+$), 605.26 ($[2M + 2H_2O + H]^+$). [Unassigned: 306.17 (20%), (<10%) 346.16, 408.14, 430.99, 456.69]

Column fractions 60-72.

^{1}H NMR (300 MHz, Chloroform-*d*) δ 9.84 (d, *J* = 1.0 Hz, 1H, H_7), 7.73 (s, 1H, $H_{11/14}$), 7.38 (d, *J* = 1.0 Hz, 1H, $H_{4/5}$), 7.33 – 7.25 (m, 1H, $H_{4/5}$), 6.28 (s, 1H, $H_{11/14}$), 6.01 (s, 2H, H_8), 3.95 (s, 3H, $H_{15/16}$), 3.75 (s, 3H, $H_{15/16}$).

MS (TOF ES+): m/z = 292.15 ($[M + H]^+$), 310.16 ($[M + H_2O + H]^+$), 314.13 ($[M + Na]^+$). [Unassigned: 430.98 (100%), 446.96 (40%), 838.96 (20%)]

R_f (10% ethyl acetate in chloroform): 0.17.

UV-Vis (Chloroform, CAH-Ana-003): 245 nm (8,900 $mol^{-1}cm^{-1}$), 288 nm (11,500 $mol^{-1}cm^{-1}$), 344 nm (4,500 $mol^{-1}cm^{-1}$).

8.2.11. Capped 2-imidazole ligand (L_{Im2}")

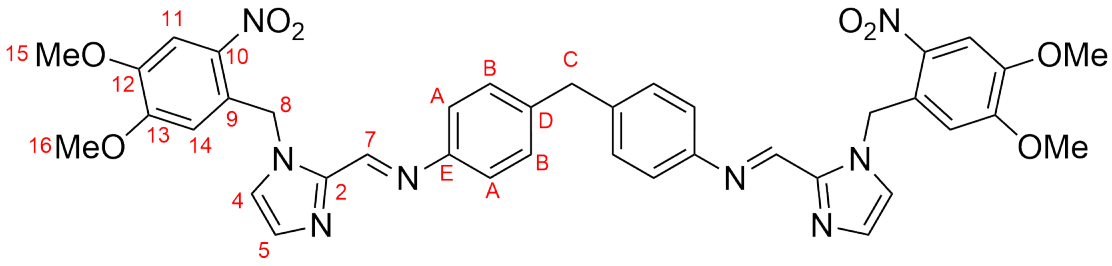

Ald_{Im2}' (0.15 g, 0.52 mmol) was dissolved in ethanol (5 mL) under dark and inert atmosphere. MDA in ethanol (10 mL) was added, followed by acetic acid (2 drops). The solution was heated to reflux overnight before cooling the suspension to room temperature. A precipitate was collected by vacuum filtration and washed with ethanol (5 mL) to yield a pale-yellow powder (0.17 g, 0.22 mmol, 86% yield).

^{1}H NMR (400 MHz, Methylene Chloride-d2): δ 8.49 (d, J = 0.6 Hz, 1H, H_7), 7.69 (s, 1H, $H_{11/14}$), 7.29 (s, 1H, $H_{4/5}$), 7.21 – 7.18 (d, J = 1.0 Hz, 1H, $H_{4/5}$), 7.17 – 7.10 (t, J = 0.8

Hz, 2H, $H_{A/B}$), 7.02 – 6.95 (m, 2H, $H_{A/B}$), 6.16 (s, 1H, $H_{11/14}$), 6.15 (s, 2H, H_8), 3.93 (s, 1H, H_C), 3.89 (s, 3H, $H_{15/16}$), 3.63 (s, 3H, $H_{15/16}$).

^{13}C NMR (101 MHz, Methylene Chloride-d_2) δ 154.41 ($C_{4/5}$), 150.53 (C_7), 148.91, 148.52, 143.97, 140.44, 140.31, 131.11, 129.98 ($C_{A/B}$), 129.02, 125.57 ($C_{4/5}$), 121.41 ($C_{A/B}$), 109.99 ($C_{11/14}$), 108.51 ($C_{11/14}$), 56.70 ($C_{15/16}$), 56.41($C_{15/16}$), 49.34 (H_8), 41.28 (H_C).

Unassigned peaks are carbons C_D, C_E, C_2, C_9, C_{10}, C_{12}, and C_{13}.

MS (TOF ES+, DCM:MeOH): m/z = 196.04 ($[C_9H_9NO_4 + H]^+$), 277.12 ($[hL_{Im2} + H]^+$), 373.12 ($[M + 2H]^{2+}$), 472.19 ($[hL_{Im2}' + H]^+$), 550.22 ($[L_{Im2}' + H]^+$), 745.29 ($[M + H]^+$), 777.32 ($[M + MeOH + H]^+$).

8.2.12. Capped nickel 2-imidazole cylinder ($[Ni_2(L_{Im2}"_{DMNB})_3]Cl_4$) via ligand

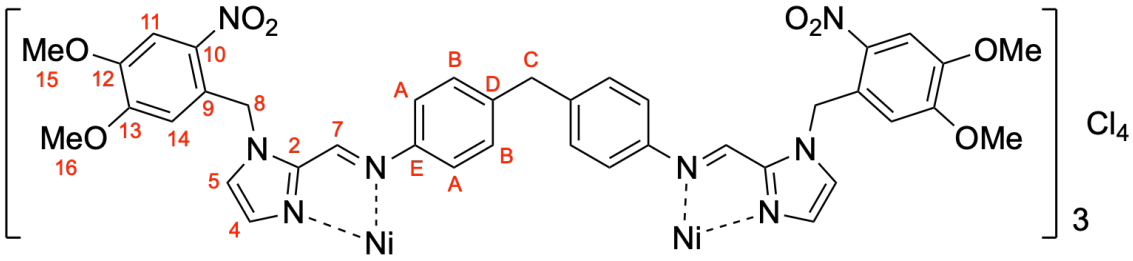

L_{Im2}" (0.10 g, 0.13 mmol) was suspended in methanol (3 ml). Nickel chloride hexahydrate (0.02 g, 0.09 mmol) was dissolved in methanol (2 mL) and added dropwise to the ligand solution which was stirred at room temperature overnight. The solution was filtered under *vacuo* and washed with methanol (5 mL) to remove a pale yellow precipitate. The yellow filtrate was collected and concentrated before addition of ammonium hexafluorophosphate (0.14 g, 0.90 mmol). The solution was stirred for 1

hour and 45 minutes before a precipitate was collected by filtration. The dark orange precipitate was washed with methanol (0.10 g, 0.03 mmol).

The orange precipitate (0.92 g) was suspended in methanol (50 mL) with Dowex resin and stirred for 1 hour at room temperature. The beads were then removed by vacuum filtration and washed with methanol. The solvent was removed from the clear yellow filtrate to leave an orange solid product (0.07g, 0.03 mmol, 67% yield).

MS (TOF ES+, MeOH): m/z = 587.67 ($[M]^{4+}$), 718.20 ($[Ni_2(L_{Im2}")_2(L_{Im2}') - H]^{3+}$), 795.21 ($[M + Cl]^{3+}$). [Unassigned (<5%): 804.55]

UV-Vis (MeOH, CAH-Ana-028): 224 nm (100,700 $mol^{-1}cm^{-1}$), 324 nm (198,200 $mol^{-1}cm^{-1}$).

8.2.13. Attempted synthesis of the iron 2-imidazole cylinder ($[Fe_2(L_{Im2}"_{DMNB})_3]Cl_4$)

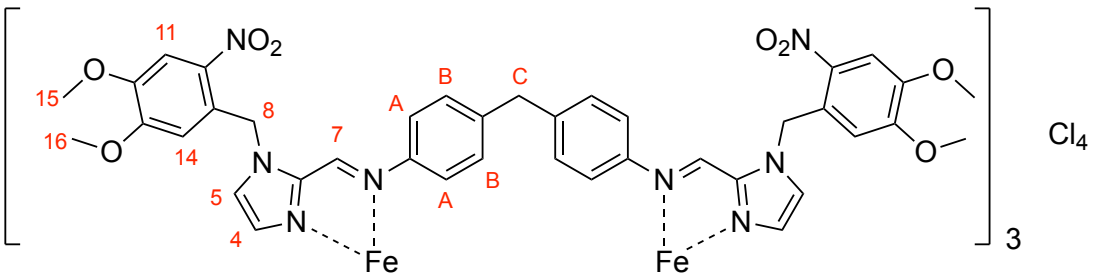

$L_{Im2}"$ (0.025 g, 0.03 mmol) was suspended in methanol (2 mL). Iron chloride tetrahydrate (0.004 g, 0.02 mmol) was dissolved in methanol (3 mL) and added dropwise to the ligand suspension under nitrogen. The reaction mixture was stirred overnight before heating to 60°C for 3 hours. The suspension was then cooled to room temperature and the solvent was removed.

8.2.14. 2-imidazole based nickel rotaxane ($[Ni_2(L_{Im2}")_3.CB10]Cl_4$) via slippage

Based on the work of J. Craig[7].

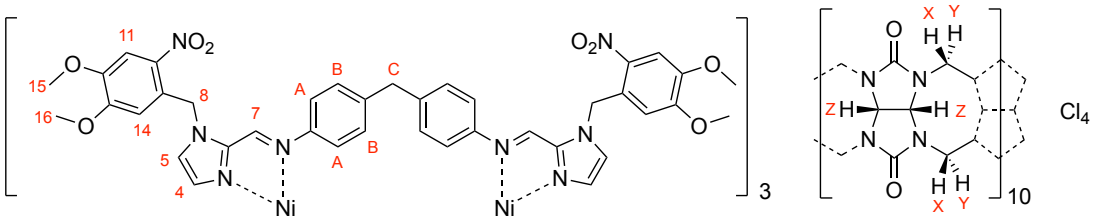

$[Ni_2(L_{Im2}")_3.CB10]Cl_4$ (0.035 g, 0.014 mmol) was suspended in 10% methanol in water (100 mL) and CB10 (0.025 g, 0.015 mmol) was added. The suspension was warmed to 40°C for 3 hours. The methanol was then removed under reduced pressure and the solution filtered (0.45 µm) under vacuo and the precipitate washed with water (5 mL) to give a clear yellow filtrate which was then freeze-dried. A yellow powder was collected (0.038 g, 0.009 mmol, 65% yield).

MS (TOF ES+, H_2O): m/z = 196.02 ($[C_9H_9NO_4 + H]^+$), 816.69 ($[Ni_2(L_{Im2}")_2]^{4+}$), 934.48 ($[Ni_2(L_{Im2}")_2(L_{Im2}')]^{4+}$), 939.24 ($[Ni_2(L_{Im2}")_2(L_{Im2}') + H_2O]^{4+}$), 1003.77 ($[M^{4+}$), 1007.51 ($[Ni_2(L_{Im2}")_3 + H_2O]^{4+}$).

UV-Vis (H_2O, CAH-Ana-030): 243 nm (75,600 $mol^{-1}cm^{-1}$), 301 nm (68,500 $mol^{-1}cm^{-1}$), 329 nm (77,900 $mol^{-1}cm^{-1}$).

8.3. Synthesis of the 5-oxypyridine based cylinders

8.3.1. Synthesis of the 5-(hydroxymethyl)picolinaldehyde

8.3.1.1. Diethylpyridine-2,5-carboxylate

Based on the work of G. Pascu.[8]

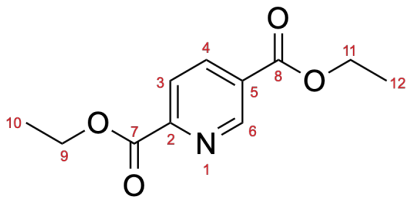

2,5-pyridinecarboxylic acid (5.00 g, 0.03 mol) was suspended in ethanol (15 mL) and cooled to 0°C under argon. Concentrated sulphuric acid (5 mL, 0.09 mmol) was added over 2 hours before refluxing at 80°C for 17 hours. A clear yellow solution was cooled to 65°C before cyclohexane (10 mL) was added and the solution was refluxed at 90°C for 6 hours.

Once cooled, the reaction mixture was poured into ice cold water (500 mL). The solution was neutralised by sodium hydrogen carbonate and extracted with ethyl acetate (210 mL). The yellow organic phase was washed with brine (10 mL), dried over $MgSO_4$ and the solvent removed under vacuo. The crude yellow solution solidified on standing. The product was isolated by silica column chromatography (25-50% ethyl acetate, hexane eluent). The product fractions were combined and the solvent removed to yield a white solid (2.82 g, 0.01 mol, 42% yield).

^{1}H NMR (300 MHz, Chloroform-*d*): δ 9.22 (dd, *J* = 2.1, 0.9 Hz, 1H, H_6), 8.35 (dd, *J* = 8.1, 2.1 Hz, 1H, H_4), 8.11 (dd, *J* = 8.1, 0.9 Hz, 1H, H_3), 4.42 (q, *J* = 7.1 Hz, 2H, $H_{9/11}$), 4.36 (q, *J* = 7.1 Hz, 2H, $H_{9/11}$), 1.37 (t, *J* = 7.1 Hz, 3H, $H_{10/12}$), 1.34 (t, *J* = 7.1 Hz, 3H, $H_{10/12}$).

MS (TOF MS ES+, DCM/MeCN:MeOH): m/z = 224.09 ($[M + H]^+$), 246.07 ($[M + Na]^+$), 469.16 ($[2M + Na]^+$).

8.3.1.2. 2,5-pyridinedimethanol

Based on work by Kramer, Nieger and Bräse.[9]

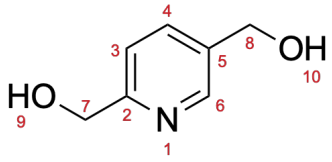

Diethylpyridine-2,5-carboxylate (2.23 g, 0.01 mol) was dissolved in dry ethanol (20 mL, with 3Å mol. sieves) and cooled to 0°C under inert atmosphere. $NaBH_4$ (1.51 g, 0.04 mol) was added portion-wise over 45 minutes. The solution was stirred for 30 minutes before warming to RT and continuing to stir for 2 hours. A clear yellow solution was then heated to reflux for 15 hours 15 mins. The solvent was removed from a cloudy cream solution and the residue was dissolved in acetone (30 mL) and aqueous K_2CO_3 (sat., 30 mL). The solution was heated to reflux at 70°C for 1 hour before cooling to RT. The solution was filtered and separated. The solvent was removed from the organic layer under vacuo to leave a yellow oil which was purified by silica gel column chromatography (12.5% MeOH in DCM). Product containing fractions were collected and the solvent removed to yield a clear oil (0.56 g, 0.004 mol, 40% yield).

^{1}H NMR (400 MHz, DMSO-d_6): δ 8.42 (dd, *J* = 2.2, 0.9 Hz, 1H, H_6), 7.72 (dd, *J* = 8.0, 2.2 Hz, 1H, H_4), 7.43 (dd, *J* = 8.0, 0.9 Hz, 1H, H_3), 5.42 (t, *J* = 5.8 Hz, 1H, H_9), 5.33 (t, *J* = 5.6 Hz, 1H, H_{10}), 4.57 (d, *J* = 4.6 Hz, 2H, H_7), 4.52 (d, *J* = 4.7 Hz, 2H, H_8).

MS (ITMS ES+, EtOH): m/z = 140.2 ($[M + H]^+$), 242.3 ($[C_{11}H_{13}NO_4 + H]^+$). [Unassigned: 214.2 (<10%), (<5%) 188.3, 277.3, 347.3

8.3.1.3. 5-(hydroxymethyl)picolinalehyde (Ald_{5MeO})

Based on the work of G. Pascu.[8]

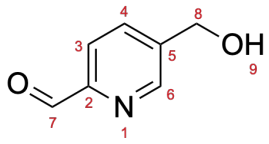

2,5-pyridinedimethanol (0.56 g, 4.0 mmol) and selenium dioxide (0.22 g, 2.0 mmol) were put under argon atmosphere before degassed dioxane (4 mL) and degassed water (0.1 mL) were added. The solution was refluxed at 100°C for 3 hours before allowing the solution to cool to room temperature. The solution was filtered through a 0.45 µm nylon filter and washed with dioxane (6 mL). The solvent was removed from the filtrate giving a cloudy orange oil which was purified by column chromatography (25% to 75% ethyl acetate in hexane eluent) to yield a crystalline off-white solid (0.32 g, 2.3 mmol 58% yield).

^{1}H NMR (300 MHz, DMSO-d_6): δ 9.98 (d, J = 0.7 Hz, 1H, H_7), 8.76 (dd, J = 2.0, 0.9 Hz, 1H, H_6), 7.97 (ddd, J = 8.1, 2.0, 0.8 Hz, 1H, H_4), 7.92 (dd, J = 7.9, 0.9 Hz, 1H, H_3), 5.55 (t, J = 5.7 Hz, 1H, H_9), 4.66 (d, J = 5.6 Hz, 2H, H_8).

MS (TOF ES+, (DCM)/MeOH:H_2O): m/z = 138.06 ($[M + H]^+$), 152.07 ($[C_8H_9O_2N + H]^+$), 170.08 ($[M + MeOH + H]^+$).

8.3.2. Attempted synthesis of the capped 5-(hydroxymethyl)picolinaldehyde

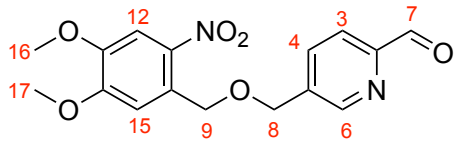

5-(hydroxymethyl)picolinaldehyde (0.07 g, 0.50 mmol) was dissolved in methanol (5 mL) under an inert atmosphere. Potassium carbonate (0.15 g, 0.55 mmol) in methanol (5 mL) and water (2 mL) was added. DMNB-Br (0.08 g, 0.55 mmol) was suspended in methanol (13 mL) was added. The reaction was heated to reflux (67°C) overnight. The sample was cooled to room temperature, filtered and the solvent removed *under vacuo* to collect a pale yellow precipitate.

8.3.3. Synthesis of 5-hydroxypicolinaldehyde

8.3.3.1. 5-hydroxy-2-methylpyridine N-oxide

Based on the work of C. Campbell.[10]

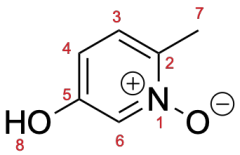

5-hydroxy-2-methylpyridine (8.19 g, 75 mmol) was suspended in acetic acid (100 mL). H_2O_2 (30% wt., aq., 34 mL, 300 mmol) was added over 30 minutes dropwise. The reaction mixture was heated to reflux for 3.5 hours giving a clear yellow solution which was cooled to room temperature and stirred for 16 hours. Solvent volume was reduced under pressure until ~25 mL of a clear yellow solution remained. The solution was poured into cold acetone (125 mL, -20°C) and left in an ice bath for 3 hours. As

no crystals formed, the solution was reduced to ~25 mL again and added to cold acetone (-20°C) in an ice bath again. After 1 hour the solution was placed in a dry ice bath (dry ice with acetone) and allowed to precipitate for 5 hours. An off-white precipitate in a yellow solution was observed and the solution was left in the fridge overnight. A beige precipitate was then collected by filtration under reduced pressure and washed with acetone (3 x 20 ml, -20°C). The precipitate was then allowed to dry under vacuum to give the product (4.03 g, 32 mmol, 43% yield).

^{1}H NMR (400 MHz, DMSO-d_6): δ 10.26 (s, 1H, H_8), 7.81 (d, J = 2.3 Hz, 1H, H_6), 7.24 (d, J = 8.6 Hz, 1H, H_3), 6.77 (dd, J = 8.6, 2.3 Hz, 1H, H_4), 2.23 (s, 3H, H_7).

MS (TOF ES+, DCM/H_2O:CH_3OH) m/z: 126.06 ([M + H]$^+$), 251.10 ([2M + H]$^+$). [Unassigned peaks (<10%): 109.05, 148.04, 164.01, 185.99, 201.97, 234.21, 273.09, 289.06, 349.00, 364.97, 376.15, 398.13]

Rf [80% ethyl acetate:20% hexane with 2 drops of MeOH]: 0.09.

8.3.3.2. 5-(acetoxylmethyl)pyridine-2-yl

Based on the work of C. Campbell[10].

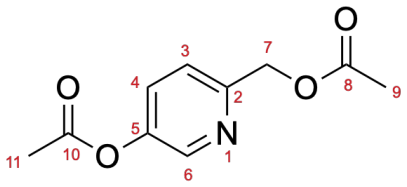

Acetic anhydride (40 mL) was heated to 110°C. 5-hydroxy-2-methylpyridine 1-oxide (3.83 g, 30.6 mol) was added portion wise over 10 minutes while stirring causing a colour change to dark red, and the solution was refluxed (130°C) for 2 hours. The reaction was then cooled to room temperature and ethanol (20 mL) was added while

stirring. The solution was concentrated as far as possible (10 mL solvent removed) before dissolving in chloroform (100 mL) and neutralizing by slow addition of sodium hydrogen carbonate (sat. aq., 30 mL) while stirring. The organic and aqueous layers were separated, and the organic layer dried over $MgSO_4$. The organic layer was then concentrated under reduced pressure to give a wet crude product.

The work up was repeated with the crude. Ethanol (20 mL) was added and stirred vigorously before removing the solvent under reduced pressure to give a brown oil. The oil was dissolved in chloroform (100 mL) and sodium hydrogen carbonate (sat. aq., 30 mL) was added to neutralize any remaining acid. Stirring was continued until no further bubbling was observed and then the organic and aqueous layers were separated. The organic layer was dried over $MgSO_4$ and the solvent removed under reduced pressure to yield a drier product (5.44 g, 26.0 mmol, 85% yield).

^{1}H NMR (400 MHz, Chloroform-*d*) δ 8.38 (dd, *J* = 2.6, 0.7 Hz, 1H, H_6), 7.48 (dd, *J* = 8.5, 2.7 Hz, 1H, H_4), 7.37 (dt, *J* = 8.6, 0.6 Hz, 1H, H_3), 5.19 (s, 2H, H_7), 2.32 (s, 3H, H_{11}), 2.14 (s, 3H, H_9).

MS (TOF ES+, MeOH) m/z: 108.05 ($[C_6H_6NO]^+$), 150.06 ($[C_8H_8NO_2]^+$), 168.06 ($[C_8H_9NO_3 + H]^+$), 210.08 ($[M + H]^+$), 232.06 ($[M + Na]^+$). [Unassigned: 488.15 (100%), 504.14 (40%), 301.12 (15%), 317.12 (15%), (≤10%) 299.10, 333.58, 362, 417.12, 434.14, 595.18]

8.3.3.3. 5-(hydroxymethyl)pyridine-2-ol

Based on the work of C. Campbell.[10]

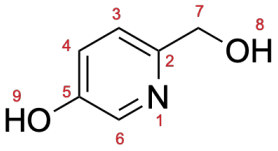

5-(acetoxymethyl)pyridine-2-yl acetate (13.3 g, 60.4 mmol) was suspended in conc. HCl (37%, 110 mL). The mixture was refluxed (90°C) for 1 hour before cooling to room temperature and reducing the volume by 75% under reduced pressure. The pH of the mixture was increased to pH 9 over an ice bath by slow addition of sodium carbonate (sat. aq., 100 mL) and chloroform (70 mL) was added. The aqueous layer was collected and the solvent removed under reduced pressure. A dark brown precipitate was washed with boiling iPrOH (200 mL). The solvent was removed from the filtrate under reduced pressure to yield a yellow solid product. The crude product was purified by SiO_2 plug (5-10% MeOH in DCM) to give an orange solid which was washed with chloroform until the filtrate ran colourless, to yield a beige solid product (3.73 g, 29.9 mmol, 49% yield).

^{1}H NMR (300 MHz, Methanol-d4) δ 8.03 (dd, J = 2.8, 0.7 Hz, 1H, H_6), 7.39 (m, 1H, H_3), 7.26 (dd, J = 8.5, 2.8 Hz, 1H, H_4), 4.61 (s, 2H, H_7).

MS (TOF ES-, MeOH) m/z: 124.04 ($[M - H]^-$). [Unassigned: 325.19 (50%), (<30%) 255.23, 283.27, 286.00, 302.00, 311.16, (<20%) 265.14, 339.19, (<10%) 242.17, 293.18, 353.19, 397.22, 409.03]

8.3.3.4. 5-hydroxypicolinaldehyde

Based on the work of C. Campbell[10].

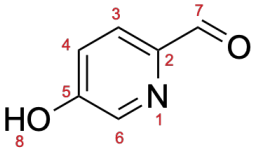

5-(hydroxymethyl)pyridine-2-ol (400 mg, 3.2 mmol) and activated MnO_2 (1 g, 2.5 x mass of starting material) were suspended in dry iPrOH (10 mL) under inert atmosphere and heated to reflux (110°C) for 2.5 hours. A clear supernatent was collected by centrifugation (6000 rpm, 15 mins) of the reaction mixture after cooling to room temperature. Dry iPrOH (15 mL) was used to resuspend the dark solids and the centrifugation repeated twice more. The supernatants were collected, filtered through Celite and the solvent removed under *vacuo*. The crude product was purified by silica gel column chromatography (5% MeOH and DCM), the product containing fractions collected and the solvent removed under vacuo to yield a bright yellow powder (256 mg, 2.1 mmol, 65%).

^{1}H NMR (400 MHz, DMSO-d_6) δ 11.09 (s, 1H, H_8), 9.82 (d, J = 0.8 Hz, 1H, H_7), 8.31 (dd, J = 2.7, 0.6 Hz, 1H, H_6), 7.84 (dd, J = 8.5, 0.6 Hz, 1H, H_3), 7.32 (ddd, J = 8.5, 2.8, 0.8 Hz, 1H, H_4).

^{13}C NMR (101 MHz, DMSO) δ 191.90 (C_7), 157.99 (C_5), 144.77 (C_2), 138.82 (C_6), 123.76 (C_3), 122.41 (C_4).

MS (TOF ES-, MeOH): m/z = 94.03 ($[C_5H_4NO]^-$), 122.02 ($[M - H]^-$). [Unassigned: 311.17 (20%), 325.19 (20%), (≤10%) 226.06, 255.23, 265.14, 283.26, 339.19]

R_f (5% MeOH in DCM): 0.53.

8.3.4. 5-hydroxypyridine based ligand (L_{5OH})

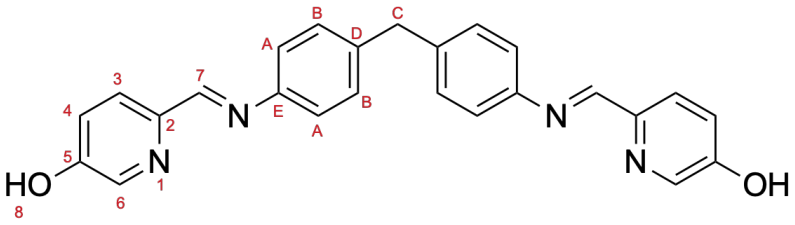

5-hydroxypicolinaldehyde (101 mg, 0.82 mmol) was dissolved in ethanol to give a yellow solution and MDA (79 mg, 0.40 mmol) in ethanol (10 mL) was added dropwise. The solution was stirred at room temperature overnight before the solution was filtered under vacuo and washed with cold ethanol (3 x 5 mL) to isolate a pale yellow precipitate (140 mg, 0.37 mmol, 87% yield).

^{1}H NMR (300 MHz, DMSO-d_6) δ 10.59 (s, 1H, H_8), 8.46 (s, 1H, H_7), 8.23 (d, J = 2.7 Hz, 1H, H_6), 8.02 (d, J = 8.6 Hz, 1H, H_3), 7.35 – 7.25 (m, 3H, H_4 and $H_{A/B}$), 7.25 – 7.15 (m, 2H, $H_{A/B}$), 3.98 (s, 1H, H_C).

MS (TOF ES-, MeOH): m/z = 302 ([hL_{5OH} - H]$^-$), 407 ([L_{5OH} - H]$^-$).

8.3.5. 5-hydroxypyridine based iron cylinder ($[Fe_2(L_{5OH})_3]Cl_4$)

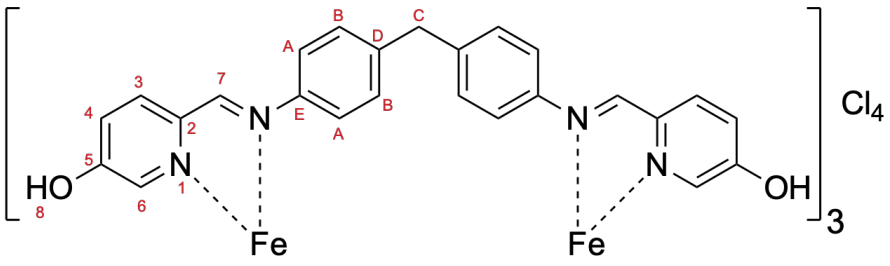

L_{5OH} (130 mg, 0.32 mmol) was suspended in methanol (5 mL) and iron chloride tetrahydrate (40 mg, 0.20 mmol) in MeOH (15 mL) was added slowly. The solution was stirred at room temperature for 3 hours before the solution was filtered and the solvent

removed from the filtrate under vacuo. The residue was redissolved in methanol as far as possible, then filtered before the filtrate was precipitated in diethyl ether (200 mL). A dark purple precipitate was collected by vacuum filtration (110 mg, 0.07 mmol, 74% yield).

^{1}H NMR (300 MHz, Methanol-d_4) δ 8.90 (s, 1H, H_7), 8.48 (d, J = 8.7 Hz, 1H, H_3), 7.74 (dd, J = 8.7, 2.4 Hz, 1H, H_4), 7.01 (d, J = 2.4 Hz, 1H, H_6), 5.60 (br s, 2H, $H_{A/B}$), 4.01 (s, 1H, H_C). [Additional: 7.00 (br s, $H_{A/B}$)]

MS (TOF MS ES+, MeOH) m/z: 199.12 ([MDA + H]$^+$), 304.15 ([hL_{5OH} + H]$^+$), 409.17 ([L_{5OH} + H]$^+$), 445.07 ([M - H]$^{3+}$), 463.03 ([$Fe_2(L_{5OH})_2$ – 2H]$^{2+}$), 534.14 ([$Fe_3(L_{5OH})_6$ + CH_3COO]$^{5+}$), 667.67 ([M – 2H]$^{2+}$), 800.80 ([3M – 7H]$^{5+}$), 889.56 ([2M – 3H]$^{3+}$), 1001.95 ([3M – 8H]$^{4+}$), 1067.47 ([4M - 11H]$^{5+}$), 1111.95 ([5M - 14H]$^{6+}$), 1334.33 ([M – 3H]$^+$).

8.3.6. 5-hydroxypyridine based nickel cylinder ($Ni_2(L_{5OH})_3]Cl_4$)

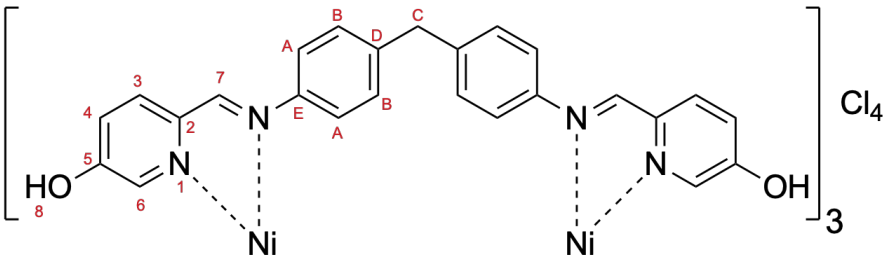

L_{5OH} (12.6 mg, 0.03 mmol) was suspended in methanol (5 mL) and nickel chloride hexahydrate (4.7 mg, 0.02 mmol) in methanol (5 mL) was added dropwise, causing a colour change to a clear orange solution. The solution was filtered (0.45 µm) to remove a white precipitate and the solvent removed under vacuo. The orange residue was redissolved in methanol (minimal) and the complex precipitated in diethyl ether (excess). The orange precipitate was collected by vacuum filtered (0.45 µm filter)

and washed with diethyl ether (10 mL) before drying under vacuo (15 mg, 0.01 mmol, 101% yield).

MS (TOF ES+, MeOH): m/z = 409.26 ($[L_{5OH} + H]^+$), 447.11 ($[M - H]^{3+}$), 466 ($[Ni_2(L_{5OH})_2 - 2H]^{2+}$), 536 ($[Ni_3(L_{5OH})_6 + CH_3COO]^{5+}$), 601.81 ($[Ni_3(L_{5OH})_4 - 3H]^{3+}$), 670.16 ($[M – 2H]^{2+}$, $[2M – 4H]^{4+}$), 804.19 ($[3M – 7H]^{5+}$), 893.20 ($[2M – 3H]^{3+}$), 1004.74 ($[3M – 8H]^{4+}$).

8.3.7. 5-((4,5-dimethoxy-2-nitrobenzyl)oxy)picolinaldehyde (Ald_{5O}')

Based on a published protocol by Alouane *et al.*[11].

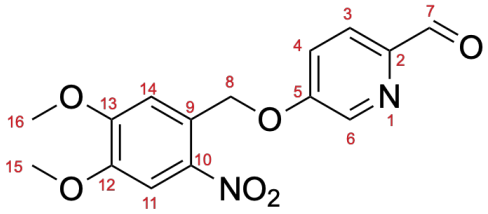

5-hydroxypicolinaldehyde (0.19 g, 1.5 mmol) and 4,5-dimethoxy-2-nitrobenzyl bromide (1.5 mmol) was dissolved in anhydrous DMF (20 mL) under dark conditions. K_2CO_3 (2.25 mmol) was added and the mixture stirred at room temperature for 2.5 hours. DCM (20 mL) and H_2O (20 mL) were added, the organic phase collected and dried over $MgSO_4$. The solvent was evaporated under reduced pressure and the crude product purified by SiO_2 column chromatography (60% DCM: 40% ethyl acetate to 100% ethyl acetate) to give a yellow solid (0.44 g, 1.37 mmol, 91%).

^{1}H NMR (400 MHz, Chloroform-d) δ 10.02 (d, J = 0.8 Hz, 1H, H_7), 8.57 (d, J = 2.8 Hz, 1H, H_6), 8.00 (dd, J = 8.7, 0.6 Hz, 1H, H_3), 7.80 (s, 1H, $H_{11/14}$), 7.43 (ddd, J = 8.7, 2.8,

0.8 Hz, 1H, H_4), 7.26 (d, J = 1.3 Hz, 2H, $H_{11/14}$), 5.63 (d, J = 0.8 Hz, 2H, H_8), 3.99 (s, 6H, H_{15} and H_{16}).

^{13}C NMR (101 MHz, $CDCl_3$) δ 191.96, 157.53, 154.11, 148.46, 147.03, 139.32, 139.22, 126.99, 123.47, 121.06, 109.32, 108.34, 67.71, 56.55, 56.50.

MS (TOF ES+, DCM:MeOH): m/z = 196.06 ($[C_9H_9NO_4 + H]^+$), 319.09 ($[M + H]^+$), 341.07 ($[M + Na]^+$), 351.12 ($[M + MeOH + H]^+$), 373.10 ($[M + MeOH + Na]^+$), 497.11 ($[3M + 2H]^{2+}$), 656.15 ($[4M + H + K]^{2+}$), 659.16 ($[2M + Na]^+$), 672.16 ($[4M + MeOH + H + K]^{2+}$), 691.19 ($[2M + MeOH + Na]^+$), 723.22 ($[2M + 2MeOH + Na]^+$).

8.3.8. DMNB-capped 5-oxypyridine based ligand (L_{5O}")

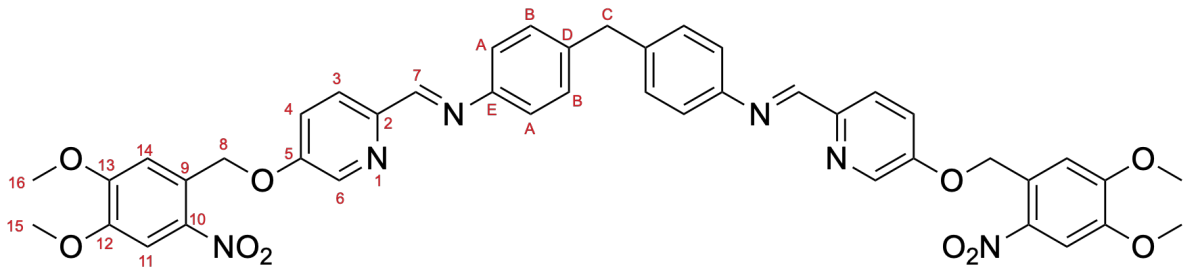

Ald_{5O}' (0.159 g, 0.50 mmol) and 4,4'-methylenedianiline (0.049 g, 0.25 mmol) were refluxed at 80°C in EtOH (20 mL) for 24 hours under dark and inert conditions. The solution was allowed to cool to room temperature before filtering under reduced pressure and wishing with cold EtOH (3 x 10 mL). An orange precipitate was collected and dried in a vacuum desiccator to yield the product (0.07 g, 0.09 mmol, 58% yield).

^{1}H NMR (400 MHz, Chloroform-d) δ 8.57 (s, 1H, H_7), 8.50 (d, J = 2.9, 1H, H_6), 8.18 (d, J = 8.8 Hz, 1H, H_3), 7.80 (s, 1H, $H_{11/14}$), 7.41 (dd, J = 8.8, 2.9 Hz, 1H, H_4), 7.29 (s, 1H, $H_{11/14}$), 7.24 (s, 4H, H_A and H_B), 5.61 (s, 2H, H_8), 4.03 (s, 1H, H_C), 3.99 (d, J = 0.8 Hz, 6H, H_{15} and H_{16}).

MS (ES+, MeCN): m/z = 499.19 ([hL_{5O}' + H]$^+$), 604.22 ([L_{5O}' + H]$^+$), 799.27 ([M + H]$^+$). [Partial assignments: 663.46 (10%), 1461.72 (20%, [M + 662]$^+$), 2125.13 (5%, [M+662+663]$^+$).

8.3.9. DMNB-capped 5-oxypyridine based iron cylinder ([$Fe_2(L_{5O}")_3$]$(PF_6)_4$)

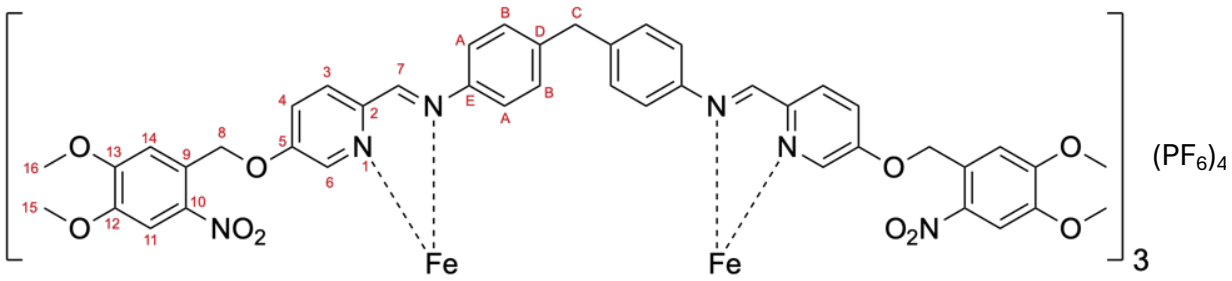

L_{5O}" (0.098 g, 0.12 mmol) was suspended in MeOH (10 mL). Iron(II) chloride tetrahydrate (0.016 g, 80.5 µmol) dissolved in MeOH (20 mL) was added slowly before reflux (75°C) for 1 hour. The dark purple solution was cooled to room temperature, filtered through celite and washed with MeOH (3 x 10 mL). The filtrate was collected, ammonium hexafluorophosphate (0.070 g, 0.43 mmol) in minimal methanol was added and the solution stirred until the solution was colourless. A solid purple precipitate (0.062 g, 0.02 mmol, 50%) was isolated by filtration under reduced pressure and washed with MeOH (2 x 10 mL).

^{1}H NMR (300 MHz, Acetonitrile-d_3, PF_6): δ 8.83 (s, 1H, H_7), 8.48 (d, J = 8.8 Hz, 1H, H_3), 7.98 (dd, J = 8.8, 2.5 Hz, 1H, H_4), 7.74 (s, 1H, H_{11}), 7.18 (s, 1H, H_{14}), 7.02 (d, J = 2.5 Hz, 1H, H_6), 6.93 (s, 2H, $H_{A/B}$), 5.68 – 5.36 (m, 2H, $H_{A/B}$* + H_8), 4.02 (s, 1H, H_C), 3.89 (s, 3H, $H_{15/16}$), 3.84 (s, 3H, $H_{15/16}$).

*Overlapping broad peak.

MS (TOF ES+, MeCN, PF_6): m/z = 338.24 ([erucamide + H]$^+$), 360.32 ([erucamide + Na]$^+$), 626.91 ([$Fe_2(L_{5O}")_3$]$^{4+}$), 675.68 (PEEK tubing), 770.53 ([$Fe_2(L_{5O}")_2(L_{5O}')$ - H]$^{3+}$), 799.27 ([$L_{5O}"$ + H]$^+$), 826.73 ([$Fe_2(L_{5O}")_4$]$^{4+}$), 850 ([$Fe_2(L_{5O}")_3$ + HCOO]$^{3+}$), 884.20 ([$Fe_2(L_{5O}")_3$ + PF_6]$^{3+}$), 1057.77 ([$Fe_2(L_{5O}")_2(L_{5OH})$]). [Unassigned (<10%): 842.21, 856.54, 873]

8.3.10. DMNB-capped 5-oxypyridine based nickel cylinder ($[Ni_2(L_{5O}")_3](PF_6)_4$)

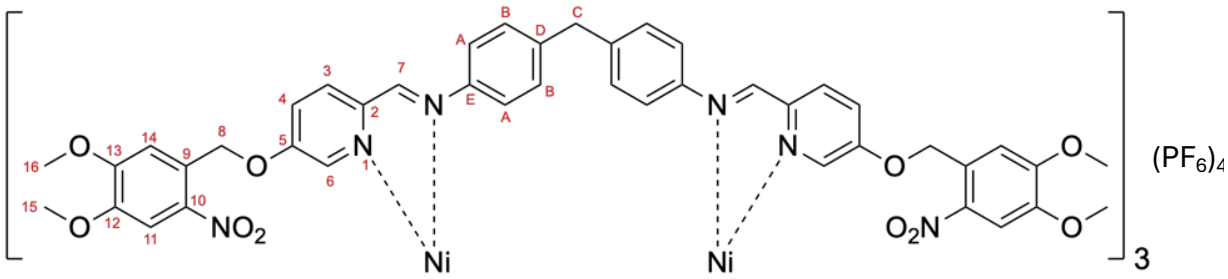

DMNB-O-ligand (0.070 g, 87 µmol) and nickel chloride hexahydrate (0.014 g, 58 µmol) were suspended in MeOH (20 mL) under dark conditions and refluxed (80°C) for 2.5 hours before cooling to room temperature. The solution was filtered through celite and washed with MeOH (minimal) before ammonium hexafluorophosphate (100 mg) was added to the filtrate and the solution allowed to precipitate at room temperature over 2.5 hours. The precipitate was collected by filtration under reduced pressure and washed with methanol (4 x 5 mL) before drying on filter in dark to yield a dark orange solid (0.043 g, 14 µmol, 47%).

MS (TOF ES+, MeCN): m/z = 628.16 ([$Ni_2(L_{5O}")_3$]$^{4+}$), 772.20 ([$Ni_2(L_{5O}")_2(L_{5O}')$ – H]$^{3+}$), 837.54 ([$Ni_2(L_{5O}")_3$ - H]$^{3+}$), 852.55 ([$Ni_2(L_{5O}")_3$ + HCOO]$^{3+}$), 885.87 ([$Ni_2(L_{5O}")_3$ + PF_6]$^{3+}$).

8.3.11. One-pot synthesis of a DMNB-capped 5-oxypryridine based iron cylinder ($[Fe_2(L_{5O}")_3]Cl_4$)

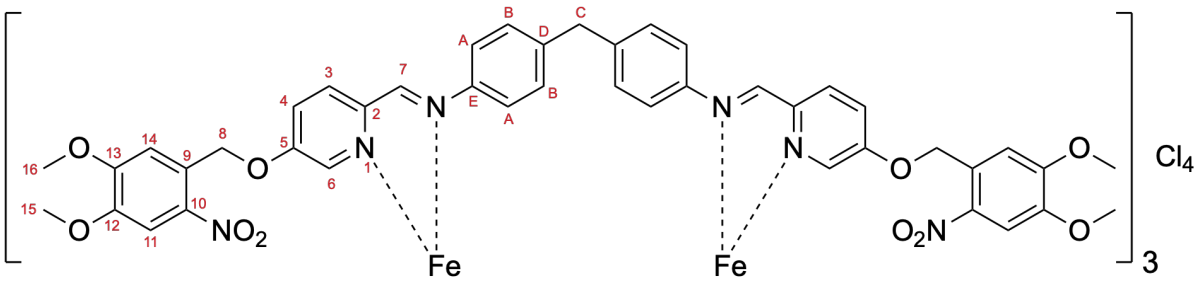

Ald_{5O}" (96 mg, 0.30 mmol), MDA (30 mg, 0.15 mmol) and iron (II) chloride tetrahydrate (18 mg, 0.09 mmol) were suspended in methanol (20 mL) and allowed to stir at room temperature under dark conditions for 17.5 hours. The reaction mixture was filtered and washed with methanol until the filtrate was colourless. The precipitate was then collected and stood in methanol (100 mL) before filtering again and the filtrate of the two filtrations combined. The solution was concentrated under vacuo and NH_4-PF_6 (166 mg, 1.02 mmol) was added and the solution allowed to stand at room temperature under dark conditions for 90 mins. The resulting suspension was filtered to give a dark purple precipitate which was washed with water (10 mL) and methanol (3 x 10 mL).

^{1}H NMR (300 MHz, Acetonitrile-d_3, PF_6) δ 8.81 (s, 1H, H_7), 8.47 (d, J = 8.7 Hz, 1H, H_3), 7.98 (dd, J = 8.9, 2.5 Hz, 1H, H_4), 7.74 (s, 1H, $H_{11/14}$), 7.18 (s, 1H, $H_{11/14}$), 7.06 – 6.77 (m, 3H, H_6 and $H_{A/B}$), 5.71 – 5.35 (m, 2H, $H_{A/B}$), 4.02 (s, 1H, H_C), 3.89 (s, 3H, $H_{15/16}$), 3.84 (s, 3H, $H_{15/16}$).

The purple precipitate was then resuspended in methanol (20 mL) with dowex beads (excess) overnight. The dowex beads were removed by filtration and the solvent

removed from the filtrate to yield a dark purple precipitate (73 mg, 0.03 mmol, 30% yield).

^{1}H NMR (300 MHz, Methanol-d_4) δ 9.03 (s, 1H, H_7), 8.63 (d, J = 8.7 Hz, 1H, H_3), 8.26 – 8.11 (m, 1H, H_4), 7.70 (s, 1H, H_{11}), 7.27 (s, 1H, H_{14}), 7.02 (br s, $H_{A/B}$) 7.00 (d, J = 2.4 Hz, 1H, H_6), 5.66 (br s, $H_{A/B}$) 5.53 (s, 2H, H_8), 4.06 (s, 1H, H_c), 3.89 (s, 3H, $H_{15/16}$), 3.88 (s, 3H, $H_{15/16}$).

MS (TOF MS ES+, MeOH) m/z: 627.91 ($[M]^{4+}$), 770.53 ($[Fe_2(L_{5O}")_2(L_{5O}') - H]^{3+}$), 826.48 ($[Fe_2(L_{5O}")_4]^{4+}$), 847 ($[M + Cl]^{3+}$), 850 ($[Fe_2(L_{5O}")_3 + HCOO]^{3+}$). [Unassigned: (<5%) 856.55, 873.54]

8.3.12. One-pot synthesis of a DMNB-capped 5-oxypyridine based nickel cylinder ($[Ni_2(L_{5O}")_3]Cl_4$)

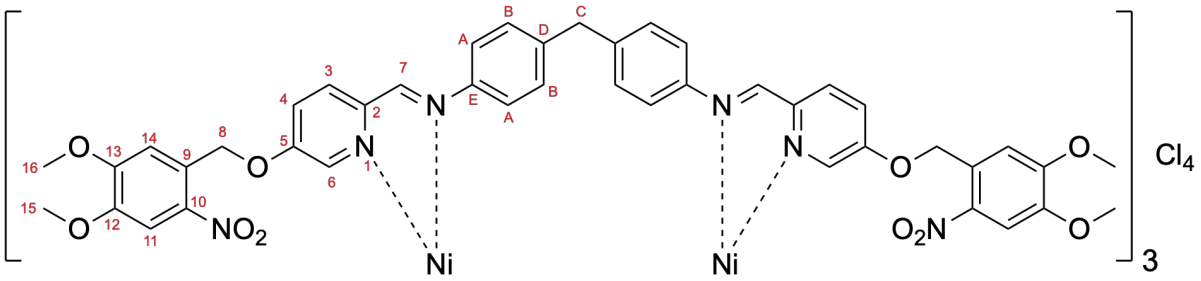

Ald_{5O}" (96 mg, 0.30 mmol), MDA (30 mg, 0.15 mmol) and nickel (II) chloride hexahydrate (21 mg, 0.09 mmol) were suspended in methanol (20 mL) and allowed to stir at room temperature under dark conditions for 17.5 hours. Methanol (100 mL) was added and stirred at room temperature before the reaction mixture was filtered and washed with methanol. NH_4PF_6 (163 mg, 1.00 mmol) was added and the solution allowed to stand at room temperature under dark conditions. The resulting suspension was filtered to give an orange precipitate which was washed with methanol (2 x 10

mL). The orange precipitate (91 mg) was then resuspended in methanol (20 mL) with Dowex resin (excess). The Dowex resin was removed by filtration and the solvent removed from the filtrate to yield an orange precipitate (64 mg, 0.02 mmol, 27% yield).

MS (TOF ES+, MeOH) m/z: 196.06 ($[C_9H_9NO_4 + H]^+$), 628.17 ($[M]^{4+}$), 772 ($[Fe_2(L_{5O}")_2(L_{5O}') - H]^{3+}$), 849.21 ($[M + Cl]^{3+}$). [Unassigned (<5%): 677.69, 749.19, 752.97]

8.3.13. 5-oxypyridine based iron rotaxane ($[Fe_2(L_{5O}")_3.CB10]Cl_4$)

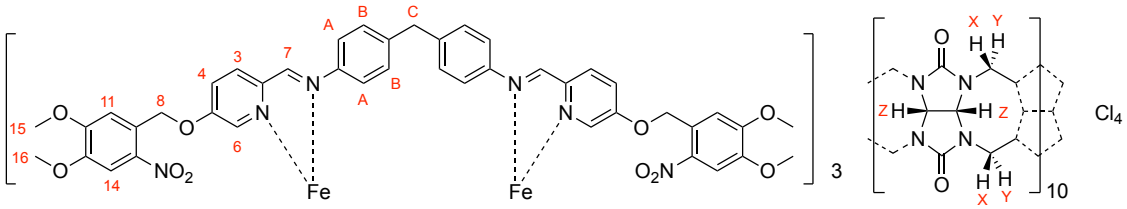

$[Fe_2(L_{5O}")_3]Cl_4$ (27 mg, 0.010 mmol) and CB[10] (18 mg, 0.011 mmol) were suspended in 20% methanol in water (100 mL) and stirred at 50°C for 24 hours under dark conditions. The solution was then filtered and the solvent removed under vacuo to give a pale purple solid.

MS (TOF ES+, MeOH): m/z = 445.13 ([dodecamethylcyclohexacyloxane + H]$^+$), 536.17 and 610.19 (seen with nanospray), 989 ($[Fe_2(L_{5O}")_2(L_{5O}') - O]^{4+}$), 993 ($[Fe_2(L_{5O}")_2(L_{5O}')]^{4+}$), 1042 ($[M]^{4+}$). [Unassigned (<20%): 128.95, (<10%): 239, 274.91, 309.21, 340.88, 429.09, 453.35]

8.3.14. 5-oxypyridine based nickel rotaxane ($[Ni_2(L_{5O}")_3.CB10]Cl_4$)

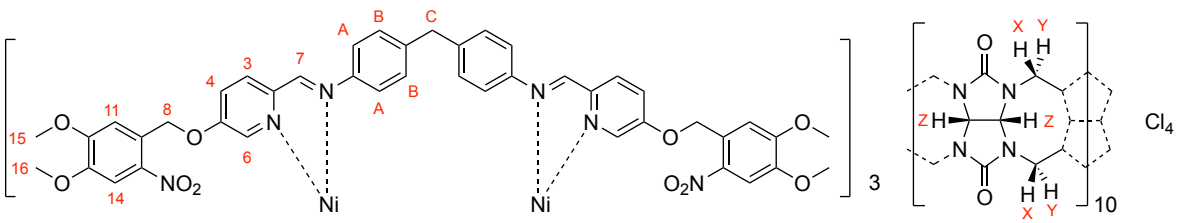

$[Ni_2(L_{5O}")_3]Cl_4$ (27 mg, 0.010 mmol) and CB[10] (18 mg, 0.011 mmol) were suspended in 20% methanol in water (100 mL) and stirred at 50°C for 24 hours under dark conditions. The solution was then filtered and the solvent removed under vacuo to give a pale yellow solid.

MS (TOF ES+, MeOH): m/z = 968.51 ($[Ni_2(L_{5O}")_2(hL_{5O}')]^{4+}$), 1043.54 ($[M]^{4+}$).

[Unassigned (≤10%) 453.34, 475.33, 677.69, 701.50, 843.72, 1303.35, 1403.37]

8.4. Synthesis of the 4-hydroxypyridine based cylinders

8.4.1. Synthesis of 4-hydroxypyridine-2-carboxaldehyde

8.4.1.1. Ethyl 4-oxo-4H-pyran-2-carboxylate

Based on a reported synthesis by Lumetzberger *et al.*[12].

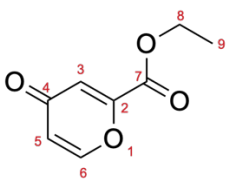

Comanic acid (2.0 g, 14 mmol, purchased from Fluorochem) was suspended in 5% ethanolic sulphuric acid (12 mL) and heated to 80°C for 20.5 hours. The solution was poured into ice water (200 mL) and neutralised with $NaHCO_3$. The solution was

then extracted with ethyl acetate (50 mL x 3) and the combined organic layers washed with brine, dried over $MgSO_4$ and the solvent removed under *vacuo*. The orange powder product (1.6 g) was dissolved in 10% ethanol in ethyl acetate and run through a silica plug using 10% ethanol in ethyl acetate as the mobile phase. All fractions containing product were collected and the solvent removed (1.4 g, 8 mmol, 59% yield).

^{1}H NMR (300 MHz, DMSO-d_6) δ 8.28 (d, J = 5.9 Hz, 1H, H_6), 6.90 (d, J = 2.6 Hz, 1H, H_3), 6.48 (dd, J = 5.9, 2.6 Hz, 1H, H_5), 4.34 (q, J = 7.1 Hz, 2H, H_8), 1.31 (t, J = 7.1 Hz, 3H, H_9).

MS (FTMS EI+, MeOH): 95.01 ($[C_5H_3O_2]^+$), 123.01 ($[C_6H_3O_3]^+$), 140 ($[C_6H_4O_4]^+$), 168 ($[M]^+$). [Unassigned: 69.00 (70%), 112.02 (70%)]

R_f (10% ethanol in ethyl acetate): 0.79

8.4.1.2. 2-hydroxylmethyl-4H-pyran-4-one

Based on a reported synthesis by Lumetzberger *et al.*[12].

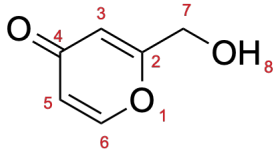

Ethyl 4-oxo-4H-pyran-2-carboxylate (1.38 g, 8.2 mmol) was suspended in methanol (12 mL) and cooled (-10°C) under an inert atmosphere. $NaBH_4$ (0.34 g, 8.9 mmol) was added causing a colour change to dark purple then clear orange and stirred for 2.5 hours. The solution was concentrated under vacuo and poured into cold water (10 mL). The solution was neutralised with H_2SO_4 (10% aq.) and the solvent removed under vacuo to leave a brown oil. The residue was suspended in 10% ethanol in ethyl

acetate (10 mL) and heated to reflux (80°C) for 10 mins. The reaction mixture was cooled to RT, dried over $MgSO_4$ and concentrated to give a brown oil. After standing overnight a white precipitate was observed in an orange oil. The residue was dissolved in 10% ethanol in ethyl acetate with gentle heating (a small amount of red solid was observed). The product was purified by silica column with 10% ethanol in ethyl acetate. Fractions containing the product were collected and the solvent removed under vacuo to give a pale yellow waxy product (0.51 g, 4.1 mmol, 50% yield).

The solid was recrystallised in ethanol with pet ether to give a white crystalline powder which was dried under vacuo (0.29 g, 2.3 mmol, 57% yield for recrystallisation, 28% overall yield).

^{1}H NMR (400 MHz, DMSO-d6): δ 8.11 (dd, J = 5.3, 0.9 Hz, 1H, H_6), 6.30 – 6.17 (m, 2H, H_3 and H_5), 5.67 (t, J = 6.1 Hz, 1H, H_8), 4.29 (dd, J = 6.1, 0.9 Hz, 2H, H_7). **MS** (FTMS EI+, MeOH): 126.03 ([M]+). [Unassigned: 69.00 (95%), 97.03 (100%)] **R_f** (10% ethanol in ethyl acetate): 0.19.

8.4.1.3. 2-(hydroxymethyl)pyridine-4(1H)-one

Based on a reported synthesis by Lumetzberger *et al.*[12].

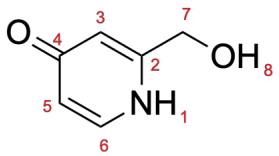

2-hydroxylmethyl-4H-pyran-4-one (269 mg, 2.1 mmol) was dissolved in water (1.8 mL), ammonium carbonate (sat. aq., 0.2 mL), and ammonia solution (28%, 2 mL) to give a yellow solution. The solution was heated to reflux (85-100°C) for 90 mins

before allowing to cool to room temperature. The orange solution was poured over ice and adjusted to pH7 with H_2SO_4. 10% ethanol in ethyl acetate (10 mL) was added and the aqueous layers collected and the solvent removed under vacuo. Ethanol (6 mL) was added to the white residue and refluxed. Water (5 mL) was added to redissolve the white solid and the solution allowed to cool to room temperature. The orange organic layer was collected, dried with $MgSO_4$. Ethanol was added causing a white suspension to form and filtered to give a pale yellow, clear solution which was dried again over $MgSO_4$. The solvent was removed under vacuo to give a white solid residue which was recrystallised from ethanol (40 mg, 0.3 mmol, 15% yield).

^{1}H NMR (300 MHz, Methanol-d4): δ 7.74 (dd, J = 6.8, 0.6 Hz, 1H, H_6), 6.52 – 6.22 (m, 2H, H3 and H5), 4.55 (d, J = 0.8 Hz, 2H, H_7). **MS** (FTMS CI-, MeOH): 96 ($[C_5H_5NO - H]^-$),124.04 ($[M - H]^-$).

Alternative method:

2-hydroxylmethyl-4H-pyran-4-one (2.00 g, 16.0 mmol) was dissolved in water (20 mL), ammonium carbonate (sat. aq., 15 mL), and ammonia solution (28%, 15 mL) to give a yellow solution. The solution was heated to reflux (85-100^{o}C) for 1 hour before allowing to cool to room temperature. The orange solution was poured over ice and neutralised with H_2SO_4 before the solvent was removed under vacuo. The residue was triturated with hot ethanol (~ 600 mL) and the solvent removed from the combined filtrates to yield a crude residue (1.75 g, 14 mmol). The crude was recrystallised from ethanol and the product collected by vacuum filtration and washed with cold ethanol (2 x 5 mL) to give beige crystals (1.06 g, 8.5 mmol, 53% yield).

^{1}H NMR (400 MHz, DMSO-d_6) δ 11.22 (br s, 1H, H_1), 7.67 (s, 1H, H_6), 6.15 (s, 2H, H_3 and H_5), 5.84 – 5.18 (m, 1H, H_8), 4.36 (s, 2H, H_7).

MS (FTMS CI-, MeOH): 80.92 ($[Br]^-$), 124.04 ($[M - H]^-$).

R_f (10% H_2O in MeCN): 0.16.

8.4.1.4. 4-hydroxypicolinaldehyde (Ald_{4OH})

Based on a reported synthesis by Lumetzberger *et al.*[12].

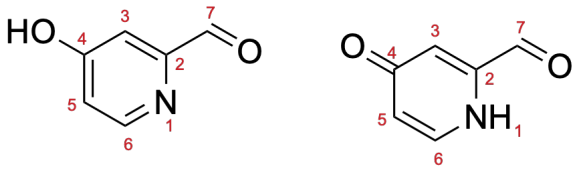

2-(hydroxymethyl)pyridin-4-(1H)-one (72 mg, 0.58 mmol) was suspended in methanol, acetone and DCM (1:1:1, 2 mL). MgO_2 (activated, 334 mg) was added portion-wise hourly (~1/4 every hour) while the suspension was heated (60°C) for four hours. The solution was filtered and washed with the solvent system (6 mL) before the solvent was removed from the filtrate under *vacuo* to leave a brown oil. The crude product was dissolved in methanol and purified by silica gel chromatography (run with ethyl acetate). Fractions containing the product were collected and the solvent removed under vacuo to leave an oily white solid (22 mg, 0.18 mmol, 31% yield).

^{1}H NMR (400 MHz, Methanol-d_4): δ 7.73 (d, J = 7.2 Hz, 1H, H_6), 6.58 (dd, J = 2.7, 0.8 Hz, 1H, H_3), 6.42 (dd, J = 7.1, 2.6 Hz, 1H, H_5), 5.47 (d, J = 0.8 Hz, 1H, H_2). (Peaks have been assigned to the diol form, however small peaks for the aldehyde are also observed.)

MS (FTMS CI-, MeOH): m/z = 94.03 ($[C_5H_4NO]^-$), 122 ($[M - H]^-$). [Unassigned: 94.03]

R_f (10% MeOH in DCM): 0.16

8.4.2. 4-hydroxypyridine based ligand (L_{4OH})

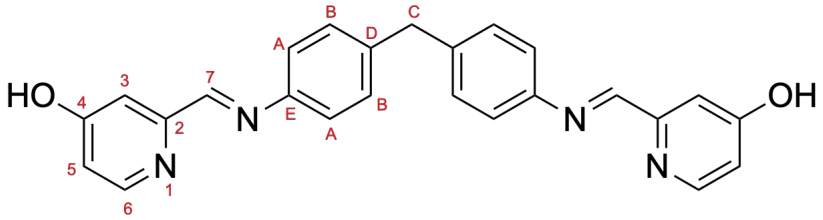

4-hydroxypicolinaldehyde hydrochloride (purchased from J&W Pharmlab, 319 mg, 2.0 mmol) was dissolved in water and neutralised with $NaHCO_3$ (aqueous). The solvent was removed under vacuo to give a pale orange-brown residue. MDA (190 mg, 1.0 mmol) was added and the reagents dissolved in ethanol (30 mL) under an inert atmosphere. The reaction was stirred at room temperature overnight before washing with water (2 x 10 mL) and ethanol (chilled, 3 x 10 mL). A white solid was collected and dried under *vacuo*.

The precipitate and filtrate was recombined and heated to reflux (80°C) in ethanol (25 mL) for 24 hours. The solution was cooled in ice before filtering under vacuo and washing with water (2 x 10 mL) and ethanol (3 x 10 mL). A white precipitate was collected (234 mg, 0.6 mmol, 60% yield).

^{1}H NMR (400 MHz, Methanol-d_4): δ 8.49 (s, 1H, H_7), 7.86 (d, J = 7.1 Hz, 1H. H_6), 7.39 – 7.27 (m, 4H, H_A and H_B), 6.86 (d, J = 2.1 Hz, 1H, H_3), 6.51 (dd, J = 7.1, 2.6 Hz, 1H, H_5), 4.06 (s, 1H, H_c).

MS (TOF MS ES-, MeOH): m/z = 302.13 ([hL_{4OH} - H]$^-$), 407.15 ([L_{4OH} - H]$^-$), 439.18 ([L_{4OH} + MeOH]$^-$).

8.4.3. 4-hydroxypyridine based iron cylinder ([$Fe_2(L_{4OH})_3$]Cl_4)

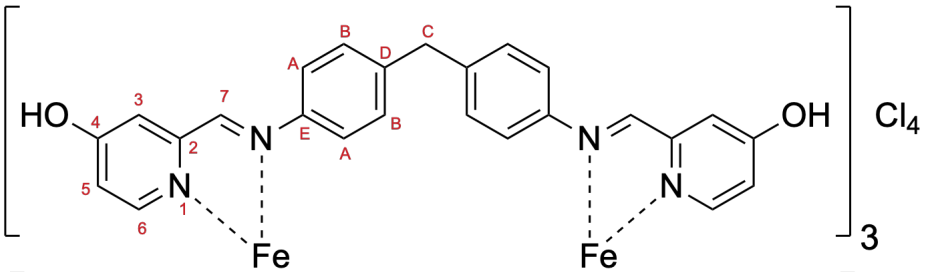

L_{4OH} (104 mg, 0.25 mmol) was suspended in methanol (20 mL) and iron(II) chloride tetrahydrate (28 mg, 0.14 mmol) in methanol (5 mL) was added dropwise. An instant colour change to purple was observed and the solution was stirred at room temperature for 5 hours before filtration under vacuo. The filtrate was collected and the solvent removed under vacuo to yield a purple solid (89 mg, 0.06 mmol, 86% yield).

^{1}H NMR (300 MHz, Methanol-d_4): δ 9.75 (s, 1H), 8.26 (d, *J* = 2.6 Hz, 1H), 7.60 (d, *J* = 6.4 Hz, 1H), 7.43 (dd, *J* = 6.3, 2.7 Hz, 1H), 7.09 – 7.00 (m, 2H), 5.68 – 5.42 (m, 2H), 4.14 (s, 1H).

MS (TOF ES+, MeOH): m/z = 205.09 ([L_{4OH} + 2H]$^{2+}$), 304.15 ([hL_{4OH} + H]$^+$), 360 ([erucamide + H]$^+$), 309.06 ([$Fe_2(L_{4OH})_2$ - H]$^{3+}$), 334.08 ([M]$^{4+}$), 409.16 ([L_{4OH} + H]$^+$), 445.11 ([M - H]$^{3+}$), 463.08 ([$Fe_2(L_{4OH})_2$ - 2H]$^{2+}$), 667.17 ([M – 2H]$^{2+}$). [Unassigned (<20%): 102.13, 274.28, 239.16, 467.10, 541.12, 553.46]

8.4.4. 4-hydroxypyridine based nickel cylinder ($[Ni_2(L_{4OH})_3]Cl_4$)

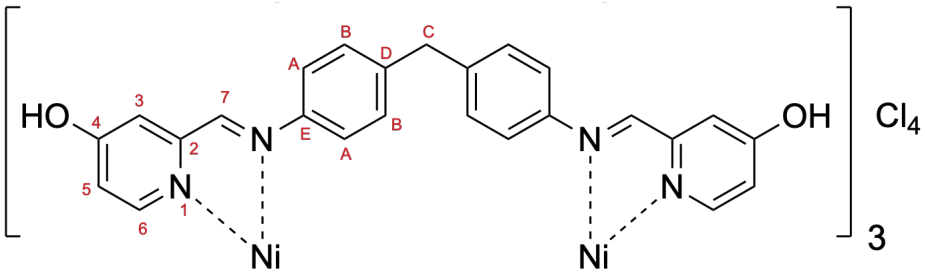

L_{4OH} (104 mg, 0.25 mmol) was suspended in methanol (20 mL) and nickel(II) chloride hexahydrate (33 mg, 0.14 mmol) in methanol (5 mL) was added dropwise. An instant colour change to orange was observed and the solution was stirred at room temperature for 5 hours before filtration under vacuo. The solvent was removed from the filtrate under vacuo and redissolved in minimal methanol to precipitate in chilled diethyl ether (150 mL). An orange precipitate was collected by vacuum filtration (110 mg, 0.07 mmol, 106% yield).

MS (TOF ES+, MeOH): 205.09 ($[L_{4OH} + 2H]^{2+}$), 304.15 ($[hL_{4OH} + H]^{+}$), 311.06 ($[Ni_2(L_{4OH})_2 - H]^{3+}$), 335.58 ($[Ni_2(L_{4OH})_3]^{4+}$), 409.16 ($[L_{4OH} + H]^{+}$), 447.11 ($[Ni_2(L_{4OH})_3 - H]^{3+}$), 465.09 ($[Ni_2(L_{4OH})_2 - 2H]^{2+}$), 670.16 ($[Ni_2(L_{4OH})_3 - 2H]^{2+}$). [Unassigned (<10%): 239.16, 245.08, 309.21, 541.12, 553.46, 568.13, 601.81]

8.4.5. 4-((4,5-dimethoxy-2-nitrobenzyl)oxy)picolinaldehyde (Ald_{4O}')

Based on the work of A. Alouane *et al.*[11].

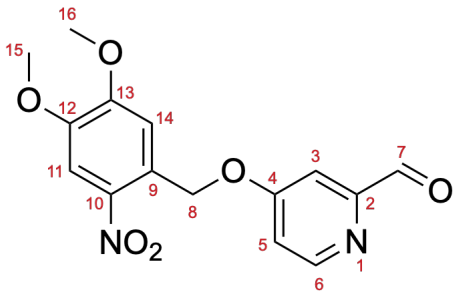

4-hydroxypicolinaldehyde hydrochloride (80 mg, 0.50 mmol) and DMNB-Br (138 mg, 0.50 mmol) were suspended in anhydrous DMF (7 mL) in the dark and under inert atmosphere. The reaction was stirred at room temperature overnight.

The reaction solution was filtered under vacuo and washed with DCM (2 x 10 mL) and water (2 x 10 mL). The combined filtrate was separated, and the organic phase washed with water (10 mL). The aqueous layer was washed with DCM (10 mL) and the organic phases combined. The solvent was removed from the organic phase to yield a yellow powder. The solvent was also removed from the aqueous phases. The precipitate from the reaction, and the residues from both the aqueous and organic phases were combined and redissolved in DMF.

The solution was filtered, and the solvent removed to yield a residue (350 mg). The residue was dry loaded onto a silica gel column using DCM with ethyl acetate (0-50%) to elute the product. Fractions containing the product were combined and the solvent removed to yield a yellow powder (59 mg, 0.19 mmol, 37% yield).

^{1}H NMR (300 MHz, Methylene Chloride-d_2): δ 10.02 (s, 1H, H_7), 8.64 (d, J = 5.7 Hz, 1H, H_6), 7.78 (s, 1H, $H_{11/14}$), 7.58 (d, J = 2.6 Hz, 1H, H_3), 7.23 (s, 1H, $H_{11/14}$), 7.17 (dd, J = 5.6, 2.7 Hz, 1H, H_5), 5.60 (d, J = 0.8 Hz, 2H, H_8), 3.94 (s, 3H, $H_{15/16}$), 3.93 (s, 3H, $H_{15/16}$).

MS (FTMS EI+, DCM): 196 ($[C_9H_9NO_4 + H]^+$), 318 ($[M]^+$). [Unassigned (<20%): 63.02, 77.04, 95.04, 107.04, 123.04, 136.04, 152.07, 165.05, 180.06]

R_f (10% ethanol in ethyl acetate) = 0.81

8.4.6. DMNB-capped 4-oxypicolinaldehyde based ligand (L_{4O}")

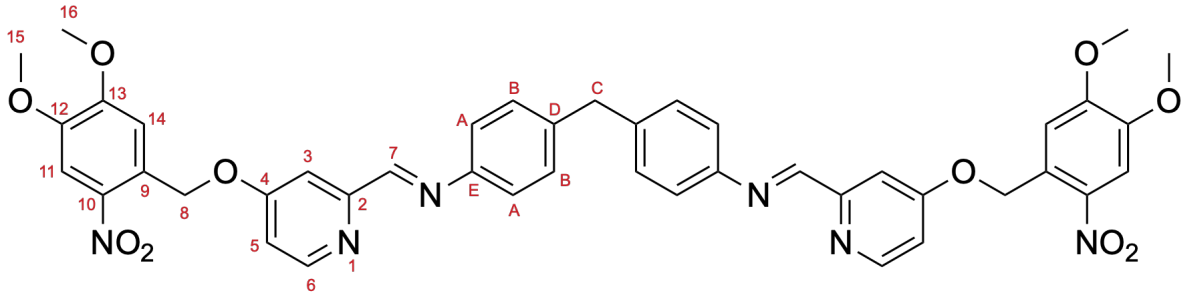

Ald_{4O}' (33 mg, 0.10 mmol) and MDA (20 mg, 0.05 mmol) were dissolved in ethanol (10 mL) under dark and inert conditions before heating to reflux (80°C) for 21 hours 15 mins. The reaction mixture was cooled to room temperature and filtered to collect a white precipitate which wash washed with ethanol (2 x 5 mL) and dried under vacuo (35 mg, 0.04 mmol, 88%).

^{1}H NMR (300 MHz, Methylene Chloride-d2) δ 8.58 (s, 1H, H_7), 8.54 (d, *J* = 5.7 Hz, 1H, H_6), 7.87 (d, *J* = 2.6 Hz, 1H, H_3), 7.78 (s, 1H, $H_{11/14}$), 7.35 – 7.19 (m, 5H, H_A + H_B + $H_{11/14}$), 7.03 (dd, *J* = 5.7, 2.6 Hz, 1H, H_5), 5.62 (d, *J* = 0.9 Hz, 2H, H_8), 4.04 (s, 1H, H_C), 3.95 (s, 3H, $H_{15/16}$), 3.94 (s, 3H, $H_{15/16}$).

MS (TOF ES+, DCM/MeCN): 196.06 ($[C_9H_9NO_4 + H]^+$), 304.15 ($[HL_{4OH} + H]^+$), 400.14 ($[L_{4O}" + 2H]^{2+}$), 409.16 ($[L_{4OH} + H]^+$), 499.20 ($[HL_{4O}' + H]^+$), 604 .22($[L_{4O}' + H]^+$), 799.27 ($[L_{4O}" + H]^+$).

8.4.7. Attempted one-pot method for the DMNB-capped 4-oxypyridine based iron cylinder ($[Fe_2(L_{4O}")_3]Cl_4$)

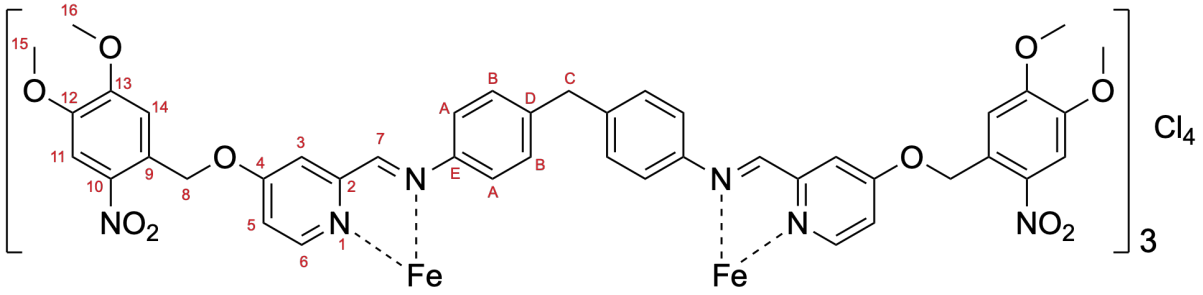

Ald_{4O}' (5.8 mg, 18 μmol), MDA (1.7 mg, 9 μmol), and iron(II) chloride tetrahydrate (1.1 mg, 5 μmol) were dissolved in methanol (10 mL) under dark and inert atmosphere. The solution was stirred at room temperature overnight and before filtering to remove any precipitate and washing with minimal methanol. NH_4PF_6 (13.0 mg, 80 μmol) was added to the filtrate and allowed to stand in the dark at room temperature (28°C) for two hours. The precipitate (6.1 mg) was collected by vacuum filtration and washed with methanol (2 x 5 mL).

^{1}H NMR (PF_6 salt, 300 MHz, Acetonitrile-d_3) δ 9.44 (s, 1H, H_7), 8.44 (d, J = 2.7 Hz, 1H, H_3), 7.83 (s, 1H, $H_{11/14}$), 7.75 – 7.48 (m, 2H, H_5 and H_6), 7.33 (s, 1H, $H_{11/14}$), 6.99 (d, J = 7.5 Hz, 2H, $H_{A/B}$), 5.78 (s, 2H, H_8), 5.51 (d, J = 7.9 Hz, 2H, $H_{A/B}$), 4.12 (s, 1H, H_C), 3.97 (d, J = 7.7 Hz, 7H, $H_{15/16}$).

The precipitate was resuspended in methanol (5 mL) with dowex beads (excess) and allowed to stir in the dark at room temperature for two hours. The solution was filtered to remove the dowex beads and washed with methanol. The solvent was removed from the filtrate and then redissolved in methanol (minimal) to precipitate in cold diethyl ether, giving a purple precipitate (3.7 mg, 1 μmol, 51%).

^{1}H NMR (Cl salt, 300 MHz, Methanol-d_4) δ 9.53 (s, 1H, H_7), 8.58 (d, J = 2.5 Hz, 1H, H_3), 7.85 (s, 1H, $H_{11/14}$), 7.75 – 7.59 (m, 2H, H_5 and H_6), 7.41 (s, 1H, $H_{11/14}$), 7.06 (s, 2H, $H_{A/B}$), 5.82 (s, 2H, H_8), 5.59 (s, 2H, $H_{A/B}$), 4.12 (s, 1H, H_C), 4.00 (s, 3H, $H_{15/16}$), 3.96 (s, 4H, $H_{15/16}$).

8.4.8. One pot method for the DMNB-capped 4-oxypyridine based nickel cylinder ($[Ni_2(L_{4O}")_3]Cl_4$)

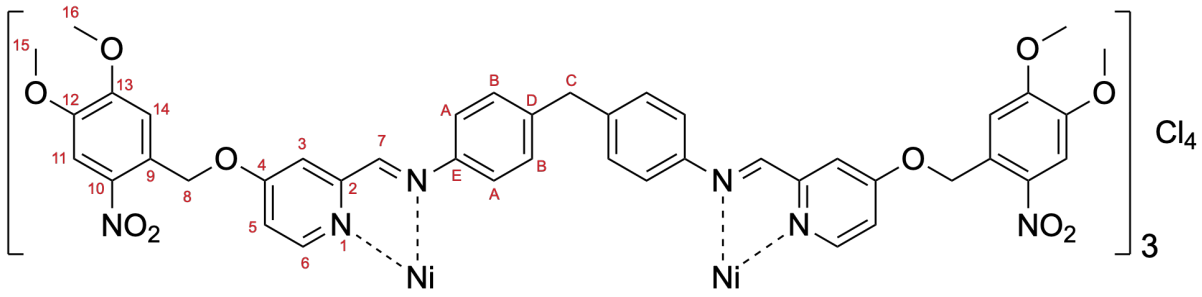

Ald_{4O}" (5.7 mg, 18 μmol), 4,4'-methylenedianiline (1.6 mg, 8 μmol), and nickel(II) chloride hexahydrate (1.2 mg, 5 μmol) were dissolved in methanol under dark and inert conditions. The solution was stirred at room temperature (27°C) overnight and before filtering to remove any precipitate. NH_4PF_6 (excess) was added to the filtrate and allowed to stand in the dark at room temperature (28°C) for two hours. The precipitate (7.1 mg) was collected by vacuum filtration and washed with methanol (2 x 5 mL). The precipitate was resuspended in methanol (5 mL) with dowex beads (excess) and allowed to stir in the dark at room temperature for two hours. The solution was filtered to remove the dowex beads and washed with methanol. The solvent was removed from the filtrate and then redissolved in methanol (minimal) to precipitate in cold diethyl ether, giving an orange precipitate (4.4 mg, 2 μmol, 33%).

MS (TOF ES+, MeOH): m/z = 196 ($[C_9H_9NO_4 + H]^+$), 579.40 ($[Ni_2(L_{4O}")_2(L_{4O}')]^{4+}$), 582.90 ($[Ni_2(L_{4O}")_2(L_{4O}') + H_2O]^{4+}$), 628 ($[M]^{4+}$), 722 ($[Ni_2(L_{4O}")_2(L_{4O}') - H]^{3+}$), 837 ($[M - H]^{3+}$), 843 ($[M + OH]^{3+}$), 850 ($[M + Cl]^{3+}$), 852 ($[M + HCOO]^{3+}$), 858 ($[M + H_2O + HCOO]^{3+}$). [Unassigned (<5%): 866]

8.4.9. DMNB-capped 4-oxypyridine based nickel rotaxane by slippage ($[Ni_2(L_{4O}")_3.CB10]Cl_4$)

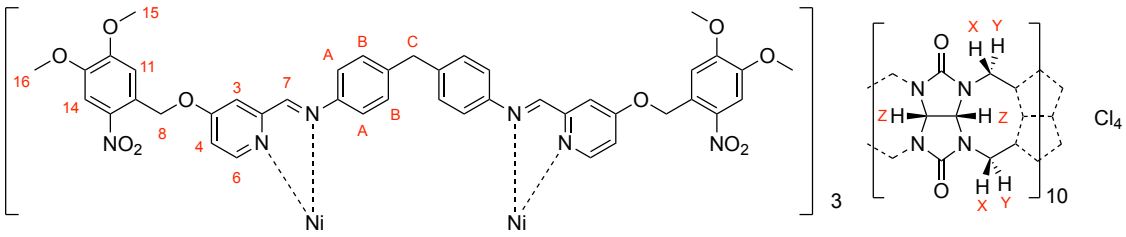

$[Ni_2(L_{4O}")_3]Cl_4$ (2.58 mg, 1.0 μmol) was dissolved in methanol (5 mL) before diluting with deionised water (20 mL). CB10 (1.84 mg, 1.1 μmol) was added and the suspension heated to 50°C overnight. The solvent was removed from the reaction mixture under *vacuo* and the yellow residue suspended in milliQ water (10 mL) overnight. The solution was filtered (0.45 μm) and washed with milliQ water (minimal) before the product was isolated by freeze-drying (1.5 mg, 0.3 μmol, 36% yield).

MS (TOF ES+, MeOH): 196.06 ($[C_9H_9NO + H]^+$), 628.17 ($[Ni_2(L_{4O}")_3]^{4+}$), 701.50 ([]), 968.53 ($[Ni_2(L_{4O}")_2(hL_{4O}').CB10]^{4+}$), 1043.55 ($[M]^{4+}$).

[Unassigned (≤10%): 249.16, 351.12, 359.23, 453.35, 475.33, 679.52, 1403.40]

8.5. Synthesis of the 3-hydroxypyridine based cylinders

8.5.1. 3-hydroxypyridine based ligand (L_{3OH})

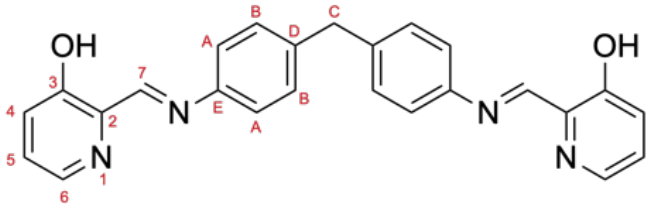

3-hydroxypicolinaldehyde (123 mg, 1.00 mmol) and 4,4'-methylenedianiline (97 mg, 0.49 mmol) were dissolved in ethanol (20 mL) and stirred at room temperature for 26 hours. A bright yellow precipitate was collected by filtration and washed with cold ethanol before drying in a vacuum desiccator overnight (165 mg, 0.40 mmol, 82% yield).

^{1}H NMR (300 MHz, Methylene Chloride-d_2) δ 13.34 (s, 1H, OH), 9.02 (s, 1H, H_7), 8.24 (dd, J = 4.4, 1.5 Hz, 1H, H_6), 7.47 – 7.27 (m, 6H, H_A, H_B, H_4, and H_5), 4.08 (s, 1H, H_C). **^{13}C NMR** (101 MHz, Methylene Chloride-d2) δ 164.43 (C_7), 158.64 ($C_{2/3/E/D}$), 146.19 ($C_{2/3/E/D}$), 142.15 (C_6), 140.47 ($C_{2/3/E/D}$), 137.76 ($C_{2/3/E/D}$), 130.37 ($C_{A/B/4/5}$), 126.95 ($C_{A/B/4/5}$), 124.96 ($C_{A/B/4/5}$), 120.52 ($C_{A/B/4/5}$), 42.26 (C_C). **MS** (TOF ES+, DCM/MeOH): 304.30 ([hL_{3OH} + H]$^+$), 326.38 ([hL_{3OH} + Na]$^+$), 409.09 ([L_{3OH} + H]$^+$). [Unassigned (<20%): 332.33, 363.20, 377.22, 391.23, 405.24, 421.24, 435.25]

R_f (10% ethyl acetate in DCM): 0.54.

8.5.2. 3-hydroxypyridine based iron cylinder ($[Fe_2(L_{3OH})_3]Cl_4$)

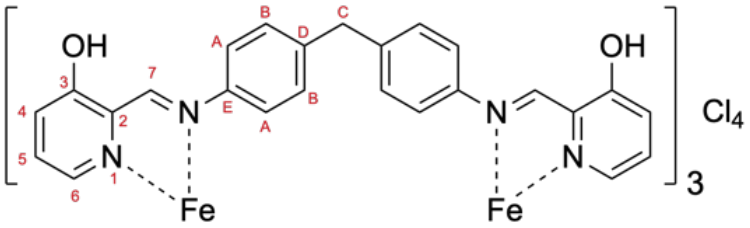

Iron chloride tetrahydrate (20 mg, 0.10 mmol) dissolved in methanol (7 mL) and added to L_{3OH} (63 mg, 0.15 mmol) suspended in methanol (3 mL) dropwise before stirring at room temperature for 75 minutes. The cylinder was filtered through celite and washed with methanol (15 mL). The solvent was removed from the filtrate and redissolved in minimal methanol before precipitating in cold diethyl ether (150 mL). A purple solid was collected by vacuum filtration.

^{1}H NMR (400 MHz, Methanol-d_4): δ 9.07 (s, 1H, H_7), 7.92 – 7.54 (m, 2H, H_4 and H_5), 7.31 (br s), 6.91 (s, 1H, H_6), 6.77 (br s), 5.87 (br s), 5.39 (br s), 4.04 (s, 1H). **MS** (TOF ES+, MeOH): 199.12 ($[MDA + H]^+$), 304.14 ($[hL_{3OH} + H]^+$), 309.06 ($[Fe_2(L_{3OH})_2 - H]^{3+}$), 409.17 ($[L_{3OH} + H]^+$), 445.11 ($[Fe_2(L_{3OH})_3 - H]^{3+}$), 463.08 ($[Fe_2(L_{3OH})_2 – 2H]^{2+}$), 667.16 ($[Fe_2(L_{3OH})_2 – 2H]^{2+}$), 889.55 ($[2Fe_2(L_{3OH})_3 - 5H]^{3+}$), 925.16 ($[Fe_2(L_{3OH})_2 – 3H]^+$), 1000.74 ($[3Fe_2(L_{3OH})_3 – 2H]^{4+}$), 1334.33 ($[Fe_2(L_{3OH})_3 – H]^+$). [Unassigned: 230 (20%), 274.27 (35%), 1002.00 (<5%)]

8.5.3. 3-hydroxypyridine based nickel cylinder ($[Ni_2(L_{3OH})_3]Cl_4$)

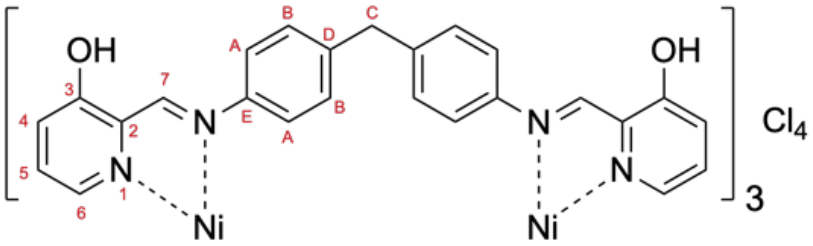

Nickel chloride hexahydrate (24 mg, 0.10 mmol) dissolved in methanol (7 mL) and added to L_{3OH} (63 mg, 0.15 mmol) suspended in methanol (3 mL) dropwise before stirring at room temperature for 2 hours. The cylinder was filtered through celite and washed with methanol (15 mL). The solvent was removed from the filtrate and redissolved in minimal methanol before precipitating in cold diethyl ether (150 mL). An orange solid was collected by vacuum filtration (63 mg, 0.04 mmol, 85% yield).

MS (TOF ES+, MeOH): 409.16 ($[L_{3OH}]^+$), 447.11 ($[Ni_2(L_{3OH})_3 - H]^{3+}$), 465.08 ($[Ni_2(L_{3OH})_2 – 2H]^{2+}$), 601.81 ($[Ni_3(L_{3OH})_4 – 3H]^{3+}$), 670.16 ($[Ni_2(L_{3OH})_3 - 2H]^{2+}$), 893.21 ($[2Ni_2(L_{3OH})_3 – 5H]^{3+}$), 1004.74 ($[3Ni_2(L_{3OH})_3 – 8H]^{4+}$). [Unassigned: 230.25 (10%), 274.27 (30%)]

8.5.4. 3-((4,5-dimethoxy-2-nitrobenzyl)oxy)picolinaldehyde (Ald_{3O}')

Based on published work by Alouane *et al.*[11].

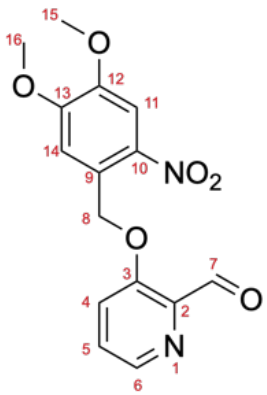

3-hydroxypicolinaldehyde (185 mg, 1.5 mmol) and 4,5-dimethoxy-2-nitrobenzyl bromide (415 mg, 1.5 mmol) were dissolved in anhydrous DMF (20 mL). K_2CO_3 (312 mg, 2.25 mmol). The mixture was stirred at room temperature under dark and inert conditions for 3 hours. A pale-yellow precipitate was collected by vacuum filtration and washed with deionised water before drying under *vacuo*. The precipitate was resuspended in ethanol and filtered to remove water before the precipitate was dried under *vacuo* (324 mg, 1.0 mmol, 68% yield).

^{1}H NMR (300 MHz, Methylene Chloride-d_2): δ 10.23 (d, J = 0.8 Hz, 1H, H_7), 8.45 (dd, J = 4.4, 1.3 Hz, 1H, H_6), 8.13 (s, 1H, $H_{11/14}$), 7.80 (s, 1H, $H_{11/14}$), 7.65 (dt, J = 8.5, 1.1 Hz, 1H, H_4), 7.57 (dd, J = 8.5, 4.4 Hz, 1H, H_5), 5.59 (d, J = 0.9 Hz, 2H, H_8), 4.17 (s, 3H, $H_{15/16}$), 3.95 (s, 3H, $H_{15/16}$).

MS (TOF ES+, DCM/MeOH): 196.06 ([$C_9H_9NO_4$ + H]$^+$), 319.09 ([M + H]$^+$), 351.12 ([M + MeOH + H]$^+$). [Unassigned: 333 (50%)]

8.5.5. DMNB-capped 3-hydroxypyridine based ligand (L_{3O}")

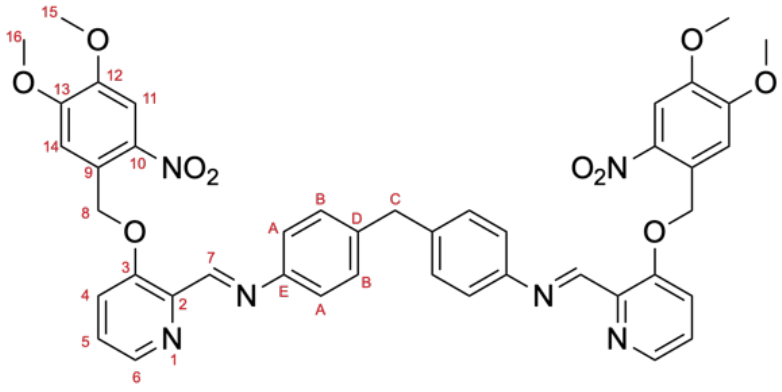

Ald_{3O}' (160 mg, 0.50 mmol) was suspended in ethanol (5 mL) and under dark and inert conditions. MDA (50 mg, 0.25 mmol) was dissolved in ethanol (15 mL) and

added dropwise to the solution before heating to reflux (80°C) for 15 hours. The precipitate was collected under vacuo and washed with methanol (2 x 10 mL) to yield a pale yellow powder (187 mg, 0.23 mmol, 94%).

^{1}H NMR (300 MHz, Chloroform-d) δ 9.00 (s, 1H, H_7), 8.48 (dd, J = 4.4, 1.4 Hz, 1H, H_6), 7.79 (s, 1H, $H_{11/14}$), 7.49 (s, 1H, $H_{11/14}$), 7.48 (dd, J = 8.6, 1.3 Hz, 1H, H_4), 7.40 (dd, J = 8.5, 4.4 Hz, 1H, H_5), 7.24 (d, J = 2.2 Hz, 4H, H_{A+B}), 5.63 (d, J = 0.8 Hz, 2H, H_8), 4.04 (s, 1H, H_C), 3.95 (s, 3H, $H_{15/16}$), 3.72 (s, 3H, $H_{15/16}$).

MS (TOF ES+, DCM/MeOH): 196.06 ([$C_9H_9NO_4$ + H]$^+$), 499.19 (HL_{3O}', [$C_{28}H_{26}N_4O_5$ + H]$^+$), 799.27 ([M + H]$^+$), 831.30 ([M + MeOH + H]$^+$). [Unassigned peaks: 274.28 (20%), (<10%) 230.25, 341.08, 432.28]

8.5.6. DMNB-capped 3-hydroxypyridine based iron cylinder ([$Fe_2(L_{3O}")_3$]Cl_4)

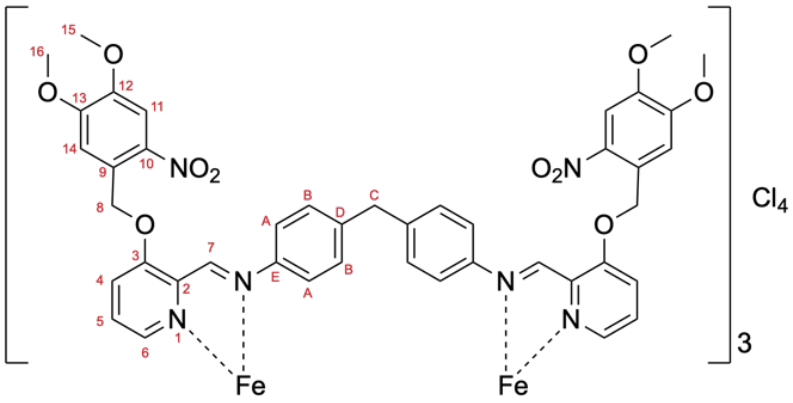

L_{3O}" (73 mg, 0.09 mmol) and iron(II) chloride tetrahydrate (12 mg, 0.06 mmol) were suspended in methanol and heated under reflux for 2 hours. The solution was allowed to cool to room temperature and filtered through Celite. The solvent was removed and redissolved in minimal methanol to precipitate in diethyl ether. The purple precipitate was then collected by vacuum filtration (21 mg, 0.01 mmol, 26% yield).

^{1}H NMR (300 MHz, Methanol-d_4) δ 8.88 (s, 1H, H_7), 8.28 (d, J = 8.9 Hz, 1H, H_3), 7.86 (dd, J = 8.8, 5.4 Hz, 1H, H_5), 7.77 (s, 1H, $H_{11/14}$), 7.45 (br s, $H_{A/B}$), 7.35 (s, 1H, $H_{11/14}$), 7.08 (d, J = 5.3 Hz, 1H, H_6), 6.67 (br s, $H_{A/B}$), 5.96 (d, J = 11.3 Hz, 1H, H_{8a}), 5.91 (br s, $H_{A/B}$) 5.70 (d, J = 11.3 Hz, 1H, H_{8b}), 4.85 (br s, $H_{A/B}$), 4.01 (s, 1H, H_C), 3.95 (s, 3H, $H_{15/16}$), 3.89 (s, 3H, $H_{15/16}$).

MS (TOF ES+, MeOH): m/z = 196.09 ([$C_9H_9NO_4$ + H]$^+$), 199.12 ([MDA + H]$^+$), 455.12 ([dodecamethylcyclohexanesiloxane + H]$^+$), 626.91 ([M^{4+}), 770.54 ($Fe_2(L_{3O}")_2(L_{3O}')$ - H]$^{3+}$), 850.89 ([M + HCOO]$^{3+}$), 855.57 ([M + H_3CCOO]$^{3+}$). [Unassigned: 429.09 (25%), 536.17 (90%), 610.19 (25%), (<20%) 102.13, 149.02, 274.27, 318.11, 341.02, 920.97]

8.5.7. Attempted synthesis of the DMNB-capped 3-oxypyridine based nickel cylinder ($[Ni_2(L_{3O}")_3]Cl_4$)

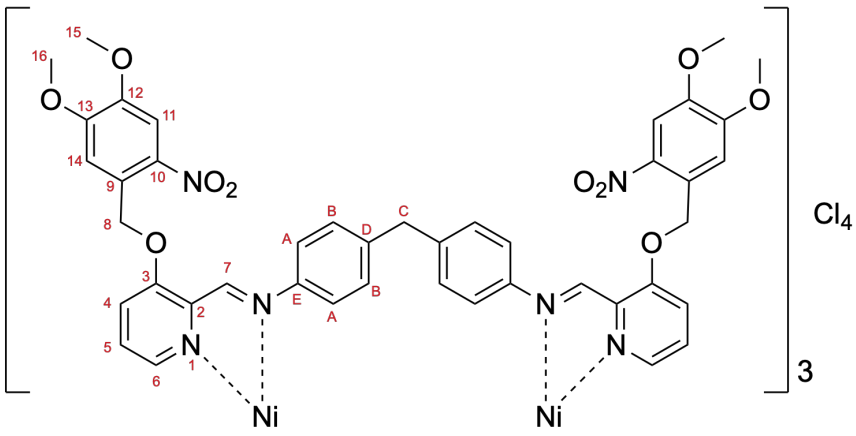

L_{3O}" (74 mg, 0.09 mmol) and nickel(II) chloride hexahydrate (14 mg, 0.06 mmol) were suspended in methanol and heated under reflux for 25.5 hours. The solution was allowed to cool to room temperature and filtered through Celite and washed with methanol (2 x 10 mL). The solvent was removed and redissolved in minimal methanol

to precipitate in diethyl ether. The purple precipitate was then collected by vacuum filtration.

8.5.8. DMNB-capped 3-hydroxypyridine based nickel cylinder ($[Ni_2(L_{3O}")_3]Cl_4$)

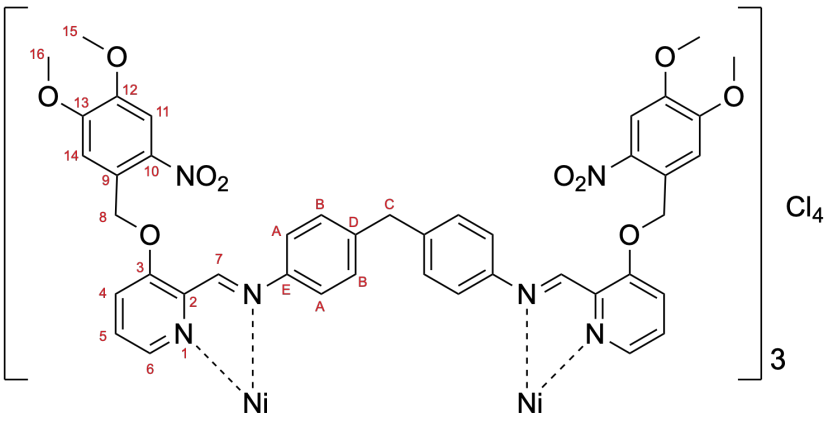

$[Ni_2(L_{3OH})_3]Cl_4$ (10 mg, 0.007 mmol) was dissolved in methanol (400 µL) and diluted with deionised water (1600 µL). K_2CO_3 (4 mg, 0.028 mmol) was added to form a cloudy solution before heating to 80°C. DMNB-Br (12 mg, 0.042 mmol) was added portion-wise over 2 hours. After two hours, three further equivalents of DMNB-Br were added portion-wise (approx. 2 mg per half hour). After a further a further hour of stirring, a further equivalent of K_2CO_3 (1 mg) was added followed by an additional equivalent of DMNB-Br (2 mg) after 30 minutes. 6 hours after the first addition the reaction was allowed to cool to room temperature, filtered under vacuo (through nylon) and washed with methanol (4 x 5 mL). NH_4PF_6 (50 mg) was added to the filtrate and allowed to stand overnight. The resulting precipitate was collected by vacuum filtration and washed with water (2 x 5 mL) and methanol (5 mL).

The isolated precipitate (12 mg) was suspended in methanol (20 mL) with Dowex beads and stirred for 1 hour. The solution was filtered and washed with

methanol (5 mL) before the filtrate was concentrated, filtered (44 μm) and added dropwise to diethyl ether to precipitate. The orange precipitate was collected by vacuum filtration (8 mg, 0.003 mmol, 41% yield).

MS (TOF ES+, MeOH): m/z= 196.06 ($[C_9H_9NO_4 + H]^+$), 579.41 ($[Ni_2(L_{3O}")_2(L_{3O}')]^{4+}$), 628.17 ($[M]^{4+}$), 707.18 ($Ni_2(L_{3O}")_2(L_{3OH}) - H]^{3+}$), 772.20 ($[Ni_2(L_{3O}")_2(L_{3O}') - H]^{3+}$), 849.55 ($[M + Cl]^{3+}$), 1060.28 ($Ni_2(L_{3O}")_2(L_{3OH}) - 2H]^{2+}$).

8.6. UV-visible spectroscopy

8.6.1. Instrumentation

All spectra were recorded using an Aligent Cary 5000 UV-Vis-NIR Spectrophotometer (Epsilon, Stability, 300 nm/min) or an Aligent Cary 60 UV-Vis Spectrophotometer (Epsilon, Photocleavage). Quartz cuvettes (1 mL or 3 mL, 1 cm pathlength) were used in all cases.

8.6.2. Epsilon Values

For each complex a minimum of three stock solutions were made and diluted to measure the absorbance (300 nm/min) at five different concentrations. The average absorbance at the peak maxima was recorded for each concentration and the epsilon calculated using the Beer-Lambert Law which was averaged across all concentrations.

8.6.3. Photocleavage

All photocleavage experiments were completed using the irradiation set up detailed in Chapter 3 (4.8 Wm^{-1}, 365-370 nm, 11 W estimated power) borrowed from the Pike research group at the Department of Chemistry, University of Birmingham. Cylinder (2 μM, MeOH) and rotaxane (2 μM, H_2O) solutions were placed in a 3 mL absorbance cuvette and irradiated in 5-minute intervals up to 30 minutes, then 10-minute intervals up to an hour. Solutions were mixed between each irradiation, and a sample (20 μL) was taken for mass spectrometry before the absorbance spectrum was recorded.

8.6.4. Stability

Methanolic stock solutions of the cylinders (0.5 mM for $[Ni_2(L_{4OH})_3]Cl_4$, 1 mM for all others) were diluted to 2 μM in either milliQ water or methanol. The absorbance spectrum was recorded (0.33 s per 1 nm) at various time intervals (*Table 4*).

Time / Hours	Interval / Mins	Number of scans
0 – 0.5	5	6
0.5 - 1	10	3
1 - 3	30	5
3 - 24	60	21

Table 4: The time intervals at which scans were taken.

8.7. Gel electrophoresis

8.7.1. Stock solution preparation

Tris-base (107.8 g), and boric acid (55 g) were dissolved in deionised water (1 L) to make a 10x TB buffer stock. This was then diluted for lower concentration buffer solutions with milliQ water (unless otherwise stated).

DNA stock solutions (S1: CGGAACGGCACTCG, S2: CGAGTGCAGCGTGG, S3: CCACGCTCGTTCCG) of 10 μM of each DNA strand and therefore is 10 μM of potential 3WJ.

1 mM stock solutions of each cylinder complex were prepared in methanol. Due to the poor solubility a 50 μM stock solution of the imidazole-based rotaxane and a 20 μM stock solution of the 5-oxypyridine rotaxane was prepared in milliQ water. Each stock solution was diluted to a 10 μM solution in milliQ water.

8.7.2. Gel preparation

A 12% polyacrylamide gel was prepared from acrylamide solution (20 mL) in milliQ water (25 mL) and 10x TB buffer (5 mL). A 10% ammonium persulphate solution (w:v, 400 μL) and TEMED (40 μL) were added quickly and the solution gently mixed before pouring into a horizontal mould with a comb to set for 1 hour.

8.7.3. Sample preparation

30 μL sample solutions were made up to be 1 μM of a 3WJ DNA stock with varying concentrations of cylinder (0.5, 1, 2 and 4 μM) in a 1x TB buffer. This was achieved using the volumes shown in *Table 5*. Samples were incubated for 1 hour at

37°C before 50% glycerol solution (7.5 µL) was added to each sample. The progress of the gels was monitored using TriTracker (5 µL) in 5x TB buffer (6 µL) and milliQ water (19 µL).

Sample Type (3WJ : Cylinder)	DNA stock solution (10 µM) / µL	Cylinder stock solution (10 µM) / µL	5x TB buffer / µL	MilliQ water / µL
3WJ only (1:0)	3.0	0.0	6.0	21.0
0.5 µM cylinder (1:0.5)	3.0	1.5	6.0	19.5
1 µM cylinder (1:1)	3.0	3.0	6.0	18.0
2 µM cylinder (1:2)	3.0	6.0	6.0	15.0
4 µM cylinder (1:4)	3.0	12.0	6.0	9.0

Table 5: Showing the volume of each stock solution required for each type of sample for gel electrophoresis.

For the imidazole-based photocleavage gel, the 10 µM stock of each imidazole-based cylinder (80 µL) was irradiated in black-walled, reduced volume (1 mL) cuvettes and a sample (10 µL) taken at each time point (0, 15, 30, and 60 mins). The irradiated samples (3 µL) were then added to the DNA solutions, before incubating and addition of glycerol as usual.

Irradiation in the presence of the DNA was achieved by making a stock solution (150 µL) from the DNA stock solution (10 µM, 15 µL) and the rotaxane solution (10 µM, 15 µL) in 5x TB buffer (30 µL) and milliQ water (90 µL). This was irradiated in a black-walled, reduced volume (1 mL) cuvette and samples (30 µL) taken at each irradiation time point (0, 15, 30, and 60 mins). These samples were then incubated and glycerol added as usual.

For the 5-oxypyridine based photocleavage gel, a 2 µM stock (1 mL) was made for each of the cylinders and rotaxane. Each stock was irradiated in a black walled cuvette and samples (50 µL) taken at each irradiation time point (0, 30, and 60 mins). Between irradiations, the UV-visible absorbance spectrum and the mass spectrum was

recorded for each sample. The irradiated cylinder or rotaxane samples (2 μM, 15 μL) were then added to the DNA solutions (3 μL of 10 μM DNA stock solution, 6 μL of 5x TB buffer solution, and 6 μL of milliQ water) and incubated as usual before glycerol was added.

For samples where irradiation was completed in the presence of the 3WJ, a stock was made for each metal complex containing the cylinder or rotaxane (10 μM stock, 9 μL), the DNA stock solution (9 μL), 5x TB buffer (18 μL), and milliQ water (54 μL). A sample (30 μL) was taken at each irradiation time point (0, 30, and 60 mins). These samples were then incubated and glycerol added as usual.

8.7.4. Running and imaging

PAGE studies were completed using a Bio-Rad Protean II xi Cell with an Amersham Bioscience EPS 301 Electrophoresis Power Supply. A running dye (12 μL) was loaded into the end wells (1 and 20) as well as any unused wells. Samples (12 μL) were loaded into the remaining wells (2-19) and the gels were run for between 2 to 2.5 hours at 140 V in 1x TB buffer (diluted with deionised water). Once finished, the gel was stained with SYBR gold solution (10 μL in 300 mL of 1x TB buffer) for 30 to 45 minutes and imaged with an AlphaImager Gel Imaging System (Alpha Innotech) using 302 nm irradiation. Images were processed using ImageJ[13].

8.8. List of References

1 G. R. Fulmer, A. J. M. Miller, N. H. Sherden, H. E. Gottlieb, A. Nudelman, B. M. Stoltz, J. E. Bercaw and K. I. Goldberg, *Organometallics*, 2010, **29**, 2176–2179.

2 M. Loos, C. Gerber, F. Corona, J. Hollender and H. Singer, *Anal. Chem.*, 2015, **87**, 5738–5744.

3 ESI+ Common Background Ions, https://www.waters.com/webassets/cms/support/docs/bkgrnd_ion_mstr_list.pdf, (accessed January 2024).

4 F. Tuna, M. R. Lees, G. J. Clarkson and M. J. Hannon, *Chem. Eur. J.*, 2004, **10**, 5737–5750.

5 M. Pascu, PhD Thesis, University of Birmingham, 2007.

6 V. Sadovnikova, PhD Thesis, University of Birmingham, 2011.

7 J. S. Craig, PhD Thesis, University of Birmingham, 2023.

8 G. I. Pascu, PhD Thesis, University of Birmingham, 2008.

9 J. J. P. Kramer, M. Nieger and S. Bräse, *Eur. J. Org. Chem.*, 2013, **2013**, 541–549.

10 C. D. J. Campbell, PhD Thesis, University of Birmingham, 2019.

11 A. Alouane, R. Labruère, K. J. Silvestre, T. Le Saux, F. Schmidt and L. Jullien, *Chem. Asian. J.*, 2014, **9**, 1334–1340.

12 A. Lumetzberger, W. Löwe, M. Weber and P. Luger, *J. Heterocycl. Chem.*, 2007, **44**, 155–159.

13 C. A. Schneider, W. S. Rasband and K. W. Eliceiri, *Nat. Methods.*, 2012, **9**, 671–675.

9. APPENDIX

9.1. Extended mass spectra assignments

The following mass spectra have been featured in this thesis (Chapter 6, Figures 148, 153, and 159) with fewer assignments for clarity. The extended assignments have been included below with the extended key shown in Table 6.

Helicates (+ CB10 for rotaxanes)

	Full Ligands		Half Ligands
0	$[M_2(L_{OH})_3]$		$[M_2(L_{OH})_2(hL_{OH})]$
1	$[M_2(L_O')(L_{OH})_2]$		$[M_2(L_{OH})(L_O')(hL_{OH})]$
2	$[M_2(L_O'')(L_{OH})_2]$		$[M_2(L_O')_2(hL_{OH})]$
3	$[M_2(L_O')_3]$		$[M_2(L_O'')(L_O')(hL_{OH})]$
4	$[M_2(L_O'')_2(L_{OH})]$		$[M_2(L_O'')_2(hL_{OH})]$
5	$[M_2(L_O'')_2(L_O')]$		$[M_2(L_O'')_2(hL_O')]$
6	$[M_2(L_O'')_3]$		

Table 6: Key for mass spectra assignments.

9.1.1. Irradiation of $[Ni_2(L_{5O}'')_3.CB10]Cl_4$ in methanol

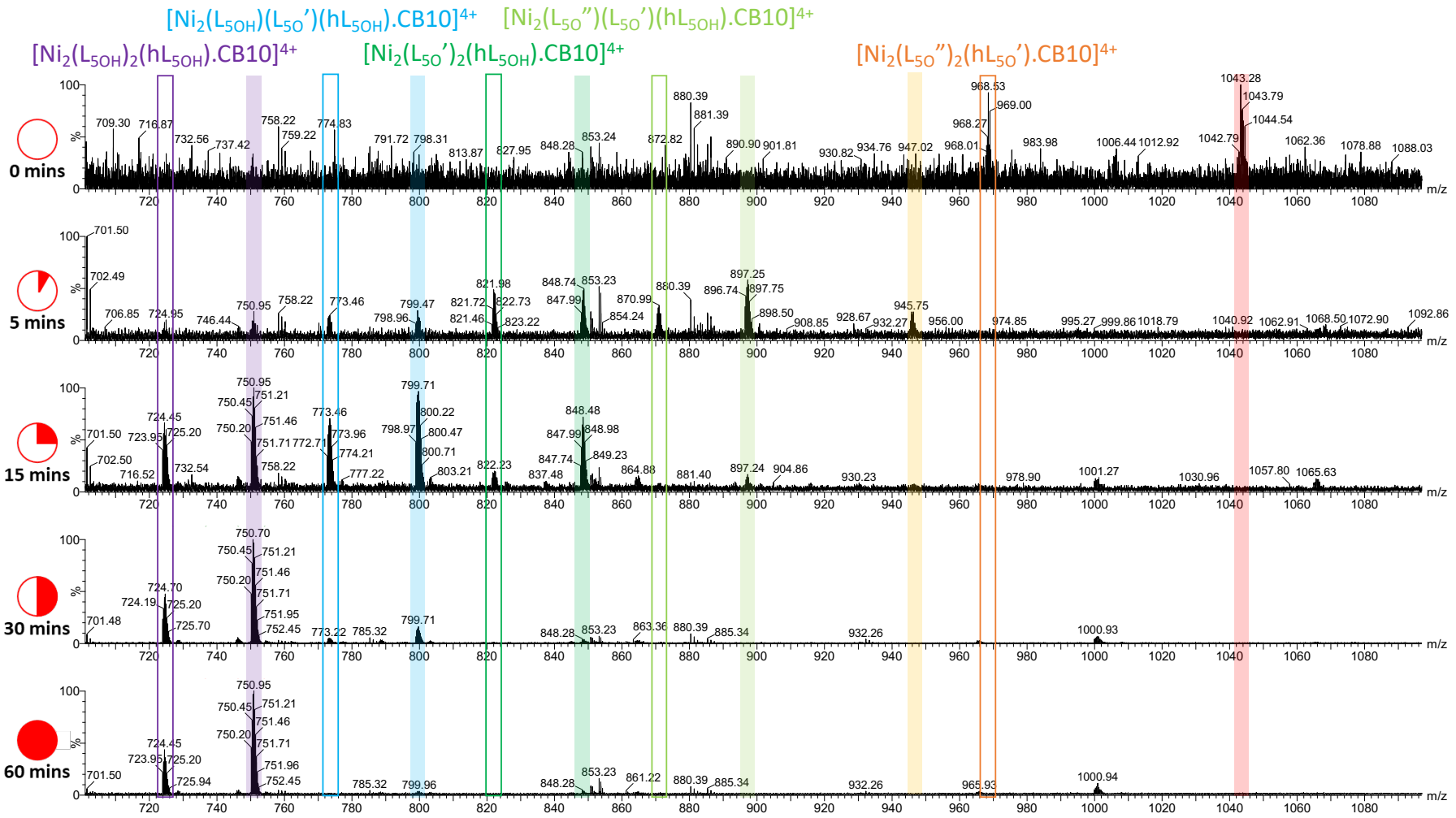

Figure 163: Mass spectra (TOF ES+, MeOH, 700-1100 m/z of $[Ni_2(L_{5O}'')_3.CB10]Cl_4$ over 60 minutes of irradiation highlighting the 4+ charged species and including half ligand containing species (see Figure 148).

9.1.2. Irradiation of $[Ni_2(L_{4O}'')_3.CB10]Cl_4$ in methanol

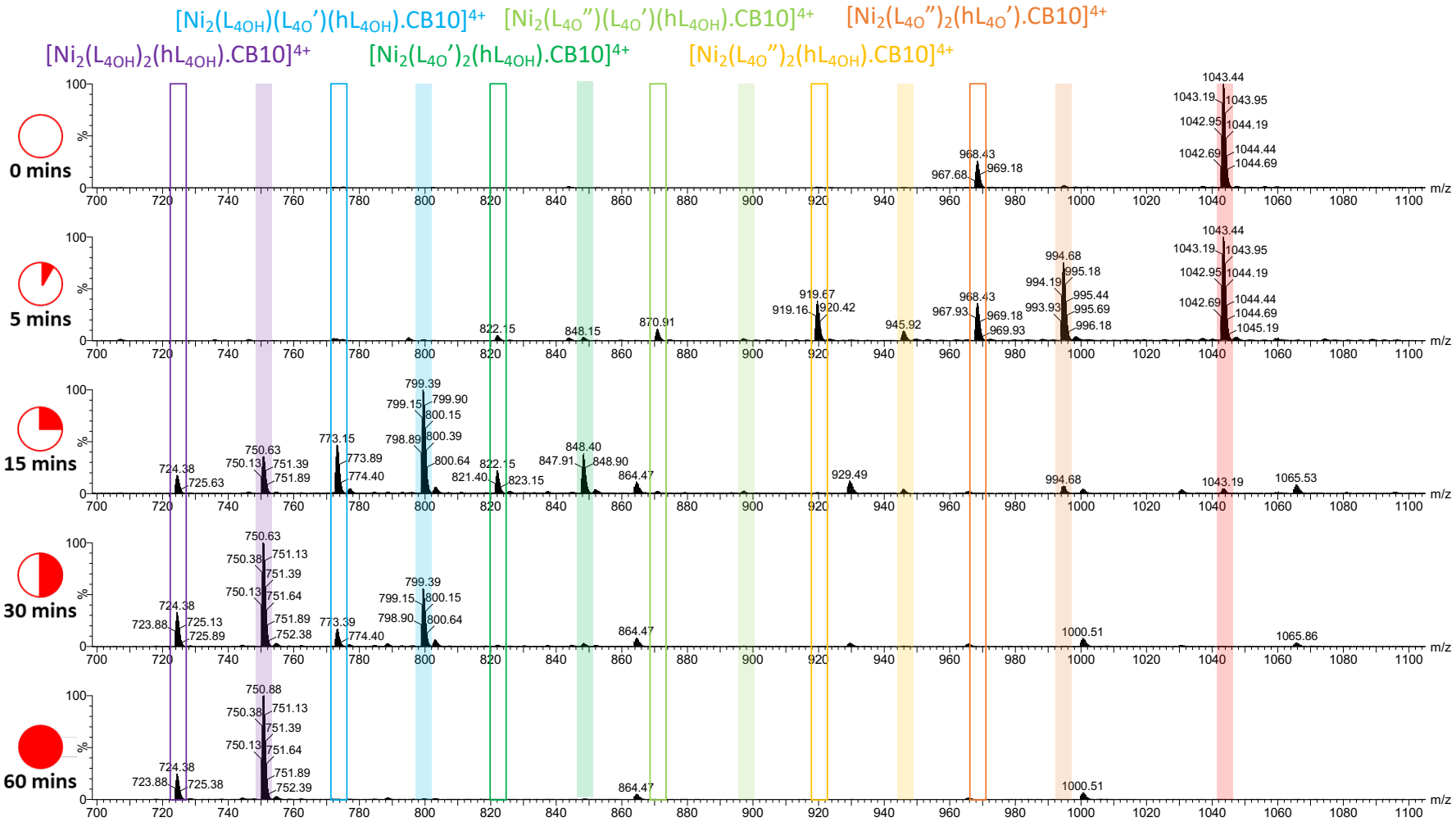

Figure 164: Mass spectra (TOF ES+, MeOH, 700-1100 m/z) of $[Ni_2(L_{4O}'')_3.CB10]Cl_4$ over 60 minutes of irradiation highlighting the 4+ charged species and including half ligand containing species (see Figure 153).

9.1.3. Irradiation of $[Ni_2(L_{5O}'')_3.CB10]Cl_4$ under aqueous conditions

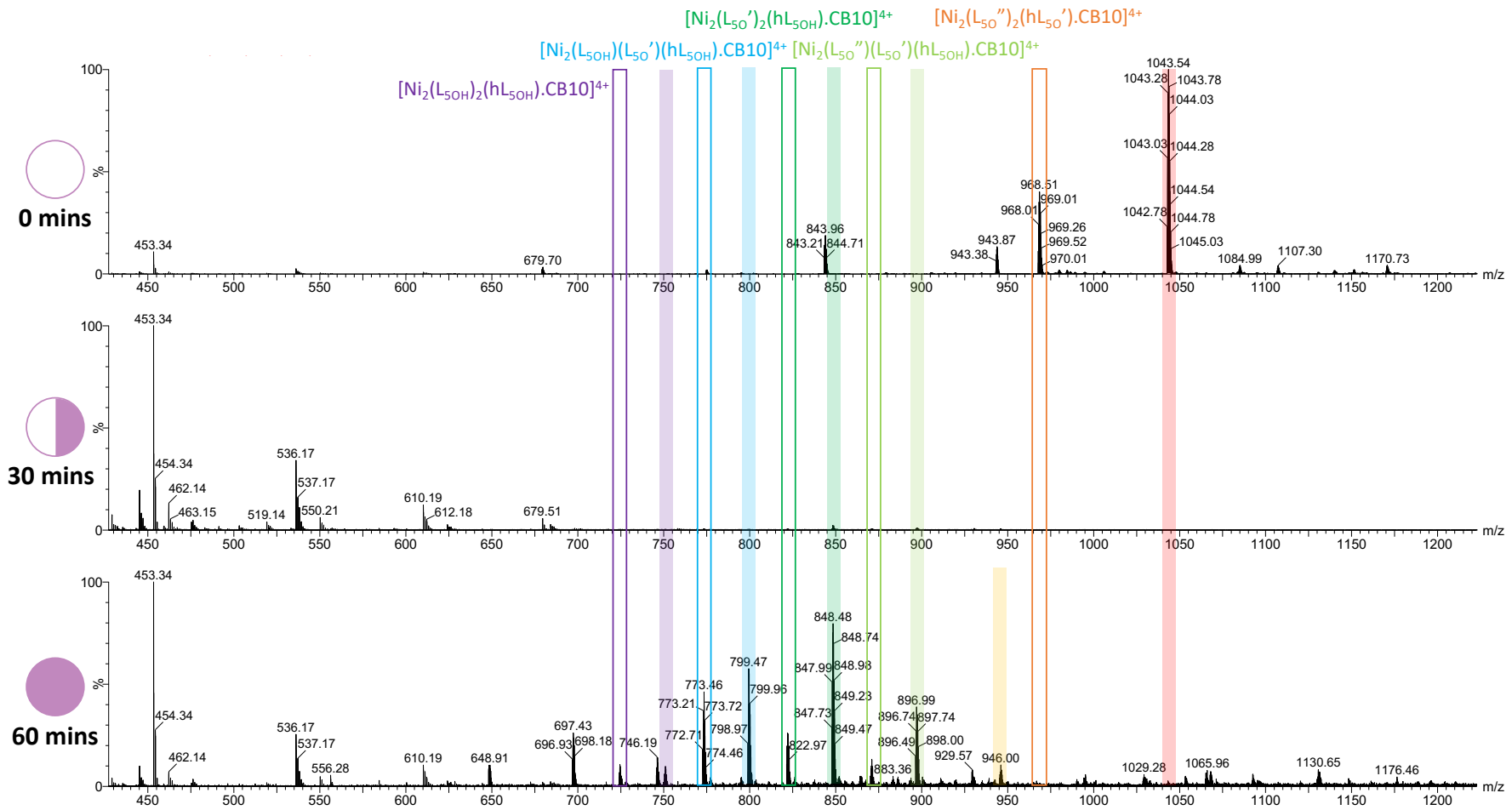

Figure 165: Mass spectra (TOF ES+, H_2O, 280-980 m/z) of the 5-oxypyridine rotaxane $[Ni_2(L_{5O}'')_3.CB10]Cl_4$ at increasing irradiation time points (see Figure 159).